

Alma Mater Studiorum – Università di Bologna

Dottorato di Ricerca in Meccanica delle Strutture

XX Ciclo

Settore scientifico disciplinare

ICAR/08 – Scienza delle Costruzioni

Probabilistic Approaches in Civil Engineering

**Generation of Random Fields and
Structural Identification with Genetic Algorithms**

Paolo Bocchini

Relatore

Prof. Erasmo Viola

Correlatore

Prof. George Deodatis

Coordinatore del Dottorato

Prof. Erasmo Viola

Esame finale anno 2008

“Probabilistic Approaches in Civil Engineering: Generation of Random Fields and Structural Identification with Genetic Algorithms”, a dissertation prepared by Paolo Bocchini, in partial fulfillment of the requirements for the degree of Doctor of Philosophy, has been accepted and approved by the following:

Prof. Mario Di Paola

Prof.ssa Lucia Faravelli

Prof. Marco Savoia

Alma Mater Studiorum – Università di Bologna

Ph.D. program in Structural Mechanics

**Probabilistic Approaches
in Civil Engineering
Generation of Random Fields and
Structural Identification with Genetic Algorithms**

Paolo Bocchini

Adviser: Prof. Erasmo Viola

Co-adviser: Prof. George Deodatis

Abstract

The inherent stochastic character of most of the physical quantities involved in engineering models has led to an always increasing interest for probabilistic analysis.

Many approaches to stochastic analysis have been proposed. However, it is widely acknowledged that the only universal method available to solve accurately any kind of stochastic mechanics problem is Monte Carlo Simulation. One of the key parts in the implementation of this technique is the accurate and efficient generation of samples of the random processes and fields involved in the problem at hand. In the present thesis an original method for the simulation of homogeneous, multi-dimensional, multi-variate, non-Gaussian random fields is proposed. The algorithm has proved to be very accurate in matching both the target spectrum and the marginal probability. The computational efficiency and robustness are very good too, even when dealing with strongly non-Gaussian distributions. What is more, the resulting samples possess all the relevant, well-defined and desired properties of “translation fields”, including crossing rates and distributions of extremes.

The topic of the second part of the thesis lies in the field of non-destructive parametric structural identification. Its objective is to evaluate the mechanical characteristics of constituent bars in existing truss structures, using static loads and strain measurements. In the cases of missing data and of damages that interest only a small portion of the bar, Genetic Algorithms have proved to be an effective tool to solve the problem.

A Nicoletta, che sa seguirmi e guidarmi

*A Federico, Giacomo, Filippo e Matteo,
che anche quando la mia mente era a Manhattan,
persa nei campi aleatori,
hanno tenuto il mio cuore a Cesena*

Acknowledgements

The present thesis is the last milestone of an educational path that started in the suburbs of Cesena twenty-three years ago and reached Columbia University in the hearth of Manhattan. A few people have shared this whole wonderful experience with me, many more have been on my side for some time and I would like to thank all of them.

The first thought goes to my tutors, Prof. Viola and Prof. Nobile, that have wisely planned and led my research and teaching activities during the Ph.D. course. In particular, I would like to thank Prof. Viola for continually reminding of the most important things in life and for his ability to find always the words that make me feel calm and serene.

To Prof. Ubertini, that is for me a professor as well as a friend, I want to say “thanks” for the time that he has always found to listen to me and to give me suggestions on countless topics.

Prof. Deodatis has changed the way I do my job and has made me feel really able to give my little contribution to the world of scientific research. I want to manifest my greatest gratitude to him for his advice and for his encouragement.

I am deeply indebted also to Prof. Popescu, for his kindness and his helpful advice on stochastic geomechanics and Dynaflo.

I can not forget the other Ph.D. students in Structural Mechanics and all the young people that study and work at “Scienza delle Costruzioni” and at “LaMC”. I do not name them all, because they have been important as single friends, but much more as a group, to which they made me feel to belong, since the very first days of the Ph.D. course.

A special thanks goes to Manuel Miranda, that initiated me into the mysteries of FFT. We have been able to spend days lost in our researches, sharing a six square meter office without saying a word. Nevertheless, we shared much more than the office, and with his kindness he has been a true friend, in a moment in which I really needed one.

I want to mention also those people that, in different ways, have always been with me: my mother, my father, my sisters, my brothers-in-law and all my friends. They are the solid foundation on which I have built my life. No matter what happens, I know I will always be able to count on them.

Last, but not least, I have to thank my four amazing nephews and my wife Nicoletta, that gave me the utmost proof of love leaving everything for me. This thesis is dedicated to you, because in the rare moments in which my love for research is not enough to support the effort and the commitment that this wonderful job requires, you give me the strength to smile, to relax, to look forward and to enjoy my life.

Contents

1	Introduction	1
I	Simulation of Random Fields	7
2	Critical Review of Previous Research Work	9
2.1	Introductory Remarks	10
2.2	SRM for Gaussian Fields	10
2.3	SRM for Non-Gaussian Fields	12
2.3.1	Yamazaki and Shinozuka (1988)	12
2.3.2	Deodatis and Micaletti (2001)	15
2.3.3	Shi and Deodatis (2004)	17
3	Simulation of 1D-1V Strongly Non-Gaussian Random Fields	21
3.1	Introductory Remarks	22
3.2	Proposed Simulation Methodology	23
3.2.1	Compute the Starting Gaussian SDF $S_{gg}(\kappa)$	23
3.2.2	Save $S_{gg}(\kappa)$	25
3.2.3	Generate a Sample Function $\hat{g}(x)$ Using SRM	25
3.2.4	Compute the Variance of $\hat{g}(x)$	27
3.2.5	Map $\hat{g}(x)$ into $\hat{f}(x)$	27

3.2.6	Compute $S_{ff}(\kappa)$	27
3.2.7	Compute the Average SDF, $\bar{S}_{ff}(\kappa)$	29
3.2.8	Compute the Error ε Between the Target and Computed SDF	30
3.2.9	Accept Iteration and Save $S_{gg}(\kappa)$	30
3.2.10	Reject Iteration and Restore the Saved $S_{gg}(\kappa)$	32
3.2.11	Apply Random Perturbation to $S_{gg}(\kappa)$	32
3.2.12	Compute the Average $\bar{S}_{gg}(\kappa)$	34
3.3	Numerical Examples	35
3.3.1	Comparison with the Algorithms Presented in Sec. 2.3	36
3.3.2	Other Strongly Non-Gaussian Distributions	41
3.3.3	Limits of Applicability of the Proposed Methodology	46
3.4	Concluding Remarks and Computational Efficiency	46
4	Simulation of nD-1V Strongly Non-Gaussian Random Fields	51
4.1	Introductory Remarks	52
4.2	Proposed Simulation Methodology	53
4.2.1	Theoretical Aspects	53
4.2.2	Computational Aspects	54
4.3	Numerical Example	55
4.4	Concluding Remarks and Computational Efficiency	59
5	Simulation of 1D-mV Strongly Non-Gaussian Random Fields	61
5.1	Introductory Remarks	62
5.2	Proposed Simulation Methodology	63
5.2.1	Simulation of Gaussian Vector Fields	64
5.2.2	Mapping to a Non-Gaussian Vector Field	65
5.3	Underlying Gaussian CSDM	66
5.3.1	Compute the Underlying Gaussian Auto-SDF's	67
5.3.2	Select a Couple of Indexes r and s	67
5.3.3	Compute the Starting Gaussian Coherence	69

5.3.4	Compact the CSDM to a 2-by-2	72
5.3.5	Save $\gamma_{rs}(\kappa)$	72
5.3.6	Compute $\mathbf{H}(\kappa_k)$	72
5.3.7	Generate Sample Functions $\hat{g}_r(x)$ and $\hat{g}_s(x)$	74
5.3.8	Compute the Variance of $\hat{g}_r(x)$ and $\hat{g}_s(x)$	75
5.3.9	Map $\hat{g}_r(x)$ and $\hat{g}_s(x)$ into $\hat{f}_r(x)$ and $\hat{f}_s(x)$	75
5.3.10	Compute the Cross-Spectrum of $\hat{f}_r(x)$ and $\hat{f}_s(x)$	75
5.3.11	Compute the Average Cross-Spectrum, $\bar{S}_{rs}^f(\kappa)$	76
5.3.12	Compute the Error ε Between the Target and Computed Cross-Spectrum	76
5.3.13	Accept Iteration and Save $\gamma_{rs}^g(\kappa)$	77
5.3.14	Reject Iteration and Restore the Saved $\gamma_{rs}^g(\kappa)$	78
5.3.15	Apply Random Perturbation to $\gamma_{rs}^g(\kappa)$	78
5.3.16	Compute the Average $\bar{\gamma}_{rs}^g(\kappa)$	79
5.3.17	Compute the Complete Underlying Gaussian CSDM	80
5.4	Numerical Examples	80
5.4.1	Kaimal-Davenport Cross-Spectral Density Matrix	80
5.4.2	Artificially Correlated Spectrum	83
5.5	Concluding Remarks and Computational Efficiency	89
6	Simulation of Multi-Variate, Gaussian, Ergodic Random Fields 93	
6.1	Introductory Remarks	94
6.2	Decomposition of the Target CSDM	95
6.3	Generation of \hat{g}_c	97
6.4	Spectrum of \hat{h}_{cd}	98
6.5	Computation of the CSDM	98
6.6	Consistency with the Proof of Ergodicity by Deodatis (1996)	102
6.7	Numerical Examples	104
6.7.1	Triangular Spectrum	104
6.7.2	Parabolic Spectrum	115

6.7.3	Kaimal Spectrum	120
6.8	Concluding Remarks	121
7	Applications to Civil Engineering	123
7.1	Introductory Remarks	124
7.2	Stochastic Geomechanics	124
7.3	Cable-Bridges Reliability	130
7.4	Other Possible Applications	132
II	Structural Identification and Damage Assessment	135
8	Identification of Truss Structures	137
8.1	Introductory Remarks	139
8.2	Proposed Methodology	140
8.2.1	Three-Dimensional Externally Statically Determinate Structures	140
8.2.2	Externally redundant structures	146
8.3	Substructure Identification	147
8.4	Numerical Examples and Remarks	150
8.4.1	Minimum number of load conditions	150
8.4.2	Non-unique solutions	153
8.4.3	Three-Dimensional Trusses	156
8.5	Error Analysis	160
8.5.1	Perturbation Technique, for Statically Determinate Structures	160
8.5.2	Monte Carlo Simulation, for Statically Indeterminate Structures	169
8.6	Concluding Remarks	174
9	Local Damage Identification with Genetic Algorithms	177
9.1	Introductory Remarks	178

9.2	Missing Measurements	180
9.2.1	Proposed Method	180
9.2.2	Numerical Application	183
9.3	Local Damages	183
9.3.1	Proposed Method	187
9.3.2	Numerical Applications	189
9.4	Concluding Remarks	193
10	General Conclusions	197
10.1	Final Remarks	198
10.2	Future Developments	200
A	Random Fields	203
A.1	Introductory Remarks	203
A.2	General Definition	204
A.3	Description of a Random Field	205
A.4	Homogeneous Random Fields	206
A.5	Properties of the Correlation Functions	207
A.5.1	General Case	207
A.5.2	Homogeneous Case	207
A.6	Ergodic Theorem	208
A.7	Spectral Density Function	210
A.7.1	Properties of the SDF	210
A.7.2	Cross-Spectral Density Function	211
A.7.3	Estimation of the SDF from One Sample	212
A.8	Gaussian Random Fields	212
A.9	Multi-Dimensional Random Fields	213
A.10	Multi-Variate Random Fields	214

Chapter 1

Introduction

*Human beings have long been
both fascinated and appalled by randomness.
-Jeffrey S. Rosenthal-*

Sommario. *La maggior parte delle grandezze fisiche utilizzate nei modelli ingegneristici ha un carattere intrinsecamente aleatorio e ciò ha determinato un interesse sempre crescente verso l'analisi probabilistica. Per la stessa ragione, tutte le leggi ed i regolamenti tecnici di più recente concezione propongono approcci probabilistici (a diversi livelli). La ricerca scientifica si spinge anche oltre, suggerendo il "performance-based design" e il "reliability-oriented design", entrambi basati su considerazioni probabilistiche.*

In letteratura si possono trovare diversi approcci all'analisi stocastica, ma è largamente condivisa l'idea che la Simulazione alla Monte Carlo sia l'unico metodo veramente universale per la soluzione di problemi di meccanica stocastica. Tale tecnica può essere scomposta in quattro fasi principali: la caratterizzazione probabilistica dei dati, la generazione di campioni casuali, la soluzione di un problema deterministico per ogni campione generato e l'analisi statistica dei risultati. La parte cruciale della procedura è la generazione di campioni che rispecchino, con la massima accuratezza possibile, le caratteristiche probabilistiche della grandezze che devono rappresentare.

La distribuzione più usata per descrivere le grandezze fisiche è sicuramente quella Gaussiana. Tuttavia, questa scelta viene spesso fatta per semplicità, più che per effettiva aderenza alla realtà. Infatti, è ben noto che molte variabili sono meglio rappresentate da distribuzioni differenti (talvolta di molto) dalla Normale. Per tale motivo sono stati sviluppati numerosi metodi per la generazione di campioni casuali con caratteristiche non-Gaussiane.

Gli studi riportati nella parte principale della tesi (Part I) si inseriscono in questo contesto. In particolare, viene proposta una tecnica originale per la simulazione di campi aleatori omogenei, multidimensionali, multivariati e fortemente non-Gaussiani. Il Capitolo 2 presenta l'analisi critica di una classe di algoritmi con alcune caratteristiche comuni. L'individuazione e la completa comprensione dei limiti delle altre metodologie hanno portato allo sviluppo della procedura proposta nel Capitolo 3, basata su un approccio "trials and errors" per l'individuazione del cosiddetto "underlying Gaussian field", secondo la teoria del "translation field". I Capitoli 4 e 5 riportano, rispettivamente, le estensioni di tale tecnica ai casi multidimensionale e multivariato. Entrambe le estensioni espandono l'applicabilità del metodo e, in particolare, la seconda consente per la prima volta l'identificazione dell'"underlying Gaussian coherence". Il Capitolo 6 tratta, invece, risultati analitici ottenuti riguardo la simulazione di campi multivariati Gaussiani: la dimostrazione generalizzata di ergodicità e l'espressione in forma chiusa della matrice di densità spettrale dei campioni casuali generati per mezzo dello "Spectral Representation Method" con "Frequency Double Indexing". Il Capitolo 7 raccoglie alcune applicazioni all'ingegneria civile (in particolare alla geomeccanica stocastica e all'affidabilità strutturale) dei metodi presentati e conclude la prima parte.

Il secondo argomento trattato (Part II) è l'identificazione strutturale. Viene presentata una tecnica non distruttiva per la stima della rigidità di aste in strutture reticolari, usando carichi statici e misure di deformazione. In questo caso, il modello utilizzato è puramente deterministico e l'approccio probabilistico risiede nello strumento numerico di ottimizzazione che viene usato. Infatti, nel Capitolo 8 viene illustrato un metodo per l'identificazione di reticolari spaziali iperstatiche sotto le ipotesi che tutte le dilatazioni siano note e che le caratteristiche meccaniche dell'asta siano uniformi. Quando la

prima ipotesi non è verificata, l'algoritmo non può essere utilizzato; quando non lo è la seconda, l'algoritmo dà risultati sbagliati. Per superare tali limitazioni, nel Capitolo 9 viene suggerito l'impiego degli Algoritmi Genetici, che sono un metodo di ricerca operativa euristica, non deterministica, che si basa su concetti ispirati alla teoria dell'evoluzione biologica, quali la mutazione casuale, la ricombinazione genetica, la sopravvivenza del più adatto. Gli esempi numerici confermano il potenziale della metodologia proposta.

Le considerazioni conclusive su entrambe le parti e alcuni cenni a possibili sviluppi futuri sono affidate al Capitolo 10.

Infine, nell'Appendice A sono brevemente riportati i concetti di base della teoria dei campi aleatori che vengono richiamati all'interno della tesi.

Sintetizzando, si può dire che nella prima parte della tesi il caso è presentato come una componente intrinseca del mondo che ci circonda, della quale dobbiamo imparare a tenere conto e con la quale dobbiamo confrontarci. Nella seconda parte, viene mostrato che il caso può anche essere considerato una risorsa preziosa.

The inherent stochastic character of most of the physical quantities involved in engineering models has led to an always increasing interest for probabilistic analysis. For the same reason, also the codes, all over the world, account for probabilistic (at different levels) approaches. The scientific and technical research goes even further, studying and proposing the “reliability-oriented” and “performance-based” designs, that are both characterized by a probabilistic perspective.

In the literature, many approaches to stochastic analysis have been proposed (see, for instance, the surveys by Schueller, 1997; Matthies et al., 1997; Ghanem and Spanos, 2003). However, it is widely acknowledged that the only universal method available to solve accurately any kind of stochastic mechanics problem is Monte Carlo Simulation (see, for instance, the survey paper by Hurtado and Barbat, 1998).

The well-known Monte Carlo Simulation can be broken down into four macro-steps: probabilistic characterization of the input quantities, input samples generation, deterministic analysis for each input sample, statistical analysis

of results. The key part in the implementation of this technique is the accurate and efficient generation of samples of the random processes and fields involved in the problem at hand. In the field of civil engineering, these random quantities can be both excitations (e.g. wind, ground motion, waves) and system characteristics (e.g. material properties, geometry, cracks, texture). To obtain accurate solutions to such problems, it is important that the generated sample functions of these processes and fields match the prescribed probabilistic characteristics as closely as possible.

The most commonly used probability distribution to model these stochastic processes and fields is certainly the Gaussian. This choice is made mostly for convenience rather than for mathematical or physical reasons. For example, various material properties are bounded for physical reasons (e.g. the elastic modulus, the yield stress, the density, and several other properties cannot become negative), while excitations like wind pressure fluctuations and ocean wave heights are known to exhibit strong non-Gaussian characteristics. For these reasons, several methodologies have been proposed for simulating non-Gaussian stochastic processes and fields according to a prescribed Spectral Density Function and a prescribed marginal Probability Distribution Function. A few representative methodologies belonging to this framework are mentioned here in chronological order: Yamazaki and Shinozuka (1988); Grigoriu (1995, 1998); Gurley et al. (1997); Popescu et al. (1998); Gurley and Kareem (1998); Deodatis and Micaletti (2001); Puig et al. (2002); Sakamoto and Ghanem (2002a,b); Graham et al. (2003); Cope et al. (2005); Shi et al. (2007); Li et al. (2007).

Along this line, in the main part of the thesis, **Part I**, an original methodology for the simulation of homogeneous, multi-dimensional, multi-variate, strongly non-Gaussian random fields is proposed. In particular, Chapter 2 presents the critical review of a class of simulation algorithms of which the newly proposed ones can be considered as the latest development. The analysis of the limits and of the drawbacks of the previous methods has led to the development of the one-dimensional, uni-variate version of the algorithm proposed in Chapter 3. It is based on a “trials and errors” approach to identify the “underlying Gaussian spectrum”, according to the classic “translation field” theory. Chapter 4 treats the extension of the same ideas to the multi-dimensional case and Chapter 5 presents the generalization to the multi-variate case. To this last purpose, the proposed code identifies the “underlying Gaussian cross-spectra” or the “underlying Gaussian coherences”. An in-depth examination of the “Spectral Representation Method” with “Frequency Double Indexing” for the simulation of multi-variate Gaussian fields is presented in Chapter 6. The results are a

closed form expression of the cross-spectral density matrix of the samples produced by this technique and a generalized proof of ergodicity. Chapter 7 collects some possible applications to civil engineering of the proposed techniques (in particular, a study involving stochastic geomechanics and a reliability analysis of a suspension bridge) and concludes this part.

Part II deals with a procedure for the static identification of truss structures, using strain measurements. In this case, the model that has been used is purely deterministic. However, the probabilistic approach resides in the numerical tool that is used to perform the analysis. In fact, the identification procedure that is presented in Chapter 8 is able to identify three-dimensional redundant truss structures under the hypotheses that all the strains are known and that the characteristics of the bars are uniform along its length. On the contrary, when the value of one strain is missing or when the damage is concentrated only in a portion of the bar, the algorithm fails. To overcome these issues, in Chapter 9 the use of Genetic Algorithm is suggested. These are a heuristic search procedure for the solution of optimization problems that uses techniques inspired by evolutionary biology such as offspring generation, inheritance, mutation, selection, crossover and recombination, all these wisely mixed with randomness, as in the real life. In this way, also local damages can be identified.

In Chapter 10 some concluding remarks on both the parts are collected.

Finally, in Appendix A, the basic concepts of random field theory that are used in the thesis are briefly recalled.

In a few words, in the first part of the thesis, randomness is presented as an inherent component of our world, we necessarily have to deal with. In the second part, it is shown that randomness can also be considered as a useful resource.

Part I

Simulation of
Random Fields

Chapter 2

Critical Review of Previous Research Work

*Random numbers should not be generated
with a method chosen at random.*

-Donald E. Knuth-

Sommario. *I metodi di simulazione originali proposti nella presente tesi sono basati sullo “Spectral Representation Method” e sulla teoria del “translation field”. Per questo motivo, essi possono venire considerati l’ultimo sviluppo di una classe di algoritmi che condividono le stesse idee di base.*

In questo Capitolo, i precedenti algoritmi che possono essere ricondotti alla classe in questione, vengono brevemente descritti ed analizzati criticamente.

Il metodo capostipite, proposto da Yamazaki e Shinozuka (1988), ha noti problemi nella simulazione di campi fortemente non-Gaussiani. Le correzioni suggerite da Deodatis e Micaletti (2001) consentono di ottenere un’accuratezza decisamente migliore, ma fanno perdere ai campioni generati la caratteristica di “translation field” e tutte le proprietà conseguenti. L’algoritmo di Shi e Deodatis (2004) raggiunge un buon livello di accuratezza e genera campioni con la caratteristica

di “translation field”, ma anch’esso non è esente da alcuni problemi di carattere teorico e numerico.

2.1 Introductory Remarks

The original simulation algorithms that are proposed in this thesis are all based on the Spectral Representation Method (Shinozuka and Jan, 1972) and on the translation field theory (Grigoriu, 1984, 1995). For this reason, they can be considered the latest developments of a class of techniques for the simulation of non-Gaussian fields that share these same foundations.

In the present Chapter, the Spectral Representation Method (SRM) and the algorithms belonging to the aforementioned class are briefly described and critically reviewed¹.

The issues enlightened by this analysis have led to the development of the algorithm presented in Chapter 3.

2.2 Spectral Representation Method for Gaussian Fields

The Spectral Representation Method for the simulation of Gaussian stochastic processes and fields has been introduced by Shinozuka and Jan (1972). Many further developments have been proposed over the years, which are reviewed and summarized in a series of papers by Shinozuka and Deodatis (Shinozuka and Deodatis, 1991, 1996; Deodatis, 1996), to which the reader is referred also for a complete bibliography. The SRM is the base of all the algorithms that will be presented in this part of the thesis.

The purpose of the method is to produce sample fields $g(x)$ with a given target Spectral Density Function $S_{gg}(\kappa)$. The basic formulation generates homogeneous Gaussian ergodic fields.

There are two alternative SRM-based algorithms in the literature (e.g. Shinozuka and Deodatis, 1991; Grigoriu, 1993). The one that will be used in this

¹The critical review and scientific results reported in this Chapter have already been presented by Bocchini and Deodatis (2008).

thesis simulates the Gaussian stochastic field $g(x)$ by the following series as $N \rightarrow \infty$:

$$g(x) = 2 \sum_{n=0}^{N-1} \sqrt{S_{gg}(\kappa_n)} \Delta\kappa \cos(\kappa_n x + \phi_n) \quad (2.1)$$

where

$$\Delta\kappa = \frac{\kappa_u}{N} \quad (2.2)$$

$$\kappa_n = n \Delta\kappa, \quad n = 0, 1, \dots, N-1 \quad (2.3)$$

and κ_u is the upper cutoff wave number, beyond which the SDF $S_{gg}(\kappa)$ can be assumed to be zero for mathematical or physical reasons. The ϕ_n 's are independent random phase angles, uniformly distributed in the interval $[0, 2\pi]$.

Since the simulated stochastic field $g(x)$ is a superposition of cosines, it is periodic, and it can be proved (Shinozuka and Deodatis, 1991) that the period is

$$L = \frac{2\pi}{\Delta\kappa} \quad (2.4)$$

The Gaussianity of the samples relies on the Central Limit Theorem, therefore the generated sample functions are Gaussian only asymptotically, as N tends to infinity.

However, the samples can be assumed to be Gaussian if N is greater than approximately 100 (Shinozuka and Deodatis, 1991). Generated sample functions also have a strong ergodic property in the mean and autocorrelation when the length of the sample is a multiple of the period L or tends to infinity (Shinozuka and Deodatis, 1991; Grigoriu, 1993). Actually, this property requires also the hypothesis

$$S_{gg}(\kappa = 0) = 0 \quad (2.5)$$

but by means of the Frequency Shifting Theorem, this constraint can be avoided (Zerva, 1992). In this case, the period of the simulated field is doubled. The Gaussianity of the random field implies that mean and autocorrelation function are sufficient to fully describe the field. The mean and autocorrelation ergodicity ensure that these two properties can be estimated by means of a single sample. Therefore, a single sample $g(x)$ produced by the SRM is sufficient to fully reconstruct the theoretical random field. It is worth noting that

this ergodic property is lost when the Gaussian sample function is mapped to a non-Gaussian one according to the classic translation field transformation.

In order to improve the computational efficiency of the SRM, the Fast Fourier Transform (FFT) can be proficiently employed, as suggested by Yang (1972, 1973). To this purpose, Eq. (2.1) can be rewritten as

$$g(x_m) = \Re \left\{ 2 \sum_{n=0}^{M-1} \sqrt{S_{gg}(\kappa_n)} \Delta\kappa \exp(i\phi_n) \exp(i\kappa_n x_m) \right\} \quad (2.6)$$

where

$$x_m = m \Delta x, \quad m = 0, 1, \dots, M - 1 \quad (2.7)$$

$\Re \{ \cdot \}$ represents the real part of the argument in brackets, M is the number of intervals in the space domain and Δx is a function of $\Delta\kappa$ through the relationship

$$\Delta x \Delta\kappa = \frac{2\pi}{M} \quad (2.8)$$

The number of intervals M must satisfy the relationship

$$M \geq 2N \quad (2.9)$$

and the length of the resultant sample is always one period. Since, as already mentioned, $S_{gg}(\kappa_n)$ is considered negligible for κ_n larger than κ_u (i.e. for every n larger than N), the value of $S_{gg}(\kappa_n)$ is set equal to zero for every n in the interval $[N; M - 1]$. The implementation of the FFT can dramatically reduce the computational cost of the simulation and becomes almost necessary in the case of two- and three-dimensional fields.

Several procedures have been developed to produce a non-Gaussian field starting from a Gaussian one. The following ones are the most significant for the purposes of this thesis.

2.3 Spectral Representation Method for Non-Gaussian Fields

2.3.1 Yamazaki and Shinozuka (1988)

Yamazaki and Shinozuka (1988) proposed an SRM-based iterative methodol-

ogy to simulate a non-Gaussian stochastic field $f(x)$ according to a target non-Gaussian SDF, $S_{ff}^T(\kappa)$, and a target non-Gaussian marginal CDF, \mathcal{F}_f , with zero mean and variance σ_f^2 compatible with that of the target SDF. Their methodology is based on Grigoriu's translation field theory (Grigoriu, 1984, 1995).

At the first iterative step, the unknown SDF of the underlying Gaussian field $g(x)$, $S_{gg}(\kappa)$, is set equal to $S_{ff}^T(\kappa)$. Then, a Gaussian sample function $g(x)$ is generated by means of the SRM. The classic translation field transformation (Grigoriu, 1984, 1995) is then used to map the homogeneous Gaussian sample into a homogeneous non-Gaussian one with the prescribed marginal PDF:

$$f(x) = \mathcal{F}_f^{-1} \{ \mathcal{F}_g [g(x)] \} \quad (2.10)$$

where \mathcal{F}_f^{-1} is the inverse target non-Gaussian Cumulative Distribution Function (CDF) and \mathcal{F}_g is the Gaussian CDF with zero mean and variance σ_g^2 equal to σ_f^2 . Although sample function $f(x)$ reflects the prescribed non-Gaussian marginal CDF, \mathcal{F}_f , its SDF is not matching, in general, the prescribed SDF, $S_{ff}^T(\kappa)$, because of the nonlinearity of the transformation in Eq. (2.10).

The basic idea of the Yamazaki and Shinozuka algorithm is to update iteratively the SDF of the underlying Gaussian field until the SDF of the non-Gaussian sample function converges to the target. This is expressed as:

$$S_{gg}^{(j+1)}(\kappa) = \frac{S_{gg}^{(j)}(\kappa)}{S_{ff}^{(j)}(\kappa)} S_{ff}^T(\kappa) \quad (2.11)$$

where $S_{gg}^{(j+1)}(\kappa)$ and $S_{gg}^{(j)}(\kappa)$ denote the SDF's of the underlying Gaussian field at the $(j+1)^{th}$ and j^{th} iterations, respectively, and $S_{ff}^{(j)}(\kappa)$ is the SDF of the non-Gaussian sample function at the j^{th} iteration computed from:

$$S_{ff}^{(j)}(\kappa) = \frac{1}{2\pi L} \left| \int_0^L f^{(j)}(x) \exp(-i\kappa x) dx \right|^2 \quad (2.12)$$

Over the years since its introduction in 1988, it has become clear that the Yamazaki and Shinozuka algorithm cannot match accurately the prescribed non-Gaussian marginal CDF when it deviates significantly from the Gaussian. Deodatis and Micaletti (2001) have identified and explained in detail the theoretical reasons for this problem that are briefly summarized here.

The first reason is that the underlying ‘‘Gaussian’’ field diverges from Gaussianity as the iterations proceed. This is due to the fact that the updating formula in Eq. (2.11) makes the SDF $S_{gg}(\kappa)$ of the underlying Gaussian field a function of all the ϕ_n 's in Eq. (2.1) –since $S_{ff}^{(j)}(\kappa)$ is a function of all the ϕ_n 's as can be seen from Eq. (2.12)–. Once $S_{gg}(\kappa)$ becomes a function of all the ϕ_n 's, each term in the summation in Eq. (2.1) becomes a function of all the ϕ_n 's too, and the condition of independence, necessary for the validity of the Central Limit Theorem, is not valid anymore. This, in turn, affects the mapping in Eq. (2.10) which assumes that sample function $g(x)$ is Gaussian, while it is not. Consequently, $f(x)$ will not reflect the target marginal distribution. A secondary side-effect is that $g(x)$ is not perfectly homogeneous and therefore $f(x)$ will not be homogeneous either. However, this deviation from homogeneity is usually negligible.

The second reason of the low accuracy of the method is the ‘‘incompatibility’’ between the target SDF and the target marginal distribution of the non-Gaussian stochastic field. Yamazaki and Shinozuka (1988) assumed that $S_{ff}^T(\kappa)$ and \mathcal{F}_f can be prescribed arbitrarily, except for the obvious condition on the compatibility of their variance

$$\sigma_f^2 = \int_{-\infty}^{\infty} S_{ff}^T(\kappa) d\kappa \quad (2.13)$$

In contrast, Grigoriu (1995) has demonstrated that if $f(x)$ is a translation field (as is the case with the Yamazaki and Shinozuka algorithm), its autocorrelation function $R_{ff}(\xi)$ and its marginal CDF are strictly linked through the relationship:

$$R_{ff}(\xi) = \int_{-\infty}^{\infty} \int_{-\infty}^{\infty} \mathcal{F}_f^{-1} \{ \mathcal{F}_g [g(x')] \} \cdot \mathcal{F}_f^{-1} \{ \mathcal{F}_g [g(x'' + \xi)] \} \cdot \mathcal{P}_{gg} [g(x'), g(x'' + \xi)] dx' dx'' \quad (2.14)$$

where ξ denotes the separation distance and \mathcal{P}_{gg} is the Gaussian joint Probability Density Function (PDF):

$$\begin{aligned} \mathcal{P}_{gg} [g(x), g(x + \xi)] &= \\ &= \frac{1}{2\pi\sigma_g^2\sqrt{1 - \rho^2(\xi)}} \cdot \exp \left\{ -\frac{g^2(x) + g^2(x + \xi) - 2\rho(\xi)g(x)g(x + \xi)}{2\sigma_g^2[1 - \rho^2(\xi)]} \right\} \end{aligned} \quad (2.15)$$

with $\rho(\xi)$ being the correlation coefficient given, in the case of zero-mean homogeneous fields, by:

$$\rho(\xi) = \frac{R_{gg}(\xi)}{\sigma_g^2} \quad (2.16)$$

Equation (2.14) works always in a forward fashion. This means that prescribing arbitrarily an underlying Gaussian field (through its autocorrelation function or SDF) and a marginal CDF for the non-Gaussian field, it is always possible to determine the autocorrelation function $R_{ff}(\xi)$ of the non-Gaussian field (and this autocorrelation function will be non-negative-definite). The inverse is not always possible. This means that it is not always possible to determine an underlying Gaussian field by arbitrarily prescribing an SDF and a marginal CDF for the non-Gaussian field. If it is not possible to determine an underlying Gaussian field, then the $S_{ff}^T(\kappa)$ and \mathcal{F}_f are said to be “incompatible”.

2.3.2 Deodatis and Micaletti (2001)

Deodatis and Micaletti (2001) proposed some modifications to the Yamazaki and Shinozuka (1988) methodology in order to overcome the problems mentioned in the previous Section.

First, Deodatis and Micaletti (2001) suggested a “compatibility check” to determine whether $S_{ff}^T(\kappa)$ and \mathcal{F}_f are compatible or not. The procedure consists in a discrete numeric inversion of Equation (2.14) in order to reconstruct $R_{gg}(\xi)$ given $R_{ff}(\xi)$. The first type of incompatibility arises if in certain points (i.e. for certain values of ξ) there is no way to find a value of R_{gg} that satisfies Eq. (2.14). In this case, the suggestion is to change either $S_{ff}^T(\kappa)$ or \mathcal{F}_f or both. The second type of incompatibility arises if it is possible to fully determine $R_{gg}(\xi)$ but it is not an admissible autocorrelation function because it is not non-negative-definite. This can be easily determined computing $S_{gg}(\kappa)$ by means of the Wiener-Khinchine Theorem in Eq. (A.32), then the non-negative-definiteness of $R_{gg}(\xi)$ is equivalent to the condition

$$S_{gg}(\kappa) \geq 0 \quad \forall \kappa \quad (2.17)$$

If in certain points $S_{gg}(\kappa)$ is negative, it will be possible to slightly modify the value of the underlying SDF in those points, setting it equal to zero. It is worth to notice that both in the case of the first type of incompatibility and in this latter case of incompatibility, this approach requires to modify (at least in some

points) the target. Although the modifications to $S_{ff}^T(\kappa)$ are generally slight (especially when \mathcal{F}_f is not very far from the Gaussian), the technique is rather arbitrary and non-unique. In this thesis, it will be shown that it is not necessary to go through such “spectral preconditioning”.

The second modification to the Yamazaki and Shinozuka methodology addresses the problem of divergence of the underlying field from the Gaussian. Deodatis and Micaletti (2001) suggested to explicitly account for this divergence by computing (numerically) the empirical CDF of $g(x)$ and using it in the mapping as follows:

$$f(x) = \mathcal{F}_f^{-1} \left\{ \hat{\mathcal{F}}_g [g(x)] \right\} \quad (2.18)$$

where $\hat{\mathcal{F}}_g$ is the (generally non-Gaussian) CDF of the sample $g(x)$ computed by means of a numerical technique (e.g. cumulative histogram or kernel smoothing, Bowman and Azzalini, 1997). In this way, the mapping scheme remains of the same form as that in Eq. (2.10), but now an underlying non-Gaussian field is mapped into the prescribed non-Gaussian field.

Since strongly non-Gaussian marginal distributions can slow down the convergence of Eq. (2.11), Deodatis and Micaletti suggested to use an exponent β to improve the convergence characteristics:

$$S_{gg}^{(j+1)}(\kappa) = S_{gg}^{(j)}(\kappa) \left[\frac{S_{ff}^T(\kappa)}{S_{ff}^{(j)}(\kappa)} \right]^\beta \quad (2.19)$$

The value of $\beta = 0.3$ is proposed (Deodatis and Micaletti, 2001) for optimum convergence (refer also to Popescu et al., 1997, 1998).

Finally, Deodatis and Micaletti suggested to discretize the wave number domain at the midpoints of the intervals shown in Eq. (2.1), using the frequency shifting technique proposed by Zerva (1992). This allows to take into account also fields with Spectral Density Functions greater than zero at $\kappa = 0$, still conserving the homogeneity, and improves convergence significantly, but doubles the period of the sample function from that in Eq. (2.4).

$$L = \frac{4\pi}{\Delta\kappa} \quad (2.20)$$

The Frequency Shifting requires also a different estimation of the Spectral Density Function, that is explained in details in Sec. 3.2.6.

Overall, the Deodatis and Micaletti algorithm dramatically improves the convergence of the CDF of the generated samples to the prescribed target non-Gaussian CDF, especially so for distributions that are strongly non-Gaussian. However, it also has a drawback. As the mapping in Eq. (2.18) is made from a non-Gaussian field $g(x)$ to another non-Gaussian field $f(x)$, the resulting stochastic field $f(x)$ is not a translation field. Consequently, all the relevant, well-defined and desired properties of translation fields are lost, including crossing rates and distributions of extremes.

2.3.3 Shi and Deodatis (2004)

Shi and Deodatis (Shi and Deodatis, 2004; Shi et al., 2005; Shi, 2006) have developed a methodology with similar accuracy to the Deodatis and Micaletti algorithm presented in the previous Section, but without the drawback of generating non-Gaussian fields that are not translation ones according to Grigoriu's classic definition (Grigoriu, 1984, 1995). The basic idea is to eliminate the unwanted correlations among the terms in Eq. (2.1) by replacing the updating formula in Eq. (2.19) with an optimization procedure.

At a typical step of the Shi and Deodatis algorithm, two wave numbers are randomly selected, and the corresponding values of the underlying Gaussian SDF, $S_{gg}(\kappa)$, are modified by small random amounts. Then the value of $S_{gg}(\kappa)$ at another (third) randomly selected wave number is modified in such a way that the variance of $g(x)$ remains constant. In this way, an updated SDF, $S_{gg}^{(j+1)}(\kappa)$, is defined for the next iterative step ($j+1$) avoiding the use of $S_{ff}^{(j)}(\kappa)$ from the previous step (j), and thus eliminating any –at least obvious– correlations among the terms in the summation in Eq. (2.1). Therefore, by virtue of the Central Limit Theorem, the generated field $g^{(j+1)}(x)$ remains Gaussian and consequently it is possible to use again Eq. (2.10) for the mapping (actually $\mathcal{F}_g^{(j+1)}$ is not strictly assumed to be perfectly Gaussian, but instead it is computed numerically). As a result, the non-Gaussian field $f^{(j+1)}(x)$ is a legitimate translation field.

The following definition for the error ε between $S_{ff}^{(j+1)}(\kappa)$ and $S_{ff}^T(\kappa)$ is

adopted as convergence criterion:

$$\varepsilon = 100 \sqrt{\frac{\sum_{n=0}^{N-1} \left[S_{ff}^{(j+1)}(\kappa_n) - S_{ff}^T(\kappa_n) \right]^2}{\sum_{n=0}^{N-1} \left[S_{ff}^T(\kappa_n) \right]^2}} \quad (2.21)$$

where the period L is given by Equation (2.20) because of the Frequency Shifting. If the error at iteration $(j + 1)$ is found to be less than the error at the previous iteration (j) , then the iteration is accepted. Otherwise, the iteration is rejected, and a new one is performed. The iterative scheme ends when no further reduction in ε is possible. Since the methodology is based on random perturbations at every iterative step, Shi and Deodatis suggested to repeat the whole procedure several (100) times to determine the SDF of the underlying Gaussian field by ensemble averaging.

The Shi and Deodatis algorithm provides high accuracy in matching both the target SDF and the target marginal distribution. Moreover, the ensemble-averaged SDF of the underlying Gaussian field can be stored and used for the direct and extremely efficient generation of non-Gaussian sample functions without any iterations. Finally, it is emphasized that the generated sample functions have all the properties of translation fields. However, this algorithm has a number of limitations and problems that are described in the following.

The first one is shared with the Yamazaki and Shinozuka and Deodatis and Micaletti algorithms. All three methodologies use essentially Eq. (2.12) to estimate the SDF of a generated sample function of the non-Gaussian stochastic field. Equation (2.12) provides an accurate estimate of the SDF when the field has ergodicity characteristics in correlation similar to the ones of samples generated by the Spectral Representation Method (Shinozuka and Deodatis, 1991). However, the non-Gaussian field $f(x)$ does not have such ergodicity characteristics (it is not ergodic in correlation). This means that Eq. (2.12) provides only an approximation of the actual SDF. The Yamazaki and Shinozuka and Deodatis and Micaletti algorithms use the estimated $S_{ff}^{(j)}(\kappa)$ to update the SDF of the underlying Gaussian field through Eqs. (2.11) and (2.19). Consequently, a poor approximation of $S_{ff}^{(j)}(\kappa)$ could be responsible for problems in the convergence and in the accuracy of these two algorithms. In contrast, the Shi and Deodatis algorithm uses the estimated $S_{ff}^{(j)}(\kappa)$ only to determine whether an iteration step should be kept or rejected. Consequently, a poor approximation of $S_{ff}^{(j)}(\kappa)$ might not affect the convergence and the accuracy of this algorithm

that much. However, it should be mentioned that the estimation of the SDF of $f(x)$ using a single sample function –Eq. (2.12)– is often very scattered. Therefore, the error ε in Eq. (2.21) is not really a measure of the convergence to the target, but essentially a measure of the scattering of $S_{ff}^{(j)}(\kappa)$. For this reason, the convergence is very slow, and the Shi and Deodatis algorithm tends to converge to underlying Gaussian fields that generate low scattering, rather than to the underlying Gaussian field that provides the best matching of the target.

Another problem with the Shi and Deodatis algorithm is the constraint it imposes on the value of the variance of the underlying Gaussian field. The classic definition of “translation field” requires the underlying Gaussian field to be standardized (zero mean and unit variance). However, it has been shown (Grigoriu, 1984) that the same results (in particular the mean crossing rate) can be obtained even if the underlying Gaussian field has variance different from unity. Therefore, the constraint on the variance of $g(x)$ is unnecessary. Furthermore, it limits the available domain for $S_{gg}(\kappa)$ that ensures the best convergence to the target. The removal of this constraint allows to search for better solutions, without any drawback.

Finally, the choice to modify three randomly selected points of the underlying Gaussian SDF causes a number of problems. First, it introduces punctual discontinuities (type 2 discontinuities) in $S_{gg}(\kappa)$ that are unnatural and almost always absent from the final solution. Moreover, it can bias the result and slow down convergence. For example, consider the case where the first two points to be modified lie in the region where the SDF reaches its highest values, while the third point is in the right tail of the SDF. If the first two values are increased by a certain amount, then the third value must decrease a lot and most probably become negative, something that is not allowable. If, on the other hand, the first two values are decreased by a certain amount, then the third value must increase a lot leading to an unnatural spike in the right tail of the SDF that is not going to be part of an optimal solution. Several other examples can be found demonstrating that random punctual modifications are not the best choice to update the SDF of the underlying Gaussian field.

The simulation methodology proposed in Chapter 3 addresses all of the aforementioned problems.

Chapter 3

Simulation of One-Dimensional, Uni-Variate, Strongly Non-Gaussian Random Fields

*Anyone who considers arithmetical methods
of producing random digits is, of course,
in a state of sin.
-John von Neumann-*

Sommario. *Nel presente Capitolo viene presentato un metodo originale per la generazione di campi aleatori omogenei, monodimensionali, monovariati (1D-1V) e fortemente non-Gaussiani.*

Lo “Spectral Representation Method” genera campioni Gaussiani che poi possono venire portati alla distribuzione di probabilità desiderata, per mezzo di una funzione biunivoca detta “mapping”. Tuttavia,

sorge il problema che la forte non linearità del mapping causa la distorsione della densità di potenza spettrale del campione.

L'idea di base è l'utilizzo di una procedura "trials and errors" per l'identificazione del cosiddetto campo Gaussiano "underlying" che dopo la distorsione dovuta al mapping avrà esattamente le caratteristiche di probabilità marginale e densità di potenza spettrale desiderate.

La descrizione della tecnica al Paragrafo 3.2 è molto dettagliata, perché essa è anche la base delle metodologie proposte nei Capitoli seguenti.

Il Paragrafo 3.3 riporta quattro esempi numerici che mostrano come il metodo proposto dia risultati globalmente migliori dei propri predecessori e sia in grado di generare campioni le cui caratteristiche non-Gaussiane raggiungono livelli estremi.

Alcune considerazioni sulla buona efficienza computazionale concludono il Capitolo.

3.1 Introductory Remarks

An original algorithm for the simulation of homogeneous, one-dimensional, univariate (1D-1V), strongly non-Gaussian random fields is presented in this Chapter¹.

The description of the procedure (Sec. 3.2) is very detailed because this is the base for all the simulation techniques proposed in this thesis.

In Sec. 3.3 a benchmark numerical application is used to compare the accuracy of the proposed algorithm to the accuracy of the other techniques belonging to the same class. Three more examples involving strongly non-Gaussian distributions are presented, to investigate the capabilities and the limits of the method.

Some concluding remarks and some considerations on the computational efficiency of the code conclude the Chapter.

¹The scientific results reported in this Chapter have already been presented by Bocchini and Deodatis (2008).

3.2 Proposed Simulation Methodology

Given the target Spectral Density Function $S_{ff}^T(\kappa)$ and the target marginal Cumulative Distribution Function \mathcal{F}_f of the non-Gaussian stochastic field $f(x)$, the proposed methodology finds an underlying Gaussian SDF $S_{gg}(\kappa)$ that can be used to generate non-Gaussian sample functions that reflect the prescribed targets ($S_{ff}^T(\kappa)$ and \mathcal{F}_f).

The flow chart of the algorithm is presented in Fig. 3.1. It is based on an iterative procedure whose general scheme is similar to that of the Shi and Deodatis algorithm (see Sec. 2.3.3). The various steps of the proposed methodology are described in detail in the following (the numbers indicated inside the boxes in Fig. 3.1 correspond to the numbering of the subparagraphs that follow).

3.2.1 Compute the Starting Gaussian SDF $S_{gg}(\kappa)$

In order to improve the computational efficiency of the algorithm, the starting values of $S_{gg}(\kappa)$ are not assumed to be equal to those of $S_{ff}^T(\kappa)$ (as was the practice with the Deodatis and Micaletti and Shi and Deodatis algorithms). Instead, they are computed using a technique which is quite similar to the basic methodology shown in Fig. 3.1, but with a much faster iterative scheme². The accuracy of this technique is rather low, but it can quickly provide a rough estimation of the underlying Gaussian SDF. This can be very helpful in cases where \mathcal{F}_f differs significantly from the Gaussian and consequently $S_{gg}(\kappa)$ is expected to be quite different from $S_{ff}^T(\kappa)$.

²The starting $S_{gg}(\kappa)$ is computed using an algorithm whose flow chart is very similar to that in Fig. 3.1. The only difference occurs in the T iterations of steps 3–6, that are substituted by the following procedure.

Using the Wiener-Khintchine transform, the autocorrelation function $R_{gg}(\xi)$ of the current underlying Gaussian field can be easily computed. The correlation coefficient $\rho_{gg}(\xi)$ is then obtained by simply renormalizing $R_{gg}(\xi)$ so that $R_{gg}(0) = 1$:

$$\rho_{gg}(\xi) = \frac{R_{gg}(\xi)}{\sigma_g^2} \quad (3.1)$$

Once $\rho_{gg}(\xi)$ is known, it is easy to obtain $R_{ff}(\xi)$ by means of Eq. (2.14). However, Eq. (2.14) involves a double integration that can be computationally slow. To address this issue, the double integration has been substituted by a lookup table that dramatically reduces the computational effort. The side effect of this is that the accuracy is somehow reduced, but it is still very good for initialization purposes.

Then, using again the Wiener-Khintchine transform, $S_{ff}(\kappa)$ is computed from $R_{ff}(\xi)$. Since this procedure is not depending on a particular choice of random variables, it is sufficient

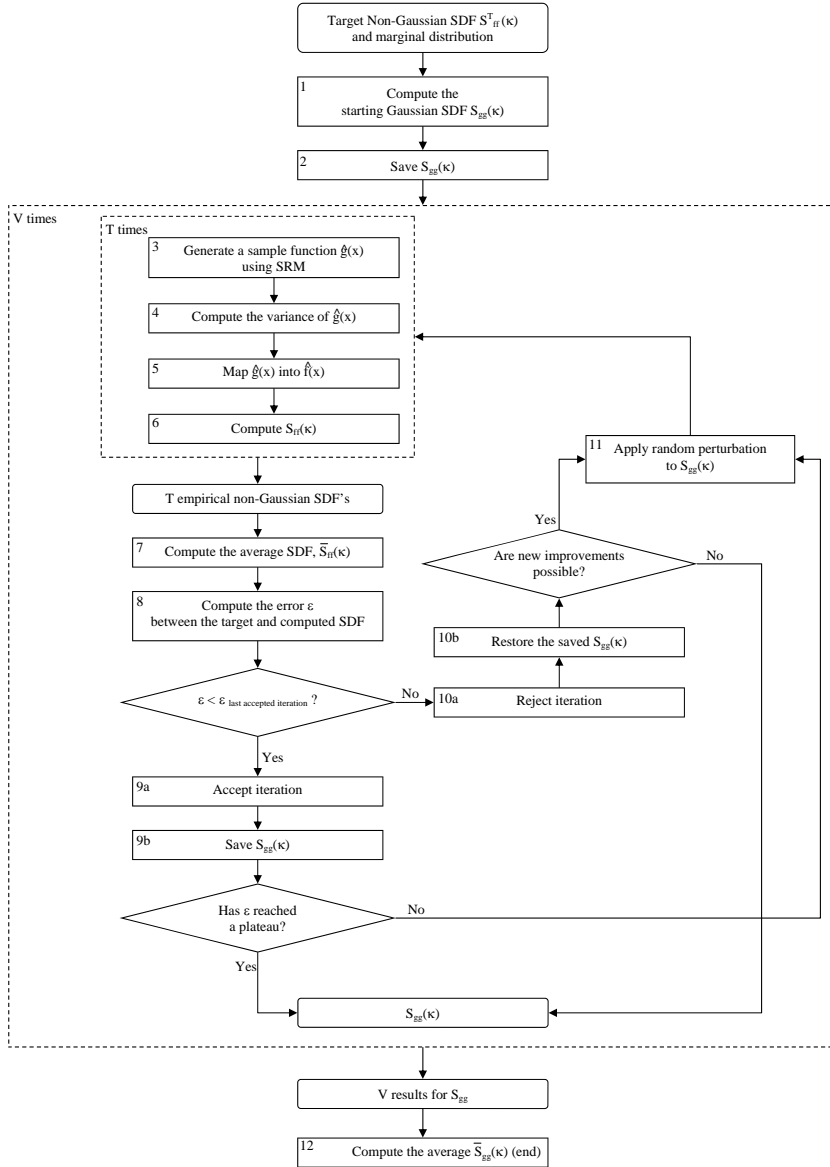


Figure 3.1: Flow chart of the proposed simulation algorithm.

3.2.2 Save $S_{gg}(\kappa)$

The methodology in Fig. 3.1 is an iterative one with potential random modifications to the SDF of the underlying Gaussian field at every step. Using an acceptance criterion that will be described later, the modifications at a specific step can be accepted or rejected. For this reason, $S_{gg}(\kappa)$ is saved at each iteration so that it can be retrieved in case the iteration is rejected.

3.2.3 Generate a Sample Function $\hat{g}(x)$ Using SRM

The Spectral Representation Method (described in Sec. 2.2) is used to generate a sample function of the underlying Gaussian field $\hat{g}(x)$. The discretization of the SDF in the wave number domain is done at the following points:

$$\kappa = \left(n + \frac{1}{2}\right) \Delta\kappa \quad n = 0, 1, \dots, N - 1 \quad (3.2)$$

where $\Delta\kappa$ is defined in Eq. (2.2). The “hat” in $\hat{g}(x)$ denotes that the sample is generated using the frequency shifting theorem as proposed by Zerva (1992) to account for the discretization in Eq. (3.2). It has been shown (Zerva, 1992) that this formulation relaxes the restrictive assumption that the SDF has to be zero at the origin for the generated samples to be ergodic. Moreover, it leads to a significantly faster convergence of the probabilistic characteristics of the underlying Gaussian field to the corresponding targets (Grigoriu, 1995). A side-effect is that the resulting doubling of the period requires a different and somehow more complex computation of a sample’s SDF, as explained in

to do it just once, and not T times. After this, the algorithm proceeds exactly as the one presented in Section 3.2.

This procedure is very fast. It allows to get a quick rough estimate of $S_{gg}(\kappa)$ that is used to start the main algorithm.

Sec. 3.2.6. Consequently, the FFT implementation of the SRM is expressed as:

$$\begin{aligned}
\hat{g}(x_m) &= \\
&= \Re \left\{ 2 \sum_{n=0}^{M-1} \sqrt{S_{gg} \left(n\Delta\kappa + \frac{\Delta\kappa}{2} \right)} \Delta\kappa \exp(i\phi_n) \exp \left[i \left(n\Delta\kappa + \frac{\Delta\kappa}{2} \right) x_m \right] \right\} = \\
&= \Re \left\{ 2 \sum_{n=0}^{M-1} \sqrt{S_{gg} \left(n\Delta\kappa + \frac{\Delta\kappa}{2} \right)} \Delta\kappa \exp(i\phi_n) \exp(i n\Delta\kappa x_m) \exp \left(i \frac{\Delta\kappa}{2} x_m \right) \right\} = \\
&= \Re \left\{ \underbrace{\text{FFT}^+ \left[2 \sqrt{S_{gg} \left(n\Delta\kappa + \frac{\Delta\kappa}{2} \right)} \Delta\kappa \exp(i\phi_n) \right]}_{\text{period } \frac{2\pi}{\Delta\kappa}} \underbrace{\exp \left(i \frac{\Delta\kappa}{2} x_m \right)}_{\text{period } \frac{2\pi}{\Delta\kappa/2} = \frac{4\pi}{\Delta\kappa}} \right\}
\end{aligned} \tag{3.3}$$

where

$$x_m = m \Delta x, \quad m = 0, 1, \dots, M - 1 \tag{3.4}$$

$\Re \{ \cdot \}$ denotes the real part, $\text{FFT}^+ [\cdot]$ denotes the Fast Fourier Transform with positive exponent, M is the number of intervals in the space / wave number domain, and Δx and $\Delta\kappa$ are related through:

$$\Delta x \Delta\kappa = \frac{2\pi}{M} \tag{3.5}$$

Equation (3.3) indicates that the period of the generated sample function is $L = \frac{4\pi}{\Delta\kappa}$, which is double the period of the classic SRM algorithm in Eq. (2.1) without frequency shifting. The $L = \frac{4\pi}{\Delta\kappa}$ period has $2M$ points. The first set of M points is determined from Eq. (3.3). The second set of M points is determined from:

$$\hat{g}(x_{m+M}) = -\hat{g}(x_m) \quad m = 0, 1, \dots, M - 1 \tag{3.6}$$

that is consistent with Eq. (3.3).

It is worth noting that as the variance of $g(x)$ is not constrained, $g(x)$ will be Gaussian, but not standardized Gaussian.

3.2.4 Compute the Variance of $\hat{g}(x)$

The mean of $\hat{g}(x)$ is always zero because of the way it is generated (using SRM and considering one period). Its variance $\sigma_{\hat{g}}^2$ can be estimated either from the generated sample function or from the SDF $S_{gg}(\kappa)$. Consequently, the Gaussian Cumulative Distribution Function of $\hat{g}(x)$ is fully known:

$$\mathcal{F}_g[\hat{g}] = \int_{-\infty}^{\hat{g}} \frac{1}{\sqrt{2\pi\hat{\sigma}_g}} \exp\left[-\frac{u^2}{2\hat{\sigma}_g^2}\right] du \quad (3.7)$$

3.2.5 Map $\hat{g}(x)$ into $\hat{f}(x)$

The classic translation field memoryless transformation (Grigoriu, 1984, 1995) is used to map the underlying Gaussian sample function to a non-Gaussian one having the prescribed marginal CDF, \mathcal{F}_f :

$$\hat{f}(x) = \mathcal{F}_f^{-1}\{\mathcal{F}_g[\hat{g}(x)]\} \quad (3.8)$$

For some distributions (e.g. the lognormal, Grigoriu, 1995), the inverse of \mathcal{F}_f is available in closed form. Otherwise, a numerical inversion is used.

It should be noted that although $\hat{g}(x)$ is not a standard Gaussian, $\hat{f}(x)$ still possesses all the properties of translation fields, as indicated by Grigoriu (1984). Another interesting point is that although $\hat{f}(x)$ conserves the ergodicity in the mean property of $\hat{g}(x)$, it does not conserve its ergodicity in autocorrelation property.

3.2.6 Compute $S_{ff}(\kappa)$

The Spectral Density Function of $\hat{f}(x)$ can not be estimated by means of the formula in Eq. (2.12) because a different discretization has been used in the wave number domain –the one shown in Eq. (3.2)–. In order to estimate the

SDF at the shifted wave numbers of Eq. (3.2), the following expression is used:

$$\begin{aligned}
 S_{ff} \left(n\Delta\kappa + \frac{\Delta\kappa}{2} \right) &= \frac{1}{2\pi L} \left| \int_0^L \hat{f}(x) \exp \left[-i \left(n\Delta\kappa + \frac{\Delta\kappa}{2} \right) x \right] dx \right|^2 = \\
 &= \frac{1}{2\pi L} \left| \int_0^L \hat{f}(x) \exp(-i n\Delta\kappa x) \exp \left(-i \frac{\Delta\kappa}{2} x \right) dx \right|^2
 \end{aligned} \tag{3.9}$$

or taking advantage of the Fast Fourier Transform:

$$\begin{aligned}
 S_{ff} \left(n\Delta\kappa + \frac{\Delta\kappa}{2} \right) &= \frac{1}{2\pi L} \left| \text{FFT}^- \left[\hat{f}(x_m) \exp \left(-i \frac{\Delta\kappa}{2} x_m \right) \right] \Delta x \right|^2 = \\
 &= \frac{1}{2\Delta\kappa M^2} \left| \text{FFT}^- \left[\underbrace{\hat{f}(x_m)}_{\text{period } \frac{4\pi}{\Delta\kappa}} \underbrace{\exp \left(-i \frac{\Delta\kappa}{2} x_m \right)}_{\text{period } \frac{4\pi}{\Delta\kappa}} \right] \right|^2
 \end{aligned} \tag{3.10}$$

where

$$x_m = m\Delta x \quad \text{with} \quad m = 0, 1, \dots, 2M - 1 \tag{3.11}$$

and $\text{FFT}^-[\cdot]$ denotes the Fast Fourier Transform with negative exponent.

The FFT in Eq. (3.10) indicates that the resulting SDF will be provided in the wave number domain over a length equivalent to $\frac{4\pi}{\Delta\kappa}$ in the space domain. However, meaningful information about the SDF in the wave number domain exists only over a length equivalent to $\frac{2\pi}{\Delta\kappa}$ in the space domain. It should be taken into account here that the property in Eq. (3.6) is lost for the non-Gaussian field. Consequently, the non-Gaussian sample function $\hat{f}(x)$ is not a sample function whose period has been artificially doubled from $\frac{2\pi}{\Delta\kappa}$ to $\frac{4\pi}{\Delta\kappa}$ —as was the case with $\hat{g}(x)$ —, but a sample function consisting of two essentially uncorrelated sub-samples, each one of length $\frac{2\pi}{\Delta\kappa}$.

Equation (3.10) is therefore applied twice, the first time to the first half of the sample, and the second time to the second half. Then the two resulting SDF's are averaged. This is expressed in the following Equations, where the

multiplying factors have been doubled because the periods are one half of L :

$$S'_{fff} \left(n\Delta\kappa + \frac{\Delta\kappa}{2} \right) = \frac{1}{\Delta\kappa M^2} \left| \text{FFT}^- \left[\hat{f}(x_m) \exp \left(-i \frac{\Delta\kappa}{2} x_m \right) \right] \right|^2 \quad (3.12)$$

with $m = 0, 1, \dots, M - 1$

$$S''_{fff} \left(n\Delta\kappa + \frac{\Delta\kappa}{2} \right) = \frac{1}{\Delta\kappa M^2} \left| \text{FFT}^- \left[\hat{f}(x_m) \exp \left(-i \frac{\Delta\kappa}{2} x_m \right) \right] \right|^2 \quad (3.13)$$

with $m = M, M + 1, \dots, 2M - 1$

$$S_{fff} \left(n\Delta\kappa + \frac{\Delta\kappa}{2} \right) = \frac{S'_{fff} \left(n\Delta\kappa + \frac{\Delta\kappa}{2} \right) + S''_{fff} \left(n\Delta\kappa + \frac{\Delta\kappa}{2} \right)}{2} \quad (3.14)$$

The SDF in Eq. (3.14) is only an approximation of the exact SDF of the non-Gaussian field, as $\hat{f}(x)$ is not ergodic in autocorrelation.

3.2.7 Compute the Average SDF, $\bar{S}_{ff}(\kappa)$

For an accurate estimation of the spectral density function of the non-Gaussian field, it is necessary to average the empirical SDF's of many sample functions –each computed using Eq. (3.14)–. For this reason, the steps described in Secs. 3.2.3–3.2.6 are repeated T times, and then the average SDF is computed from:

$$\bar{S}_{ff}(\kappa) = \frac{1}{T} \sum_{t=1}^T S_{ff}^{(t)}(\kappa) \quad (3.15)$$

An extensive numerical investigation has revealed that a value of $T = 60$ is usually sufficient to get a very good and smooth approximation of $\bar{S}_{ff}(\kappa)$, as represented in Fig. 3.2.

3.2.8 Compute the Error ε Between the Target and Computed SDF

The error between the target SDF of the non-Gaussian field and the computed SDF at a specific iteration is measured by means of the following expression:

$$\varepsilon = 100 \sqrt{\frac{\sum_{n=0}^{N-1} \left[\bar{S}_{ff}(\kappa_n) - S_{ff}^T(\kappa_n) \right]^2}{\sum_{n=0}^{N-1} \left[S_{ff}^T(\kappa_n) \right]^2}} \quad (3.16)$$

Since $\bar{S}_{ff}(\kappa)$ is usually smooth from the ensemble averaging, Eq. (3.16) gives an accurate estimate of the difference between the target and the computed SDF's. Figure 3.2 shows that if only a single $S_{ff}^{(t)}(\kappa)$ were used instead –as done by the Shi and Deodatis algorithm, according to Eq. (2.21)–, the value of ε would be governed more by the scattering of $S_{ff}^{(t)}(\kappa)$, than by the real difference between the shapes of the target and the computed SDF's. In contrast, using $\bar{S}_{ff}(\kappa)$ to estimate the error, reflects better the true difference between the shapes of the two SDF's and results in an overall faster convergence of the iterative scheme (although T samples have to be generated at every iteration).

3.2.9 Accept Iteration and Save $S_{gg}(\kappa)$

If the error computed through Eq. (3.16) is smaller than that computed in the last accepted iteration, then the current iteration is accepted. For the same reason as explained in Section 3.2.2, the current Gaussian SDF $S_{gg}(\kappa)$ is saved.

Then, a check is performed to determine whether convergence is met or not. The criterion for reaching convergence is for the value of ε to be reduced by less than 0.01% during the last 20 accepted iterations (“Plateau reached”). The values 20 and 0.01% have been determined after an extensive numerical investigation. If the convergence criterion is satisfied, the iterative scheme ends. Otherwise, the iterations continue and a random perturbation is applied to $S_{gg}(\kappa)$, as explained in Section 3.2.11.

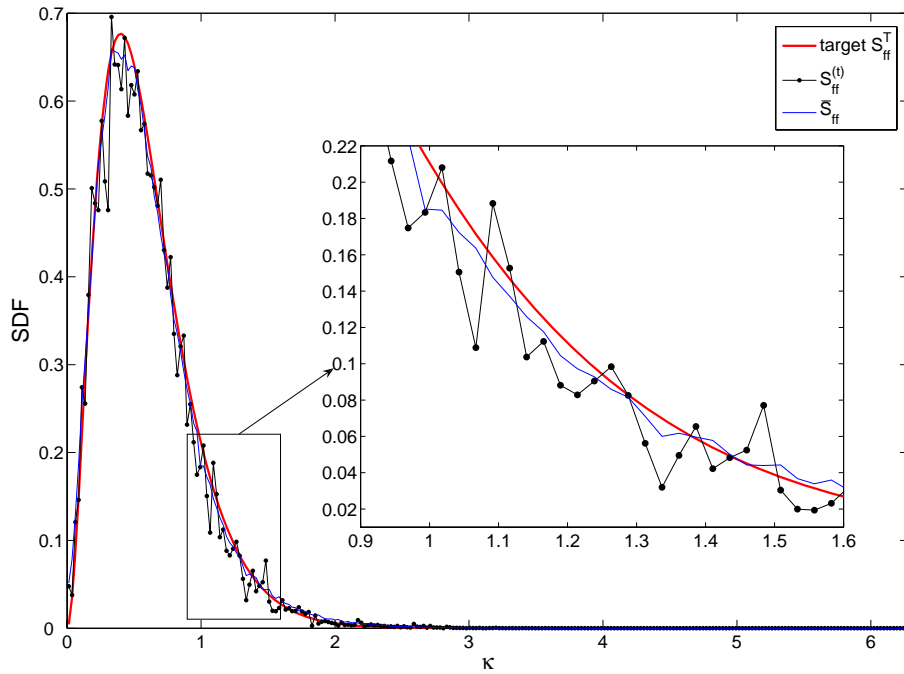


Figure 3.2: Comparison between the SDF estimated using one sample function $\hat{f}(x)$ and the SDF estimated using 60 sample functions $\hat{f}(x)$.

3.2.10 Reject Iteration and Restore the Saved $S_{gg}(\kappa)$

If the error computed through Eq. (3.16) is greater than that computed in the last accepted iteration, then the current iteration is rejected. This means that the random perturbation previously applied to $S_{gg}(\kappa)$ has led to a non-Gaussian SDF that is further away from the target. Therefore, the saved $S_{gg}(\kappa)$ of the last accepted iteration is restored.

Furthermore, a convergence check is performed at this point. The algorithm keeps track of whether all of the last $4N$ iterations have been rejected (“Maximum improvement reached”). The meaning of the value $4N$ will become clear in Section 3.2.11. If all of the last $4N$ iterations have been rejected, the iterative scheme ends. Otherwise, the iterations go on and a random perturbation is applied to $S_{gg}(\kappa)$, as explained in the next Section.

3.2.11 Apply Random Perturbation to $S_{gg}(\kappa)$

As mentioned earlier, if the convergence checks are not satisfied, the iterations continue and a random perturbation is applied to the current $S_{gg}(\kappa)$. Specifically, the following perturbation ΔS is added to the underlying Gaussian spectrum:

$$\Delta S = A \exp \left[-\frac{(\kappa - \kappa_0)^2}{40} \right] \quad (3.17)$$

where κ_0 is a point selected randomly in the interval $[0, \kappa_u]$, and A is equal to $\pm \frac{S_{gg}(\kappa_0)}{10}$ with its sign randomly selected.

This perturbation ΔS obviously dies down quickly to the left and to the right of κ_0 . Consequently, only $\frac{N}{16}$ points of $S_{gg}(\kappa)$ are modified according to Eq. (3.17) (beyond these $\frac{N}{16}$ points the modifications are negligible and therefore disregarded). If κ_0 is too close to 0 or κ_u , then the perturbation involves less than $\frac{N}{16}$ points. Different functional forms and extensions of the perturbation scheme have been tried. The one selected—Eq. (3.17)—provided the best convergence characteristics. Figure 3.3 displays a representative example of this random perturbation.

In an average sense, every $4N$ iterations, each point of $S_{gg}(\kappa)$ should be chosen twice as κ_0 with a positive sign for ΔS , and twice as κ_0 with a negative sign for ΔS . Since the number of iterations is finite and limited, it appears reasonable to assume only that every $4N$ iterations, each region of $S_{gg}(\kappa)$ has gone through an iteration with a positive sign for ΔS and an iteration with a

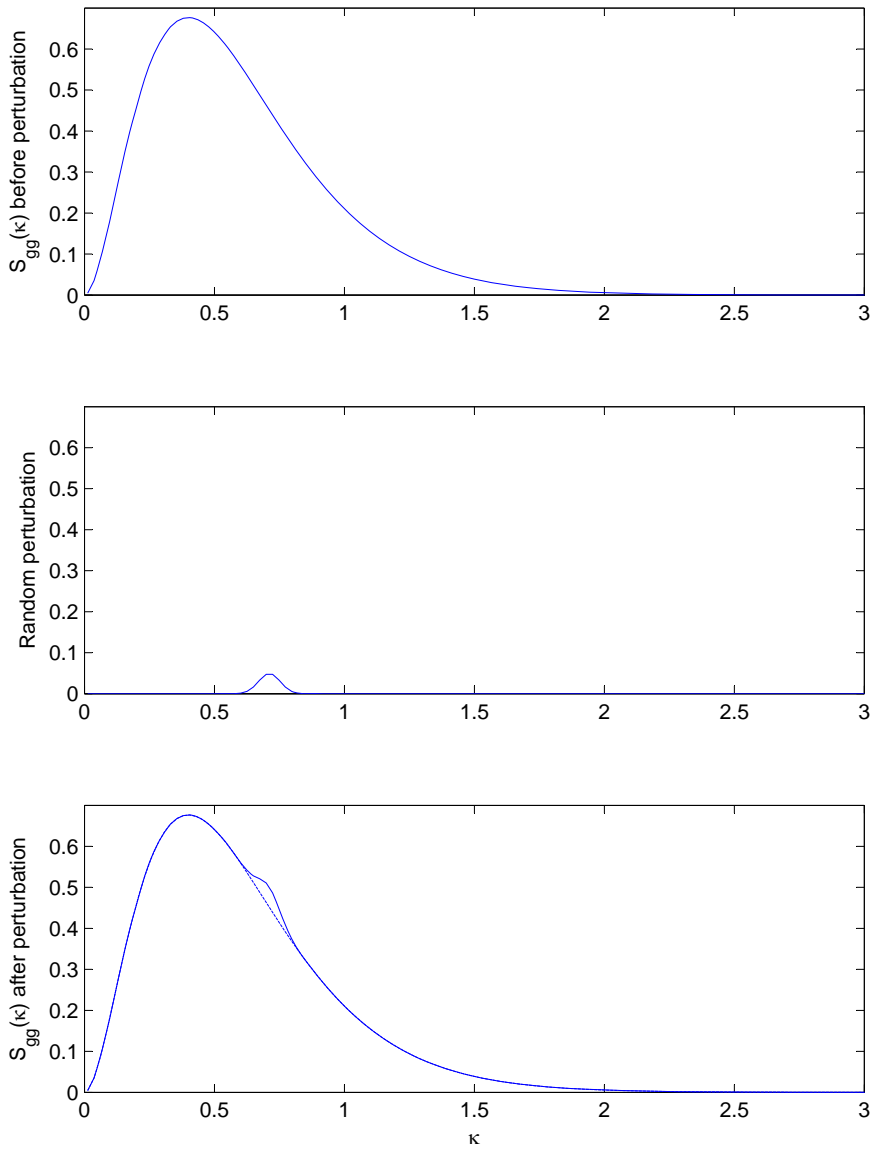


Figure 3.3: Representative example of random perturbation of $S_{gg}(\kappa)$.

negative sign for ΔS . Consequently, if $4N$ consecutive iterations are rejected, it is considered unlikely that further improvements in the convergence are possible and the iterative scheme ends (see Section 3.2.10).

A significant advantage of this perturbation scheme is that it is not inducing sharp discontinuities in $S_{gg}(\kappa)$. This translates into faster convergence. It should be noticed that this perturbation scheme changes the area underneath the $S_{gg}(\kappa)$. Consequently, the variance of the underlying Gaussian field $g(x)$ is not constant. As already mentioned, this allows to search for the most suitable $S_{gg}(\kappa)$ from a larger range of admissible SDF's, and, in general, leads to a better overall solution.

After a random perturbation is implemented and a new $S_{gg}(\kappa)$ is determined, the iterative scheme continues with the simulation of $\hat{g}(x)$ as described in Section 3.2.3.

3.2.12 Compute the Average $\bar{S}_{gg}(\kappa)$

The resulting SDF $S_{gg}(\kappa)$ after completing the steps in Secs. 3.2.3–3.2.11 (called a “run”) is not unique. A slightly different $S_{gg}(\kappa)$ will be obtained from a different run. Consequently, a total of V runs are performed and an average SDF of the underlying Gaussian field is estimated as:

$$\bar{S}_{gg}(\kappa) = \frac{1}{V} \sum_{v=1}^V S_{gg}^{(v)}(\kappa) \quad (3.18)$$

A numerical investigation has suggested that a value of $V = 10$ is sufficient for an accurate estimation of $\bar{S}_{gg}(\kappa)$. However, to ensure even higher accuracy, a value of $V = 50$ is used throughout the “Numerical Examples” Section that follows.

Once the ensemble-averaged SDF of the underlying Gaussian field $\bar{S}_{gg}(\kappa)$ is available, the generation of sample functions of the non-Gaussian random field $f(x)$ is straightforward and extremely efficient computationally. In fact, only the steps described in Secs. 3.2.3 and 3.2.5 are necessary and no iterations are involved. The generated non-Gaussian random fields will perfectly match the target distribution \mathcal{F}_f , they will have a SDF very close to the target (in ensemble-average sense) $S_{ff}^T(\kappa)$, and they will also possess all the properties of translation fields according to Grigoriu's theory (Grigoriu, 1984, 1995).

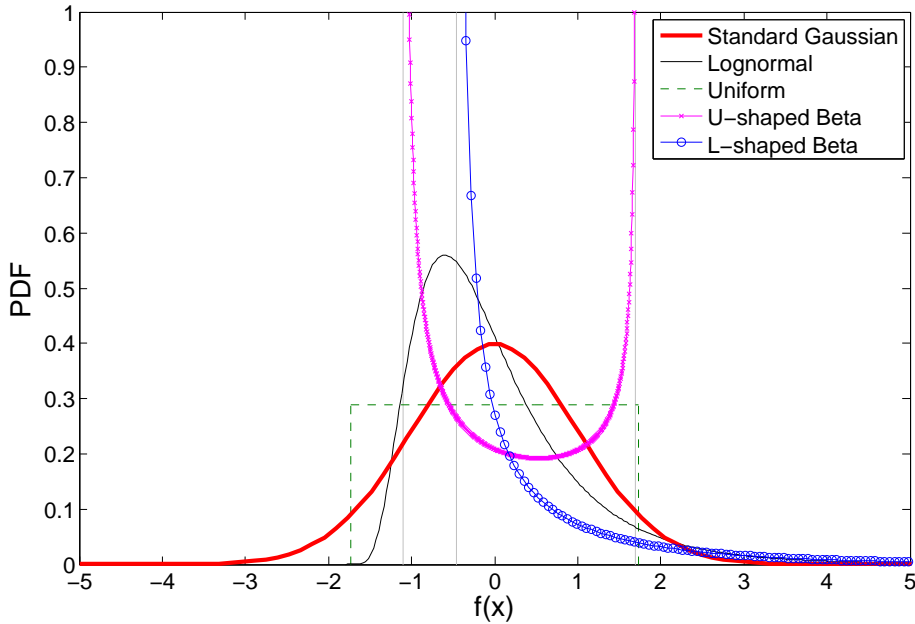


Figure 3.4: Four probability density functions compared with the Standard Gaussian.

3.3 Numerical Examples

Four numerical examples are provided involving four different marginal distributions for the non-Gaussian field: (1) a Lognormal distribution is used to compare the proposed method with those described in Sec. 2.3, (2 & 3) a Uniform distribution and a U-shaped Beta distribution are used to demonstrate the capabilities of the methodology when dealing with strongly non-Gaussian distributions, (4) an L-shaped Beta distribution with coefficient of skewness 4 and coefficient of kurtosis 25 is used to explore the limits of applicability of the method. The probability density functions of all four distributions are plotted in Fig. 3.4.

For all examples, the target spectral density function is selected as:

$$S_{ff}^T(\kappa) = \frac{125}{4} \sigma_f^2 \kappa^2 \exp(-5|\kappa|) \quad (3.19)$$

with $\sigma_f^2 = 1$. The cutoff wave number is set equal to $\kappa_u = 6.28$ rad/sec, the number of intervals in the wave number domain is $N = 256$, and the number of intervals used for the Fast Fourier Transform is $M = 2^{10} = 1024$. The random phase angles ϕ are generated by means of the Mersenne Twister (Matsumoto and Kurita, 1992; Matsumoto and Nishimura, 1998).

3.3.1 Comparison with the Algorithms Presented in Sec. 2.3

Results for the three previously developed methods presented in Sec. 2.3 are available in the literature (Deodatis and Micaletti, 2001; Shi, 2006) for the Lognormal distribution with the following PDF:

$$\mathcal{P}(x) = \frac{1}{\sqrt{2\pi}\sigma_N \bar{x}} \exp\left[-\frac{(\ln \bar{x} - \mu_N)^2}{2\sigma_N^2}\right] \quad (3.20)$$

where:

$$\sigma_N^2 = \ln\left(1 + \frac{\sigma}{\bar{\mu}}\right) \quad ; \quad \mu_N = \ln \bar{\mu} - \frac{\sigma_N^2}{2} \quad ; \quad \bar{x} = x - \bar{\mu} \quad (3.21)$$

The choice of the following values for parameters $\bar{\mu}$ and σ :

$$\bar{\mu} = 1.8 \quad ; \quad \sigma^2 = 1 \quad (3.22)$$

leads to the following moments for the Lognormal distribution:

$$\text{mean: } \mu = 0 \quad ; \quad \text{variance: } \sigma^2 = 1 \quad ; \quad \text{skewness: } \gamma = 1.838 \quad ; \quad \text{kurtosis} = 9.553$$

This distribution is defined over the interval $[-1.8, \infty]$. Figure 3.4 and the skewness and kurtosis coefficients give an idea of the strong deviation of this distribution from the Gaussian.

For comparison purposes, 100 sample functions are generated using each one of the four methodologies. Their ensemble-averaged SDF's and PDF's are plotted in Figs. 3.5 and 3.6 respectively.

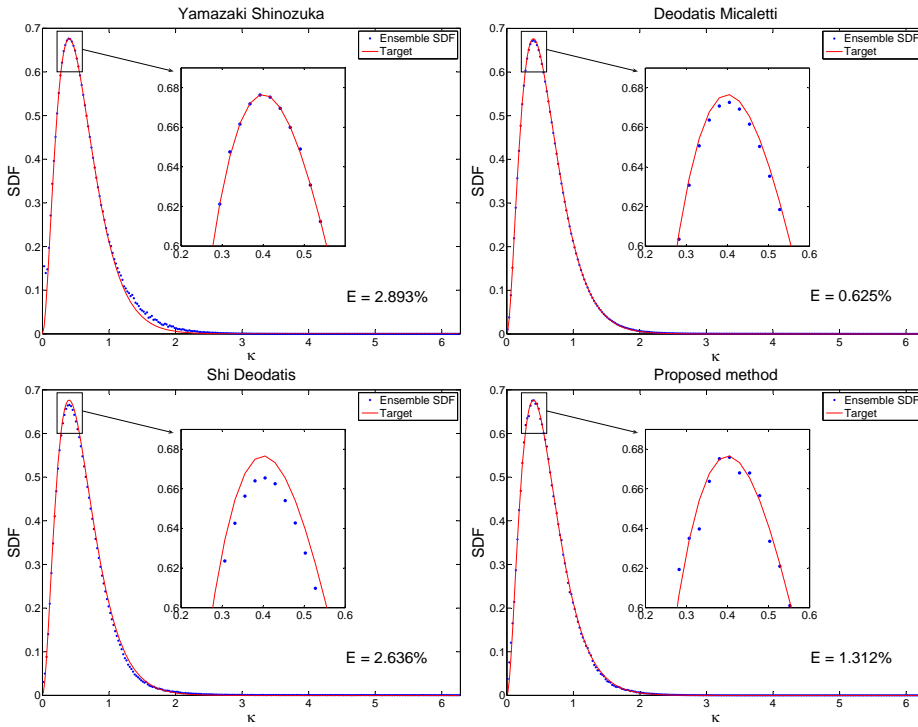


Figure 3.5: Lognormal distribution: non-Gaussian ensemble-averaged spectral density functions compared with the corresponding target (E denotes the error).

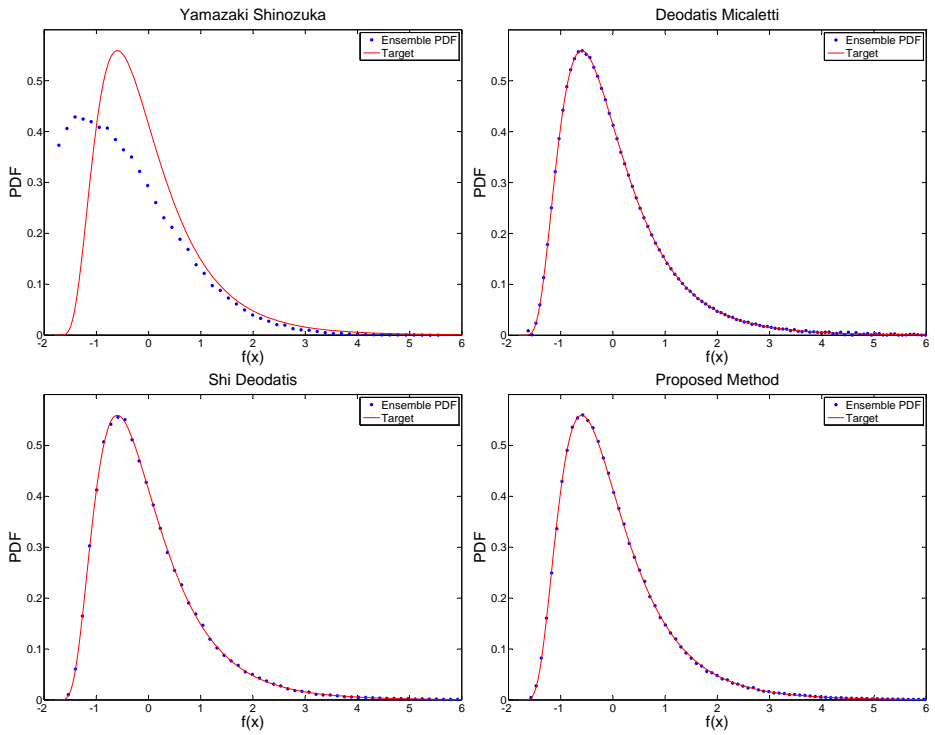


Figure 3.6: Lognormal distribution: non-Gaussian ensemble-averaged probability density functions compared with the corresponding target.

It is generally acknowledged that the spectral density function of a non-Gaussian translation field cannot be equal to zero at zero wave number (even when the SDF of the underlying Gaussian field is zero at zero wave number, refer to Eq. (2.14) and see for example Grigoriu, 1995, Par. 3.1). The target SDF of the non-Gaussian field in this work is selected to be equal to zero at zero wave number –see Eq. (3.19)–, an a priori known incompatibility (Deodatis and Micaletti, 2001). For this reason, all errors reported in Fig. 3.5 disregard the first four points in the wave number domain. However, these first four points are considered in the error calculations during the iterative schemes of all four methodologies.

The following conclusions are drawn by studying Figs. 3.5 and 3.6. The Yamazaki and Shinozuka algorithm has shown convergence problems in the past when dealing with this Lognormal distribution. To enhance its performance, the updating formula proposed by Deodatis and Micaletti –see Eq. (2.19)– is used to obtain the results shown in this paper. However, as can be seen in Fig. 3.6, it is still unsuccessful in matching the target PDF. The Deodatis and Micaletti algorithm shows exceptional accuracy in matching both the target SDF and PDF. However, it is not producing sample functions that have the properties of translation fields. In contrast, the sample functions generated by the Shi and Deodatis algorithm are translation fields. They match the target PDF with great accuracy. The match of the target SDF is good, but not as good as that of the PDF. The methodology proposed in this paper matches almost perfectly the target PDF, but loses some accuracy in the matching of the SDF. However, as can be seen in Fig. 3.5, the error in the SDF is reduced to one half the corresponding error obtained by the Shi and Deodatis algorithm. It should be mentioned that the samples generated by the proposed methodology possess all the properties of translation fields.

Since the last two methodologies have similar characteristics, a further comparison is conducted. Both methods are aiming to determine an underlying Gaussian field that provides the best match of the non-Gaussian targets. For this purpose, the two $S_{gg}(\kappa)$'s resulting from the two methods have been plugged into the “double integration formula” reported in Eq. (2.14). This way, the comparison is not affected by the (random) choice of ϕ angles. The two resulting non-Gaussian SDF's are plotted in Fig. 3.7 where it can be seen that the matching of the proposed algorithm is essentially perfect (except for the region close to $\kappa = 0$ where the non-Gaussian spectrum can not be zero).

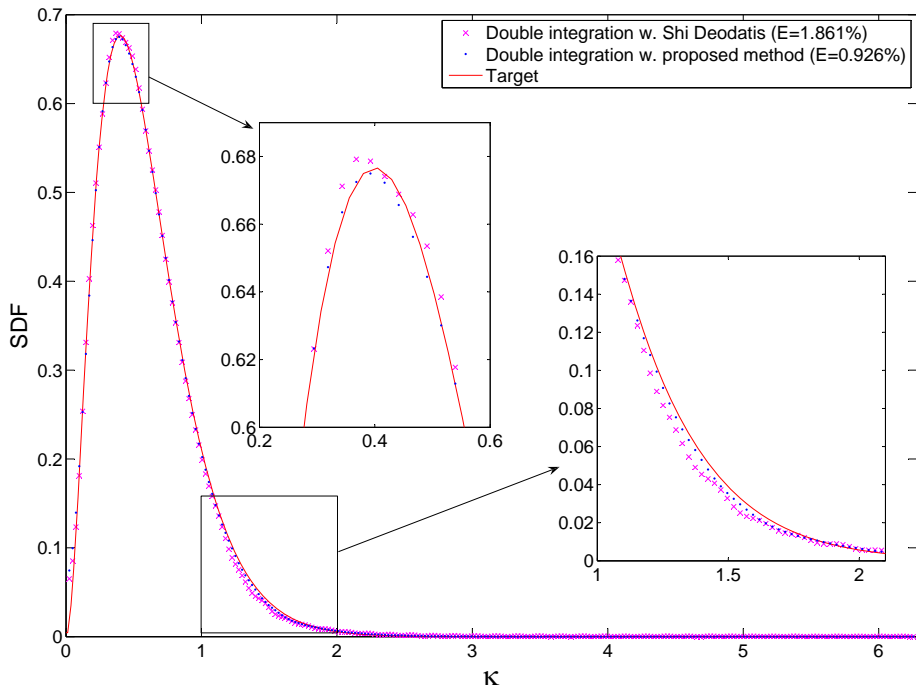


Figure 3.7: Lognormal distribution: computed non-Gaussian spectral density functions compared with the corresponding target. The computed SDF's have been determined using the double integration formula (E denotes the error).

3.3.2 Other Strongly Non-Gaussian Distributions

The proposed algorithm has been tested with two more strongly non-Gaussian marginal distributions: the Uniform and the U-shaped Beta.

The Uniform distribution used has PDF given by:

$$\mathcal{P}(x) = \begin{cases} \frac{1}{b-a} & a \leq x \leq b \\ 0 & \text{otherwise} \end{cases} \quad (3.23)$$

with parameters:

$$a = -\sqrt{3} \quad ; \quad b = \sqrt{3} \quad (3.24)$$

resulting in the following moments:

$$\text{mean: } \mu = 0 \ ; \ \text{variance: } \sigma^2 = 1 \ ; \ \text{skewness: } \gamma = 0 \ ; \ \text{kurtosis} = 1.8 \quad (3.25)$$

Results concerning the matching of the SDF and the PDF are presented in Figs. 3.8 and 3.9, respectively. Both matchings are highly accurate. For reasons already mentioned, the computed SDF in Fig. 3.8 is obtained through the double integration formula in Eq. (2.14).

The U-shaped Beta distribution used has PDF given by:

$$\mathcal{P}(x) = \frac{\Gamma(C+D)}{\Gamma(C)\Gamma(D)(B-A)^{C+D-1}} (x-A)^{C-1} (B-x)^{D-1} ; \quad A < x < B \quad (3.26)$$

with parameters:

$$A = -1.1 \quad ; \quad B = 1.7 \quad ; \quad C = 0.341785714 \quad ; \quad D = 0.528214286 \quad (3.27)$$

resulting in the following moments:

$$\text{mean: } \mu = 0 \ ; \ \text{variance: } \sigma^2 = 1 \ ; \ \text{skewness: } \gamma = 0.418 \ ; \ \text{kurtosis} = 1.644 \quad (3.28)$$

The distribution is defined over the interval $[-1.1, 1.7]$. Results concerning the matching of the SDF and the PDF are presented in Figs. 3.10 and 3.11, respectively. Both matchings are again highly accurate. For reasons already mentioned, the computed SDF in Fig. 3.10 is obtained through the double integration formula in Eq. (2.14).

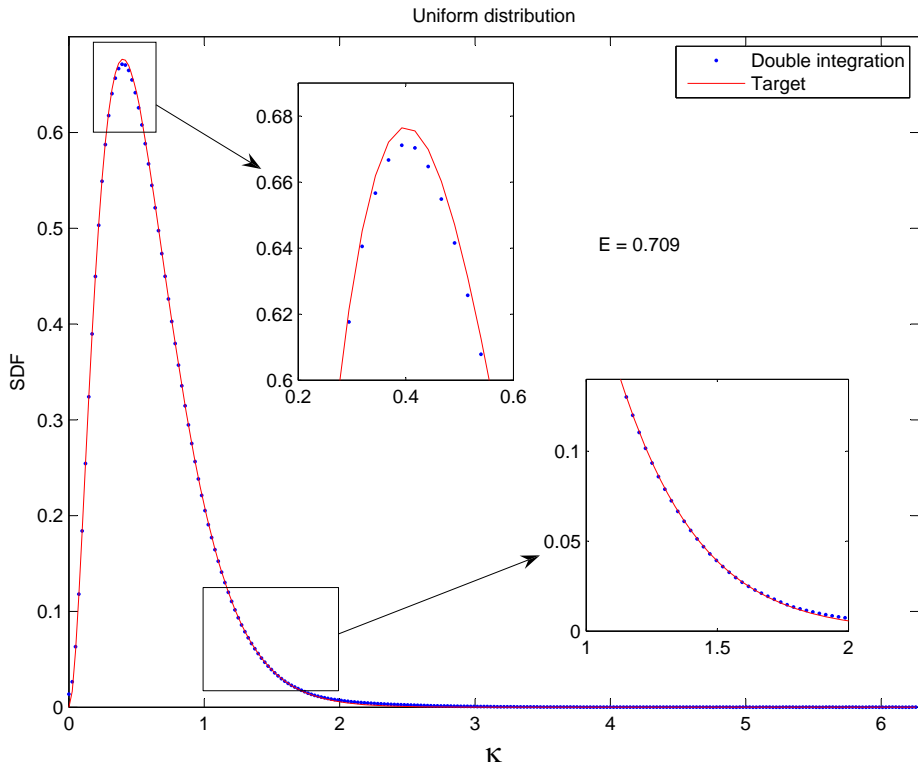


Figure 3.8: Uniform distribution: non-Gaussian spectral density function compared with the corresponding target. The computed SDF has been determined using the double integration formula (E denotes the error).

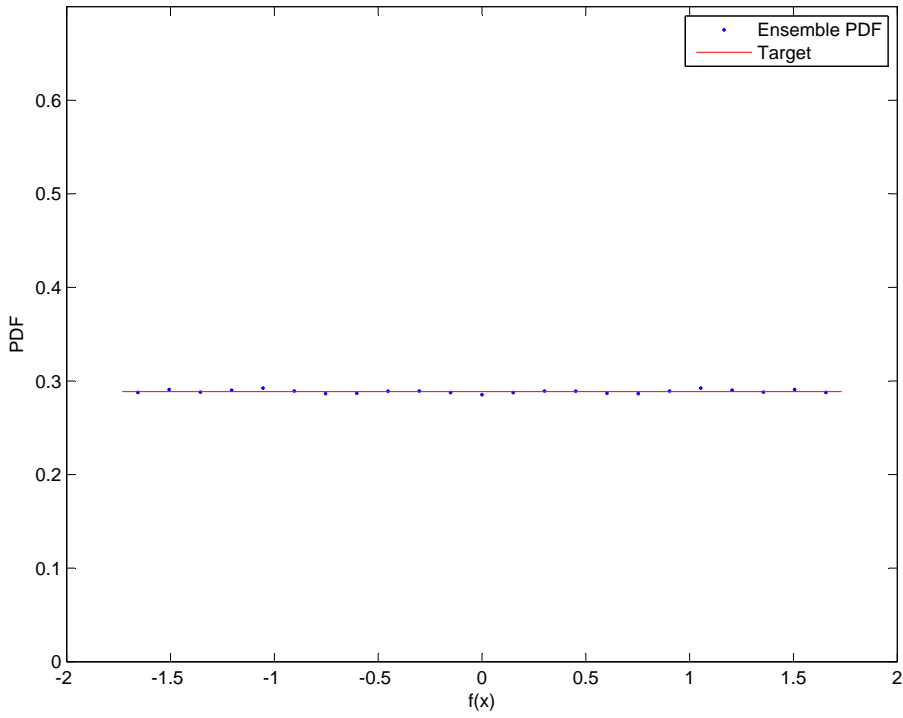


Figure 3.9: Ensemble-averaged Uniform probability density function compared with the corresponding target.

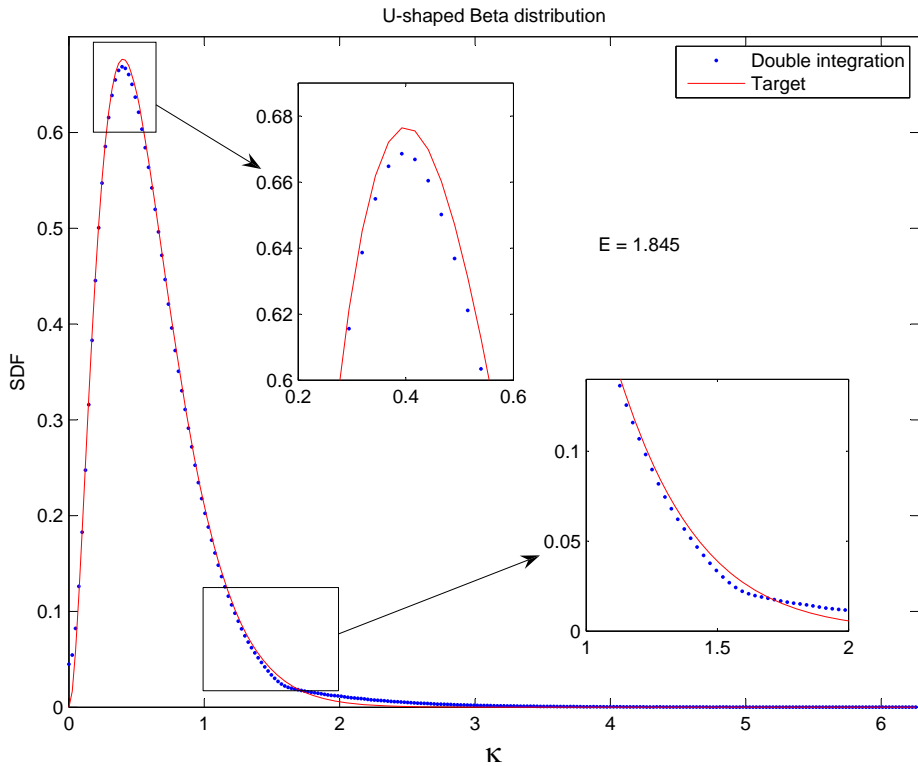


Figure 3.10: U-shaped Beta distribution: non-Gaussian spectral density function compared with the corresponding target. The computed SDF has been determined using the double integration formula (E denotes the error).

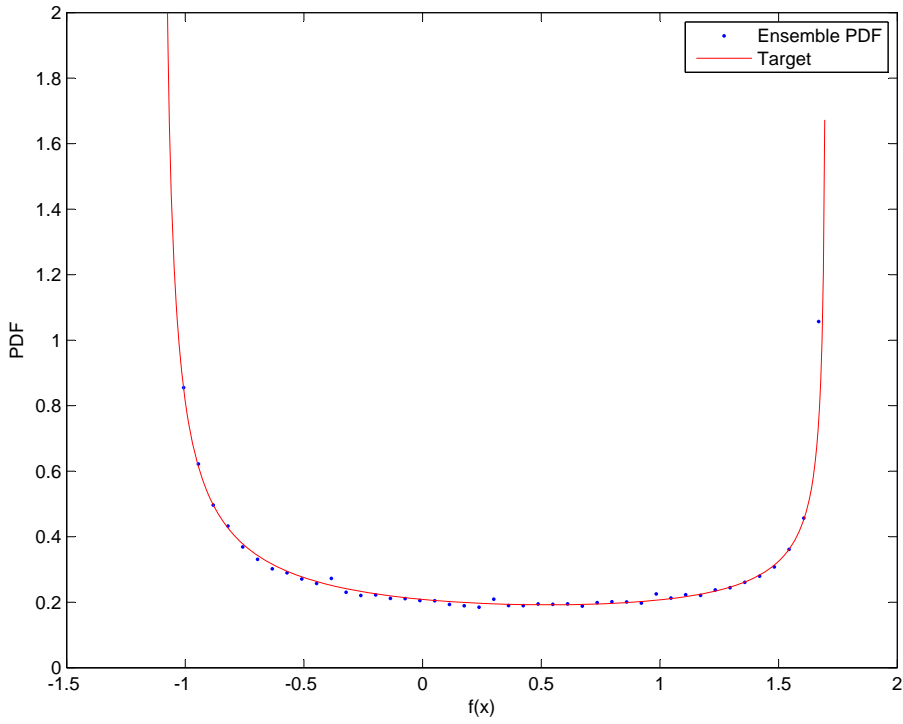


Figure 3.11: Ensemble-averaged U-shaped Beta probability density function compared with the corresponding target.

3.3.3 Limits of Applicability of the Proposed Methodology

To investigate the limits of applicability of the proposed algorithm, a Beta distribution with coefficient of skewness 4 and coefficient of Kurtosis 25 has been considered (always with zero mean and unit variance). In order to obtain these moments, the parameters of the Beta distribution –refer to Eq. (3.26)– have been set equal to:

$$A = -0.457 \quad ; \quad B = 28.43 \quad ; \quad C = 0.1895 \quad ; \quad D = 11.795 \quad (3.29)$$

The distribution (known as an L-shaped Beta) is defined over the interval $[-0.457, 28.43]$. Results concerning the matching of the SDF and the PDF are presented in Figs. 3.12 and 3.13, respectively. There are obvious problems in matching the SDF. This distribution could be therefore considered outside the limit of applicability of the methodology. However, even in this extreme case, the matching of the SDF is still respectable. For reasons already mentioned, the computed SDF in Fig. 3.12 is obtained through the double integration formula in Eq. (2.14).

3.4 Concluding Remarks and Computational Efficiency

The proposed methodology is the latest development in a class of simulation algorithms for non-Gaussian fields that started in 1988 with the Yamazaki and Shinozuka algorithm, and continued with the Deodatis and Micaletti algorithm in 2001, and the Shi and Deodatis algorithm in 2004 (all described earlier in this paper). The algorithm proposed in this paper introduces three main modifications to the algorithm by Shi and Deodatis.

The first modification is that the non-Gaussian field is not assumed to be ergodic (and indeed it is not). Therefore, its SDF is estimated at each iteration using a set of T sample functions. The main objective of this modification is to establish an error that constitutes a true measure of the convergence of the computed SDF to the prescribed target.

The second modification is the removal of the constraint on the variance of the underlying Gaussian field. This way the algorithm searches for the best

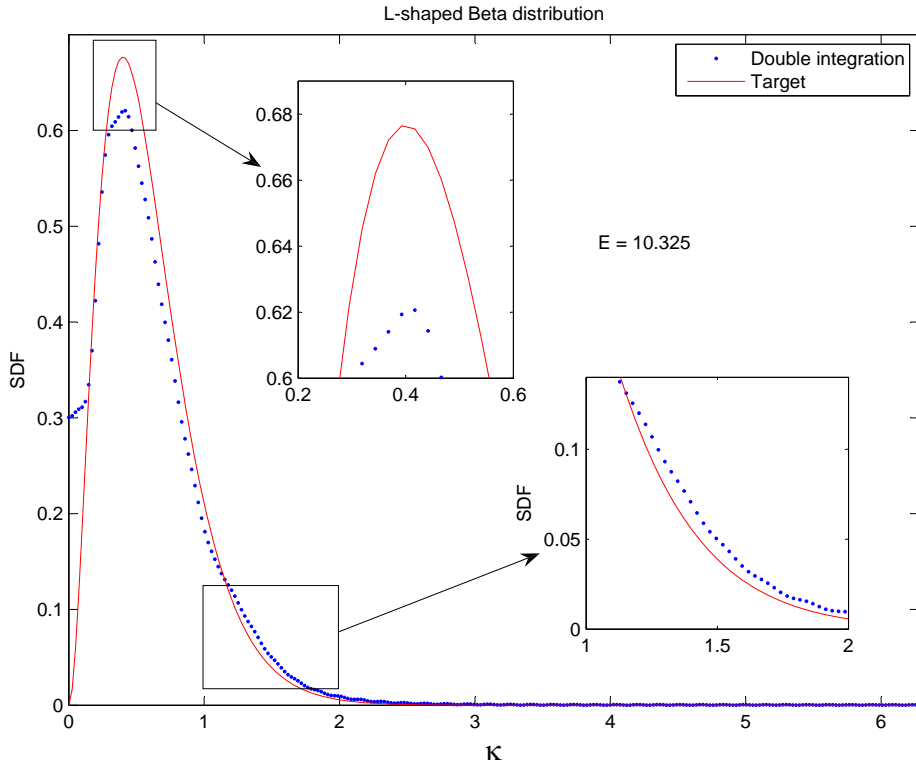


Figure 3.12: L-shaped Beta distribution: non-Gaussian spectral density function compared with the corresponding target. The computed SDF has been determined using the double integration formula (E denotes the error).

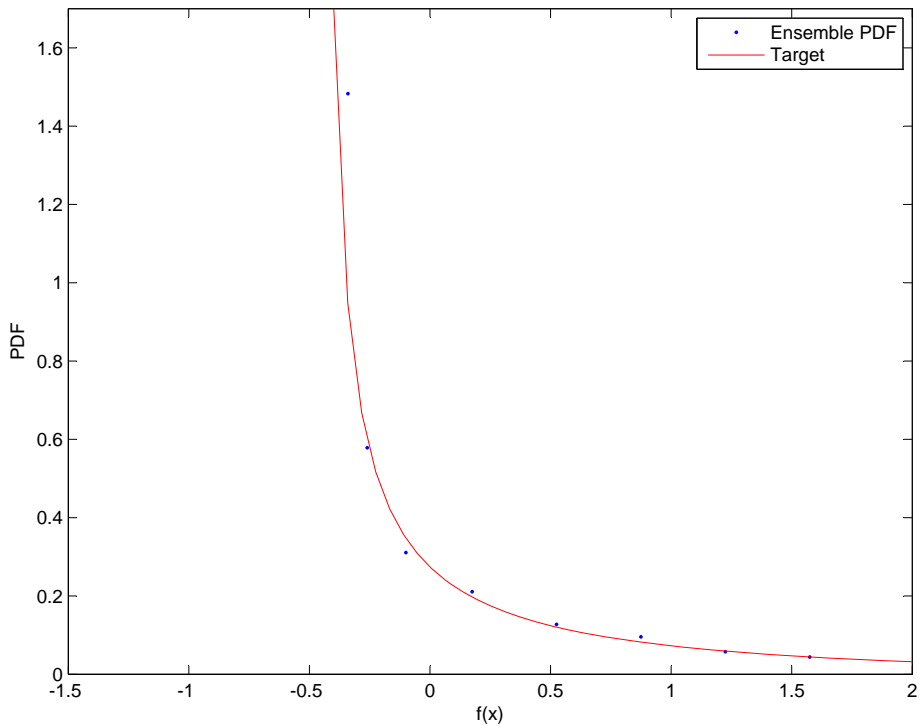


Figure 3.13: Ensemble-averaged L-shaped Beta probability density function compared with the corresponding target.

possible underlying Gaussian field over a wider range of possible solutions, and consequently it can determine in general a better solution.

The third modification involves the updating mechanism of the underlying Gaussian field. The proposed algorithm performs this updating over a prescribed wave number domain with an exponentially decaying pattern from the center of the domain, thus preserving the smoothness of the SDF. A smooth SDF is more realistic than one with sharp discontinuities (as was the case in the Shi and Deodatis algorithm), and this leads to faster convergence.

Other minor modifications are also introduced. For example, an initialization step is proposed to reduce the computational time and the Gaussian to non-Gaussian mapping is fully analytical if possible.

The numerical examples considered demonstrate that the proposed methodology is capable of simulating strongly non-Gaussian fields with high accuracy in matching both the target SDF and marginal PDF. Moreover, the generated sample functions possess all the properties of classic translation fields.

The issue of compatibility between the target non-Gaussian SDF and CDF seems to be less important than what was thought in the past. This is due to the fact that the proposed algorithm is capable of determining a compatible non-Gaussian SDF (computed by double integration) that is very close to the (arbitrarily chosen) target SDF. This is possible for the majority of marginal distributions with reasonably large deviations from the Gaussian. However, this capability is partially lost when the deviations from the Gaussian become extreme (as was shown in the example involving the L-shaped Beta distribution).

Finally, a few notes about the computational efficiency of the proposed algorithm when compared to the Shi and Deodatis one. The comparison is made for the time required to estimate the underlying Gaussian SDF $\bar{S}_{gg}(\kappa)$ (this is the part that consumes the vast majority of the computational effort for both methodologies). It has been determined that the proposed methodology requires one-half to one-third the computational effort of the Shi and Deodatis algorithm. Furthermore, the $\bar{S}_{gg}(\kappa)$ established by the proposed algorithm has approximately one-half the error of the corresponding $\bar{S}_{gg}(\kappa)$ determined by the Shi and Deodatis method. As a general conclusion, the proposed methodology reduces the computational cost, while at the same time it increases the accuracy.

Chapter 4

Simulation of Multi-Dimensional, Uni-Variate, Strongly Non-Gaussian Random Fields

*Nature permits us to calculate only probabilities,
yet science has not collapsed
-Richard P. Feynman-*

Sommario. *Le grandezze fisiche che appaiono nei modelli ingegneristici devono talvolta essere definite su domini a più dimensioni. Ad esempio, l'analisi del comportamento meccanico di un suolo o di una lastra devono essere condotte in un dominio almeno bidimensionale. Di conseguenza, i campi aleatori che modellano tali grandezze devono essere definiti nel piano o nello spazio.*

Per tale motivo, in questo Capitolo viene presentata l'estensione al

caso multidimensionale ($nD-1V$) della tecnica introdotta al Capitolo 3.

Tale generalizzazione non ha presentato particolari difficoltà analitiche, ma ha richiesto la completa riscrittura del codice numerico. Infatti la struttura dati precedentemente utilizzata per il caso monodimensionale non è parsa adeguata e sufficientemente versatile per problemi di ordine superiore. Inoltre il cospicuo aumento dell'onere computazionale ha richiesto un'ottimizzazione del codice molto più spinta, per poter tenere contenuti i tempi di calcolo.

Un esempio numerico che mostra l'efficacia del metodo ed alcune considerazioni conclusive completano il Capitolo.

4.1 Introductory Remarks

When a random field is used to simulate a physical quantity, it can happen that the domain of definition has more than one dimension. For instance, a problem involving the mechanical properties of the soil is necessarily modelled at least in a two-dimensional space, and sometimes in 3D.

For this reason, over the years many authors have proposed techniques for the simulation of multi-dimensional random fields. From the rich bibliography available, a few representative examples are mentioned here: Shinozuka (1974), Zerva (1992), Shinozuka and Deodatis (1996), Puig et al. (2002), Sakamoto and Ghanem (2002a,b), Graham et al. (2003).

In this Chapter, the methodology presented in Chapter 3 is extended to the multi-dimensional, uni-variate ($nD-1V$), non-Gaussian, homogeneous random fields. Note that the case of random waves (e.g. Shinozuka et al., 1989) is not considered, the n -dimension are all in the space domain.

A numerical example is then presented to show the accuracy of the method. Some final remarks on the computational issues involved in the problem conclude the Chapter.

4.2 Proposed Simulation Methodology

4.2.1 Theoretical Aspects

From a theoretical point of view, there are no differences between the procedure presented in this Chapter and the one treated in Chapter 3 (refer to the flow chart in Fig. 3.1). Therefore, the algorithm will not be presented here in details. Only some remarks on the main equations will be made.

The frequency shifting technique (Zerva, 1992) has been employed together with the standard multi-dimensional Spectral Representation Method (Shinozuka and Deodatis, 1996). For a two-dimensional random field, the governing equation is:

$$\begin{aligned} \hat{g}(r \Delta x_1, s \Delta x_2) = & \\ = \sqrt{2\Re} & \left[e^{\frac{i\pi r}{M_1}} e^{\frac{i\pi s}{M_2}} \left\{ \sum_{p=0}^{M_1-1} \sum_{q=0}^{M_2-1} \left[\sqrt{2S_{gg}(\kappa_p, \kappa_q)} \Delta\kappa_1 \Delta\kappa_2 e^{i\phi_{pq}^{(1)}} \right] e^{\frac{i2\pi r p}{M_1}} e^{\frac{i2\pi s q}{M_2}} \right\} \right] \\ \cdot \sqrt{2\Re} & \left[e^{\frac{i\pi r}{M_1}} e^{-\frac{i\pi s}{M_2}} \left\{ \sum_{p=0}^{M_1-1} \sum_{q=0}^{M_2-1} \left[\sqrt{2S_{gg}(\kappa_p, -\kappa_q)} \Delta\kappa_1 \Delta\kappa_2 e^{i\phi_{pq}^{(2)}} \right] e^{\frac{i2\pi r p}{M_1}} e^{-\frac{i2\pi s q}{M_2}} \right\} \right] \end{aligned} \quad (4.1)$$

where

$$\Delta x_1 = \frac{2\pi}{M_1 \Delta\kappa_1}, \quad \Delta x_2 = \frac{2\pi}{M_2 \Delta\kappa_2} \quad (4.2)$$

$$\Delta\kappa_1 = \frac{\kappa_{u1}}{N_1}, \quad \Delta\kappa_2 = \frac{\kappa_{u2}}{N_2} \quad (4.3)$$

$$\kappa_p = \left(p + \frac{1}{2} \right) \Delta\kappa_1, \quad \kappa_q = \left(q + \frac{1}{2} \right) \Delta\kappa_2 \quad (4.4)$$

$$r = 0, 1, \dots, M_1 - 1, \quad s = 0, 1, \dots, M_2 - 1 \quad (4.5)$$

$$p = 0, 1, \dots, N_1 - 1, \quad q = 0, 1, \dots, N_2 - 1 \quad (4.6)$$

and $\phi_{pq}^{(1)}, \phi_{pq}^{(2)}$ are two sets of independent random phase angles. The meaning of the other variables is a straightforward extension of the meaning of the variables of Chapter 3. The discrete notation has been adopted here to stress that the numerical implementation takes advantage of the FFT technique also in n -dimensions.

The random perturbation in Eq. (3.17) is replaced by:

$$\Delta S = A \exp \left[-\frac{(\kappa_1 - \kappa_{01})^2}{40} - \frac{(\kappa_2 - \kappa_{02})^2}{40} \right] \quad (4.7)$$

For the three-dimensional case the equations are similar but more complex.

Note also that the case of quadrant fields (see Sec. A.9) has been chosen for the sake of simplicity.

4.2.2 Computational Aspects

A detailed analysis of the numerical implementation of the code is not in the focus of this thesis. However, it should be noticed that while from a theoretical point of view no new concepts have been introduced with respect to the one-dimensional case, from a numerical point of view the code has been completely rewritten. This has been necessary for the following two reasons.

First of all, the computational effort grows enormously when increasing the number of dimensions. Therefore an optimization of the code has been necessary, to keep the computational time sufficiently moderate. To reach this goal, a large use of heavily optimized subroutines has been adopted, the loops have been substituted by vector functions (e.g. Kronecker product, matrix product) in any possible case and the multi-dimensional FFT has been employed (the summation of cosines would have a prohibitive cost in the two-dimensional case). In particular the FFTW code (Frigo and Johnson, 2005) is used for an optimized tuning of the FFT procedure with respect to the specific hardware architecture.

The second reason is that the data-structure adopted for the one-dimensional case is not suitable and flexible enough. In particular, the choice of “structures” rather than multidimensional matrices has been taken. In fact, different discretizations in the various physical dimensions (demanded by many practical applications¹) require that the variables relative to the various physical dimensions have different “lengths”. This can be accomplished either by using a more complex and very flexible data-structure or by wasting an enormous amount of allocated memory. Unfortunately, the required memory is another issue of the multi-dimensional case, so it was definitely not possible to waste it.

¹For instance, in soil mechanics, the variability along the vertical dimension is usually much higher than that in the horizontal dimensions. Therefore the vertical and horizontal discretizations are usually very different.

The final code has shown good performance in managing multi-dimensional problems both in terms of computational cost and in term of allocated memory.

4.3 Numerical Example

Consider a two-dimensional field with target SDF given by:

$$S_{ff}^T(\kappa_1, \kappa_2) = \sigma^2 \frac{b_1 b_2}{4\pi} \exp \left[- \left(\frac{b_1 \kappa_1}{2} \right)^2 - \left(\frac{b_2 \kappa_2}{2} \right)^2 \right] \quad (4.8)$$

where both parameters b_1 and b_2 (that are proportional to the correlation distance) have been set equal to 1 and σ is the standard deviation of the field. The wave number domain has been discretized according to the following definition of the parameters:

$$N_1 = 128; \quad M_1 = 2^8 = 256; \quad \kappa_{u1} = 1.6\pi \frac{rad}{m} \quad (4.9)$$

$$N_2 = 256; \quad M_2 = 2^9 = 512; \quad \kappa_{u2} = 1.6\pi \frac{rad}{m} \quad (4.10)$$

The marginal distribution is the same Lognormal used for the benchmark test of Sec. 3.3.1:

$$\mathcal{P}(x) = \frac{1}{\sqrt{2\pi\sigma_N \bar{x}}} \exp \left[- \frac{(\ln \bar{x} - \mu_N)^2}{2\sigma_N^2} \right] \quad (4.11)$$

where:

$$\sigma_N^2 = \ln \left(1 + \frac{\sigma}{\bar{\mu}^2} \right) \quad ; \quad \mu_N = \ln \bar{\mu} - \frac{\sigma_N^2}{2} \quad ; \quad \bar{x} = x - \bar{\mu} \quad (4.12)$$

The choice of the following values for parameters $\bar{\mu}$ and σ :

$$\bar{\mu} = 1.8 \quad ; \quad \sigma^2 = 1 \quad (4.13)$$

leads to the following moments for the Lognormal distribution:

$$\text{mean: } \mu = 0 \quad ; \quad \text{variance: } \sigma^2 = 1 \quad ; \quad \text{skewness: } \gamma = 1.838 \quad ; \quad \text{kurtosis} = 9.553$$

This distribution is defined over the interval $[-1.8, \infty]$.

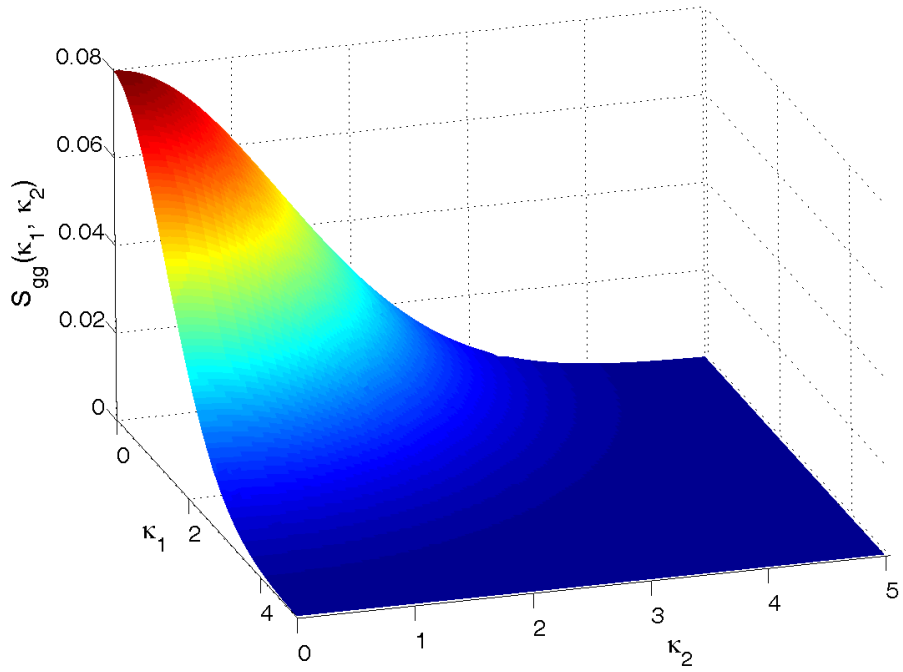


Figure 4.1: Two-dimensional underlying Gaussian spectrum.

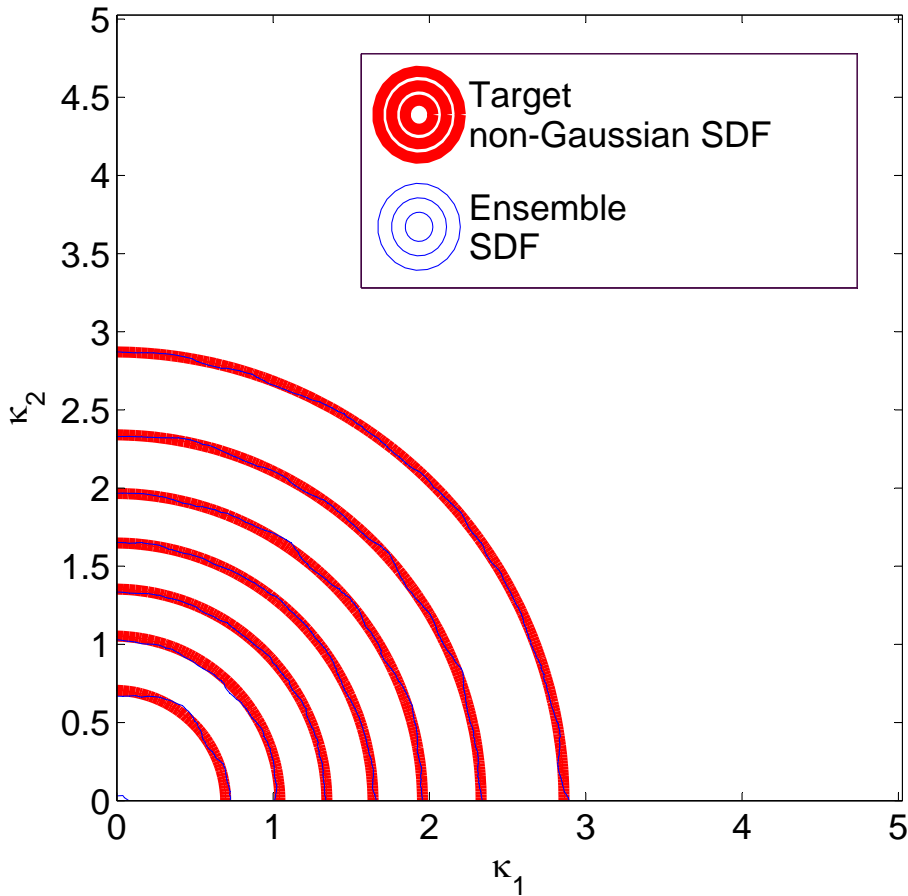


Figure 4.2: Contour plot of the “empirical” SDF estimated using 20 sample functions compared to the target SDF. The lines represent equipotential curves at the levels 0.07, 0.06, 0.05, 0.04, 0.03, 0.02, 0.01, starting from the origin.

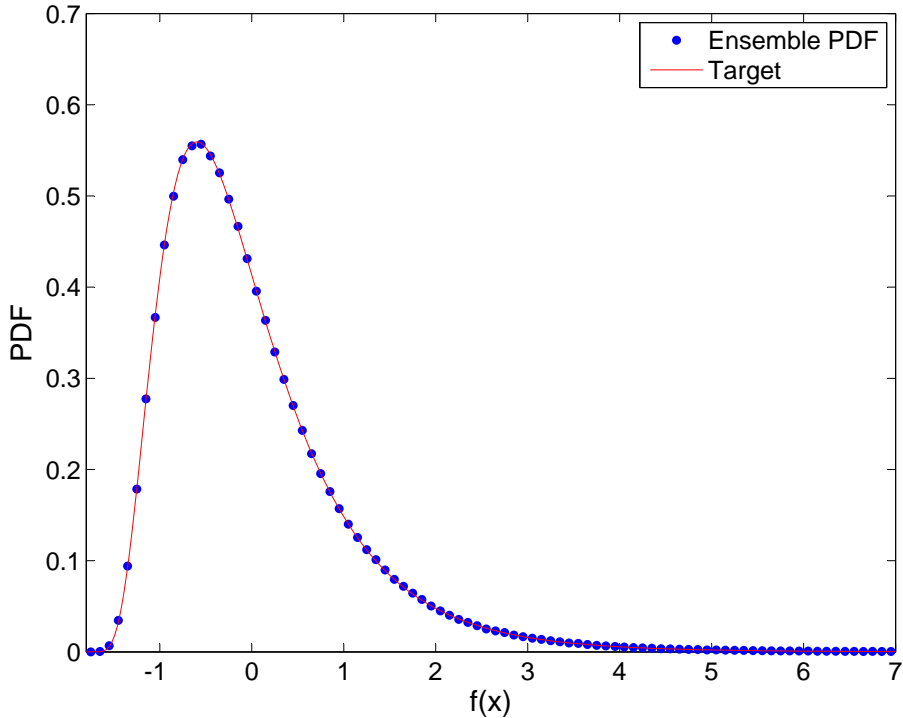


Figure 4.3: Marginal PDF estimated using 20 sample functions compared to the target Lognormal.

The code has identified the SDF represented in Fig. 4.1 as underlying Gaussian Spectrum. Fig. 4.2 compares the target spectral density $S_{ff}^T(\kappa)$ with the ensemble averaged SDF of 20 generated samples. This representation has been chosen to make the visual comparison possible. It can be noticed that the two sets of equipotential curves are almost superimposing and, therefore, the result is good (the square error is 3.5%). The matching of the prescribed marginal density is practically perfect, as Fig. 4.3 shows.

On a normal workstation², this result can be obtained in about one hour of computation.

²“Normal workstation” is referring, for instance, to a dual core 2.0GHz processor with 2Gb

4.4 Concluding Remarks and Computational Efficiency

The approach presented in Chapter 3 can be applied also to multi-dimensional random fields.

In this case, the main issue is the computational cost and the data storage. However, the rapidly increasing amount of commonly available computational power and storage capability, as well as the highly optimized code have made the algorithm suitable also for a common workstation. Moreover, in the framework of the Monte Carlo Simulation, the most time expensive task is certainly the solution of the deterministic problems, and the time required by the generation of random fields is usually negligible with respect to that.

The numerical application shows that in two-dimensions the generation of strongly non-Gaussian fields with the proposed approach is very accurate too.

Chapter 5

Simulation of One-Dimensional, Multi-Variate, Strongly Non-Gaussian Random Fields

*Randomness is originality,
and originality is art.
-Anonymous-*

Sommario. *Molto spesso i modelli ingegneristici coinvolgono grandezze aleatorie in qualche misura correlate. Ad esempio, lo sono la resistenza a trazione e l'allungamento ultimo di un cavo, così come le varie caratteristiche meccaniche di un suolo.*

In altri casi può essere conveniente sostituire un campo ad n dimensioni con un insieme di campi correlati ad $(n - 1)$ dimensioni. Ciò viene fatto solitamente nella modellazione delle fluttuazioni della velocità del vento. Queste dovrebbero essere descritte da un'onda

stocastica (cioè da un campo nel dominio del spazio e del tempo), ma vengono di solito rappresentate da una serie di processi aleatori correlati, relativi ciascuno ad un particolare punto dello spazio.

In entrambi i casi esposti, è richiesta la simulazione di campi aleatori multivariati (1D-mV), in generale non-Gaussiani.

Per tale motivo, in questo Capitolo viene presentata una metodologia che svolge tale compito sfruttando le stesse idee di base di quella illustrata al Capitolo 3. In particolare, per i termini non diagonali della matrice di densità spettrale viene identificata la cosiddetta “underlying Gaussian coherence”, o direttamente la densità spettrale congiunta.

Gli esempi numerici mostrano le capacità del metodo, che vengono riassunte e commentate nel Paragrafo conclusivo.

5.1 Introductory Remarks

The physical quantities involved in the Monte Carlo Simulation of problems in mechanics are very often described by a number of correlated variables, for instance the ultimate strength and ultimate elongation of a cable wire are correlated, the various mechanical properties of a soil are correlated. Other times, it is very useful to substitute an n -dimensional random field (or wave, meaning that one dimension is in the time domain, and the others are in the space domain) by a set of correlated $(n - 1)$ -dimensional fields/processes/waves. For instance, the wind speed is a random wave that is usually modeled as a set of random processes, each of them relative to a particular point (e.g. see Gioffre et al., 2000). In both of these cases, a multi-variate (in general non-Gaussian) random field generator is required.

Many authors have proposed methodologies for the simulation of Gaussian vector fields and processes. Among these, some of the most considerable have been done by Li and Kareem (1993), Deodatis (1996), Di Paola and Gullo (2001). Other papers consider also the case of non-Gaussian multi-variate fields, some of which are here reported in chronological order: Popescu et al. (1997), Gurley and Kareem (1998), Popescu et al. (1998), Gioffre et al. (2000), Puig et al. (2002), Gioffre and Gusella (2002), Chen and Deodatis (2004).

This Chapter presents an extension of the same basic ideas of the technique

described in Chapter 3 to the simulation of homogeneous, one-dimensional, multi-variate (1D-mV) strongly non-Gaussian random fields.

In the numerical examples only the special case in which the cross-terms of the Cross-Spectral Density Matrix (CSDM) can be expressed as:

$$S_{rs}^T(\kappa) = \gamma_{rs}^T(\kappa) \sqrt{S_{rr}^T(\kappa) S_{ss}^T(\kappa)} \quad (5.1)$$

$$0 \leq \gamma_{rs}^T(\kappa) \leq 1 \quad (5.2)$$

where γ_{rs} denotes the “coherence” function between the variables r and s is considered, for the sake of clearness of the presentation. However, the code is perfectly able to consider also the most general case of (complex) cross-spectra not described by Eq. (5.1).

The algorithm identifies an “underlying Gaussian coherence” or an “underlying Gaussian cross-spectrum” so that the resulting non-Gaussian vector (i.e. multi-variate) field has the prescribed properties.

The original contributions of the method proposed in this Chapter include high accuracy and high efficiency, especially when a very large number of samples is required (i.e. every application of the Monte Carlo Simulation).

In Sec 5.2, only random fields will be considered for simplicity. The extension to random processes is trivial, one example is presented in Sec. 6.7.3.

5.2 Proposed Simulation Methodology

In order to produce multi-variate random fields, the following macro-procedures are performed:

1. identification of the underlying Gaussian Spectral Density Function for every component (Chapter 3);
2. identification of the underlying Gaussian coherences or cross-spectra (Sec. 5.3);
3. production of the underlying Gaussian samples (Deodatis, 1996);
4. mapping of the underlying Gaussian samples to the prescribed marginal distributions (Grigoriu, 1984).

The first task is accomplished through the procedure presented in Chapter 3. The present Chapter focuses on the second step. As for the other two steps, there are a number of methodologies available in the literature. In the following paragraphs, the two that are employed are briefly described.

5.2.1 Simulation of Gaussian Vector Fields

Deodatis (1996) has proposed the algorithm that is adopted to perform the third step.

Given a certain target cross-correlation matrix $\mathbf{R}^T(\xi)$:

$$\mathbf{R}^T(\xi) = \begin{bmatrix} R_{11}^T(\xi) & R_{12}^T(\xi) & \cdots & R_{1m}^T(\xi) \\ R_{21}^T(\xi) & R_{22}^T(\xi) & \cdots & R_{2m}^T(\xi) \\ \vdots & \vdots & \ddots & \vdots \\ R_{m1}^T(\xi) & R_{m2}^T(\xi) & \cdots & R_{mm}^T(\xi) \end{bmatrix} \quad (5.3)$$

or the equivalent CSDM $\mathbf{S}^T(\kappa)$:

$$\mathbf{S}^T(\kappa) = \begin{bmatrix} S_{11}^T(\kappa) & S_{12}^T(\kappa) & \cdots & S_{1m}^T(\kappa) \\ S_{21}^T(\kappa) & S_{22}^T(\kappa) & \cdots & S_{2m}^T(\kappa) \\ \vdots & \vdots & \ddots & \vdots \\ S_{m1}^T(\kappa) & S_{m2}^T(\kappa) & \cdots & S_{mm}^T(\kappa) \end{bmatrix} \quad (5.4)$$

the algorithm produces Gaussian samples $g_c(x)$ of the m components. The formula that is used is an extension of the ‘‘Spectral Representation’’ (Shinozuka and Jan, 1972):

$$g_c(x) = 2 \sum_{n=1}^c \sum_{l=1}^N |H_{cn}(\kappa_{nl})| \sqrt{\Delta\kappa} \cos[\kappa_{nl}x - \theta_{cn}(\kappa_{nl}) + \phi_{nl}]; \quad (5.5)$$

$$c = 1, 2, \dots, m$$

where the elements $H_{cn}(\kappa)$ of the matrix $\mathbf{H}(\kappa)$ are defined so that

$$\mathbf{S}^T(\kappa) = \mathbf{H}(\kappa)\mathbf{H}^{*T}(\kappa) \quad (5.6)$$

and can be obtained, for instance, by means of a Cholesky decomposition; the phase angles $\theta_{cn}(\kappa)$ are defined as

$$\theta_{cn}(\kappa) = \tan^{-1} \left\{ \frac{\Im[H_{cn}(\kappa)]}{\Re[H_{cn}(\kappa)]} \right\}, \quad -\frac{\pi}{2} \leq \theta \leq \frac{\pi}{2} \quad (5.7)$$

and the quantities ϕ_{nl} are sequences of independent random phase angles uniformly distributed over the interval $[0, 2\pi]$. Equation (5.5) shows that the “frequency double-indexing” technique (Shinozuka et al., 1989) has been adopted for the wave number:

$$\kappa_{nl} = l \Delta\kappa - \frac{m-n}{m} \Delta\kappa; \quad n = 1, 2, \dots, c; \quad l = 1, 2, \dots, N; \quad \Delta\kappa = \frac{\kappa_u}{N} \quad (5.8)$$

where κ_u is the cutoff wave number beyond which the SDF is considered negligible and N is the number of intervals in the wave number domain.

The samples produced in this way are asymptotically Gaussian as $N \rightarrow \infty$ because of the central limit theorem and ergodic in the autocorrelation (see Chapter 6). Moreover, it is possible to take advantage of the Fast Fourier Transform to dramatically reduce the computational cost of the generation (Deodatis, 1996).

5.2.2 Mapping to a Non-Gaussian Vector Field

The memoryless transformation proposed by Grigoriu (1984, 1995, 1998) and already used in Chapter 3 to map a Gaussian field $g(x)$ into a non-Gaussian one $f(x)$ with a prescribed distribution can be proficiently employed also for the multi-variate case, using the marginal distribution of each component. The mapping formula is repeated here for completeness:

$$f_c(x) = \mathcal{F}_{f_c}^{-1} \{ \mathcal{F}_{g_c} [g_c(x)] \} \quad (5.9)$$

where $\mathcal{F}_{f_c}^{-1}$ is the inverse target marginal non-Gaussian Cumulative Distribution Function (CDF) of component c and \mathcal{F}_{g_c} is the Gaussian CDF with zero mean and variance $\sigma_{g_c}^2$ equal to $\sigma_{f_c}^2$. In particular, when the Gaussian field is a standard Gaussian, the resulting field is called “translation field”. However, Grigoriu (1984, 1995, 1998) proved a set of very interesting properties (e.g. crossing rates and distributions of extremes) valid both for proper translation fields and for the general case of fields obtained through the mapping of non-standard Gaussian fields. Therefore, since the properties are the same, in the remainder of the Chapter, “translation field” will refer to any field obtained by means of the mapping in Eq. (5.9).

5.3 Identification of the Underlying Gaussian Cross-Spectral Density Matrix

Given the m -by- m target Cross-Spectral Density Matrix $\mathbf{S}_f^T(\kappa)$ and the m target marginal Cumulative Distribution Functions \mathcal{F}_{f_c} of the non-Gaussian m -variate stochastic field, the proposed methodology finds the underlying Gaussian CSDM $\mathbf{S}_g(\kappa)$ that can be used to generate sets of non-Gaussian sample functions that reflect the prescribed targets¹.

This technique is able to identify either the underlying coherences $\gamma_{rs}^g(\kappa)$ or directly the underlying cross-spectra $S_{rs}^g(\kappa)$. If the $\gamma_{rs}^g(\kappa)$'s are estimated, the computation of the underlying cross-spectra is straightforward, by using

$$S_{rs}^g(\kappa) = \gamma_{rs}^g(\kappa) \sqrt{S_{rr}^g(\kappa) S_{ss}^g(\kappa)} \quad (5.12)$$

It is well known that the estimation of coherences either from empirical data (samples) or from a numerical description of the CSDM (in contrast with an analytical description of it) is not trivial. In fact, even in the latter case, the very low values of the tails of the spectra determine numerical problems in the inversion of Eq. (5.12). For this reason, in order to obtain both $\gamma_{rs}^g(\kappa)$

¹As in the one-dimensional, uni-variate case, also here some compatibility issues can arise if the target distributions and cross-spectra are defined arbitrarily (Gioffre et al., 2000).

Considering two components named "1" and "2", the first condition is an extension of the one in Eq. (2.14). The cross-correlation of the non-Gaussian field is given by

$$R_{f_1 f_2}(\xi) = \int_{-\infty}^{\infty} \int_{-\infty}^{\infty} \mathcal{F}_{f_1}^{-1} \{ \mathcal{F}_{g_1} [g_1(x')] \} \cdot \mathcal{F}_{f_2}^{-1} \{ \mathcal{F}_{g_2} [g_2(x'' + \xi)] \} \cdot \mathcal{P}_{g_1 g_2} [g_1(x'), g_2(x'' + \xi)] dx' dx'' \quad (5.10)$$

where $\mathcal{P}_{g_1 g_2}$ is the Gaussian joint PDF and the mean values of the non-Gaussian components have been assumed to be zero for the sake of simplicity. As in the uni-variate case, the underlying Gaussian field identified by the proposed algorithm automatically satisfies this condition.

The second condition is that

$$|R_{f_1 f_2}(\xi)| \leq |R_{g_1 g_2}(\xi)| \quad (5.11)$$

that is intuitive, because the non-linear mapping process tends to reduce the correlation between components. In Sec. 5.4 this will be confirmed by numerical examples.

The third condition is that the correlations are non-negative definite, and this is obtained requiring that the spectra are non-negative.

The fourth condition is that the covariance matrix is non-negative definite, and this is obtained requiring that the CSDM is non-negative definite.

and $S_{rs}^g(\kappa)$, the identification of the underlying coherence is preferable, and in the remainder of this Chapter this procedure will be presented, with only some remarks on the steps in which the direct computation of $S_{rs}^g(\kappa)$ requires different considerations.

It is worth noting that even if the underlying Gaussian coherences are used –and therefore the underlying Gaussian cross-spectra have the form defined in Eq. (5.12)–, no assumptions are required on the non-Gaussian target.

The algorithm is based on an iterative scheme and its flow chart is presented in Fig. 5.1. The various steps of the proposed methodology are described in detail in the following (the numbers indicated inside the boxes in Fig. 5.1 correspond to the numbering of the subparagraphs that follow).

5.3.1 Compute the Underlying Gaussian Auto-SDF's

To compute the Gaussian autospectra

$$S_{cc}^g(\kappa), \quad c = 1, 2, \dots, m \quad (5.13)$$

the procedure described in Chapter 3 is applied to each component of the vector field. In fact, it is assumed that the diagonal elements of the underlying Gaussian CSDM can be analyzed independently. Actually, the multi-variate Spectral Representation Method (that is used for the production step) couples the elements of the CSDM. However, the numerical investigations confirm that the coupling effect is negligible to the purposes of the identification of the underlying CSDM and therefore the assumption is reasonable in this phase and determines a considerable saving of computational time.

The discretization used to compute the underlying Gaussian Spectra (“frequency shifting” technique) is different from the one required by the present method (“frequency double-indexing” technique). Therefore, an interpolation is required. In the performed numerical applications, the spline interpolation has proved to be effective.

5.3.2 Select a Couple of Indexes r and s

Consistently with the previous assumption of independence, also the off-diagonal terms of the CSDM are analyzed separately. The matrix is symmetric, so there

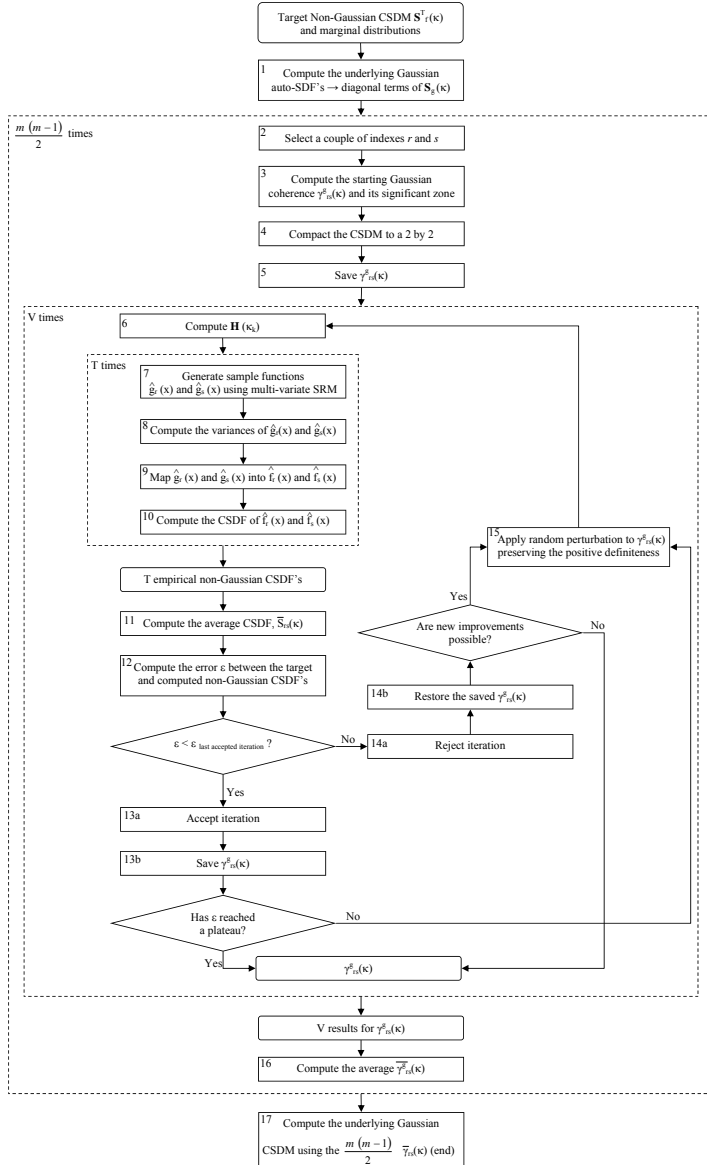


Figure 5.1: Flow chart of the proposed algorithm.

are

$$\frac{m(m-1)}{2} \quad (5.14)$$

different off-diagonal terms, where m is the number of components of the field. Therefore $\frac{m(m-1)}{2}$ underlying coherences (or cross-spectra) have to be separately computed. To accomplish this task, the algorithm performs the following steps for every couple of indexes r and s , with

$$\begin{aligned} r &= 2, 3, \dots, m \\ s &= 1, 2, \dots, r-1 \end{aligned} \quad (5.15)$$

5.3.3 Compute the Starting Gaussian Coherence

As already said, the procedure adopts an iterative scheme, so a starting value for the underlying Gaussian coherence γ_{rs}^g is required. If the non-Gaussian target CSDM has been defined by means of coherences (“target coherences”, γ_{rs}^T), the starting coherence is set equal to the corresponding target:

$$\gamma_{rs}^g(\kappa) = \gamma_{rs}^T \quad (5.16)$$

If the non-Gaussian target CSDM has been defined in closed form, then again it is possible to set the starting coherence equal to the target one, inverting Eq. (5.1),

$$\gamma_{rs}^g(\kappa) = \gamma_{rs}^T(\kappa) = \frac{S_{rs}^T(\kappa)}{\sqrt{S_{rr}^T(\kappa)S_{ss}^T(\kappa)}} \quad (5.17)$$

If the non-Gaussian target CSDM is available only in digital form, then it is preferable to avoid the use of Eq. (5.17) because of the already mentioned numerical problems. Thus, in this case the starting value of the coherence is defined as the average value of its admissible domain:

$$\gamma_{rs}(\kappa) = \frac{\text{lb}(\kappa) + \text{ub}(\kappa)}{2} \quad (5.18)$$

where $\text{lb}(\kappa)$ and $\text{ub}(\kappa)$ are the lower and upper bounds of the admissible domain, defined, for instance, by Eqs. (5.26) and (5.27), respectively.

If the option to look directly for the underlying cross-spectra has been chosen, then the starting value is set equal to the target:

$$S_{rs}^g(\kappa) = S_{rs}^T \quad (5.19)$$

The domain of the wave number κ is $[0, \kappa_u]$ where the “cutoff” wave number κ_u is the value beyond which the spectra are negligible. This domain is divided into N intervals of length

$$\Delta\kappa = \frac{\kappa_u}{N} \quad (5.20)$$

Then, according to the frequency double-indexing technique, every interval is divided into m sub-intervals.

The target SDF’s are defined at the discrete wave numbers

$$\kappa_j = j\Delta\kappa, \quad j = 0, 1, \dots, N - 1 \quad (5.21)$$

while the underlying Gaussian coherences (and spectra), that have to be used for the productions by means of the spectral representation with frequency double-indexing, are defined at

$$\kappa_k = k\frac{\Delta\kappa}{m}, \quad k = 1, 2, \dots, mN \quad (5.22)$$

To ensure the Gaussianity of the produced samples, N has to be greater than approximately 100 (Shinozuka and Deodatis, 1991). In the numerical applications, N has been set equal to 256.

Equation (5.1) shows that the value of the coherence affects the value of the cross-spectral density functions only when the involved autospectra are significantly different from zero. Therefore, only the region where the product $S_{rr}^g(\kappa)S_{ss}^g(\kappa)$ is greater than the 5% of its maximum value is considered. In the rest of the wave number domain, the value of the Gaussian cross-spectrum $S_{rs}^g(\kappa)$ is almost zero, independently of the value of $\gamma_{rs}(\kappa)$. Thus, the iterative optimization procedure will focus only on the “significant zone”.

The coherences are defined (and physically meaningful) in the interval $[0, 1]$. This condition determines a domain of admissible solutions for $\gamma_{rs}^g(\kappa)$ –or for $S_{rs}^g(\kappa)$ –. Moreover, as already mentioned, the multi-variate Spectral Representation, makes use of the Cholesky decomposition (see Sec. 5.2.1). Therefore, the underlying Gaussian CSDM has to be always positive definite. This implies a further restriction to the domain of admissible solutions. When few components are involved, closed form expressions for the upper and lower bounds of the domain can be computed. For instance, when $m = 2$ it is trivial to prove that the CSDM is always positive definite when $0 < \gamma_{rs}^g(\kappa) < 1$. So the lower

and upper bounds are:

$$\begin{aligned}\text{lb}(\kappa) &= \text{sm} \\ \text{ub}(\kappa) &= 1 - \text{sm}\end{aligned}\tag{5.23}$$

where sm is a very small “safety margin”, used to avoid numerical problems. In the numerical applications, sm has been set equal to 10^{-4} . When $m = 3$, using Sylvester’s criterion, the bounds in Eq. (5.23) for $\gamma_{12}^g(\kappa)$ guarantee the positiveness of the 2×2 principal minor. The positiveness of the 3×3 determinant is given by:

$$S_{11}^g S_{22}^g S_{33}^g + 2 S_{23}^g S_{13}^g S_{12}^g - S_{11}^g (S_{23}^g)^2 - S_{22}^g (S_{13}^g)^2 - S_{33}^g (S_{12}^g)^2 > 0\tag{5.24}$$

that dividing by $S_{11}^g S_{22}^g S_{33}^g$ gives

$$1 + 2 \gamma_{23}^g \gamma_{13}^g \gamma_{12}^g - (\gamma_{23}^g)^2 - (\gamma_{13}^g)^2 - (\gamma_{12}^g)^2 > 0\tag{5.25}$$

Equation (5.25) can be used to find the bounds either for $\gamma_{13}^g(\kappa)$ or for $\gamma_{23}^g(\kappa)$. The choice should depend on the order that has been chosen for the analysis of the coherences. Indeed, it is better to leave the larger possible range of variation to the firstly computed coherences. For instance, if we consider the components in the order 12, 13, 23, the bounds for $\gamma_{13}^g(\kappa)$ are set again using the always valid Eq. (5.23), and from Eq. (5.25) the bounds for $\gamma_{23}^g(\kappa)$ are set as

$$\text{lb}(\kappa) = \gamma_{12}^g \gamma_{13}^g - \sqrt{[1 - (\gamma_{12}^g)^2] [1 - (\gamma_{13}^g)^2]}\tag{5.26}$$

$$\text{ub}(\kappa) = \gamma_{12}^g \gamma_{13}^g + \sqrt{[1 - (\gamma_{12}^g)^2] [1 - (\gamma_{13}^g)^2]}\tag{5.27}$$

For a large number of components, it is suggested to use only the “basic” bounds in Eq. (5.23) and check the positive definiteness all along the iterative procedure, as will be explained in Sec. 5.3.15².

Similar considerations apply in the case of direct computation of $S_{rs}^g(\kappa)$.

²It should be noticed that the positive definiteness of the CSDM is a numerical and analytical issue, but it reflects also a physical meaning. Eq. (5.25) can be seen as a limit to the variability of one of the coherences, when the other two are fixed. If, for instance, the coherence between components 1 and 2 is high, then $\gamma_{13}(\kappa)$ and $\gamma_{23}(\kappa)$ have to be very similar. This is perfectly intuitive and reasonable. Therefore, the condition of positive definiteness is not an annoying analytical problem that restricts the domain of possible solutions (thus, in general, determining worse solutions) but a useful tool to test the consistency of our model.

5.3.4 Compact the CSDM to a 2-by-2

Considering again the influence of the other components to be negligible, in order to save computational time, the underlying Gaussian CSDM that is considered in the steps 4–15 is not an $m \times m$ matrix, instead it is condensed to a 2×2 matrix $\mathbf{S}_{rs}^g(\kappa)$, with only the elements corresponding to the components r and s :

$$\mathbf{S}_{rs}^g(\kappa) = \begin{bmatrix} S_{rr}^g(\kappa) & S_{rs}^g(\kappa) \\ S_{rs}^g(\kappa) & S_{ss}^g(\kappa) \end{bmatrix} \quad (5.28)$$

In this way, only one off-diagonal term $S_{rs}^g(\kappa)$ (so only one coherence) is involved.

Some benchmarks performed using the whole CSDM all along the procedure (without the condensation) shown that the influence of the other components is truly negligible for the purposes of the identification of the underlying coherences.

5.3.5 Save $\gamma_{rs}(\kappa)$

The methodology in Fig. 5.1 is an iterative one with potential random modifications to the coherence (or to the cross-spectrum) at every step. Using an acceptance criterion that will be described later, the modifications at a specific step can be accepted or rejected. For this reason, $\gamma_{rs}(\kappa)$ is saved at each iteration so that it can be retrieved in case the iteration is rejected.

5.3.6 Compute $\mathbf{H}(\kappa_k)$

To produce Gaussian samples, the multi-variate Spectral Representation Method (mV-SRM) described in Sec. 5.2.1 is applied. To take advantage of the FFT transform (Deodatis, 1996), the following function is defined

$$t_{cd}^{(i)}(p \Delta x) = \text{FFT}_l^+ \left[2H_{cd} \left(l\Delta\kappa + \frac{d}{m}\Delta\kappa \right) \sqrt{\Delta\kappa} \cdot \exp \left(i\phi_{dl}^{(i)} \right) \right]; \quad (5.29)$$

$$c = 1, 2, \dots, m; \quad d = 1, 2, \dots, c;$$

$$p = 0, 1, \dots, M - 1; \quad l = 0, 1, \dots, M - 1;$$

$$\Delta x = \frac{2\pi}{M \Delta\kappa}$$

where $\text{FFT}_l^+ [\cdot]$ denotes the FFT with M points and positive exponent over the index l of the function in brackets. The superscript (i) stands for the fact that a specific set of random phase angles $\phi^{(i)}$ determines a specific function $t_{cd}^{(i)}$

The terms H_{cd} can be computed once for every iteration (steps 6–15) using Cholesky's decomposition. The decomposition of the Gaussian CSDM $\mathbf{S}_{rs}^g(\kappa)$ is defined as

$$\begin{aligned} H_{cc} &= \sqrt{S_{cc}^g - \sum_{e=1}^{c-1} H_{ce}^2} \\ H_{cd} &= \frac{1}{H_{dd}} \left(S_{cd}^g - \sum_{e=1}^{d-1} H_{ce} H_{de} \right), \quad \text{for } c > d \end{aligned} \quad (5.30)$$

where the dependence on the wave number has been omitted for the sake of simplicity. If the algorithm is searching the underlying coherence, it can take advantage of Eq. (5.12). Substituting Eq. (5.12) into Eq. (5.30) we obtain the matrix $\mathbf{H}(\kappa)$ written as a function of the autospectra and of the coherences:

$$\begin{aligned} H_{cc} &= \sqrt{S_{cc}^g - \sum_{e=1}^{c-1} H_{ce}^2} \\ H_{cd} &= \frac{1}{H_{dd}} \left(\sqrt{S_{cc}^g S_{dd}^g} \gamma_{cd} - \sum_{e=1}^{d-1} H_{ce} H_{de} \right), \quad \text{for } c > d \end{aligned} \quad (5.31)$$

and in particular

$$\mathbf{H}(\kappa) = \begin{pmatrix} \sqrt{S_{rr}^g} & 0 \\ \gamma_{rs}^g \sqrt{S_{ss}^g} & \sqrt{1 - (\gamma_{rs}^g)^2} \sqrt{S_{ss}^g} \end{pmatrix} \quad (5.32)$$

If the algorithm computes directly the underlying cross-spectra, a traditional Cholesky decomposition is performed instead.

5.3.7 Generate Sample Functions $\hat{g}_r(x)$ and $\hat{g}_s(x)$

The production of Gaussian samples goes through the definition of the functions $t_{cd}^{(i)}$ in Eq. (5.29) and here reported:

$$\begin{aligned}
 t_{cd}^{(i)}(p \Delta x) &= \text{FFT}_l^+ \left[2H_{cd} \left(l\Delta\kappa + \frac{d}{m}\Delta\kappa \right) \sqrt{\Delta\kappa} \cdot \exp \left(i\phi_{dl}^{(i)} \right) \right]; \\
 &\quad c = 1, 2, \dots, m; \quad d = 1, 2, \dots, c; \\
 &\quad p = 0, 1, \dots, M-1; \quad l = 0, 1, \dots, M-1; \\
 &\quad \Delta x = \frac{2\pi}{M \Delta\kappa}
 \end{aligned} \tag{5.33}$$

Then, m copies of $t_{cd}^{(i)}$ are concatenated to generate $h_{cd}^{(i)}$:

$$h_{cd}^{(i)}(q\Delta x) = t_{cd}^{(i)}(\text{mod}(q, M)\Delta x); \quad q = 0, 1, \dots, mM-1 \tag{5.34}$$

where $\text{mod}(q, M)$ denotes the remainder of division of q by M and M is the number of points used for the FFT. Note that in order to avoid aliasing, M has to be at least $M = 2N$. In the numerical applications we have set $M = 2^{10} = 1024$.

Because of the frequency shifting (for the theory, refer also to Sec. 3.2.6) $h_{ij}^{(i)}$ has to be multiplied by a shifting factor:

$$\hat{h}_{cd}^{(i)}(q\Delta x) = \Re \left[h_{cd}^{(i)}(q\Delta x) \cdot \exp \left(i \frac{d}{m} \Delta\kappa x \right) \right] \tag{5.35}$$

where $\Re[\cdot]$ denotes the real part.

Finally, the various components $\hat{g}_c(q\Delta x)$ are obtained as sums of the functions $\hat{h}_{cd}^{(i)}(q\Delta x)$:

$$\hat{g}_c(q\Delta x) = \sum_{d=1}^c \hat{h}_{cd}^{(i)}(q\Delta x); \quad q = 0, 1, \dots, mM-1 \tag{5.36}$$

In particular, one sample each for the components r and s are generated.

It is worth noticing that the period of the samples (i.e. the length of \hat{g}_c) as expressed by Eq. (5.36) is $L = mM \Delta x = m \frac{2\pi}{\Delta\kappa}$ that is m times the period of the classic SRM without frequency double-indexing (Shinozuka and Deodatis, 1991; Deodatis, 1996).

5.3.8 Compute the Variance of $\hat{g}_r(x)$ and $\hat{g}_s(x)$

The mean of the generic $\hat{g}_c(x)$ is always zero because of the way it is generated (using mV-SRM and considering one period). Its variance $\sigma_{\hat{g}_c}$ is not constrained, so $\hat{g}_c(x)$ is Gaussian, but not standardized Gaussian.

The variance can be estimated numerically either from the generated sample function or from the SDF $S_{cc}^g(\kappa)$. Consequently, the Gaussian Cumulative Distribution Function of $\hat{g}_c(x)$ is fully known:

$$\mathcal{F}_{\hat{g}_c} = \int_{-\infty}^{\hat{g}_c} \frac{1}{\sqrt{2\pi}\hat{\sigma}_g} \exp\left[-\frac{u^2}{2\hat{\sigma}_g^2}\right] du \quad (5.37)$$

In particular, $\mathcal{F}_{\hat{g}_r}$ and $\mathcal{F}_{\hat{g}_s}$ are computed.

5.3.9 Map $\hat{g}_r(x)$ and $\hat{g}_s(x)$ into $\hat{f}_r(x)$ and $\hat{f}_s(x)$

The classic translation field memoryless transformation (Grigoriu, 1984, 1995) is used to map the underlying Gaussian sample functions of both components r and s to non-Gaussian ones having the prescribed marginal CDF's \mathcal{F}_f , as explained in Sec. 5.2.2:

$$\hat{f}_r(x) = \mathcal{F}_{\hat{f}_r}^{-1}\{\mathcal{F}_{\hat{g}_r}\} \quad (5.38)$$

$$\hat{f}_s(x) = \mathcal{F}_{\hat{f}_s}^{-1}\{\mathcal{F}_{\hat{g}_s}\} \quad (5.39)$$

For some distributions –e.g. the lognormal (Grigoriu, 1995)–, the inverse of \mathcal{F}_f is available in closed form. Otherwise, a numerical inversion is used.

It should be noted that although $\hat{g}_c(x)$ are not standard Gaussian, $\hat{f}_c(x)$ still possess all the properties of translation fields (Grigoriu, 1984). Another interesting point is that although $\hat{f}_c(x)$ conserve the ergodicity in the mean property of $\hat{g}_c(x)$, they do not conserve their ergodicity in autocorrelation property.

5.3.10 Compute the Cross-Spectrum of $\hat{f}_r(x)$ and $\hat{f}_s(x)$

The Cross-Spectral Density Function (CSDF) of the samples $\hat{f}_r(x)$ and $\hat{f}_s(x)$ can be computed using the formula (Bendat and Piersol, 1986, p. 130):

$$S_{rs}^f = \frac{1}{2\pi(mL)} \text{FFT}^{-1}[\hat{f}_r]^* \Delta x \text{FFT}^{-1}[\hat{f}_s] \Delta x \quad (5.40)$$

where $\text{FFT}^-[\cdot]$ denotes the FFT with negative exponent and the asterisk denotes the complex conjugate. The second half of the fourier transform is the mirror image of the first one, therefore only the first (meaningful) mN values are considered. Moreover, the resulting values of S_{rs}^f are given at intervals of width $\frac{\Delta\kappa}{m}$, while the target cross-spectrum S_{rs}^f is defined at intervals $\Delta\kappa$. Therefore, to make the two functions comparable, the power belonging to m intervals of width $\frac{\Delta\kappa}{m}$ has to be summed up:

$$S_{rs}^f(j\Delta\kappa) = \sum_{c=0}^{m-1} S_{rs}^f\left(mj + c\frac{\Delta\kappa}{m}\right) \quad (5.41)$$

$$j = 0, 1, \dots, N-1$$

5.3.11 Compute the Average Cross-Spectrum, $\bar{S}_{rs}^f(\kappa)$

As already mentioned, the translation field does not possess the ergodic properties of the Gaussian one. Therefore, for an accurate estimation of the spectral density function of the non-Gaussian field, it is necessary to average the empirical cross-spectra of many sample functions. For this reason, the steps described in Secs. 5.3.7–5.3.10 are repeated T times, and then the average cross-spectrum is computed from:

$$\bar{S}_{rs}^f(\kappa) = \frac{1}{T} \sum_{t=1}^T S_{rs}^{f(t)}(\kappa) \quad (5.42)$$

An extensive numerical investigation has revealed that a value of $T = 100$ is usually sufficient to get a very good and smooth approximation of $\bar{S}_{rs}^f(\kappa)$.

5.3.12 Compute the Error ε Between the Target and Computed Cross-Spectrum

The variable adopted as convergence criterion of the computed $\bar{S}_{rs}^f(\kappa)$ to the target cross-spectrum of the non-Gaussian field is defined as:

$$\varepsilon = 100 \sqrt{\frac{\sum_{j=0}^{N-1} \left| \bar{S}_{rs}^f(\kappa_j) - S_{rs}^T(\kappa_j) \right|^2}{\sum_{j=0}^{N-1} |S_{rs}^T(\kappa_j)|^2}} \quad (5.43)$$

where the modulus operator is used because in practice the empirical cross-spectra obtained by Eq. (5.40) have always an imaginary part. In the cases in which the target cross-spectrum is real valued, the imaginary part of \bar{S}_{rs}^f should be identically zero. Minimizing the error function, the code tends to minimize the imaginary part of the resulting non-Gaussian cross-spectra³. In the cases in which the target cross-spectrum is complex, the code –thanks to the definition of the error function in Eq. (5.43)– tends to make the real part of the resulting non-Gaussian cross-spectrum match the real part of the target and the imaginary part of the resulting non-Gaussian cross-spectrum match the imaginary part of the target.

Similarly to what has already been observed in Sec. 3.2.8, the smoothness of $\bar{S}_{rs}^f(\kappa)$ determined by Eq. (5.42) guarantees a true measure of the distance between the two functions and therefore a fast convergence of the algorithm.

5.3.13 Accept Iteration and Save $\gamma_{rs}^g(\kappa)$

If the error computed through Eq. (5.43) is smaller than that computed in the last accepted iteration, then the current iteration is accepted. For the same reason as explained in Sec. 5.3.5, the current Gaussian coherence (or cross-spectrum) is saved.

Then, a check is performed to determine whether convergence is met or not. The criterion for reaching convergence is for the value of ε to be reduced by less than 0.01% during the last 20 accepted iterations (“Plateau reached”). The values 20 and 0.01% have been determined after an extensive numerical investigation. If the convergence criterion is satisfied, the iterative scheme ends. Otherwise, the iterations continue and a random perturbation is applied to $\gamma_{rs}^g(\kappa)$ (or directly to the underlying Gaussian cross-spectrum), as explained in Sec. 5.3.15.

³Because of the non-ergodicity of the produced samples, even if the theoretical cross-spectrum is real, the average of a finite number of S_{rs}^f has always a small imaginary part, that tends to zero when the number of samples tends to infinity. The empirical cross-spectra of 100 samples (with real valued target CSDM) usually has an imaginary part that is negligible with respect to the real part.

5.3.14 Reject Iteration and Restore the Saved $\gamma_{rs}^g(\kappa)$

If the error computed through Eq. (5.43) is greater than that computed in the last accepted iteration, then the current iteration is rejected. This means that the random perturbation previously applied to $\gamma_{rs}^g(\kappa)$ has led to a non-Gaussian cross-spectrum that is further away from the target. Therefore, the saved $\gamma_{rs}^g(\kappa)$ of the last accepted iteration is restored.

Furthermore, a convergence check is performed at this point. The algorithm keeps track of whether all of the last $4N$ iterations have been rejected (“Maximum improvement reached”). The meaning of the value $4N$ is the same as in the uni-variate case (see Sec. 3.2.11). If all of the last $4N$ iterations have been rejected, the iterative scheme ends. Otherwise, the iterations go on and a random perturbation is applied to $\gamma_{rs}^g(\kappa)$ (or directly to the underlying Gaussian cross-spectrum), as explained in the next Section.

5.3.15 Apply Random Perturbation to $\gamma_{rs}^g(\kappa)$

As mentioned earlier, if the convergence checks are not satisfied, the iterations continue and a random perturbation is applied to the current $\gamma_{rs}^g(\kappa)$. Specifically, the following perturbation ΔS is added to the underlying Gaussian coherence:

$$\Delta S = A \exp \left[-\frac{(\kappa - \kappa_0)^2}{40} \right] \quad (5.44)$$

where κ_0 is a point selected randomly in the interval $[0, \kappa_u]$, and A is equal to $\pm \frac{\gamma_{rs}^g(\kappa_0)}{20}$ with its sign randomly selected (see also Fig. 3.3).

This perturbation ΔS obviously dies down quickly to the left and to the right of κ_0 . Consequently, only $\frac{N}{16}$ points of γ_{rs}^g are modified according to Eq. (5.44) (beyond these $\frac{N}{16}$ points the modifications are negligible and therefore disregarded). If κ_0 is too close to 0 or κ_u , then the perturbation involves less than $\frac{N}{16}$ points.

A significant advantage of this perturbation scheme is that it is not inducing sharp discontinuities in $\gamma_{rs}^g(\kappa)$, with all the consequent advantages already mentioned in Sec. 3.2.11.

At this point, it is necessary to make sure that the random perturbation keeps the complete $(m \times m)$ underlying Gaussian CSDM positive definite⁴. If a closed form is available for the bounds –e.g. Eqs. (5.26) and (5.27)– this task is

accomplished setting:

$$\left. \begin{aligned} \gamma_{rs}^g(\kappa) &= \max[\gamma_{rs}^g(\kappa), \text{lb}(\kappa)] \\ \gamma_{rs}^g(\kappa) &= \min[\gamma_{rs}^g(\kappa), \text{ub}(\kappa)] \end{aligned} \right\} \quad \forall \kappa \quad (5.45)$$

Otherwise, if only the “generic” bounds in Eq. (5.23) are available, then a different technique is adopted. First of all, Eq. (5.45) is used to impose the generic bounds. Then, the determinant of the $m \times m$ underlying Gaussian CSDM is computed. Note that according to Sylvester’s theorem, if we start with a positive definite matrix and we change only one element (and its symmetric one), the positive definiteness of the new matrix is guaranteed by the positiveness of the new global determinant⁵. Thus, if the determinant is negative, the random perturbation is discarded and a new one is performed.

A very similar procedure is applied in the case of direct determination of $S_{rs}^g(\kappa)$.

After a random perturbation is implemented and a new γ_{rs}^g or S_{rs}^g is determined, the iterative scheme continues with the decomposition of $\mathbf{S}_{rs}^g(\kappa)$ as described in Section 5.3.6.

5.3.16 Compute the Average $\bar{\gamma}_{rs}^g(\kappa)$

The resulting underlying Gaussian coherence (or cross-spectrum) after completing the steps in Secs. 5.3.6–5.3.15 (called a “run”) is not unique. A slightly different $\gamma_{rs}^g(\kappa)$ will be obtained from a different run. Consequently, a total of V runs are performed and an average coherence is estimated as:

$$\bar{\gamma}_{rs}^g(\kappa) = \frac{1}{V} \sum_{v=1}^V \gamma_{rs}^{g(v)}(\kappa) \quad (5.46)$$

⁴As mentioned in Sec. 5.3.3, if the number of components is 2, no bounds are necessary, except the “generic bounds” in Eq. (5.23). If the number of components is 3, for the first two coherences no bounds are required, while for the thirdly computed one, the bounds in Eqs. (5.26) and (5.27) have to be used. As the number of components increases, the conditions on the lastly computed coherences are stricter.

⁵In fact, we can permute rows and columns (“even permutation”) so that the element that is going to be modified is in the bottom row of the permuted matrix (and its symmetric is in the last column). The evenly permuted matrix is obviously still positive definite (the eigenvalues are invariant to even permutations). Therefore all the principal minors of the permuted matrix have positive determinant. If we change a term that is in the bottom row and its symmetric in the last column, only the global determinant is affected. If the global determinant is positive, then the permuted and perturbed matrix is certainly positive definite and therefore, an inverse permutation gives a perturbed positive definite matrix.

A numerical investigation has suggested that a value of $V = 5$ is sufficient for an accurate estimation of $\bar{\gamma}_{rs}^g(\kappa)$.

5.3.17 Compute the Complete Underlying Gaussian CSDM

When all the $\frac{m(m-1)}{2}$ coherences have been computed using the procedure described above, it is possible to assemble the complete underlying Cross-Spectral Density Matrix, using Eq. (5.12). If the underlying cross-spectra have been computed directly, it is sufficient to collect them, together with the autospectra, into the CSDM.

Once the CSDM of the underlying Gaussian field is available, the generation of sample functions of the non-Gaussian random field is straightforward and extremely efficient computationally. In fact, only one decomposition (Sec. 5.3.6) and the steps described in Sections 5.3.7, and 5.3.9 are necessary and no iterations are involved. The generated non-Gaussian random fields will perfectly match the target distribution \mathcal{F}_f , they will have a CSDM very close to the target (in ensemble-average sense), and they will also possess all the characteristics of translation fields according to Grigoriu's theory (Grigoriu, 1984, 1995).

5.4 Numerical Examples

Two numerical examples are provided to show the capabilities of the proposed method. In both cases, the estimation of the underlying coherences and the direct computation of the cross-spectra have been performed and have given very similar results. Therefore, in the remainder of this Chapter, only the results obtained with the underlying coherences will be presented, since they are considered more interesting.

5.4.1 Kaimal-Davenport Cross-Spectral Density Matrix

The first example involves the simulation of wind velocity fluctuations. In particular, the longitudinal velocity fluctuations at two points along a vertical line are considered a two-variate stationary stochastic process (in this case the domain is time⁶).

⁶Even if the algorithm has been presented for the simulation of random fields in the space domain, in this case it is better be consistent with the physical meaning of the application.

The model proposed by Kaimal et al. (1972) is chosen for the SDF's at different heights:

$$S^T(z, \omega) = A \frac{1}{2} \frac{200}{2\pi} u_*^2 \frac{z}{U(z)} \frac{1}{\left[1 + 50 \frac{\omega z}{2\pi U(z)}\right]^{5/3}} \quad (5.47)$$

where z is the heights in meters, ω is the frequency in $\frac{rad}{s}$, u_* is the shear velocity of the flow in $\frac{m}{s}$ and $U(z)$ is the mean wind speed at height z in $\frac{m}{s}$. A is a scale factor that reduces the variance of the process (i.e. the integral of the SDF) to 1 and can be computed as

$$A = \frac{1}{6u_*^2} \quad (5.48)$$

This is done because usually the benchmark test for a simulation algorithm is performed using distributions with zero mean and unit variance.

Simiu and Scanlan (1986), for instance, suggest to assume that at $z_1 = 35m$, the mean wind speed is

$$U(z_1 = 35m) = 45 \frac{m}{s} \quad (5.49)$$

and the roughness z_0 is

$$z_0 = 0.001266 m \quad (5.50)$$

The so called "logarithmic law" of fluid dynamics

$$U(z) = \frac{1}{k} u_* \ln \frac{z}{z_0} \quad (5.51)$$

$$k = 0.4 \quad (\text{von Karman's constant}) \quad (5.52)$$

gives:

$$u_* = \frac{kU(z)}{\ln \frac{z}{z_0}} = \frac{0.4 \cdot 45}{\ln \frac{35}{0.001266}} = 1.76 \frac{m}{s} \quad (5.53)$$

At the second height $z_2 = 40m$, the mean wind speed is given by Eq. (5.51):

$$U(z_2 = 40m) = \frac{1}{k} u_* \ln \frac{z_2}{z_0} = \frac{1}{0.4} 1.76 \ln \frac{40}{0.001266} = 45.6 \frac{m}{s} \quad (5.54)$$

Therefore, the usual notation for random fields is substituted by the common notation for stochastic processes in this paragraph. In particular, the time t takes the place of the space x and the frequency ω takes the place of the wave number κ .

Plugging the numerical values into Eq. (5.47) the two autospectra are computed as:

$$S_{11}^T(\omega) = \frac{2.06}{(1 + 6.19\omega)^{5/3}} \quad (5.55)$$

$$S_{22}^T(\omega) = \frac{2.33}{(1 + 21.8\omega)^{5/3}} \quad (5.56)$$

The target coherence function between the wind velocity fluctuations at the two heights z_1 and z_2 has the form proposed by Davenport (1968) and widely used in wind engineering:

$$\gamma(\Delta z, \omega) = \exp \left[-\frac{\omega}{2\pi} \frac{C_z \Delta z}{\frac{U(z_1) + U(z_2)}{2}} \right] \quad (5.57)$$

where $\Delta z = |z_1 - z_2|$ and C_z is a constant usually set equal to 10 for structural design purposes (Kristensen and Jensen, 1979; Simiu and Scanlan, 1986). In this particular example, the coherence is

$$\gamma_{12}(\omega) = \exp(-0.157\omega) \quad (5.58)$$

and the target cross-spectrum can be computed by means of Eq. (5.1).

The marginal distributions are assumed to be Lognormal, as usually assumed for wind velocity fluctuations (e.g. Gioffre et al., 2000):

$$\mathcal{P}(x) = \frac{1}{\sqrt{2\pi}\sigma_N \bar{x}} \exp \left[-\frac{(\ln \bar{x} - \mu_N)^2}{2\sigma_N^2} \right] \quad (5.59)$$

where:

$$\sigma_N^2 = \ln \left(1 + \frac{\sigma}{\bar{\mu}^2} \right) \quad ; \quad \mu_N = \ln \bar{\mu} - \frac{\sigma_N^2}{2} \quad ; \quad \bar{x} = x - \bar{\mu} \quad (5.60)$$

For the first component ($z_1 = 35m$), the parameters $\bar{\mu}_1$ and σ_1 have been set as follows:

$$\bar{\mu}_1 = 1.8 \quad ; \quad \sigma_1 = 1 \quad (5.61)$$

and therefore the moments of the distribution are:

$$\text{mean: } \mu_1 = 0 \quad ; \quad \text{variance: } \sigma_1^2 = 1 \quad ; \quad \text{skewness: } \gamma_1 = 1.838 \quad ; \quad \text{kurtosis}_1 = 9.553$$

For the second component, the parameters $\bar{\mu}_2$ and σ_2^2 are:

$$\bar{\mu}_2 = 2.3 \quad ; \quad \sigma_2 = 1 \quad (5.62)$$

and therefore the moments of the Lognormal distribution are:

mean: $\mu_2 = 0$; variance: $\sigma_2^2 = 1$; skewness: $\gamma_2 = 1.3865$; kurtosis₂ = 6.6024

The cutoff frequency and the other parameters of the algorithm have been set as follows:

$$N = 256; \quad M = 2^{10} = 1024; \quad \omega_u = 4 \frac{\text{rad}}{s} \quad (5.63)$$

The results of the simulation procedure are presented in Figs. 5.2–5.4. In particular, Fig. 5.2 compares the target non-Gaussian coherence defined by Eq. (5.58) to the underlying Gaussian coherence computed by the proposed algorithm. The code has computed that the significant zone (see Sec. 5.3.3) is the interval $[0, 0.22]$ therefore only the first part has been modified. In general, the non-linear mapping causes a reduction of the coherence between the non-Gaussian samples with respect to that between the original Gaussian ones (especially if the mapping functions for the various components are different). Therefore, the global trend is that the underlying Gaussian coherence has to be larger than the desired target. In this example it is extremely clear, that in order to match the target, the underlying coherence tends to become as large as possible, reaching the upper bound.

Figure 5.3 shows the matching between the Cross-Spectral Density Matrix obtained by ensemble averaging over 100 generated samples and the target non-Gaussian CSDM. It is immediately obvious that the match is almost perfect. Not only the autospectra perfectly match the strongly non-Gaussian targets, but also the cross-spectra practically coincide.

Also the marginal probabilities of the two components match their targets, as shown in Fig. 5.4.

5.4.2 Artificially Correlated Spectrum

The second numerical example involves the simulation of a tri-variate vector field. In this case the SDF's are defined as in Sec. 3.3 by:

$$S_{cc}^T(\kappa) = \frac{125}{4} \sigma_c^2 \kappa^2 \exp(-5|\kappa|), \quad c = 1, 2, 3 \quad (5.64)$$

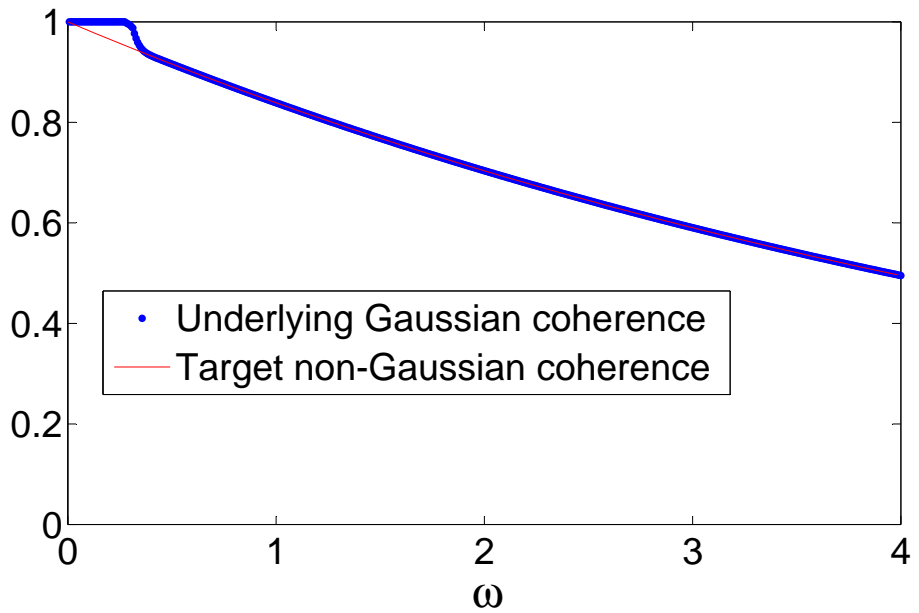


Figure 5.2: Wind velocity fluctuation simulation. The underlying Gaussian coherence computed by the algorithm is compared to the target non-Gaussian coherence defined by Eq. (5.58). Only the “significant zone” of the coherence is affected by the modifications.

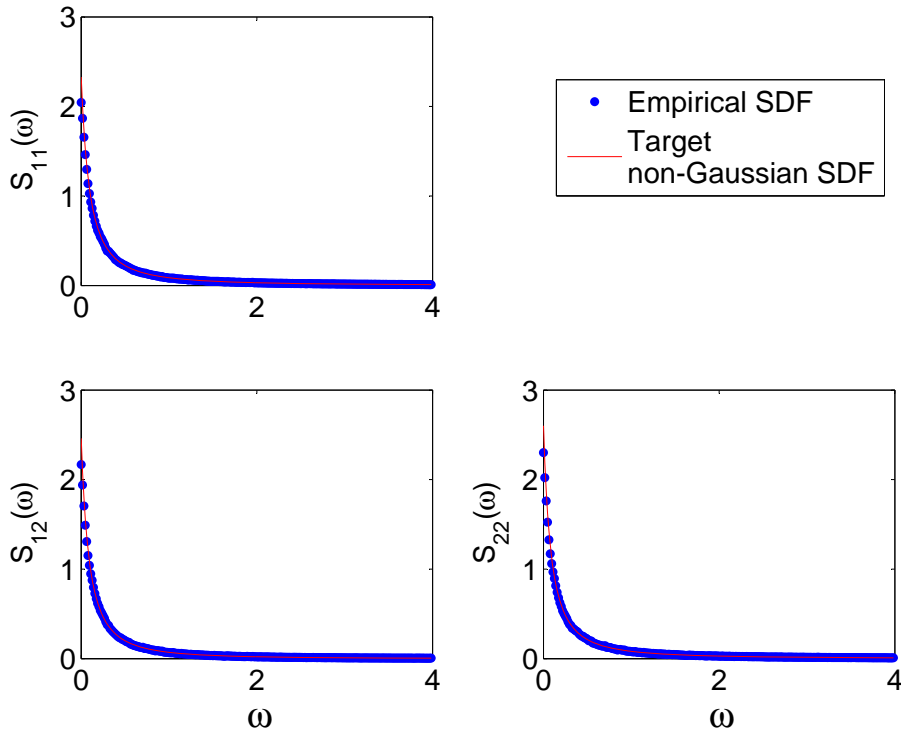


Figure 5.3: Wind velocity fluctuation simulation. The “empirical” spectral density functions and the cross-spectral density obtained by ensemble averaging over 100 generated samples match the target non-Gaussian functions almost perfectly. The graphs are sorted as the elements of the CSDM. Only the lower part is plotted, because the upper part is symmetric. The negligible imaginary part present in the empirical cross-spectrum because of the non-ergodicity of the produced samples has been disregarded.

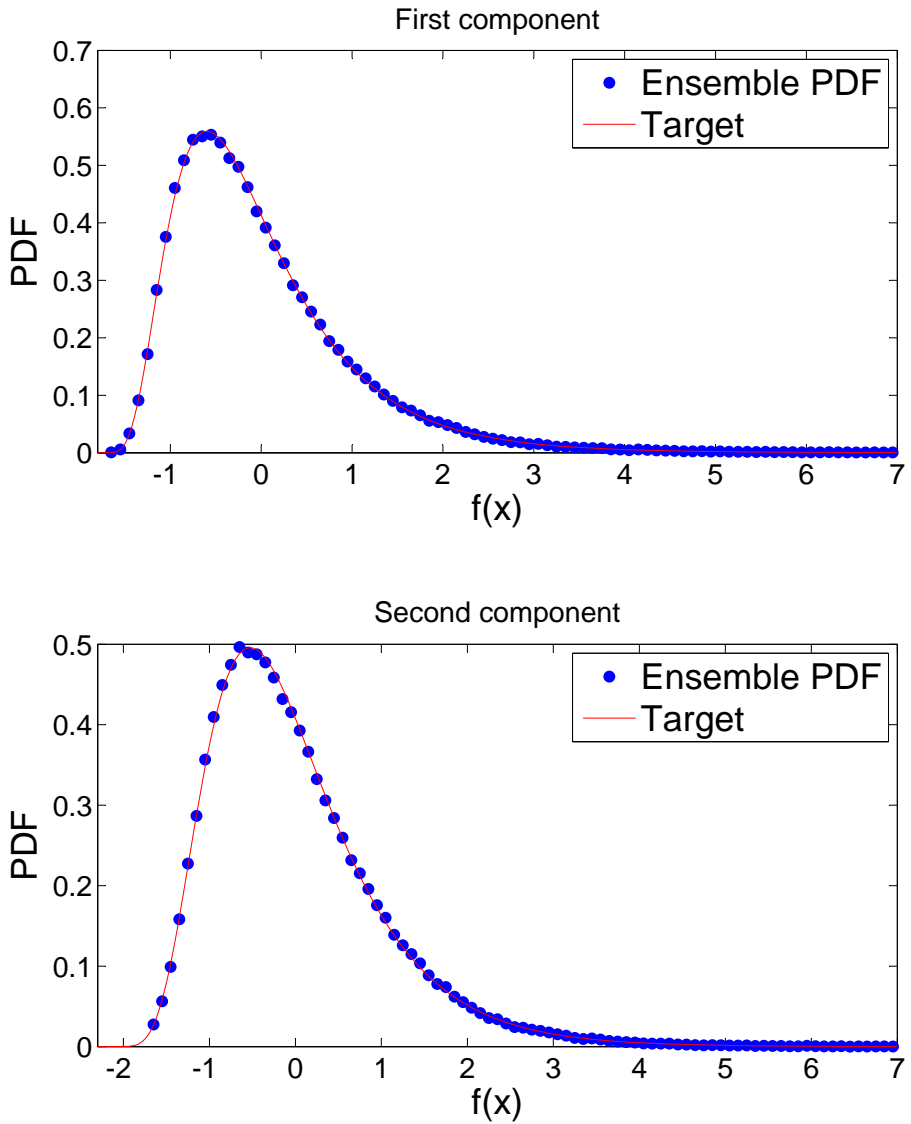


Figure 5.4: Wind velocity fluctuation simulation. Both the PDF computed by ensemble averaging of 100 generated samples match the respective Lognormal targets.

The coherences have been defined artificially with an almost constant plateau in the interval $[0, \kappa_u/3]$ using the linear equation:

$$\gamma_{cd} = -0.02\gamma_{cd}^0\kappa + \gamma_{cd}^0; \quad c, d = 1, 2, 3; \quad d > c \quad (5.65)$$

where the parameter γ_{cd}^0 has been set as follows:

$$\gamma_{12}^0 = \gamma_{12}(\kappa = 0) = 0.8 \quad (5.66)$$

$$\gamma_{13}^0 = \gamma_{13}(\kappa = 0) = 1.0 \quad (5.67)$$

$$\gamma_{23}^0 = \gamma_{23}(\kappa = 0) = 0.6 \quad (5.68)$$

At $\kappa = \kappa_u/3$ the coherences drop down to zero with a sinusoidal function over the interval $[\kappa_u/3, 7\kappa_u/12]^7$. For $\kappa > 7\kappa_u/12$ all the coherences are identically equal to zero. The three target coherences are collected in Fig. 5.5. Also in this case the target cross-spectra can be computed by means of Eq. (5.1). It should be noted that in both numerical examples, the cross-spectra have been defined by means of coherence functions, but this is not required by the algorithm. The code does not use the target coherences, only the target cross-spectra are required.

The first and the third components have the strongly non-Gaussian Lognormal distribution considered in Sec. 3.3.1:

$$\mathcal{P}(x) = \frac{1}{\sqrt{2\pi}\sigma_N\bar{x}} \exp\left[-\frac{(\ln\bar{x} - \mu_N)^2}{2\sigma_N^2}\right] \quad (5.69)$$

where:

$$\sigma_N^2 = \ln\left(1 + \frac{\sigma}{\bar{\mu}^2}\right) \quad ; \quad \mu_N = \ln\bar{\mu} - \frac{\sigma_N^2}{2} \quad ; \quad \bar{x} = x - \bar{\mu} \quad (5.70)$$

with parameters set as follows:

$$\bar{\mu}_1 = \bar{\mu}_3 = 1.8 \quad ; \quad \sigma_1 = \sigma_3 = 1 \quad (5.71)$$

consequently, the moments of the first and third marginal distributions are:

$$\begin{aligned} \text{mean: } \mu_1 = \mu_3 = 0 \quad ; \quad \text{variance: } \sigma_1^2 = \sigma_3^2 = 1; \\ \text{skewness: } \gamma_1 = \gamma_3 = 1.838 \quad ; \quad \text{kurtosis}_1 = \text{kurtosis}_3 = 9.553 \end{aligned}$$

⁷The sinusoidal joint has the extension of $\kappa_u/4$

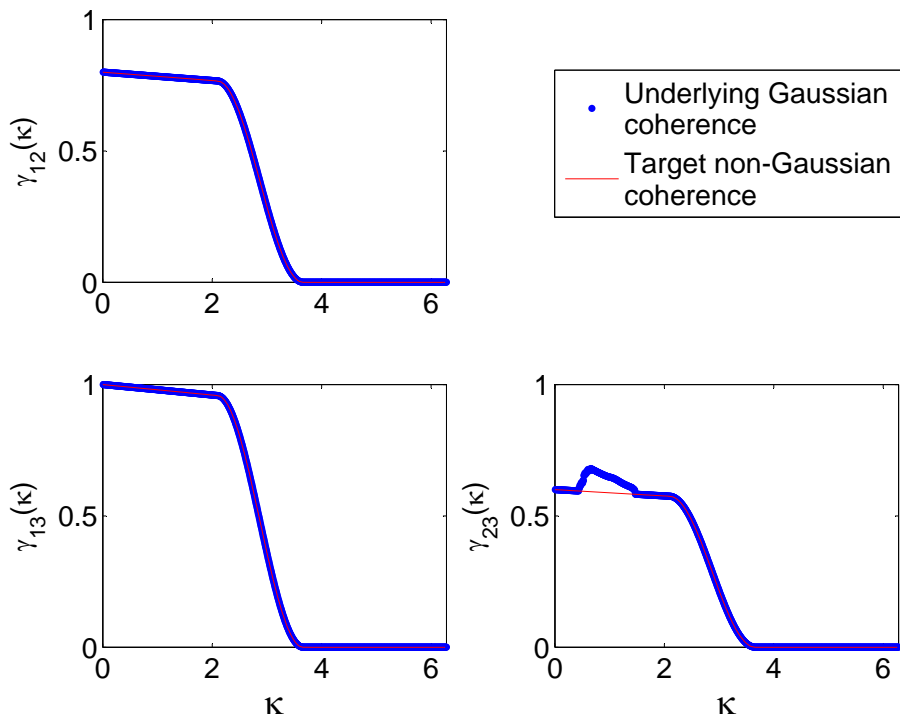


Figure 5.5: Artificially Correlated Spectrum. The underlying Gaussian coherences computed by the algorithm are compared to the target non-Gaussian coherences.

The second component has the Uniform marginal distribution considered in Sec. 3.3.2:

$$\mathcal{P}(x) = \begin{cases} \frac{1}{b-a} & a \leq x \leq b \\ 0 & \text{otherwise} \end{cases} \quad (5.72)$$

with parameters:

$$a = -\sqrt{3} \quad ; \quad b = \sqrt{3} \quad (5.73)$$

resulting in the following moments:

$$\text{mean: } \mu_2 = 0 \ ; \ \text{variance: } \sigma_2^2 = 1 \ ; \ \text{skewness: } \gamma_2 = 0 \ ; \ \text{kurtosis}_2 = 1.8 \quad (5.74)$$

The number of intervals, the number of points used for the FFT and the cutoff wave number are:

$$N = 256; \quad M = 2^{10} = 1024; \quad \kappa_u = 4 \frac{\text{rad}}{m} \quad (5.75)$$

The three coherences are plotted in Fig. 5.5. The underlying Gaussian coherences between components 1-2 and 1-3 are very close to the target non-Gaussian coherences. On the contrary, γ_{23}^g is considerably different from the target within the significant zone. Again, it is clear that, for component 2-3, the underlying Gaussian coherence tends to be larger than the target non-Gaussian because the non-linear mapping reduces the coherence.

A hundred samples have been generated using the underlying Gaussian CSDM computed by the proposed algorithm. Figs. 5.6 and 5.7 demonstrate that both the CSDM obtained by ensemble averaging and the marginal PDF's of the samples exhibit a good matching of the respective targets.

5.5 Concluding Remarks and Computational Efficiency

The ‘‘trial and error’’ iterative approach used for the underlying Gaussian autospectra has been applied also to the establishment of the underlying coherences or cross-spectra. In this way, an original technique for simulation of vector fields with strongly non-Gaussian marginal distributions is provided.

The numerical examples have shown the high accuracy of the proposed algorithm.

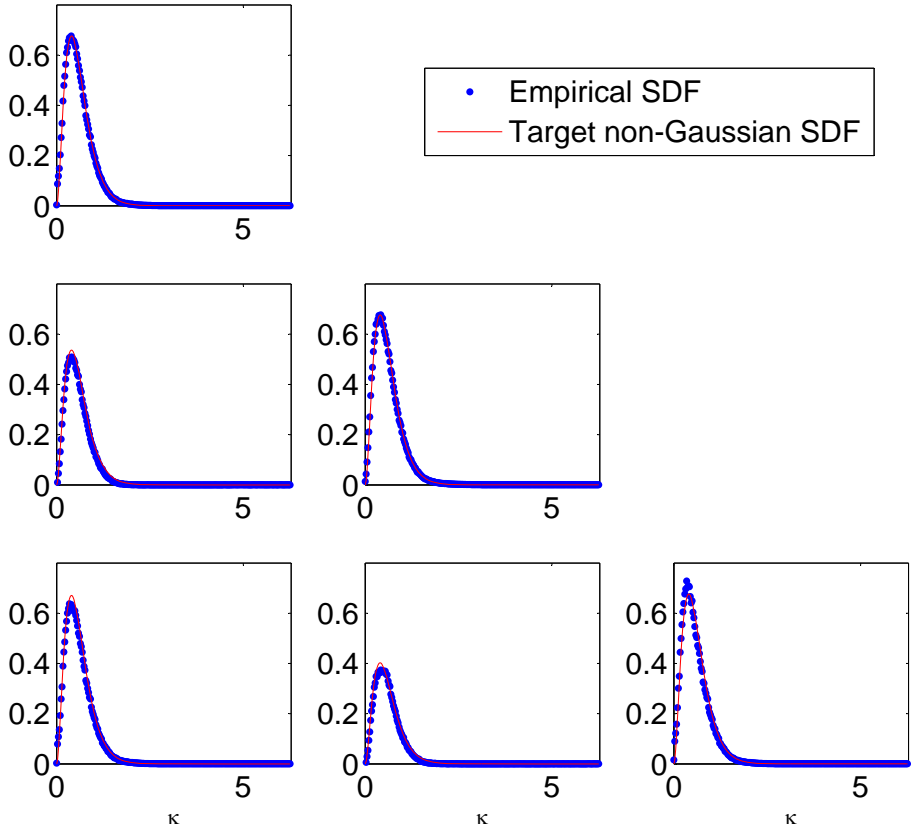


Figure 5.6: Artificially Correlated Spectrum. The “empirical” spectral density functions and the cross-spectral densities obtained by ensemble averaging over 100 generated samples match the target non-Gaussian functions almost perfectly. The graphs are sorted as the elements of the CSDM. Only the lower part is plotted, because the upper part is symmetric. The negligible imaginary part present in the empirical cross-spectra because of the non-ergodicity of the produced samples has been disregarded.

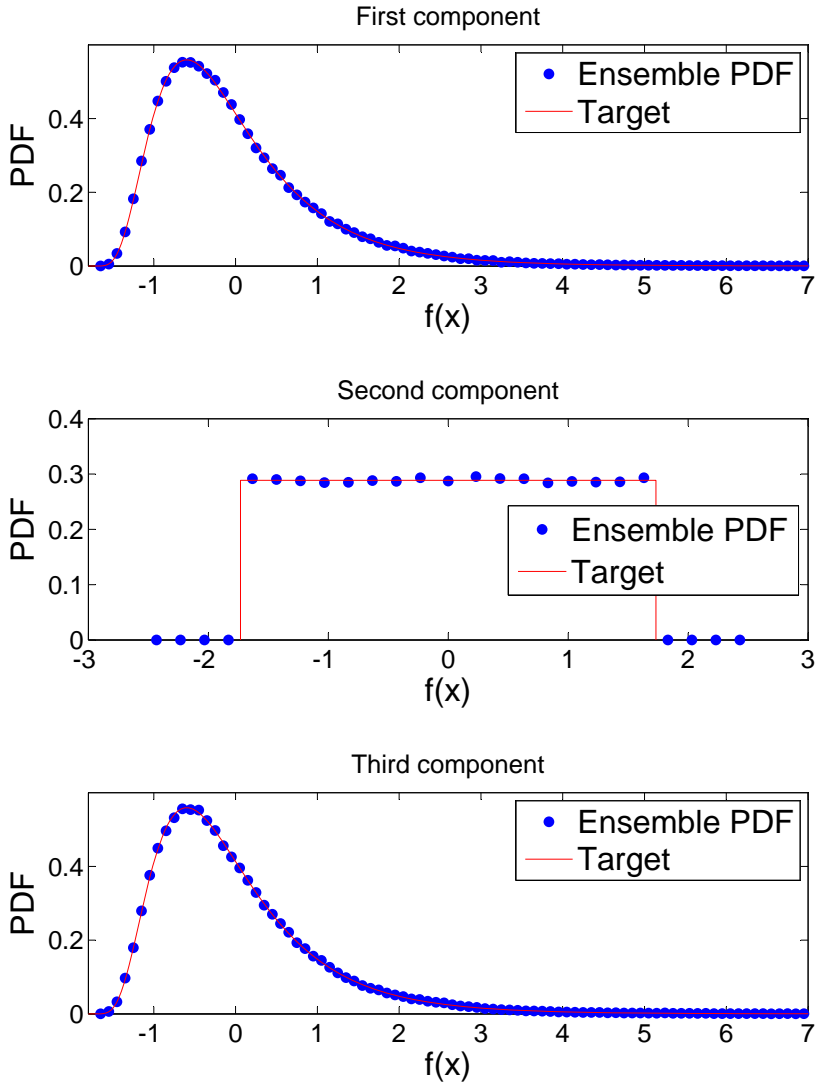


Figure 5.7: Artificially Correlated Spectrum. All three PDF's computed by ensemble averaging of 100 generated samples match the respective non-Gaussian targets.

The code presents similar characteristics to the uni-variate version. In particular, the identification of the underlying CSDM is the most computationally expensive task. After it is completed, the generation procedure is extremely fast.

The last consideration suggests to build a data-base of results on the underlying CSDM that can be used to reduce the computational time. For instance, the three underlying autospectra used in the second numerical example were already known from the analyses presented in Sec. 3.3. Even when the desired targets are not exactly equal to those of a previous analysis, still if they are similar, the already known underlying Gaussian spectrum or coherence can be used as starting guess of the iterative procedure, thus saving a considerable amount of computational time.

Finally, it is worth mentioning that the discretization used for the estimation of the underlying field, does not necessarily has to be the same used for the samples generation. A lower resolution in the wave number domain is sufficient for the identification of $\gamma_{ij}(\kappa)$ or $S_{ij}(\kappa)$ (so reducing the CPU time in the most expensive phase). Then by means of a numerical interpolation, it can assume the resolution required in the production phase.

In the future, a comparison between the proposed algorithm and other techniques for the generation of strongly non-Gaussian vector fields will be performed.

Chapter 6

Simulation of Multi-Variate, Gaussian, Ergodic Random Fields

*How dare we speak of the laws of chance?
Is not chance the antithesis of all law?
-Bertrand Russell-*

Sommario. *Per mezzo di un'opportuna versione dello "Spectral Representation Method" è possibile generare campioni aleatori Gaussiani multivariati. Affinché tali campioni siano anche ergodici, è necessario l'impiego di una tecnica chiamata "Frequency Double Indexing". Essa comporta che i valori numerici degli spettri da riprodurre siano forniti ai numeri d'onda "principali" ed anche a numeri d'onda "secondari", il cui numero cresce con le componenti del campo.*

In questo Capitolo viene dimostrato che lo spettro dei campioni generati è una media pesata dei valori dello spettro obiettivo ai numeri d'onda primari e secondari. L'espressione analitica in forma chiusa

che viene ricavata può anche essere considerata l'estensione al caso discreto della dimostrazione di ergodicità fornita da Deodatis (1996) per il caso continuo. Nella pratica comune, infatti, i campioni vengono sempre generati per mezzo di elaboratori elettronici che sfruttano descrizioni discrete delle variabili e funzioni di calcolo numerico (come ad esempio la Fast Fourier Transform). Inoltre, la descrizione in forma chiusa dell'effettiva densità di potenza spettrale dei campioni può permettere di regolare lo spettro impostato come obiettivo in modo da ottenere esattamente lo spettro risultante desiderato.

6.1 Introductory Remarks

Deodatis (1996) proposed the extension of the Spectral Representation Method (SRM) that generates multivariate samples and that have been described in Sec. 5.2.1. In the same paper, the author proved that the generated samples are ergodic if the Frequency Double Indexing (FDI) technique is employed. However, this proof is valid when $\Delta\kappa$ tends to zero. On the contrary, these simulations are always performed by a digital computer, so the spectra are defined at discrete frequencies and $\Delta\kappa$ is always finite. The original contribution of this Chapter is the proof that even in this case, the samples are ergodic, meaning that they all have exactly the same Cross-Spectral Density Matrix (CSDM) and that therefore the CSDM can be computed by space averaging rather than ensemble averaging.

The basic hypothesis that is made is that the decomposition used for the CSDM is the Cholesky's one. An interesting particular case that will be investigated is the one in which the cross-spectra $S_{ij}^0(\kappa)$ can be described by the coherence function $\gamma_{ij}(\kappa)$ already defined as

$$S_{ij}^0(\kappa) = \sqrt{S_{ii}^0(\kappa)S_{jj}^0(\kappa)}\gamma_{ij}(\kappa) \quad (6.1)$$

$$0 \leq \gamma_{ij}(\kappa) \leq 1 \quad (6.2)$$

In the most general case as well as in the particular case described by Eq. (6.1), a closed form expression of the CSDM of the generated samples can be computed a priori as a “weighted” average of the values of the autospectra at the various “primary” wave numbers (at intervals $\Delta\kappa$) and “secondary” wave numbers (at intervals $\frac{\Delta\kappa}{m}$) introduced by the FDI technique.

6.2 Decomposition of the Target CSDM

As suggested by Deodatis (1996), the CSDM is decomposed using the Cholesky method (see Sec. 5.3.5). The terms of \mathbf{H} are defined as

$$\begin{aligned} H_{cc} &= \sqrt{S_{cc} - \sum_{e=1}^{c-1} H_{ce}^2} \\ H_{cd} &= \frac{1}{H_{dd}} \left(S_{cd} - \sum_{e=1}^{d-1} H_{ce} H_{de} \right), \quad \text{for } c > d \end{aligned} \quad (6.3)$$

where in Eq. (6.3), as well as in the remainder of this Section, the dependence on the wave number κ of all the variables has been omitted for the sake of simplicity.

Substituting Eq. (6.1) into Eq. (6.3), we obtain the matrix $\mathbf{H}(\kappa)$ written as a function of the autospectra and of the coherences:

$$\begin{aligned} H_{cc} &= \sqrt{S_{cc} - \sum_{e=1}^{c-1} H_{ce}^2} \\ H_{cd} &= \frac{1}{H_{dd}} \left(\sqrt{S_{cc} S_{dd}} \gamma_{cd} - \sum_{e=1}^{d-1} H_{ce} H_{de} \right), \quad \text{for } c > d \end{aligned} \quad (6.4)$$

Now, let us define the quantities $w_{cd}(\kappa)$ as

$$w_{cd}(\kappa) := \frac{H_{cd}(\kappa)}{\sqrt{S_{cc}(\kappa)}} \quad \Rightarrow \quad H_{cd}(\kappa) = w_{cd}(\kappa) \sqrt{S_{cc}(\kappa)} \quad (6.5)$$

In this way, the diagonal terms of $\mathbf{H}(\kappa)$ can be written as

$$H_{cc} = \sqrt{S_{cc} - \sum_{e=1}^{c-1} w_{ce}^2 S_{cc}} = \sqrt{S_{cc}} \sqrt{1 - \sum_{e=1}^{c-1} w_{ce}^2} \quad (6.6)$$

so, by definition, w_{cc} is

$$w_{cc} = \sqrt{1 - \sum_{e=1}^{c-1} w_{ce}^2} \quad (6.7)$$

and w_{cd} is given by

$$\begin{aligned}
 w_{cd} &:= \frac{H_{cd}}{\sqrt{S_{cc}}} = \\
 &= \frac{1}{\sqrt{S_{cc}}} \frac{1}{H_{dd}} \left(\sqrt{S_{cc}S_{dd}}\gamma_{cd} - \sum_{e=1}^{d-1} H_{ce}H_{de} \right) = \\
 &= \frac{1}{\sqrt{S_{cc}}} \frac{1}{\sqrt{S_{dd}}\sqrt{1 - \sum_{e=1}^{d-1} w_{de}^2}} \left(\sqrt{S_{cc}S_{dd}}\gamma_{cd} - \sum_{e=1}^{d-1} w_{ce}\sqrt{S_{cc}}w_{de}\sqrt{S_{dd}} \right) = \\
 &= \frac{1}{\sqrt{S_{cc}}} \frac{1}{\sqrt{S_{dd}}\sqrt{1 - \sum_{e=1}^{d-1} w_{de}^2}} \sqrt{S_{cc}S_{dd}} \left(\gamma_{cd} - \sum_{e=1}^{d-1} w_{ce}w_{de} \right) = \\
 &= \frac{1}{\sqrt{1 - \sum_{e=1}^{d-1} w_{de}^2}} \left(\gamma_{cd} - \sum_{e=1}^{d-1} w_{ce}w_{de} \right), \quad \text{for } c > d
 \end{aligned} \tag{6.8}$$

The recursive Eqs. (6.7) and (6.8) show that the variables $w(\kappa)$ are functions only of the coherences $\gamma(\kappa)$. So, in general,

$$H_{cd}(\kappa) = w_{cd}(\gamma(\kappa)) \sqrt{S_{cc}(\kappa)} \tag{6.9}$$

In this way, the Cholesky decomposition of $\mathbf{S}(\kappa)$ can be quickly computed knowing only the underlying Gaussian autospectra and the coherences. For the special case of $m = 3$ we obtain

$$\mathbf{w}(\kappa) = \begin{pmatrix} 1 & 0 & 0 \\ \gamma_{12} & \sqrt{1 - \gamma_{12}^2} & 0 \\ \gamma_{13} & \frac{\gamma_{23} - \gamma_{12}\gamma_{13}}{\sqrt{1 - \gamma_{12}^2}} & \sqrt{1 - \gamma_{13}^2 - \frac{(\gamma_{23} - \gamma_{12}\gamma_{13})^2}{1 - \gamma_{12}^2}} \end{pmatrix} \tag{6.10}$$

$$\mathbf{H}(\kappa) = \begin{pmatrix} \sqrt{S_{11}} & 0 & 0 \\ \gamma_{12}\sqrt{S_{22}} & \sqrt{1 - \gamma_{12}^2}\sqrt{S_{22}} & 0 \\ \gamma_{13}\sqrt{S_{33}} & \frac{\gamma_{23} - \gamma_{12}\gamma_{13}}{\sqrt{1 - \gamma_{12}^2}}\sqrt{S_{33}} & \sqrt{1 - \gamma_{13}^2 - \frac{(\gamma_{23} - \gamma_{12}\gamma_{13})^2}{1 - \gamma_{12}^2}}\sqrt{S_{33}} \end{pmatrix} \quad (6.11)$$

It will be shown in the following Sections that the w_{ij} 's can be used as weights to determine the CSDM of the generated samples.

6.3 Generation of \hat{g}_c

Always referring to the same article (Deodatis, 1996), for the generation of the samples, the adopted procedure is the one already summarized in Sec. 5.3.7 and here reported.

The following functions are defined:

$$t_{cd}^{(i)}(p \Delta x) = \text{FFT}_l^+ \left[2H_{cd} \left(l\Delta\kappa + \frac{d}{m}\Delta\kappa \right) \sqrt{\Delta\kappa} \cdot \exp \left(i\phi_{dl}^{(i)} \right) \right];$$

$$c = 1, 2, \dots, m; \quad d = 1, 2, \dots, c; \quad (6.12)$$

$$p = 0, 1, \dots, M - 1; \quad l = 0, 1, \dots, M - 1;$$

$$\Delta x = \frac{M}{2\pi \Delta\kappa}$$

where $\text{FFT}_l^+ [\cdot]$ denotes the FFT with M points and positive exponent over the index l of the function in brackets. The superscript (i) stands for the fact that a specific set of random phase angles $\phi^{(i)}$ determines a specific function $t_{cd}^{(i)}$ and m is the number of components.

Then, m copies of $t_{cd}^{(i)}$ are concatenated to generate $h_{cd}^{(i)}$:

$$h_{cd}^{(i)}(q\Delta x) = t_{cd}^{(i)}(\text{mod}(q, M)\Delta x); \quad q = 0, 1, \dots, mM - 1 \quad (6.13)$$

where $\text{mod}(q, M)$ denotes the remainder of division of q by M .

Because of the frequency shifting (for the theory, refer also to Sec. 3.2.6), $h_{ij}^{(i)}$ has to be multiplied by a shifting factor:

$$\hat{h}_{cd}^{(i)}(q\Delta x) = \Re \left[h_{cd}^{(i)}(q\Delta x) \cdot \exp \left(i \frac{d}{m} \Delta\kappa x \right) \right] \quad (6.14)$$

where $\Re[\cdot]$ denotes the real part.

Finally, the various components $\hat{g}_c(q\Delta x)$ are obtained as sums of the functions $\hat{h}_{cd}^{(i)}(q\Delta x)$:

$$\hat{g}_c(q\Delta x) = \sum_{d=1}^c \hat{h}_{cd}(q\Delta x) \quad (6.15)$$

6.4 Spectrum of \hat{h}_{cd}

The analogy between Eqs. (6.12)–(6.14) and the SRM with frequency shifting –recall Eq. (3.3)– is evident, therefore the spectrum of \hat{h}_{cd} is very closely related to

$$H_{cd}^2 \left(l\Delta\kappa + \frac{d}{m}\Delta\kappa \right) \quad l = 0, 1, \dots, N-1 \quad (6.16)$$

Actually, because of the frequency shifting, when the empirical spectrum is computed, the results will be relative to intervals $\frac{\Delta\kappa}{m}$ in the wave number domain. So, at the frequencies $l\Delta\kappa + \frac{d}{m}\Delta\kappa$ the spectrum is a delta function of magnitude

$$m \cdot H_{cd}^2 \left(l\Delta\kappa + \frac{d}{m}\Delta\kappa \right) \quad (6.17)$$

while at the other frequencies it is zero. In this way the variance (area underneath the spectrum) is conserved:

$$m \cdot H_{cd}^2 \left(l\Delta\kappa + \frac{d}{m}\Delta\kappa \right) \cdot \frac{\Delta\kappa}{m} = H_{cd}^2 \left(l\Delta\kappa + \frac{d}{m}\Delta\kappa \right) \cdot \Delta\kappa \quad (6.18)$$

6.5 Computation of the CSDFM

The Cross-Spectral Density Function (CSDF) of the samples $\hat{g}_r(x)$ and $\hat{g}_s(x)$ can be computed at the discrete frequencies $\bar{\kappa}$ using the formula (Bendat and Piersol, 1986, p. 130):

$$S_{rs}^g(\bar{\kappa}) = \frac{1}{2\pi(mL)} \text{FFT}^{-1}[\hat{g}_r]^* \Delta x \text{FFT}^{-1}[\hat{g}_s] \Delta x; \quad (6.19)$$

$$\bar{\kappa} = 0, \frac{1}{m}\Delta\kappa, \frac{2}{m}\Delta\kappa, \dots, (N-1)\Delta\kappa + \frac{(m-1)}{m}\Delta\kappa$$

where $\text{FFT}^- [\cdot]$ denotes the FFT with negative exponent and the asterisk denotes the complex conjugate. When the FFT is performed, the result has as many points as the input function $\hat{g}(x)$; however only the first half of the resulting points is meaningful, the second half is only its mirror image, due to the assumption of periodicity. For this reason, $\bar{\kappa}$ goes up only to $(N-1)\Delta\kappa + \frac{(m-1)}{m}\Delta\kappa$ instead of $(M-1)\Delta\kappa + \frac{(m-1)}{m}\Delta\kappa$, assuming that $M = 2N$.

Substituting Eq. (6.15) into Eq. (6.19) and taking advantage of the linearity of the FFT operator, we get

$$\begin{aligned} S_{rs}^g(\bar{\kappa}) &= \frac{\Delta x^2}{2\pi mL} \text{FFT}^- \left[\sum_{c=1}^r \hat{h}_{rc} \right]^* \text{FFT}^- \left[\sum_{d=1}^s \hat{h}_{sd} \right] = \\ &= \frac{\Delta x^2}{2\pi mL} \sum_{c=1}^r \text{FFT}^- \left[\hat{h}_{rc} \right]^* \sum_{d=1}^s \text{FFT}^- \left[\hat{h}_{sd} \right] \end{aligned} \quad (6.20)$$

Now, we know from Sec. 6.4 that the autospectrum of \hat{h}_{cd} is

$$\begin{aligned} S_{\hat{h}_{cd}}(\bar{\kappa}) &= \frac{1}{2\pi(mL)} \left| \text{FFT}^- \left[\hat{h}_{cd} \right] \Delta x \right|^2 = \\ &= \begin{cases} m \cdot H_{cd}^2 \left(l\Delta\kappa + \frac{d}{m}\Delta\kappa \right) & \text{for } \bar{\kappa} = \left(l + \frac{d}{m} \right) \Delta\kappa \\ 0 & \text{everywhere else} \end{cases} \quad (6.21) \\ & \quad l = 0, 1, 2, \dots, N-1 \end{aligned}$$

that gives

$$\left| \text{FFT}^- \left[\hat{h}_{cd} \right] \right| = \begin{cases} \frac{m}{\Delta x} \sqrt{2\pi L} H_{cd} \left(l\Delta\kappa + \frac{d}{m}\Delta\kappa \right) & \text{at } \bar{\kappa} = \left(l + \frac{d}{m} \right) \Delta\kappa \\ 0 & \text{everywhere else} \end{cases} \quad (6.22)$$

Note that \mathbf{S}^0 and \mathbf{H} are real, according to Eqs. (6.1) and (6.11).

The complex function $\text{FFT}^- \left[\hat{h}_{cd} \right]$ can be expressed as

$$\begin{aligned} \text{FFT}^- \left[\hat{h}_{cd} \right] &= \left| \text{FFT}^- \left[\hat{h}_{ij} \right] \right| \cdot \exp(i\theta_{cd}) = \\ &= \begin{cases} \frac{m}{\Delta x} \sqrt{2\pi T} H_{cd} \left(l\Delta\kappa + \frac{d}{m}\Delta\kappa \right) \cdot \exp(i\theta_{cd}) & \text{at } \bar{\kappa} = \left(l + \frac{d}{m} \right) \Delta\kappa \\ 0 & \text{everywhere else} \end{cases} \end{aligned} \quad (6.23)$$

where

$$\theta_{cd} = \arctan \left[\frac{\Im(\text{FFT}^{-1} \hat{h}_{cd})}{\Re(\text{FFT}^{-1} \hat{h}_{cd})} \right] \quad (6.24)$$

Now, considering again Eq. (6.20) and Eq. (6.23), we can observe that the product of sums gives terms different from zero only when both functions $\text{FFT}^{-1} [\hat{h}_{rc}]^*$ and $\text{FFT}^{-1} [\hat{h}_{sd}]$ have moduli different from zero, that means when $\bar{\kappa} = \left(l + \frac{c}{m}\right) \Delta\kappa = \left(l + \frac{d}{m}\right) \Delta\kappa$. For this reason it is possible to consider just the terms with $c = d$ and, therefore get rid of the sums:

$$S_{rs}^g(\bar{\kappa}) = \begin{cases} 0 & \text{for } \bar{\kappa} = 0 \\ mH_{rc} \left(l\Delta\kappa + \frac{c}{m}\Delta\kappa\right) \cdot \\ \cdot H_{sc} \left(l\Delta\kappa + \frac{c}{m}\Delta\kappa\right) \cdot \\ \cdot \exp[i(\theta_{sc} - \theta_{rc})] & \text{for } \bar{\kappa} = \left(l + \frac{c}{m}\right) \Delta\kappa \end{cases} \quad (6.25)$$

Moreover, the phase θ_{cd} is governed only by the set of random phase angles ϕ_d , therefore it is not a function of the first index¹. In particular $\theta_{sc} = \theta_{rc}$. For this reason, Eq. (6.25) reduces to:

$$\begin{aligned} S_{rs}^g(\bar{\kappa}) &= \\ &= \begin{cases} 0 & \text{for } \bar{\kappa} = 0 \\ mH_{rc} \left(l\Delta\kappa + \frac{c}{m}\Delta\kappa\right) H_{sc} \left(l\Delta\kappa + \frac{c}{m}\Delta\kappa\right) & \text{for } \bar{\kappa} = \left(l + \frac{c}{m}\right) \Delta\kappa \end{cases} \\ l = 0, 1, \dots, N-1; \quad c = 1, 2, \dots, m \end{aligned} \quad (6.26)$$

Equation (6.26) is a closed form expression of the results that can be obtained computing the empirical spectrum from a single sample using FFT.

¹Note that in Eq. (6.12) and, thus, in Eqs. (6.13) and (6.14) only the set of random phase angles $\phi_d^{(i)}$ is involved, while $\phi_c^{(i)}$ is not.

Now, recalling the results of Sec. 6.2, Eq. (6.26) can also be expressed as:

$$\begin{aligned}
 S_{rs}^g(\bar{\kappa}) &= \\
 &= \begin{cases} 0 & \text{for } \bar{\kappa} = 0 \\ mw_{rc}(l\Delta\kappa + \frac{c}{m}\Delta\kappa) \cdot \sqrt{S_{rr}^0(l\Delta\kappa + \frac{c}{m}\Delta\kappa)} \cdot \\ \cdot w_{sc}(l\Delta\kappa + \frac{c}{m}\Delta\kappa) \cdot \sqrt{S_{ss}^0(l\Delta\kappa + \frac{c}{m}\Delta\kappa)} & \text{for } \bar{\kappa} = \left(l + \frac{c}{m}\right)\Delta\kappa \end{cases} \\
 l = 0, 1, \dots, N-1; \quad c = 1, 2, \dots, m
 \end{aligned} \tag{6.27}$$

And for the special case of the diagonal terms:

$$\begin{aligned}
 S_{rr}^g(\bar{\kappa}) &= \\
 &= \begin{cases} 0 & \text{for } \bar{\kappa} = 0 \\ mw_{rc}^2(l\Delta\kappa + \frac{c}{m}\Delta\kappa) \cdot S_{rr}^0(l\Delta\kappa + \frac{c}{m}\Delta\kappa) & \text{for } \bar{\kappa} = \left(l + \frac{c}{m}\right)\Delta\kappa \end{cases} \\
 l = 0, 1, \dots, N-1; \quad c = 1, 2, \dots, m
 \end{aligned} \tag{6.28}$$

Equations (6.26)–(6.28) compute the spectrum of the samples as it is naturally given by their digital representation, that means at intervals of $\frac{\Delta\kappa}{m}$. If we want to measure the spectral density over intervals of width $\Delta\kappa$, the most reasonable way is to average the results at m sub-frequencies (i.e. sum up the areas underneath the SDF). Thus, Eqs. (6.26)–(6.28) become, respectively

$$\begin{aligned}
 S_{rs}^g(\tilde{\kappa}) &= \begin{cases} \sum_{c=1}^{m-1} H_{rc}(l\Delta\kappa + \frac{c}{m}\Delta\kappa) H_{sc}(l\Delta\kappa + \frac{c}{m}\Delta\kappa) & \text{for } \tilde{\kappa} = 0 \\ H_{rc}(l\Delta\kappa) H_{sc}(l\Delta\kappa) + \\ + \sum_{c=1}^{m-1} H_{rc}(l\Delta\kappa + \frac{c}{m}\Delta\kappa) H_{sc}(l\Delta\kappa + \frac{c}{m}\Delta\kappa) & \text{for } \tilde{\kappa} = l\Delta\kappa \neq 0 \end{cases} \\
 l = 0, 1, \dots, N-1
 \end{aligned} \tag{6.29}$$

$$\begin{aligned}
S_{rs}^g(\tilde{\kappa}) &= \\
&= \begin{cases} \sum_{c=1}^{m-1} w_{rc}(l\Delta\kappa + \frac{c}{m}\Delta\kappa) \cdot \sqrt{S_{rr}^0(l\Delta\kappa + \frac{c}{m}\Delta\kappa)} \cdot \\ \cdot w_{sc}(l\Delta\kappa + \frac{c}{m}\Delta\kappa) \cdot \sqrt{S_{ss}^0(l\Delta\kappa + \frac{c}{m}\Delta\kappa)} & \text{for } \tilde{\kappa} = 0 \\ w_{rc}(l\Delta\kappa) \cdot \sqrt{S_{rr}^0(l\Delta\kappa)} \cdot w_{sc}(l\Delta\kappa) \cdot \sqrt{S_{ss}^0(l\Delta\kappa)} + \\ + \sum_{c=1}^{m-1} w_{rc}(l\Delta\kappa + \frac{c}{m}\Delta\kappa) \cdot \sqrt{S_{rr}^0(l\Delta\kappa + \frac{c}{m}\Delta\kappa)} \cdot \\ \cdot w_{sc}(l\Delta\kappa + \frac{c}{m}\Delta\kappa) \cdot \sqrt{S_{ss}^0(l\Delta\kappa + \frac{c}{m}\Delta\kappa)} & \text{for } \tilde{\kappa} = l\Delta\kappa \neq 0 \end{cases} \\
l &= 0, 1, \dots, N-1
\end{aligned} \tag{6.30}$$

$$\begin{aligned}
S_{rr}^g(\tilde{\kappa}) &= \\
&= \begin{cases} \sum_{c=1}^{m-1} w_{rc}^2(l\Delta\kappa + \frac{c}{m}\Delta\kappa) \cdot S_{rr}^0(l\Delta\kappa + \frac{c}{m}\Delta\kappa) & \text{for } \tilde{\kappa} = 0 \\ w_{rc}^2(l\Delta\kappa) \cdot S_{rr}^0(l\Delta\kappa) + \\ + \sum_{c=1}^{m-1} w_{rc}^2(l\Delta\kappa + \frac{c}{m}\Delta\kappa) \cdot S_{rr}^0(l\Delta\kappa + \frac{c}{m}\Delta\kappa) & \text{for } \tilde{\kappa} = l\Delta\kappa \neq 0 \end{cases} \\
l &= 0, 1, \dots, N-1
\end{aligned} \tag{6.31}$$

This last equation clearly shows that the quantities w defined in Sec. 6.2 can be interpreted as square roots of the weights that have to be applied to the values of the target autospectra at the primary and secondary discretization points to compute the actual spectra of the produced samples.

6.6 Consistency with the Proof of Ergodicity by Deodatis (1996)

Deodatis (1996) proved that the samples produced by this algorithm are ergodic and that they all have the same correlations and CSDM that are equal to the targets. That proof is valid for $\Delta\kappa$ that goes to zero, as the author clearly stated. The results of the previous Section are perfectly consistent with this. In fact, when $\Delta\kappa \rightarrow 0$, all the secondary discretization points tend to coincide (collapse) and the values of the spectra at those points have to be averaged (or,

that is equivalent, the areas have to be summed). Therefore, Eq. (6.26) reduces to

$$\begin{aligned}
 S_{rs}^g(\kappa) &= \begin{cases} 0 & \kappa = 0 \\ \frac{\sum_{c=1}^m H_{rc}(\kappa)H_{sc}(\kappa)}{m} & \text{otherwise} \end{cases} \\
 &= \begin{cases} 0 & \kappa = 0 \\ \sum_{c=1}^m H_{rc}(\kappa)H_{sc}(\kappa) & \text{otherwise} \end{cases}
 \end{aligned} \tag{6.32}$$

Considering the definitions of matrix product and of Cholesky decomposition, we obtain

$$\begin{aligned}
 \mathbf{S}^g(\kappa) &= \begin{cases} 0 & \kappa = 0 \\ \mathbf{H}(\kappa)\mathbf{H}^T(\kappa) & \text{otherwise} \end{cases} \\
 &= \begin{cases} 0 & \kappa = 0 \\ \mathbf{S}^0(\kappa) & \text{otherwise} \end{cases}
 \end{aligned} \tag{6.33}$$

That is equivalent to what Deodatis (1996) proved considering the correlations.

From this point of view, Eq. (6.26) or (6.29) can be considered a generalization of the proof of ergodicity, valid also for finite $\Delta\kappa$. In fact it proves that all the produced samples have the same spectrum and, therefore, it can be computed from one single sample, by space averaging, rather than by ensemble averaging of an infinite number of samples. For periodic functions, this is an alternative definition of the ergodic property.

6.7 Numerical Examples

6.7.1 Triangular Spectrum

Assume that we want to produce one sample with the following characteristics:

$$N = 2 \quad (6.34)$$

$$\kappa_u = 6 \quad (6.35)$$

$$\Delta\kappa = \frac{\kappa_u}{N} = 3 \quad (6.36)$$

$$M = 2N = 4 \quad (6.37)$$

$$m = 3 \quad (6.38)$$

$$S_{rr}^0(\kappa) = \begin{cases} \kappa, & 0 \leq \kappa \leq \frac{\kappa_u}{2} \\ \kappa_u - \kappa, & \frac{\kappa_u}{2} < \kappa \leq \kappa_u \end{cases} \quad \forall r \in [1, m] \quad (6.39)$$

$$\gamma_{rs}^0(\kappa) = 0.4 \quad \forall r \in [2, m]; s \in [1, r - 1] \quad (6.40)$$

Obviously N is too low to get Gaussianity, but ergodicity is guaranteed anyway.

The theoretical spectrum in Fig. 6.1 can not be directly used as input, its values computed at the following primary and secondary frequencies are required by the code:

$$\kappa_n = n \frac{\Delta\kappa}{m}, \quad n = 1, 2, \dots, mN \quad (6.41)$$

so that the spectrum represented in Fig. 6.2 is the one actually used as input of the code.

The produced samples have $mM = 12$ discrete points. The empirical SDF's computed using the samples have 12 points as well. However, only the first half of the points ($\kappa = 0, 1, \dots, 5$) is meaningful, the second half is artificially introduced by the FFT because of the assumption of periodicity and is just a mirror image of the first half. For instance, S_{22} and S_{33} are reported in Figs. 6.3 and 6.4, respectively.

It is evident that the empirical spectra does not match the target. This could be attributed to the fact that the "resolution" we can count on is not $\frac{\Delta\kappa}{m}$ but $\Delta\kappa$. However, even averaging (if we consider the values) or summing (if we consider the areas) the results in intervals of width $\Delta\kappa$, still the resulting spectra does not match the target (see Tab. 6.1 and Figs. 6.5–6.6).

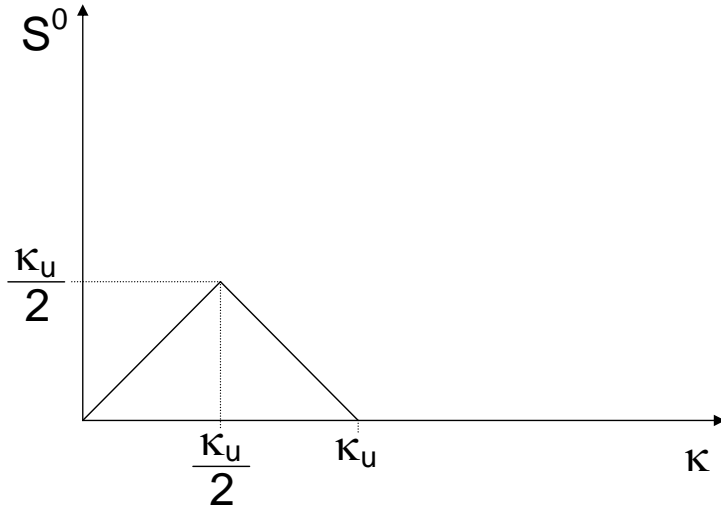


Figure 6.1: Theoretical target triangular spectrum. It is the same for every component.

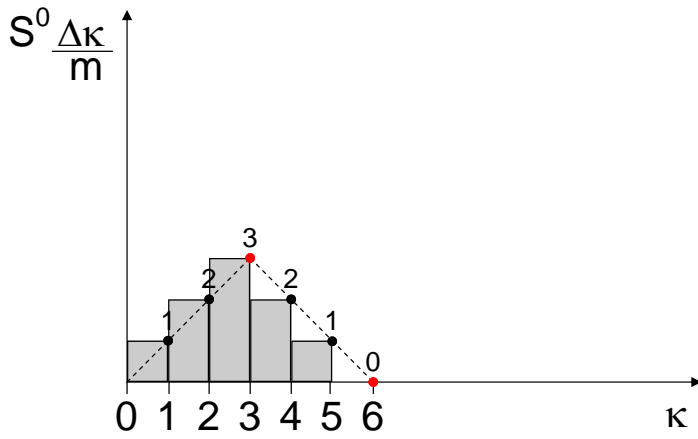


Figure 6.2: The values given to the code as target are $S^0 \frac{\Delta \kappa}{m} = [1, 2, 3, 2, 1, 0]'$.

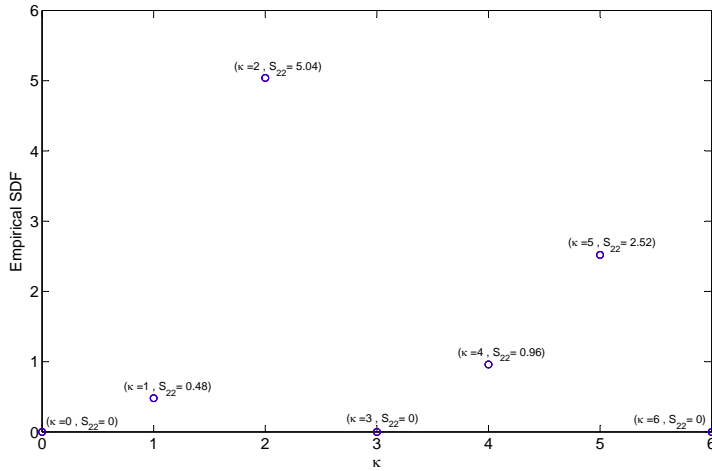


Figure 6.3: Triangular spectrum, empirical autospectrum of the second component.

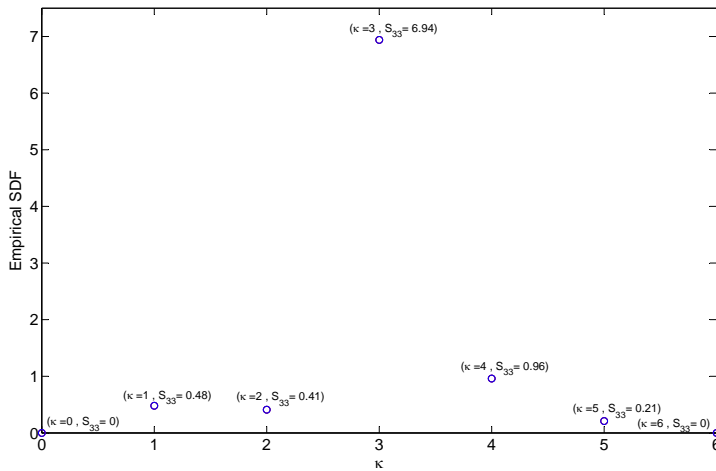


Figure 6.4: Triangular spectrum, empirical autospectrum of the third component.

κ	Target	S_{22}	S_{33}
$1 \cup 2 \cup 3$	$1+2+3=6$	$0.48+5.04+0=5.52$	$0.48+0.41+6.94=7.83$
$4 \cup 5 \cup 6$	$2+1+0=3$	$0.96+2.52+0=3.48$	$0.96+0.21+0=1.17$

Table 6.1: Triangular spectrum. The empirical spectra do not match the target neither in an average sense.

The values of the empirical spectra can be computed a priori by means of Eqs. (6.27) and (6.28).

In Sec. 6.6, we saw that when $\Delta\kappa$ tends to zero, the CSDM of the samples tends to the target. In fact, increasing the number of intervals N , that is reducing $\Delta\kappa$, the CSDM computed with resolution $\Delta\kappa$ becomes closer to the target, as Fig. 6.8 shows. On the contrary, no matter how small $\Delta\kappa$ is, if we compute the CSDM with a resolution of $\frac{\Delta\kappa}{m}$, we see that it is scattered, because the contributions at the various secondary frequencies have different weights (see Fig. 6.7). Figures 6.7 and 6.8 clearly show that the fairest way to compute the CSDM is to consider intervals of width $\Delta\kappa$, so this is what will be done in the remainder of the Chapter.

The difference between the spectra of the produced samples and the target remains finite even increasing N , as the blow-up in Fig. 6.8 shows. Figures 6.9–6.11 represent the difference between the empirical spectrum and the target for the triangular SDF. As already said, the difference is due to the fact that each single point of the actual spectra of the samples is a combination of the values of the target spectrum at m points over the interval $\Delta\kappa$. Therefore, this difference increases with the difference between the values of the target spectra over one interval of width $\Delta\kappa$. We can conclude that the difference is larger when $\Delta\kappa$ is larger and when the derivative of the target autospectrum is larger. In fact, for a linear (triangular) spectrum, the difference assumes constant values, while the next numerical example will show that for a parabolic target spectrum, the difference is a linear function.

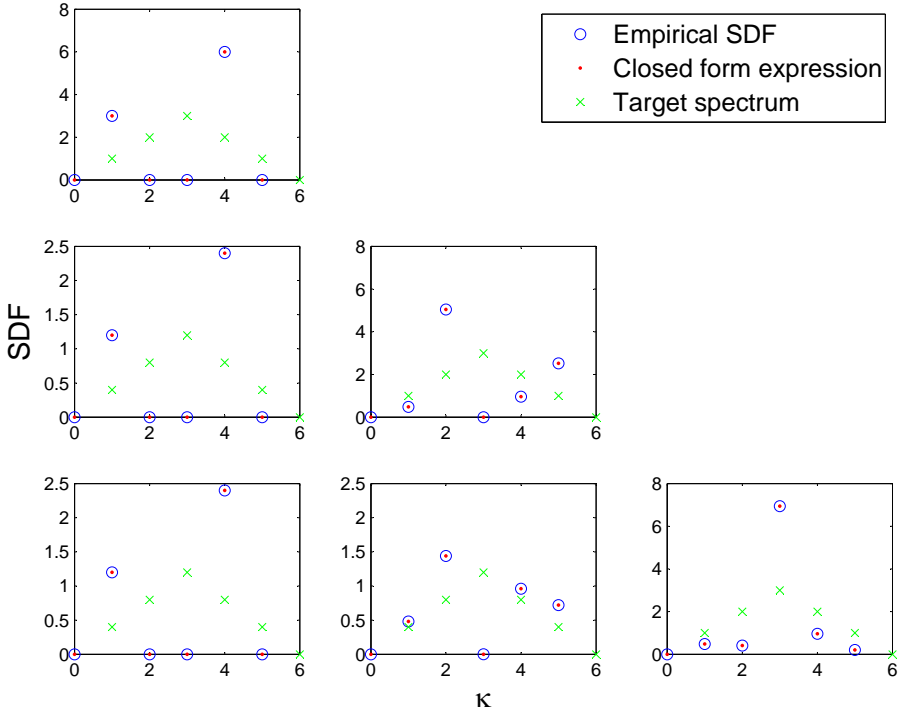


Figure 6.5: Triangular spectrum, cross-spectral density matrix. The “Empirical SDF” has been computed applying Eq. (6.19) to one produced sample; the “Closed form expression” represents the results of Eq. (6.26) or Eqs. (6.27)–(6.28); the “Target spectrum” is the input given to the simulation algorithm.

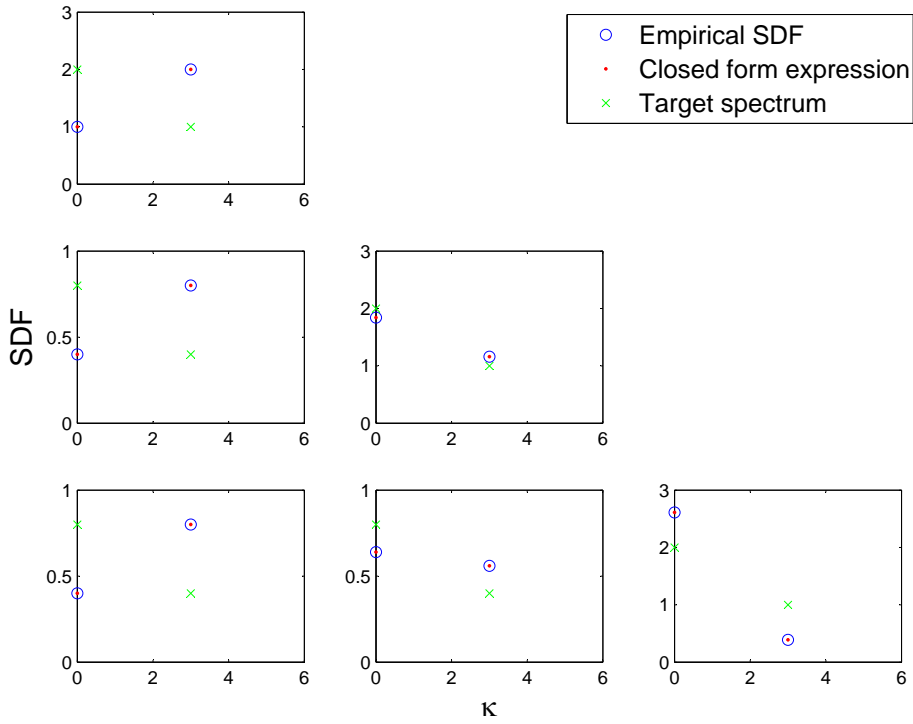


Figure 6.6: Triangular spectrum, cross-spectral density matrix. Data are computed as in Fig. 6.5, but at intervals of width $\Delta\kappa$, rather than $\frac{\Delta\kappa}{m}$. Each value in this plot is the sum of m values in Fig. 6.5. It is clear that also with this “resolution”, the closed form expression perfectly describes the spectrum of the produced samples but it is different from the target one.

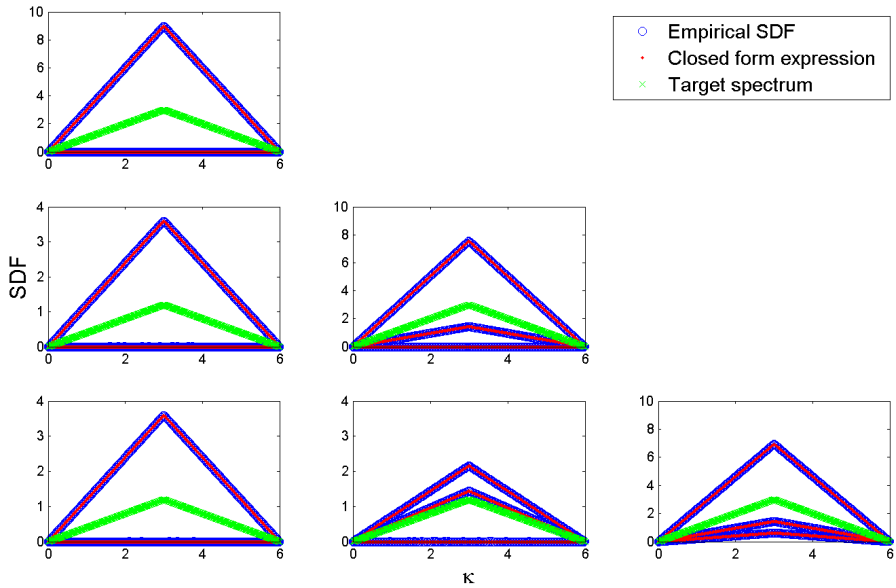


Figure 6.7: Triangular spectrum, cross-spectral density matrix. Data are computed as in Fig. 6.5. N has been set equal to 256, therefore $\frac{\Delta\kappa}{m} = \frac{6}{3 \cdot 256} \cong 0.0078$. Measuring the CSDM at intervals of $\frac{\Delta\kappa}{m}$, the empirical CSDM is always scattered, as long as $\Delta\kappa$ is finite.

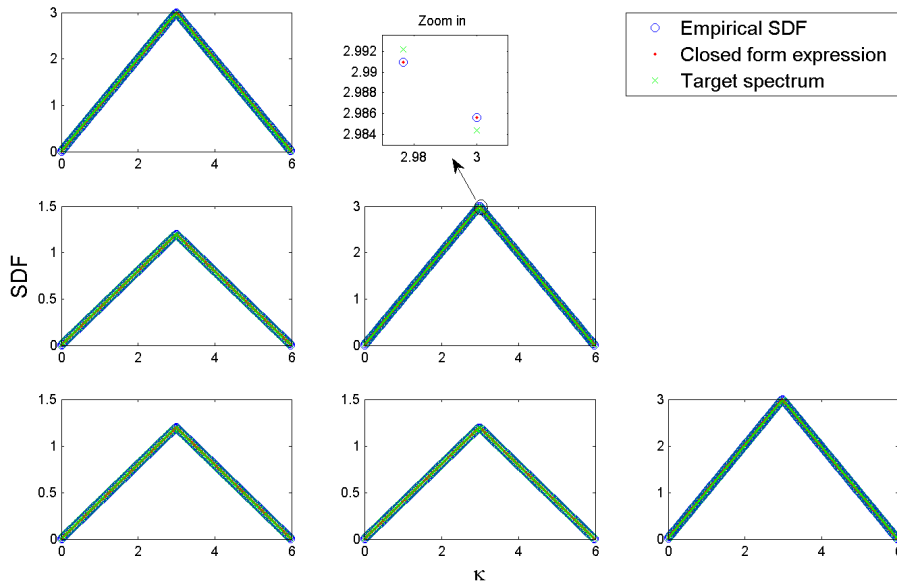


Figure 6.8: Triangular spectrum, cross-spectral density matrix. Data are computed as in Fig. 6.6. N has been set equal to 256, therefore $\Delta\kappa = \frac{6}{256} \cong 0.0234$. The empirical CSDM is much closer to the target than the one in Fig. 6.6.

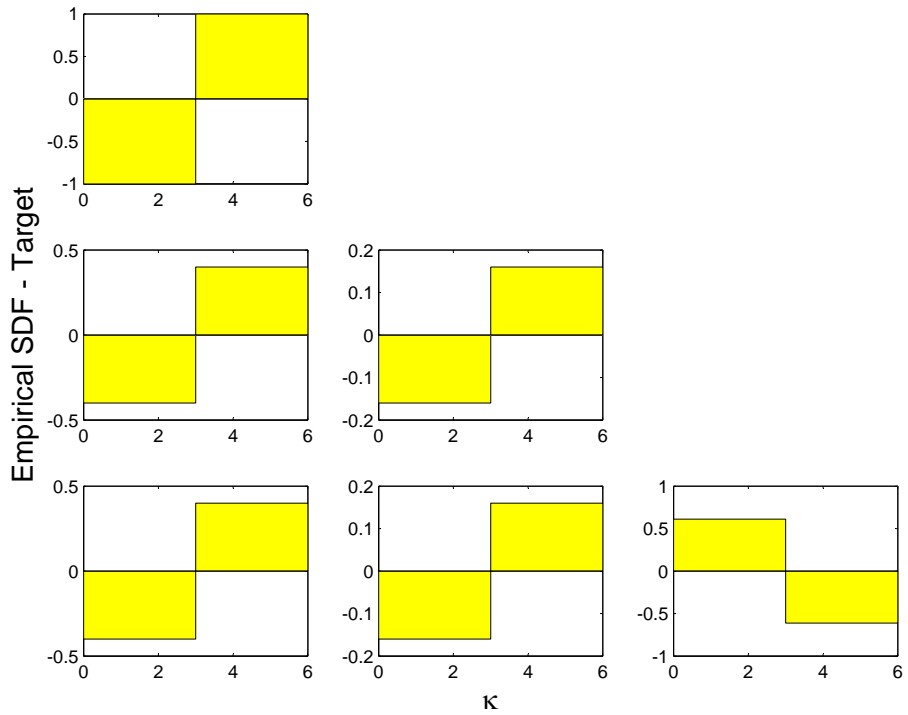


Figure 6.9: Triangular spectrum, difference between the “empirical spectrum” computed as in Fig. 6.6 and the target. N has been set equal to 2.

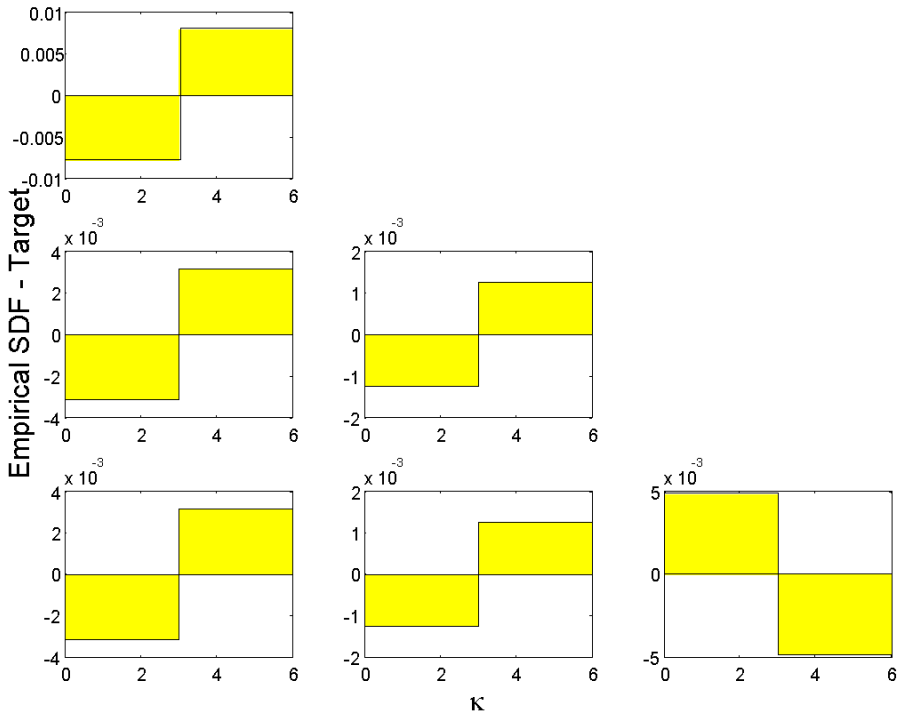


Figure 6.10: Triangular spectrum, difference between the “empirical spectrum” computed as in Fig. 6.6 and the target. N has been set equal to 256. The absolute value of the difference is constant, because the derivatives of the SDF’s are constant.

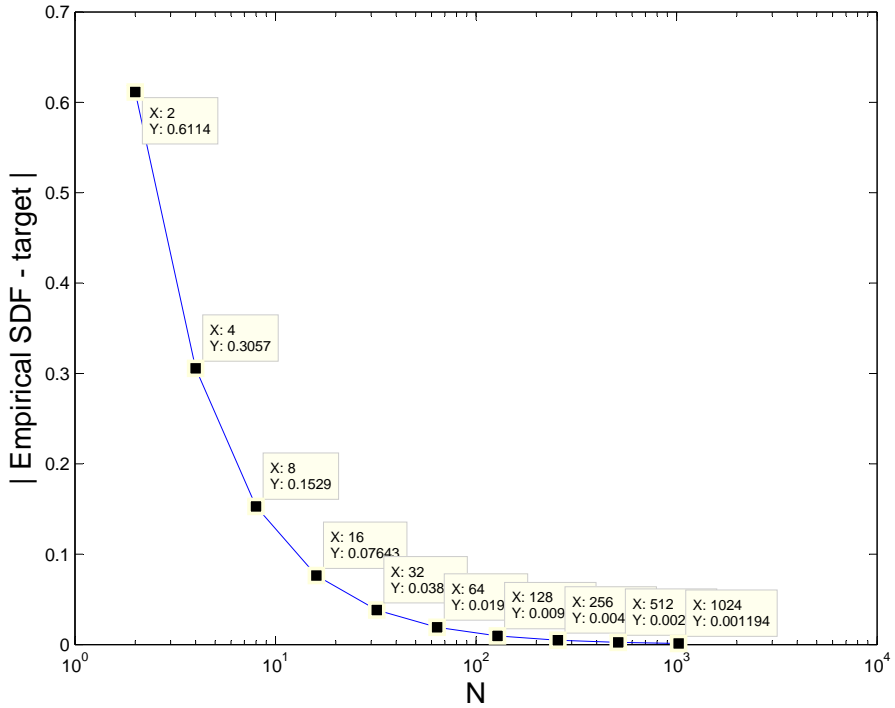


Figure 6.11: Triangular spectrum, difference between the “empirical spectrum” computed as in Fig. 6.6 and the target for different values of N . The absolute value of the difference is constant, as shown by Figs. 6.9–6.10 and it decreases as N increases (i.e. as $\Delta\kappa$ decreases).

6.7.2 Parabolic Spectrum

Consider now the following parabolic target spectrum:

$$N = 2 \quad (6.42)$$

$$\kappa_u = 6 \quad (6.43)$$

$$\Delta\kappa = \frac{\kappa_u}{N} = 3 \quad (6.44)$$

$$M = 2N = 4 \quad (6.45)$$

$$m = 3 \quad (6.46)$$

$$S_{rr}^0(\kappa) = 2\kappa - 2\frac{\kappa^2}{\kappa_u} \quad \forall r \in [1, m] \quad (6.47)$$

$$\gamma_{rs}^0(\kappa) = 0.4 \quad \forall r \in [2, m]; s \in [1, r-1] \quad (6.48)$$

Figures 6.12 and 6.13 represent the actual CSDM of the produced samples for $N = 2$ and $N = 64$, respectively. In this case (see Figs. 6.14–6.15) the difference between the target and the empirical spectrum is linear because the derivatives of the SDF's are linear.

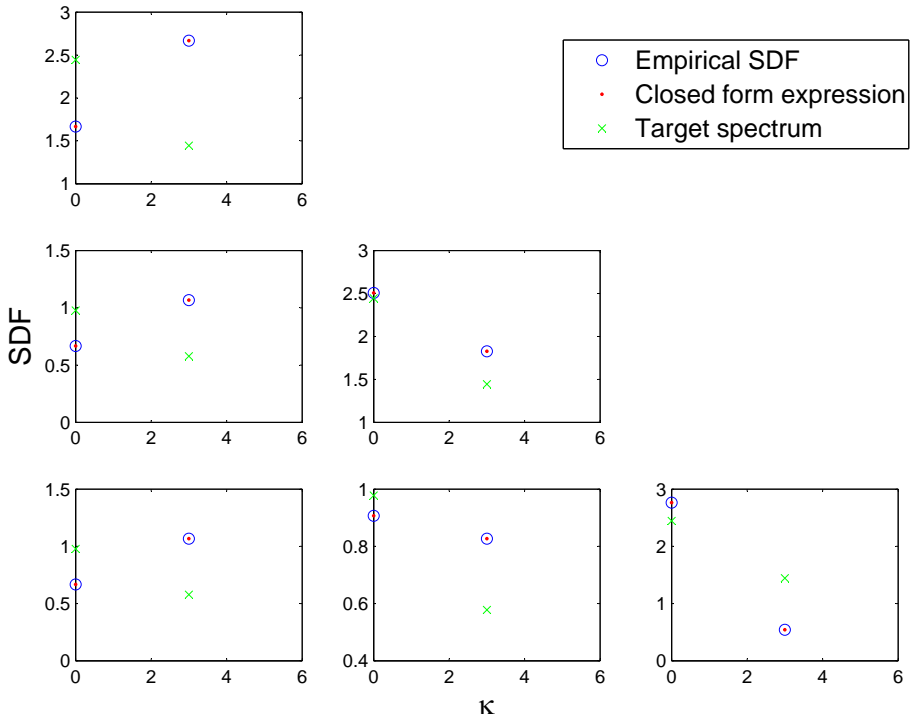


Figure 6.12: Parabolic spectrum, cross-spectral density matrix. The “Empirical SDF” has been computed applying Eq. (6.19) to one produced sample; the “Closed form expression” represents the results of Eq. (6.26) or Eqs. (6.27)–(6.28); the “Target spectrum” is the input given to the simulation algorithm. The values are computed at intervals of width $\Delta\kappa$ and N is equal to 2.

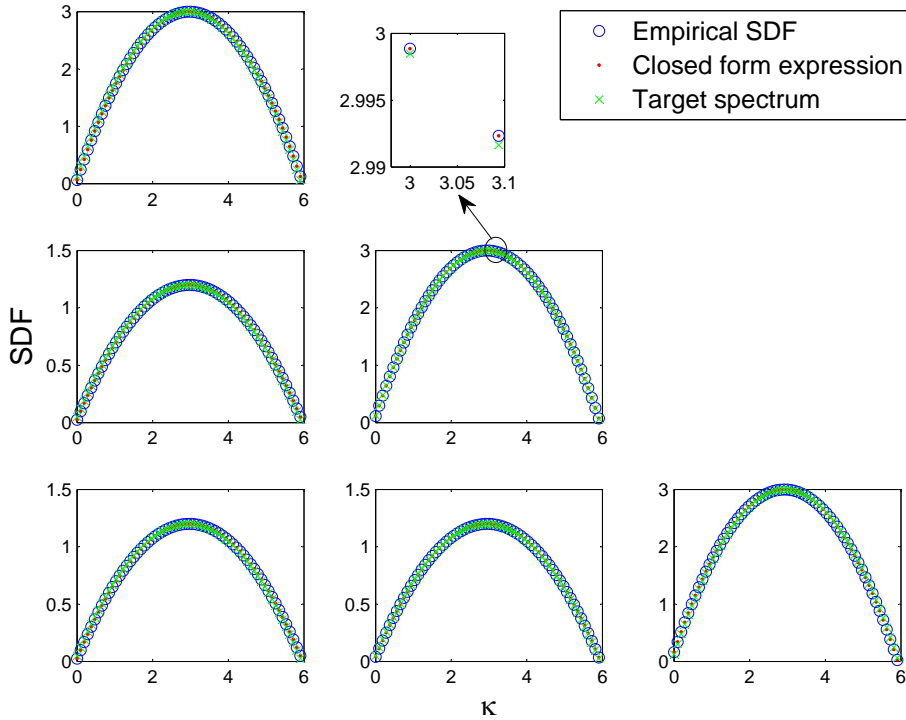


Figure 6.13: Parabolic spectrum, cross-spectral density matrix. The “Empirical SDF” has been computed applying Eq. (6.19) to one produced sample; the “Closed form expression” represents the results of Eq. (6.26) or Eqs. (6.27)–(6.28); the “Target spectrum” is the input given to the simulation algorithm. The values are computed at intervals of width $\Delta\kappa$ and N is equal to 64.

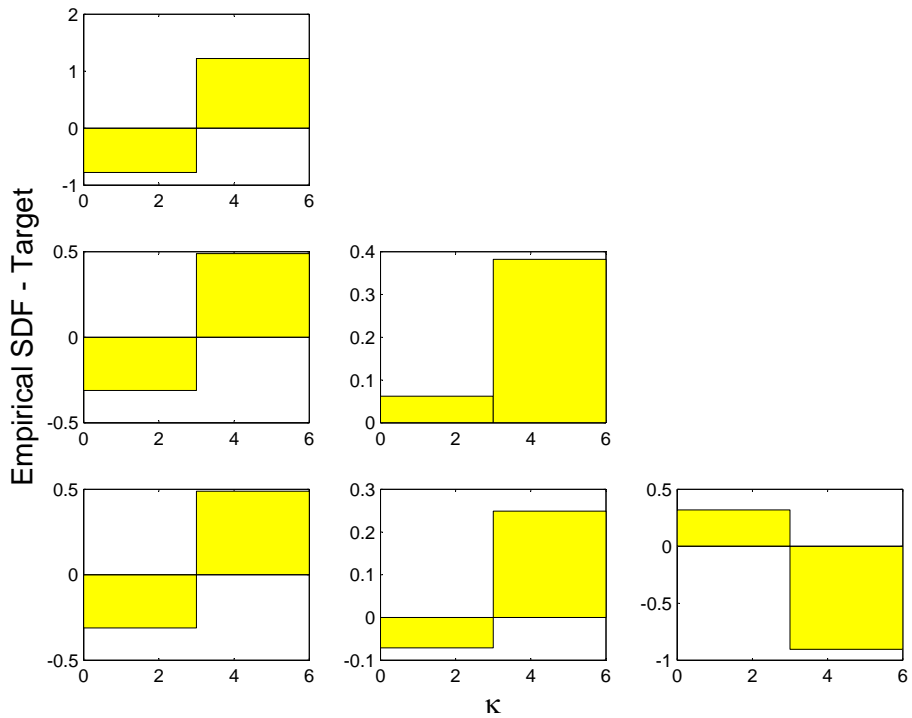


Figure 6.14: Parabolic spectrum, difference between the “empirical spectrum” computed as in Fig. 6.12 and the target. N has been set equal to 2. Note that in this case the difference appears a constant function because only 2 values are available. Its nature of linear function is clearly represented in Fig. 6.15.

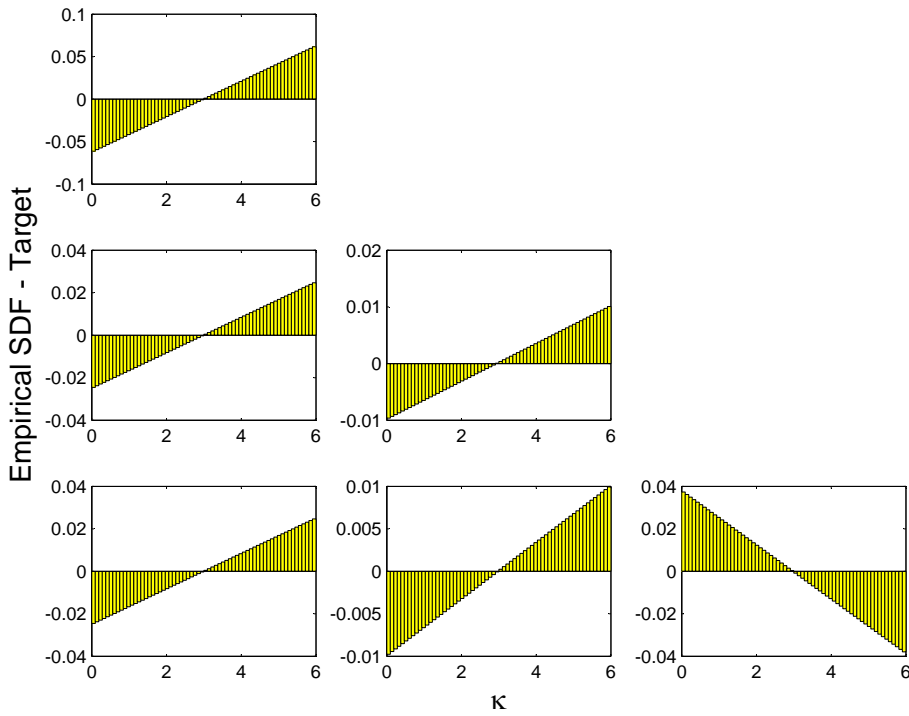


Figure 6.15: Parabolic spectrum, difference between the “empirical spectrum” computed as in Fig. 6.6 and the target. N has been set equal to 64. The difference is a linear function, because the derivatives of the SDF’s are linear.

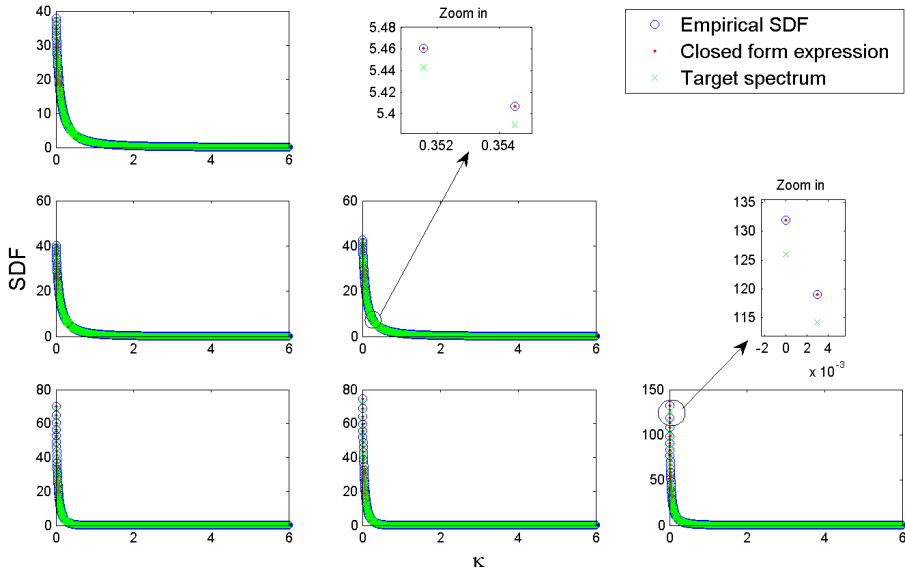


Figure 6.16: Kaimal spectrum, cross-spectral density matrix. The “Empirical SDF” has been computed applying Eq. (6.19) to one produced sample; the “Closed form expression” represents the results of Eq. (6.26) or Eqs. (6.27)–(6.28); the “Target spectrum” is the input given to the simulation algorithm. The values are computed at intervals of width $\Delta\kappa$ and N is equal to 2048.

6.7.3 Kaimal Spectrum

Finally, consider the same Kaimal spectrum with Davenport coherence used by Deodatis (1996). With the number of intervals used in that paper $N = 2048$, the difference between the target and the empirical spectrum is very small but not zero (Fig. 6.16).

Also in this case the closed form Eq. (6.26) –or Eqs. (6.27)–(6.28)– describes perfectly the resulting CSDM.

6.8 Concluding Remarks

When the Spectral Representation Method is used together with the Frequency Double Indexing technique to produce multi-variate ergodic Gaussian samples, the Cross-Spectral Density Matrix of the results do not match exactly the target. The difference is generally small, and can be easily reduced increasing the number of intervals N (i.e. reducing their width $\Delta\kappa$).

A closed form expression that allows to compute a priori the actual CSDM of the produced samples has been provided. This can be also considered a generalization of the proof of ergodicity, that in this way is valid also for finite $\Delta\kappa$.

A possible development could be the inversion (analytical or numerical) of the closed form Eq. (6.26) to compute the CSDM that has to be given as input to the algorithm to obtain exactly the desired empirical CSDM.

Chapter 7

Applications to Civil Engineering

*When a rule is extremely complex,
that which conforms to it passes for random.
-Gottfried Leibniz-*

Sommario. *Nei Capitoli precedenti sono stati mostrati diversi esempi numerici, ma nessuna applicazione diretta all'ingegneria civile. In questo Capitolo vengono invece presentate due applicazioni sulle quali si sta già lavorando ed altri possibili campi d'impiego futuri.*

La prima applicazione riguarda la geomeccanica stocastica. Le proprietà meccaniche dei suoli, infatti, sono caratterizzate da coefficienti di variazione enormi, se confrontati con le proprietà degli altri materiali per l'ingegneria civile. La variabilità, quindi, è tale da causare comportamenti che spesso divergono non solo negli aspetti quantitativi, ma anche in quelli qualitativi da ciò che viene descritto dai modelli deterministici. Per tale motivo, il comportamento reale può essere colto solo da un'analisi probabilistica basata sulla simulazione. Numerosi studi hanno investigato problemi di questo tipo che sfociano nel raggiungimento di uno stato limite da parte del suolo. Meno attenzione, invece, è stata rivolta all'effetto che tale variabilità

dei suoli può indurre sulle costruzioni, attraverso i cedimenti differenziali. La prima applicazione concreta dei metodi presentati nei Capitoli precedenti è, quindi, lo studio di questo tipo di problemi.

Il secondo settore di utilizzo è l'affidabilità strutturale. In particolare, sono disponibili dati sullo stato di conservazione dei cavi principali del ponte di Williamsburg a New York alla fine degli anni Ottanta. Si vuole ora utilizzare tali dati insieme ad un modello di corrosione per simulare lo stato di conservazione attuale e programmare gli interventi di manutenzione. Anche in questo contesto, lo studio può essere condotto solo con un approccio probabilistico e, in particolare, si vuole fare uso delle tecniche di simulazione presentate in precedenza.

Altre possibili applicazioni vengono ipotizzate nel Paragrafo conclusivo.

7.1 Introductory Remarks

In the previous Chapters, some numerical examples have been presented. However, none of them is directly related to a specific practical application. In this Chapter some relevant civil engineering problems in which the proposed techniques have already been applied or could be applied in the future are briefly introduced.

The first is an application to stochastic geomechanics, aimed to the investigation of the possible effects on the structures of soil random variability. The second application involves the reliability assessment of suspended bridges. In both these case, a preliminary part is completed and now the generation of samples for the simulation should start. Finally, some new ideas and interests in different fields will be presented.

7.2 Stochastic Geomechanics

The coefficients of variation of soil properties are extremely larger than those relative to the other structural engineering materials. In fact, in this case there are series of uncertainties arising from several sources: statistical errors (because of the usually small sample sizes), measurement errors, uncertainties in

transforming the index soil properties obtained from soil tests into desired mechanical properties and, most of all, the inherent random heterogeneity (also referred to as “spatial variability”).

For this reason, in the last decades a series of papers appeared in the literature analyzing the effects of the random soil variability on the failure due to insufficient bearing capacity (e.g. Griffiths and Fenton, 2001; Fenton and Griffiths, 2003; Popescu, Deodatis and Nobahar, 2005), slope instability (e.g. Griffiths and Fenton, 2004) and soil liquefaction (e.g. Ohtomo and Shinozuka, 1990; Popescu et al., 1997; Fenton and Vanmarcke, 1998; Koutsourelakis et al., 2002; Popescu, Prevost and Deodatis, 2005). The most widely used approach for this kind of problems is Monte Carlo Simulation. In fact, the strong non-linearity of the deterministic model and the very large coefficients of variation make any other possible probabilistic technique very inaccurate. All the studies concluded that considering the inherent variability of soil properties the attainment of a limit state is extremely more probable than in the case of a uniform soil deposit with the same mean properties.

All the aforementioned papers analyze the soil crisis. Other authors have studied the settlements caused by the inherent heterogeneity (e.g. Paice et al., 1996; Fenton and Griffiths, 2002). Usually the structure is modeled as a rigid body, and even in the cases in which the foundation is a flexible strip, the effects on the structure are not analyzed. Actually, the random variability of the soil properties causes differential settlements that induce stresses in the structures. Therefore, significantly before the soil crisis, the soil heterogeneity can cause the attainment of a limit state in the structure. These kind of problems require expertise in many fields (geomechanics, structural engineering, probability, computational mechanics) and, to the author’s knowledge, have not been studied thoroughly yet.

The main goal that has required the development of the methods presented in the previous Chapters is exactly the analysis of the effects on the structures of the soil variability. In fact, empirical data show that the mechanical soil properties have to be modeled as non-Gaussian, multi-variate, multi-dimensional random fields.

The deterministic analyses will be performed using the non-linear finite element code Dynaflo (Prevost, 2002). Since the software does not ship with a post-processing graphical interface¹, a companion user interface has been written to the purposes of this study (see Figs. 7.1–7.4).

¹The output of Dynaflo is compatible with some third party post-processors, but only

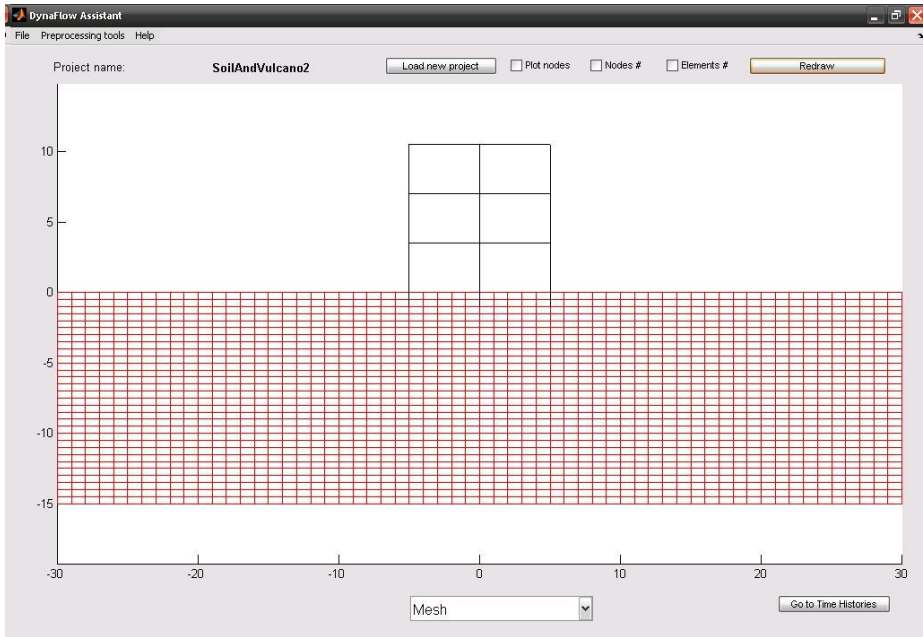


Figure 7.1: Graphical post-processor for Dynaflow. Meshes of the plane frame and of the soil.

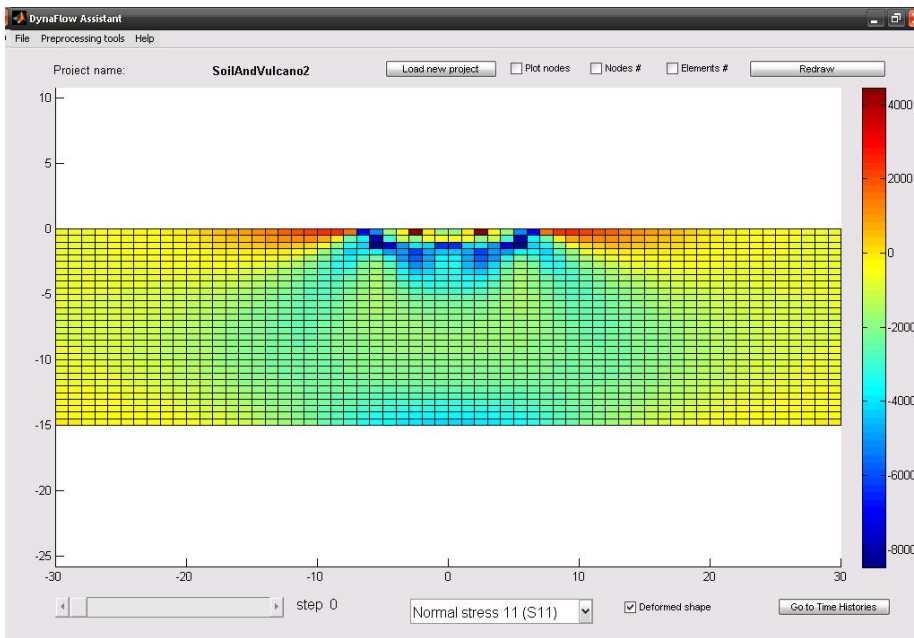


Figure 7.2: Graphical post-processor for Dynaflow. Nominal stresses in the soil at the first step of the non-linear analysis.

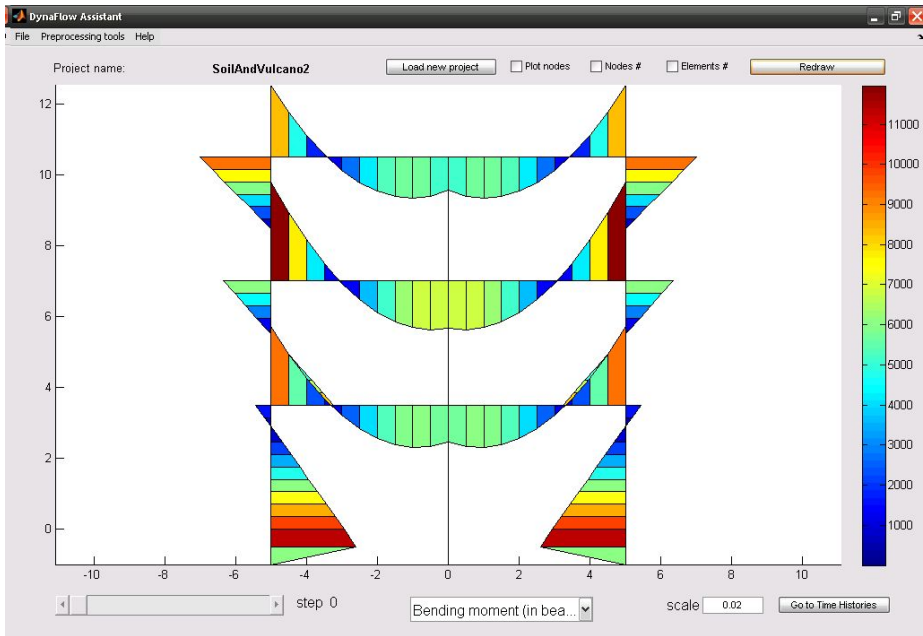


Figure 7.3: Graphical post-processor for Dynaflow. Bending moments in the frame at the first step of the non-linear analysis.

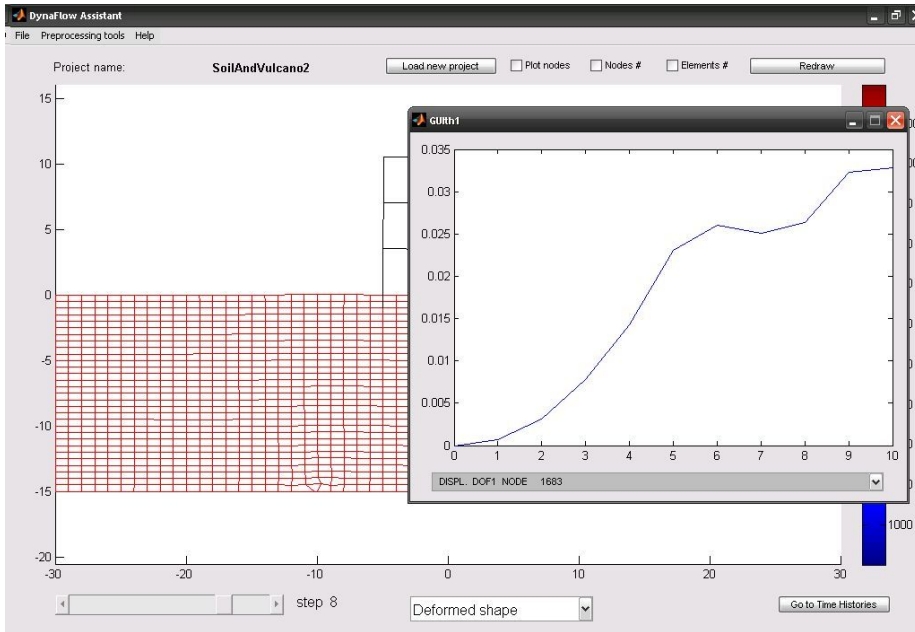


Figure 7.4: Graphical post-processor for Dynaflow. Time history of the displacement of a specific node in the soil.

At the moment, the algorithms for the simulation of the mechanical parameters are complete, the mechanical model and the statistical description of the soil properties will be provided by Prof. Radu Popescu (Memorial University of Newfoundland - Princeton University) and the software for the deterministic analyses with its companion post-processor is available. Hopefully, the Monte Carlo Simulation will start soon.

7.3 Cable-Bridges Reliability

In the late eighties, the commissioners of transportation of the city and state of New York asked to the Civil Engineering and Engineering Mechanics department of Columbia University to coordinate a study aimed to the assessment of the structural reliability of the Williamsburg bridge over the East river (Steinman et al., 1988). Over the years the data collected in that occasion have continued to be studied (Matteo et al., 1994; Shi et al., 2007) and are still used for research purposes. Today, the interest focuses on corrosion, and an original corrosion model, based on theoretical considerations, data available in the literature and new experimental results, have been developed by researchers at Columbia University².

Within this framework, the techniques presented in the previous Chapters are used for the testing and the improvement of the available models. In particular, in the previous works only data regarding the strength of the sample wires have been used, even if also data on the ultimate elongation were available. A first analysis consists in the use of both the sets of data to improve the knowledge about the wire condition. An estimation of the autocorrelations and of the cross-correlation (and therefore of the cross-spectral density matrix) along the length in consecutive wire segments and a fitting of marginal distributions for both the variables have been performed. These results will be used for the simulation of random fields representing the characteristics of the wires, aimed to the estimation of the overall strength of the principal cables of the bridge. Taking the minimum value of the strength of a wire over the selected clamping length³ and adding the strength for each wire, the total cable strength can be

one of them is fully supported. For this reason a more versatile (and free of charge) user interface appeared useful.

²The results have not been published yet. The study is done by Mr. Efe Karanci, Prof. Raimondo Betti and Prof. George Deodatis.



Figure 7.5: The Williamsburg Bridge, between Manhattan and Brooklyn, New York City.

estimated. Then the corrosion model will be applied to estimate the amount of area loss by the wires and thus to compute how much strength of the cable is lost due to that amount. The updated cable strength can be used to estimate the structural reliability and to plan the maintenance.

The use of the random fields simulation, together with the corrosion model, allows to assess (in a probabilistic sense) the future conditions of the main cables of a suspension bridge.

7.4 Other Possible Applications

The scientific and technical interest in the analysis and recovery of masonry buildings is increasing. Lately, a procedure for the stochastic characterization of masonry has been proposed by Falsone and Lombardo (2007). Starting from a picture (or a series of pictures) of a wall, the code is able to estimate correlation and distribution of that particular texture. This innovative procedure can produce as output the data that are required by the simulation algorithms as input. Therefore, even if only a small portion of wall is visually accessible, it is possible to reconstruct, in a probabilistic sense, the whole masonry structure. Thus, a Monte Carlo Simulation can be performed to evaluate the structural behavior. Further investigations about the applicability of the proposed techniques in this field will be carried out.

Mechanical and, in particular, aerospace engineering are the fields in which reliability theory is more applied. In the industrial design of an aircraft a huge amount of resources are involved and it is particularly important that the final result is as flawless as possible. For this reason, different kinds of probabilistic analyses are performed during the design process. Monte Carlo Simulation is widely acknowledged as the only truly universal stochastic approach and is used as benchmark for the other techniques. In the case of major projects (as certainly aircrafts are) also the issue of required computational power can

³In a suspension bridge cable, the wrapping of the wires as well as the cable bands cause a clamping effect and therefore induce strong compaction forces inside the cable. These forces generate friction among the cable's parallel wires. For this reason, at the fracture location, the load previously carried by a broken wire is transmitted to the surrounding intact wires that gradually transmit the load back to the broken cable, as it recovers its load-carrying capacity away from the fracture location. Thanks to this mechanism, a broken wire can gradually regain its load-carrying capacity over some distance along the length of the cable. This is the reason why the strength of an individual wire is considered over a limited length ("clamping length"), and not over the entire length of the cable (Steinman et al., 1988).

be easily addressed and overcome, using clusters for parallel computing⁴. A joint research program between the DISTART department of the University of Bologna and an important aerospace company is going to start. In this framework, the application of the techniques presented in the previous Chapters will be proposed. In fact, they appear particularly suitable for this field. First of all, the sample generation is extremely efficient and it is not necessary to repeat the underlying Gaussian field identification every time the aircraft design changes. Moreover, also the codes presented in Chapters 3–5 have been written for parallel computing, so, in case of need, it is possible to take advantage of all the computational power provided by a high performance computing facility. Finally, the versatility of the proposed methods (strongly non-Gaussian, multi-dimensional, multi-variate) makes them suitable for many problems that can arise during the design procedure.

Besides the aforementioned ones, the Monte Carlo Simulation (and therefore the generation of random fields) is applicable to an extremely wide range of practical application.

⁴Note that the parallel implementation of the Monte Carlo Simulation is straightforward

Part II

Structural Identification and Damage Assessment

Chapter 8

Identification of Truss Structures

In theory, there is no difference between theory and practice.

But, in practice, there is.

-Jan L. A. van de Snepscheut-

Sommario. *L'identificazione strutturale è un processo attraverso il quale si determinano a posteriori le caratteristiche di una struttura realizzata ("metodi parametrici") o la funzione di trasferimento del sistema-struttura ("metodi non parametrici"). Per mezzo dei metodi di identificazione, quindi, si possono ricavare utili informazioni, ad esempio, su edifici storici per i quali non si hanno progetti, sullo stato di strutture (anche meccaniche) dopo un certo periodo di utilizzo, sulla presenza, posizione ed entità di eventuali danneggiamenti in alcuni elementi.*

Poiché operano su strutture effettivamente realizzate, i metodi di identificazione più interessanti ed utilizzati sono quelli "non distruttivi". Tali metodi, infatti, consentono di ricavare le informazioni necessarie senza bisogno di portare né la struttura, né una parte di essa ad uno stato limite.

In letteratura si possono trovare numerosi metodi per l'identificazione di ogni tipologia strutturale. In questo Capitolo viene presentato

un metodo di identificazione non distruttivo per valutare la rigidità delle aste di una struttura reticolare. Nel caso in cui la struttura presenti aste danneggiate, queste vengono localizzate e viene stimata la rigidità residua. Si è scelto di utilizzare prove di caricamento statico e misure di dilatazioni per rendere le prove in situ semplici e poco costose. L'algoritmo suggerito opera su strutture piane oppure tridimensionali, isostatiche e iperstatiche.

Liu e Chian (1997) hanno proposto un metodo per l'identificazione parametrica di strutture reticolari basato sull'impiego di sollecitazioni statiche e misure di deformazione. Tali scelte vanno nella direzione di semplificare al massimo le prove in situ e di ridurre il numero di variabili coinvolte nel problema. Infatti, le prove dinamiche coinvolgono anche la matrice delle masse e i parametri di smorzamento e, quindi, aumentano il numero di parametri da stimare rendendo così più complesso il problema. Le risposte statiche, inoltre, riescono a dare maggiori informazioni sulla localizzazione nella determinazione del danno rispetto all'utilizzo di forme modali che, al contrario, sono più adatte a ricavare informazioni globali sulla struttura.

La misura della risposta strutturale in termini di spostamenti nodali consente una trattazione analitica più semplice. Tuttavia, la misura di spostamenti implica sempre la definizione di un sistema di riferimento assoluto che è spesso un'operazione difficile ed onerosa. La misura delle dilatazioni per mezzo di estensimetri, invece, è molto economica e, se si contengono le numerose possibili fonti di piccoli errori, può dare risultati più precisi delle misure di spostamenti.

Il presente approccio generalizza quello proposto da Liu e Chian, applicabile a strutture e sottostrutture piane e staticamente determinate. Innanzitutto, vengono considerate anche le reticolari tridimensionali. Inoltre, per la soluzione di strutture vincolate esternamente in maniera iperstatica, viene proposto un algoritmo iterativo che presenta ottimi livelli di convergenza in tutte le applicazioni empiriche, a prescindere dalla precisione delle ipotesi iniziali sulle rigidità degli elementi strutturali.

Viene, infine, presentata l'applicazione del metodo proposto all'identificazione di sottostrutture.

8.1 Introductory Remarks

The present Chapter introduces a method that belongs to the framework of the non-destructive parametric identification¹. Its objective is to evaluate the mechanical characteristics of the bars that constitute existent truss structures. Many different procedures have been proposed in the literature (see, for example, the survey by Liu and Han, 2003). Most of them use dynamic experimental data (e.g. Hearn and Testa, 1991; Salawu, 1997) because, in general, it is easier to obtain them.

However, for certain types of structures, as truss structures, static data can be obtained even more easily than dynamic ones. Nevertheless, only a few papers deal with structural identification through static tests. Some of the most representative have been written by Sanayei and Onipede (1991); Banan et al. (1994a,b); Sanayei and Saletnik (1996a,b); Hjelmstad and Shin (1997); Di Paola and Bilello (2004). Liu and Chian (1997) presented a method that belongs to this class. Its declared principal goal is to use simple and low-cost tests. For this reason static loads and strain measurements are adopted.

Static loads can be easily applied by means of suspended masses and (in case) pulleys. Moreover, Jenkins et al. (1997) enlightened that the static structural response show significantly higher sensitivity to local damage than natural frequencies in many cases. In fact, the latter are well suited to describe the overall behavior of a structure, rather than local properties. In addition to this, dynamic analysis involves also the mass matrix and the damping parameters, while the static analysis does not, so treating a lower number of uncertainties. Finally, static data can be acquired and managed easily, while dynamic time histories require a more expensive acquisition and a higher computational effort.

The axial strains of truss elements can be easily obtained by means of strain gauges at low cost. Strain measurements have several sources of small errors (as, for example, temperature effects, electronic noise and wrong balancing of the Wheatstone bridge), but they can be managed and controlled, so that static strain can be measured with a higher precision than displacement, thus this approach is preferable (Sanayei and Saletnik, 1996a,b). However, the usual compatible Finite Element Methods (FEMs) use displacements as configuration variables. For this reason, an alternative formulation of the equilibrium equation that takes into account the strains is presented.

¹Part of the scientific results reported in this Chapter have already been presented by Viola and Bocchini (2007).

In the case of large structures, the measurement of the strain in every bar is considered neither realistic nor, often, interesting. For this reason, in many cases, a substructure identification procedure is preferable. In fact, it allows to take into account only the relevant parts of the structure, or the substructures where damages are supposed to be. Moreover, in this way more complex structures can be analyzed splitting them into many parts.

The procedure presented by Liu and Chian (1997), is applicable to externally statically determinate plane structures. The method proposed in this Chapter and the following one generalizes the above mentioned. In fact, first of all it takes into account also three-dimensional structures, and in this way some peculiarities of the approach can be more easily enlightened. Then, a modified iterative algorithm is introduced in order to be applicable to structures with redundant external constrains.

In Chapter 9 two more extensions will be proposed.

8.2 Proposed Methodology

8.2.1 Three-Dimensional Externally Statically Determinate Structures

The equilibrium equation of a bar in a three-dimensional space in the Finite Element Analysis (FEA) is

$$\mathbf{k}_e \boldsymbol{\eta}_e = \mathbf{N}_e \quad (8.1)$$

where \mathbf{k}_e , $\boldsymbol{\eta}_e$ and \mathbf{N}_e are, respectively, the stiffness matrix, the displacement vector and the force vector of the e^{th} element in local coordinates, as represented in Fig. 8.1. In Eq. (8.1) the measured quantities (strains) does not appear; the cinematic behavior is described by the displacements. For this reason, Liu and Chian (1997) proposed a new formulation that is here presented in a revised version and extended to three-dimensional truss structures.

The stiffness matrix is computed using the standard Finite Element Method (FEM) and results as follows:

$$\frac{E_e A_e}{l_e} \begin{bmatrix} 1 & -1 \\ -1 & 1 \end{bmatrix} \begin{bmatrix} \eta_{e1} \\ \eta_{e2} \end{bmatrix} = \begin{bmatrix} N_{e1} \\ N_{e2} \end{bmatrix} \quad (8.2)$$

being E_e , A_e and l_e the Young's modulus, the cross-sectional area and the length of the e^{th} bar, respectively. The product $E_e A_e$ is the objective of the estimation

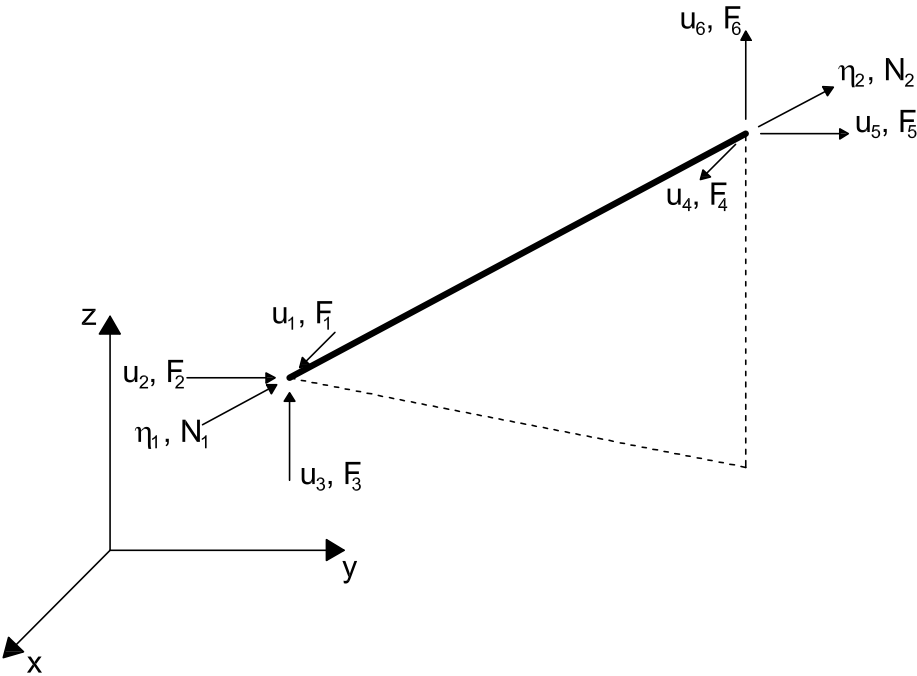


Figure 8.1: Bar in a three-dimensional reference system: vectors.

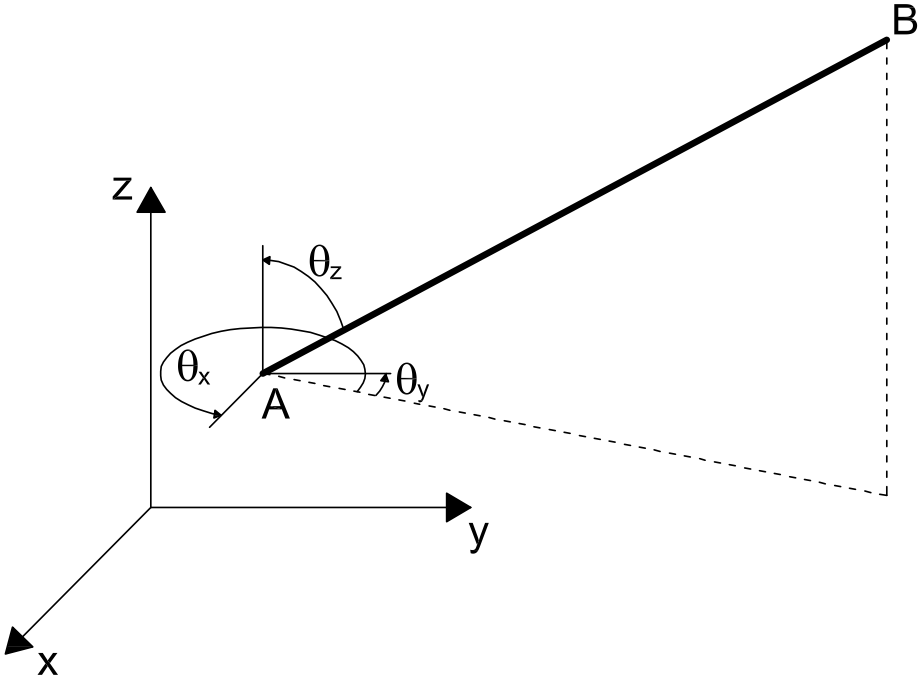


Figure 8.2: Bar in a three-dimensional reference system: angles.

procedure and, in the remainder, it is represented by α_e and called “element stiffness”. In order to express the equilibrium equation in global coordinates, a three-dimensional rotation matrix \mathbf{R}_e is used

$$\frac{\alpha_e}{l_e} \mathbf{R}_e^T \begin{bmatrix} 1 & -1 \\ -1 & 1 \end{bmatrix} \boldsymbol{\eta}_e = \mathbf{R}_e^T \mathbf{N}_e \quad (8.3)$$

where

$$\mathbf{R}_e = \begin{bmatrix} \cos \theta_{ex} & \cos \theta_{ey} & \cos \theta_{ez} & 0 & 0 & 0 \\ 0 & 0 & 0 & \cos \theta_{ex} & \cos \theta_{ey} & \cos \theta_{ez} \end{bmatrix} \quad (8.4)$$

with θ_{ex} , θ_{ey} and θ_{ez} measured as reported in Fig. 8.2. In global coordinates,

the force vector is expressed by $\mathbf{F}_e = \mathbf{R}_e^T \mathbf{N}_e$, thus

$$\frac{\alpha_e}{l_e} \mathbf{R}_e^T \begin{bmatrix} 1 & -1 \\ -1 & 1 \end{bmatrix} \boldsymbol{\eta}_e = \mathbf{F}_e \quad (8.5)$$

Each row of the connectivity matrix \mathbf{L}_e ($n \times 6$) is related to a degree of freedom (DOF) of the global truss structure (n DOF's) and each column represents one DOF of the e^{th} element (6 DOFs in a three-dimensional space). The correspondence between local and global DOFs is represented by "ones" in the intersection of the rows and of the columns belonging to homologous DOF's. For example, if the DOF's of the e^{th} element correspond to the DOF's 1,2,3,7,8 and 9 of a structure, \mathbf{L}_e results in:

$$\mathbf{L}_e = \begin{bmatrix} 1 & 0 & 0 & 0 & 0 & 0 \\ 0 & 1 & 0 & 0 & 0 & 0 \\ 0 & 0 & 1 & 0 & 0 & 0 \\ 0 & 0 & 0 & 0 & 0 & 0 \\ 0 & 0 & 0 & 0 & 0 & 0 \\ 0 & 0 & 0 & 0 & 0 & 0 \\ 0 & 0 & 0 & 1 & 0 & 0 \\ 0 & 0 & 0 & 0 & 1 & 0 \\ 0 & 0 & 0 & 0 & 0 & 1 \\ 0 & 0 & 0 & 0 & 0 & 0 \\ \vdots & \vdots & \vdots & \vdots & \vdots & \vdots \\ 0 & 0 & 0 & 0 & 0 & 0 \end{bmatrix} \quad (8.6)$$

The connectivity matrix and the assembly procedure allow to take into account the m elements of the overall structure:

$$\frac{\alpha_e}{l_e} \mathbf{L}_e \mathbf{R}_e^T \begin{bmatrix} 1 & -1 \\ -1 & 1 \end{bmatrix} \boldsymbol{\eta}_e = \mathbf{L}_e \mathbf{F}_e \quad (8.7)$$

$$\sum_{e=1}^m \frac{\alpha_e}{l_e} \mathbf{L}_e \mathbf{R}_e^T \begin{bmatrix} 1 & -1 \\ -1 & 1 \end{bmatrix} \boldsymbol{\eta}_e = \mathbf{F} \quad (8.8)$$

being $\mathbf{F} = \sum_{e=1}^m \mathbf{L}_e \mathbf{F}_e$ the complete vector of loads applied to the structure (external loads and constrains reactions).

In order to put in evidence the measured strains, the equilibrium Eq. (8.8) is restated as

$$\sum_{e=1}^m \frac{\alpha_e}{l_e} \mathbf{L}_e \mathbf{R}_e^T \begin{bmatrix} -1 \\ 1 \end{bmatrix} \begin{bmatrix} -1 & 1 \end{bmatrix} \boldsymbol{\eta}_e = \mathbf{F} \quad (8.9)$$

$$\sum_{e=1}^m \frac{\alpha_e}{l_e} \mathbf{L}_e \mathbf{R}_e^T \begin{bmatrix} -1 \\ 1 \end{bmatrix} \begin{bmatrix} -1 & 1 \end{bmatrix} \begin{bmatrix} \eta_{e1} \\ \eta_{e2} \end{bmatrix} = \mathbf{F} \quad (8.10)$$

$$\sum_{e=1}^m \frac{\alpha_e}{l_e} \mathbf{L}_e \mathbf{R}_e^T \begin{bmatrix} -1 \\ 1 \end{bmatrix} (-\eta_{e1} + \eta_{e2}) = \mathbf{F} \quad (8.11)$$

$$\sum_{e=1}^m \alpha_e \mathbf{L}_e \mathbf{R}_e^T \begin{bmatrix} -1 \\ 1 \end{bmatrix} \frac{\eta_{e2} - \eta_{e1}}{l_e} = \mathbf{F} \quad (8.12)$$

In Eq. (8.12) it is easy to recognize $\frac{\eta_{e2} - \eta_{e1}}{l_e} = \varepsilon_e$, the axial dilatation of the e^{th} bar:

$$\sum_{e=1}^m \alpha_e \mathbf{L}_e \mathbf{R}_e^T \begin{bmatrix} -1 \\ 1 \end{bmatrix} \varepsilon_e = \mathbf{F} \quad (8.13)$$

Equation (8.13) shows the explicit relationship between the unknowns of the analysis α_e , the measured quantities ε_e and the external loads \mathbf{F} .

The geometrical data of the problem are condensed in the vector \mathbf{I}_e :

$$\mathbf{I}_e = \mathbf{L}_e \mathbf{R}_e^T \begin{bmatrix} -1 \\ 1 \end{bmatrix} = \mathbf{L}_e \begin{bmatrix} \cos \theta_{ex} & 0 \\ \cos \theta_{ey} & 0 \\ \cos \theta_{ez} & 0 \\ 0 & \cos \theta_{ex} \\ 0 & \cos \theta_{ey} \\ 0 & \cos \theta_{ez} \end{bmatrix} \begin{bmatrix} -1 \\ 1 \end{bmatrix} = \mathbf{L}_e \begin{bmatrix} -\cos \theta_{ex} \\ -\cos \theta_{ey} \\ -\cos \theta_{ez} \\ \cos \theta_{ex} \\ \cos \theta_{ey} \\ \cos \theta_{ez} \end{bmatrix} \quad (8.14)$$

and the equilibrium equation is rewritten as

$$\sum_{e=1}^m \alpha_e \varepsilon_e \mathbf{I}_e = \mathbf{F} \quad (8.15)$$

The vector \mathbf{S} of the unknown stiffnesses and the matrix \mathbf{P} are defined as

$$\begin{aligned} \mathbf{S} &= [\alpha_1 \quad \alpha_2 \quad \cdots \quad \alpha_m]^T \\ \mathbf{P} &= [\varepsilon_1 \mathbf{I}_1 \quad \varepsilon_2 \mathbf{I}_2 \quad \cdots \quad \varepsilon_m \mathbf{I}_m] \end{aligned} \quad (8.16)$$

This way, the sum expressed in Eq. (8.15) can be replaced by the matrix product

$$\mathbf{PS} = \mathbf{F} \quad (8.17)$$

where $\mathbf{P}(\varepsilon_e)$ is a function of the measured strains, $\mathbf{S}(\alpha_e)$ is a function of the unknown stiffnesses and \mathbf{F} collects external loads.

In this way, the identification problem has been reduced to the optimization of Eq. (8.17). The least square method is adopted as solution technique, therefore, the “error function” to minimize is:

$$E = \sum_{k=1}^K |\mathbf{P}_k \mathbf{S} - \mathbf{F}_k|^2 \quad (8.18)$$

where K is the number of loading tests, and the subscript k identifies the k^{th} loading test. It is worth noticing that the formulation in Eq. (8.18) does not require to solve the equilibrium equation. Moreover, it can be proved that the solution of the minimization problem is unique. In fact, the stationarity of the error is given by

$$\begin{aligned} \frac{dE}{d\mathbf{S}} &= \sum_{k=1}^K \frac{d}{d\mathbf{S}} (\mathbf{S}^T \mathbf{P}_k^T \mathbf{P}_k \mathbf{S} - \mathbf{S}^T \mathbf{P}_k^T \mathbf{F}_k - \mathbf{F}_k^T \mathbf{P}_k \mathbf{S} + \mathbf{F}_k^T \mathbf{F}_k) = \\ &= \sum_{k=1}^K \frac{d}{d\mathbf{S}} (\mathbf{S}^T \mathbf{P}_k^T \mathbf{P}_k \mathbf{S} - 2\mathbf{S}^T \mathbf{P}_k^T \mathbf{F}_k + \mathbf{F}_k^T \mathbf{F}_k) = \\ &= \sum_{k=1}^K 2\mathbf{P}_k^T \mathbf{P}_k \mathbf{S} - 2\mathbf{P}_k^T \mathbf{F}_k = 0 \end{aligned} \quad (8.19)$$

therefore

$$\sum_{k=1}^K 2\mathbf{P}_k^T \mathbf{P}_k \mathbf{S} = \sum_{k=1}^K 2\mathbf{P}_k^T \mathbf{F}_k \quad (8.20)$$

$$\sum_{k=1}^K \mathbf{P}_k^T \mathbf{P}_k \mathbf{S} = \sum_{k=1}^K \mathbf{P}_k^T \mathbf{F}_k \quad (8.21)$$

$$\mathbf{H} \mathbf{S} = \mathbf{R} \quad (8.22)$$

where matrix \mathbf{H} and vector \mathbf{R} are defined as

$$\mathbf{H} = \sum_{k=1}^K \mathbf{P}_k^T \mathbf{P}_k; \quad \mathbf{R} = \sum_{k=1}^K \mathbf{P}_k^T \mathbf{F}_k \quad (8.23)$$

If \mathbf{H} is non-singular, then Eq. (8.22) can be directly solved for the vector of the unknowns \mathbf{S} .

To verify that the point of stationary corresponds to a minimum, it can be observed that the function in Eq. (8.18) is a sum of quadratic terms, thus it is a convex quadratic function. Otherwise, the Hessian matrix can be computed:

$$\begin{aligned} \frac{d^2 E}{d\mathbf{S}^2} &= \frac{d}{d\mathbf{S}} \frac{dE}{d\mathbf{S}} = \\ &= \sum_{k=1}^K \frac{d}{d\mathbf{S}} 2\mathbf{P}_k^T \mathbf{P}_k \mathbf{S} - 2\mathbf{P}_k^T \mathbf{F}_k = \\ &= \sum_{k=1}^K 2\mathbf{P}_k^T \mathbf{P}_k = 2\mathbf{H} \end{aligned} \quad (8.24)$$

Therefore, the Hessian matrix has the same sign of the constant matrix \mathbf{H} . This matrix is positive semidefinite, in fact

$$\mathbf{x}^T \mathbf{H} \mathbf{x} = \sum_{k=1}^K \mathbf{x}^T \mathbf{P}_k^T \mathbf{P}_k \mathbf{x} = \sum_{k=1}^K |\mathbf{P}_k \mathbf{x}|^2 \geq 0 \quad \forall \mathbf{x} \quad (8.25)$$

Moreover Eq. (8.25) shows that the Hessian is positive definite if \mathbf{H} is non-singular. From these considerations, it appears evident that the rank of matrix \mathbf{H} is of utmost importance. First of all, it guarantees a unique solution. Moreover, this kind of problems are solved using quadratic programming (see, for example, Shapiro, 1979; Strang, 1986) or polynomial regression methods (Wang et al., 2005). In quadratic programming it is proved (and intuitive) that if the Hessian of the objective function is positive definite, then the solution is a global minimum. A deeper analysis of this topic will be presented in Sec. 8.4.1.

8.2.2 Externally redundant structures

The solution of the problem consists in the minimization of Eq. (8.17) or, that is the same, in the solution of the system in Eq. (8.22). In the first case, the right-hand vector is \mathbf{F} and in the latter it is a function of \mathbf{F} , in fact $\mathbf{R} = \mathbf{R}(\mathbf{F})$. Therefore, a condition for the direct solution of the problem is to know all the elements of vector \mathbf{F} . Actually, \mathbf{F} collects all the loads applied to the structure. In the case of small displacements (according to the use of a non-destructive technique) the superimposition principle is applicable. Thus, the measured strains depend only on the loads applied for the test. However, the constrains reactions are still unknown. In the case of externally statically determinate structures,

reactions can be computed using only the equilibrium equations. On the contrary, in the case of externally redundant structures, a set of strain-compatibility equations is required. However, the element stiffnesses are still unknown (they are the object of the identification procedure), therefore compatibility equations can not be solved.

The bottom line is that in the case of externally redundant structures some elements of vector \mathbf{F} are unknown. To overcome this issue, a procedure based on the iterative scheme represented in Fig. 8.3 is proposed.

The inputs of the algorithm are the geometrical description of the structure, the constraints, the applied loads and a starting value for the stiffnesses. It should be noticed that a rough estimation, obtained by multiplying the approximate cross sectional area by the average Young modulus of the material is more than sufficient, as it will be shown in Sec. 8.4. Moreover, the code requires the data on the strains.

Then the algorithm computes the constraint reactions through a FEA, using the assumed stiffnesses. Since the stiffnesses are not the real ones, also the value of the reactions will not be accurate.

The vector of external forces \mathbf{F} can now be updated using the reactions. In this way, the identification procedure can estimate a new set of stiffnesses (as in Sec. 8.2.1) that, in general, is different from the one used for the computation of the external reactions.

The algorithm proceeds updating alternately stiffnesses and constrain reactions until convergence is met.

8.3 Substructure Identification

In the case of large structures, the measurement of every strain is usually neither possible, nor interesting. In fact, the structure can be damaged only in a small portion. Otherwise, the tester might prefer to divide the whole structure into many parts, owing to reduce the number of contemporary measurements. Therefore, in both these cases, a substructure identification procedure is more suitable.

First of all “internal” and “external” elements must be recognized. Internal bars are the ones where strain gauges are applied and internal nodes are the ones that connects only internal bars. External bars are the ones without strain indicators and external nodes are the ones that belong to at least one external

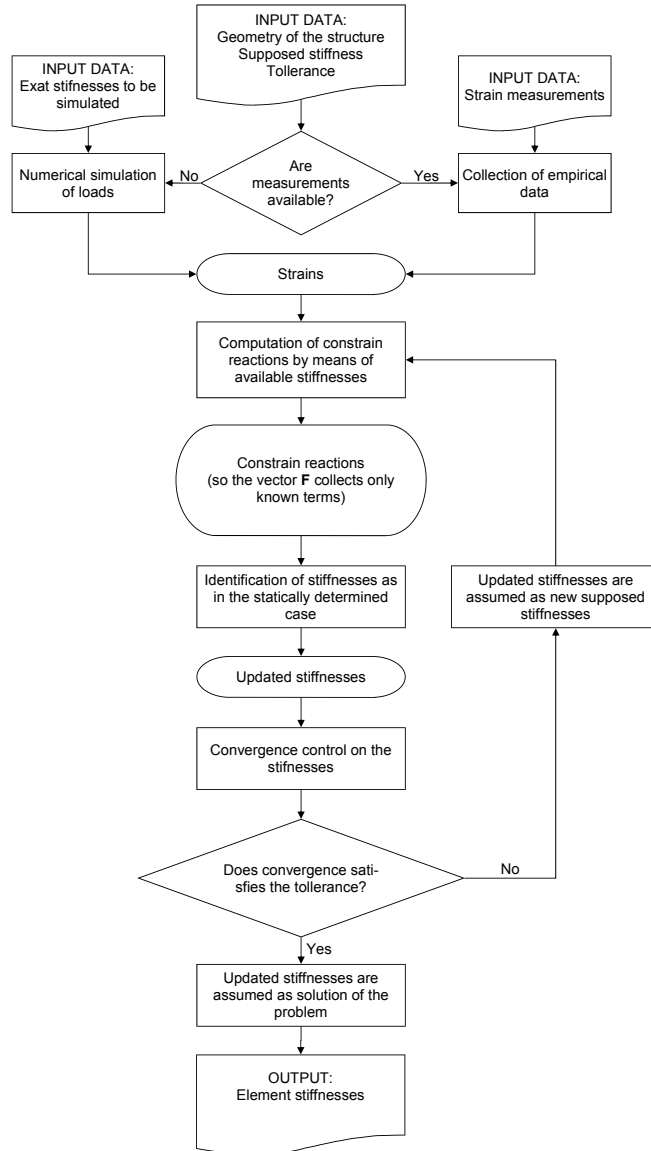


Figure 8.3: Flow chart of the proposed iterative procedure.

bar.

Then, Eq. (8.18) can be restated referring to internal (denoted by the superscript “ i ”) elements

$$E^i = \sum_{k=1}^K |\mathbf{P}_k^{ii} \mathbf{S}^i - \mathbf{F}_k^i|^2 \quad (8.26)$$

where E^i is the new error function, \mathbf{P}_k^{ii} is defined as in Eq. (8.16), but considering only internal nodes and bars, \mathbf{S}^i are the stiffnesses of internal bars, \mathbf{F}_k^i are the external forces (loads and constrain reactions) applied to internal nodes.

From here onward, the procedure continues as explained in Secs. 8.2.1 or 8.2.2, depending on the external constraints.

Some further remarks are necessary. First, this technique is not able, in any case, to identify the stiffness of an element whose nodes are both external. In this case, in fact, the column of \mathbf{P}_k^{ii} corresponding to that element is composed by zeros, because the rows of the matrix \mathbf{L} corresponding to the internal nodes are full of zeros. This can be seen also considering that this element is involved in none of the equations that computes the residual forces in the internal nodes. Therefore E^i is independent on the stiffness of such an element, thus its minimization gives no information at all on this element.

Secondly, it should be noticed that in the case of externally redundant structures, the FEA requires to know the stiffness of all the elements of the structure, not only of the internal elements. Therefore, to use this approach, an approximate value for the stiffness of external bars is required. If a main structure is analyzed dividing it into substructures, the identification procedure has to be repeated alternately on the different substructures, until convergence is met.

Third, obviously, in every load condition, at least one external force (including loads and reactions) has to be applied to one internal node. Otherwise, only the trivial solution can be obtained for the vector \mathbf{S} relative to that load test.

Finally, it is worth noticing that in the case of substructure identification, the equilibrium is imposed only in the internal nodes. So, each load condition allows to write only a few equilibrium equations, in a few nodes. However, this problem can be easily avoided studying convex substructures. In fact, in this way the number of internal nodes is maximum, for a fixed number of internal elements.

8.4 Numerical Examples and Remarks

Three numerical simulations of applications to real structures of the proposed methodology are presented in this Section. Each of them is also used to enlighten a particular aspect of the technique.

8.4.1 Minimum number of load conditions

As already mentioned in Section 8.2.1, loading tests must be designed owing to obtain a non-singular \mathbf{H} matrix. Sanayei and Onipede (1991) analyzed the minimum number of independent measurements for a method similar to the one here presented. They also stated it as a function of the number of loads and measurements. Liu and Chian (1997) studied the rank of \mathbf{H} in order to obtain a more complete information on the more effective and convenient set of loads.

\mathbf{H} is a square matrix, its rank depend on the rank of \mathbf{P}_k and in the case of only one load condition it is

$$\text{rank}(\mathbf{H}) = \text{rank}(\mathbf{P}_1^T \mathbf{P}_1) = \text{rank}(\mathbf{P}_1) \leq (m - n_i) \quad (8.27)$$

being m the number of bars and n_i the degree of internal redundancy. The rank of \mathbf{H} can be increased adding loads conditions and it can be proved that (Liu and Chian, 1997):

$$\text{rank}(\mathbf{H}) = \text{rank} \begin{bmatrix} \mathbf{P}_1 \\ \mathbf{P}_2 \\ \vdots \\ \mathbf{P}_K \end{bmatrix} \quad (8.28)$$

Therefore, adding load conditions, the rank can become full. However, the most restrictive requirement on the load conditions is that every bar has to reach a “sufficient” stress level, as will be shown by the following numerical example.

The structure represented in Fig. 8.4 is a plane truss, with redundant external constrains. All the bars have the same characteristics, elastic modulus $E = 7 \cdot 10^9 N/m^2$, cross sectional area $A = 10cm^2$, therefore, original stiffness $\alpha = 70MN$. Bars number 5 and 9 are supposed to be damaged, with residual stiffness reduced to $7MN$. Each node has two translational degrees of freedom, so the degrees of freedom of the structure are twelve. Four degrees are constrained, so the actual degrees of freedom are eight. The number of internal redundant bars is two ($n_i = 2$), while the total number of elements is eleven

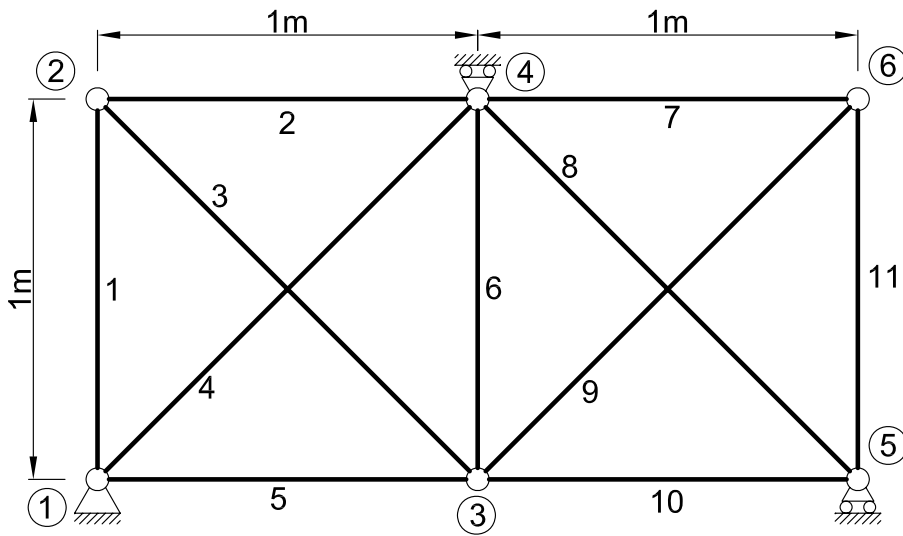


Figure 8.4: Externally redundant plane truss structure.

Bar No.	Load condition	
	1	2
1	25.9	24.3
2	-116.6	24.4
3	-38.4	-33.3
4	158.3	-143.3
5	305.8	-419.7
6	26.3	19.0
7	-0.5	-4.1
8	-4.5	-101.4
9	16.0	71.9
10	1.9	-71.1
11	-1.0	-5.5

Table 8.1: Axial strains (10^{-6}) simulated for the redundant plane truss in Fig. 8.4.

($m = 11$). Recalling Eq. (8.27), it can be concluded that the maximum rank of \mathbf{P}_k is nine, but the unknowns (and therefore the rows of \mathbf{H}) are eleven. Therefore, at least two load conditions are required to obtain a full rank Hessian.

The first load condition is a horizontal force of modulus $10kN$ applied to the node number 2, the second is a horizontal force of modulus $10kN$ applied to the node number 5. Tests are conducted by means of a numerical simulation. A random noise with a uniform probability distribution of amplitude $0.1kN$ has been superimposed to the applied forces, owing to simulate uncertainties in the application of the forces. The response of the structure has been simulated by using a Finite Element Analysis (FEA). Then, a second random noise with a uniform probability distribution of amplitude 10^{-6} has been superimposed to resultant strains with the aim of simulating the actual accuracy of the strain gauges. The results obtained are reported in Table 8.1. Finally, the obtained strains have been used as input data for the statical identification for externally redundant trusses, as explained in Sec. 8.2.2. As already mentioned, the first-step supposed stiffness required by the iterative algorithm presented in Fig. 8.3 may also have a low accuracy. For example, it can be estimated by means of an approximated cross sectional area and of the supposed original elastic modulus. In this case, $\alpha_0 = 60MN$ has been assumed as first-step stiffness for each bar. Notice that it is an inaccurate value for the undamaged bars, and a

Bar No.	Stiffness EA <i>MN</i>
1	69.72
2	69.91
3	69.38
4	70.82
5	6.77
6	69.03
7	71.59
8	72.35
9	6.15
10	67.58
11	58.56

Table 8.2: Stiffnesses estimated for the redundant plane truss in Fig. 8.4.

completely wrong assessment for bars 5 and 9. The results of the identification are reported in Table 8.2 and in Fig. 8.5. The method gives good results both for the intact bars and for the damaged ones. In fact, it estimates the correct original stiffness ($70MN$), even if the first-step stiffness was incorrect. Moreover, it identifies the two damaged bars and evaluates the residual stiffness ($7MN$) with good accuracy. The presented results has a precision comparable with the one obtained by Liu and Chian (1997), but it is worth noticing that in this case the improved procedure is applied to an externally redundant structure.

The estimated value of the stiffness of bar 11 is not accurate. This is due to the fact that bar 11 is significantly loaded in neither of the two considered load tests. This is an example of the fact that the condition on the strain level is usually more restrictive than the analytical condition on the rank of \mathbf{H} . In Sec. 8.5.2 a better estimation of the same structure is presented.

8.4.2 Non-unique solutions

Consider a truss similar to the one previously described, but with different constrains, as represented in Fig. 8.6. In this case nodes 1 and 5 can not move horizontally, therefore the strains of the bars 5 and 10 are correlated by the relationship

$$\varepsilon_5 + \varepsilon_{10} = 0 \quad (8.29)$$

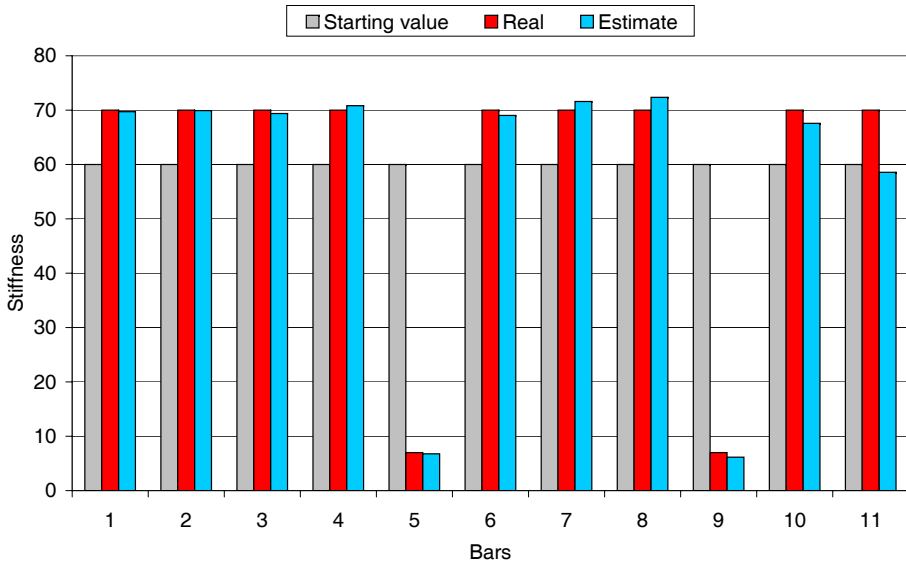


Figure 8.5: Stiffnesses estimated for the redundant plane truss in Fig. 8.4, compared to the starting values of the iterative procedure and to the real values. The accuracy is good for all the bars except bar 11, for which other load tests are required (see Sec. 8.5.2 and Fig. 8.12).

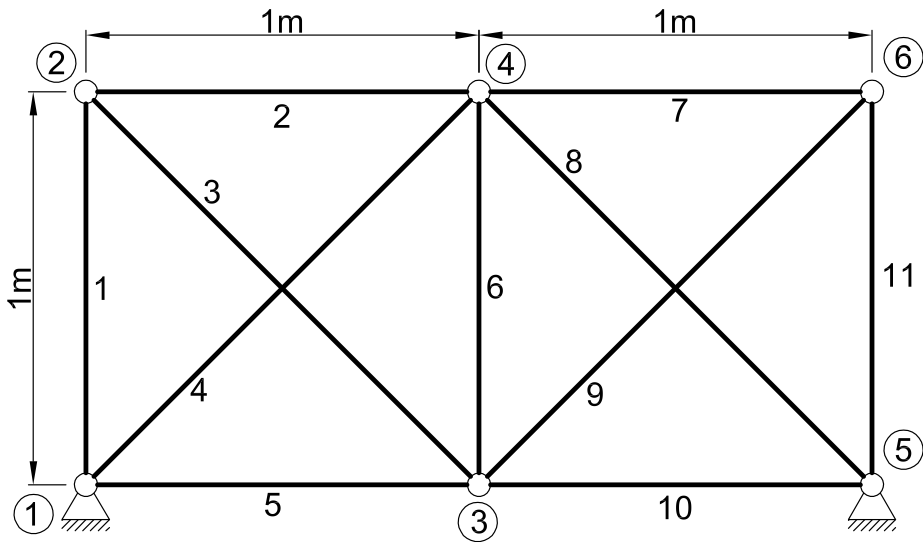


Figure 8.6: Externally redundant plane truss structure.

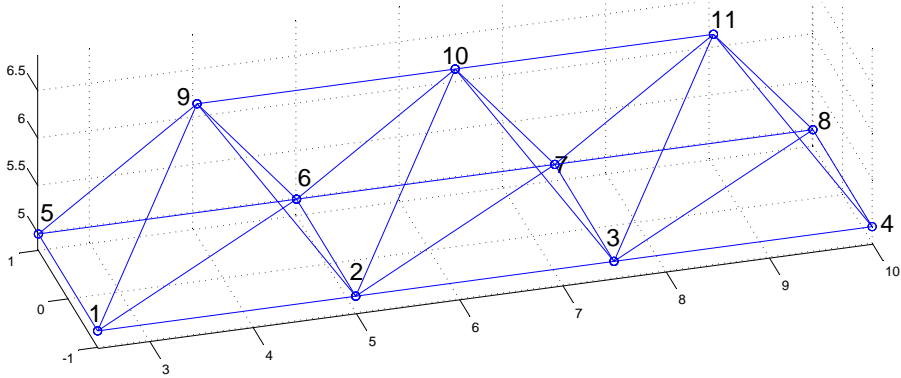


Figure 8.7: Three-dimensional redundant truss structure. The displacements in the x direction are restrained at nodes 1 and 5; the displacements in the y direction are restrained at nodes 1 and 4; the vertical displacements are restrained at nodes 1, 4, 5, 8 and 10.

It means that the two measurements are linearly dependent, thus actually there is a lack of information. It is not possible to distribute the correct stiffness between bars 5 and 10. This example belongs to the well known fields of the “non-unique solution” of inverse problems.

The coefficients of variation related to bars 5 and 10 are 90.7% and 97.6% respectively. This means that any result on the stiffnesses of bars 5 and 10 is meaningless. However, the coefficient of variation of the sum $\alpha_5 + \alpha_{10}$ is 1.5%, almost the same as for other bars. The mean of $\alpha_5 + \alpha_{10}$ is $77.4MN$ that is a very good estimation of the real value ($7 + 70 = 77MN$). Thus, in cases like this one, the proposed procedure is not able to identify the correct stiffness of each bar, but it still gives a good description of the overall behavior and characteristics.

8.4.3 Three-Dimensional Trusses

The algorithm has been applied also to the three-dimensional redundant truss structure represented in Fig. 8.7. The eight longitudinal bars have a product $E_e A_e = 500MN$, while the braces have $E_e A_e = 260MN$. Bars 6–7, 9–10, 3–11

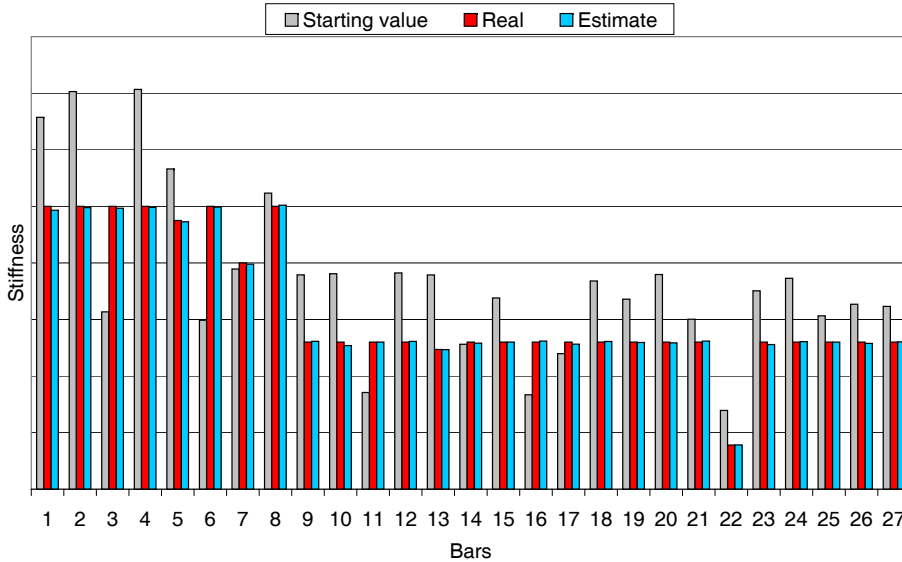


Figure 8.8: Stiffnesses estimated for the redundant three-dimensional truss in Fig. 8.7, compared to the starting values of the iterative procedure and to the real values. The accuracy is good for all the bars.

and 1–6 are damaged and their stiffnesses have been reduced by 5%, 20%, 5% and 70%, respectively.

Vertical test loads have been applied to nodes 2, 9 and 11; horizontal loads in the x direction have been applied to nodes 4, 8 and 11; horizontal loads in the y direction have been applied to nodes 2, 3, 5, 8 and 9. All the forces have a modulus of $100kN$. A random noise, uniformly distributed in the interval $[-1kN, 1kN]$, has been applied to the loads and another one, uniformly distributed in the interval $[-10^{-6}, 10^{-6}]$, has been superimposed to the resulting strains.

The starting value for the stiffnesses have been computed multiplying the real $E_e A_e$ by a random factor uniformly distributed in the interval $[0.5, 1.5]$.

The results are reported in Table 8.3 and in Fig. 8.8, while in Fig. 8.9 the reduction of the error along the iterations is shown.

Bar number	Bar nodes	Starting stiffness <i>MN</i>	Real stiffness <i>MN</i>	Estimated stiffness <i>MN</i>
1	1-2	657.3618	500	493.0925
2	2-3	702.896	500	497.724
3	3-4	313.4934	500	496.6511
4	5-6	706.6879	500	498.1389
5	6-7	566.1796	475	472.8125
6	7-8	298.7702	500	498.6634
7	9-10	389.2491	400	397.6299
8	10-11	523.4408	500	502.1229
9	1-9	378.9518	260	261.3789
10	9-2	380.871	260	253.9057
11	2-10	170.9794	260	260.0137
12	10-3	382.3541	260	261.2851
13	3-11	378.8634	247	246.7285
14	11-4	256.1977	260	258.1524
15	5-9	338.0729	260	259.9985
16	9-6	166.8904	260	261.8802
17	6-10	239.6579	260	256.348
18	10-7	368.0912	260	261.0997
19	7-11	335.9739	260	259.3641
20	11-8	379.468	260	258.6365
21	5-1	300.4926	260	261.8636
22	1-6	139.285	78	78.3059
23	6-2	350.7736	260	255.7666
24	2-7	372.8382	260	260.9403
25	7-3	306.4711	260	260.0612
26	3-8	327.0124	260	257.7487
27	8-4	323.2144	260	260.4722

Table 8.3: Stiffnesses estimated for the redundant three-dimensional truss in Fig. 8.7.

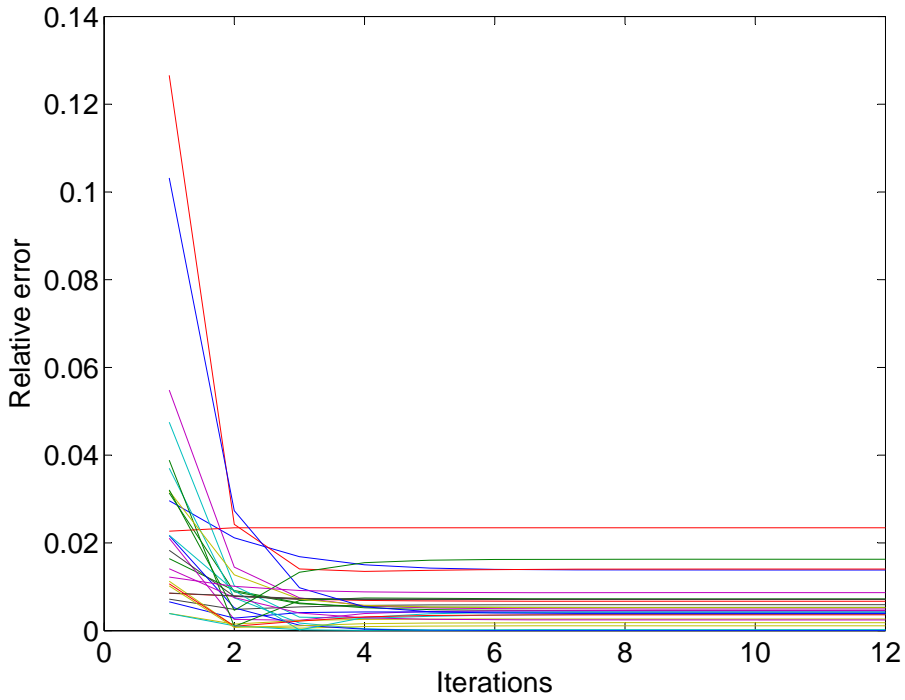


Figure 8.9: Convergence of the iterative procedure. Each line represents the evolution of the relative error between the estimated stiffnesses and the real values. Even if the starting values are completely wrong the estimates rapidly converges to the real values.

The results are really good. The real stiffnesses of all the bars have been correctly identified. Both for the strongly damaged elements (6–7 and 3–11) and for the weekly damaged ones (9–10 and 1–6) the accuracy is very high.

8.5 Error Analysis

In order to obtain information on the reliability of the method, on the influence of the measurement precision and on the importance of the number of load conditions, an error analysis has been performed.

The perturbation method (see, for example, Matthies et al., 1997) can be applied in the case of statically determinate structures. In fact, in this case the solution is given by Eq. (8.17). A closed form expression of the estimation error as a function of the measurement errors is provided in Sec. 8.5.1 and can be used to estimate the necessary load conditions.

On the contrary the procedure for externally redundant structures presented in Sec. 8.2.2 involves also an iterative loop that impedes the use of perturbation techniques. In this case, the error of the identification method is estimated by Monte Carlo simulation (see, for example, the survey paper by Hurtado and Barbat, 1998). A practical application is presented in Sec: 8.5.2.

8.5.1 Perturbation Technique, for Statically Determinate Structures

The random uncertainties of the problem affects strains and loads and are numerically simulated by random noises. From here onward, the “hat” is used for the measured quantities:

$$\varepsilon_e^k = \hat{\varepsilon}_e^k + \gamma_e^k \quad (8.30)$$

$$f_i^k = \hat{f}_i^k + \varphi_i^k \quad (8.31)$$

where γ and φ are the random measurement errors associated to loads and strains respectively, the index e runs over the m elements, the index i runs over the n degrees of freedom of the structure and the index k runs over the K load conditions. Owing to use the perturbation technique, the random variables are collected in one random vector \mathbf{r} :

$$\boldsymbol{\gamma} = [\gamma_1^1 \quad \gamma_2^1 \quad \cdots \quad \gamma_m^1 \quad \gamma_1^2 \quad \gamma_2^2 \quad \cdots \quad \gamma_m^K]^T \quad (8.32)$$

$$\boldsymbol{\varphi} = [\varphi_1^1 \quad \varphi_2^1 \quad \cdots \quad \varphi_n^1 \quad \varphi_1^2 \quad \varphi_2^2 \quad \cdots \quad \varphi_n^K]^T \quad (8.33)$$

$$\mathbf{r} = \begin{bmatrix} \boldsymbol{\gamma} \\ \boldsymbol{\varphi} \end{bmatrix} \quad (8.34)$$

A second order MacLaurin expansion is performed on the matrices that appear in Equation (8.22):

$$\mathbf{H}(\mathbf{r}) = \mathbf{H}^0 + \sum_i \mathbf{H}_i^1 r_i + \sum_i \sum_j \mathbf{H}_{ij}^2 r_i r_j \quad (8.35)$$

$$\mathbf{S}(\mathbf{r}) = \mathbf{S}^0 + \sum_i \mathbf{S}_i^1 r_i + \sum_i \sum_j \mathbf{S}_{ij}^2 r_i r_j \quad (8.36)$$

$$\mathbf{R}(\mathbf{r}) = \mathbf{R}^0 + \sum_i \mathbf{R}_i^1 r_i + \sum_i \sum_j \mathbf{R}_{ij}^2 r_i r_j \quad (8.37)$$

being

$$\mathbf{H}^0 = \mathbf{H}|_{\mathbf{0}}; \quad \mathbf{H}_i^1 = \left. \frac{\partial \mathbf{H}}{\partial r_i} \right|_{\mathbf{0}}; \quad \mathbf{H}_{ij}^2 = \left. \frac{\partial^2 \mathbf{H}}{2 \partial r_i \partial r_j} \right|_{\mathbf{0}} \quad (8.38)$$

$$\mathbf{S}^0 = \mathbf{S}|_{\mathbf{0}}; \quad \mathbf{S}_i^1 = \left. \frac{\partial \mathbf{S}}{\partial r_i} \right|_{\mathbf{0}}; \quad \mathbf{S}_{ij}^2 = \left. \frac{\partial^2 \mathbf{S}}{2 \partial r_i \partial r_j} \right|_{\mathbf{0}} \quad (8.39)$$

$$\mathbf{R}^0 = \mathbf{R}|_{\mathbf{0}}; \quad \mathbf{R}_i^1 = \left. \frac{\partial \mathbf{R}}{\partial r_i} \right|_{\mathbf{0}}; \quad \mathbf{R}_{ij}^2 = \left. \frac{\partial^2 \mathbf{R}}{2 \partial r_i \partial r_j} \right|_{\mathbf{0}} \quad (8.40)$$

where indexes i and j run from 1 to $K(m+n)$. By substituting the expansions, Eq. (8.22) is restated as:

$$\begin{aligned} & \left(\mathbf{H}^0 + \sum_i \mathbf{H}_i^1 r_i + \sum_i \sum_j \mathbf{H}_{ij}^2 r_i r_j \right) \cdot \\ & \cdot \left(\mathbf{S}^0 + \sum_i \mathbf{S}_i^1 r_i + \sum_i \sum_j \mathbf{S}_{ij}^2 r_i r_j \right) = \\ & = \left(\mathbf{R}^0 + \sum_i \mathbf{R}_i^1 r_i + \sum_i \sum_j \mathbf{R}_{ij}^2 r_i r_j \right) \end{aligned} \quad (8.41)$$

Then the equation is simplified and terms of the same order are equated

$$\text{order zero} \rightarrow \mathbf{H}^0 \mathbf{S}^0 = \mathbf{R}^0 \quad (8.42)$$

$$\text{first order} \rightarrow \mathbf{H}_i^1 \mathbf{S}^0 + \mathbf{H}^0 \mathbf{S}_i^1 = \mathbf{R}_i^1 \quad (8.43)$$

$$\text{second order} \rightarrow \mathbf{H}_{ij}^2 \mathbf{S}^0 + \mathbf{H}_i^1 \mathbf{S}_j^1 + \mathbf{H}^0 \mathbf{S}_{ij}^2 = \mathbf{R}_{ij}^2 \quad (8.44)$$

If \mathbf{H} is non-singular, from Eqs. (8.42)–(8.44) \mathbf{S}^0 , \mathbf{S}_i^1 and \mathbf{S}_{ij}^2 can be computed:

$$\mathbf{S}^0 = (\mathbf{H}^0)^{-1} \mathbf{R}^0 \quad (8.45)$$

$$\mathbf{S}_i^1 = (\mathbf{H}^0)^{-1} (\mathbf{R}_i^1 - \mathbf{H}_i^1 \mathbf{S}^0) \quad (8.46)$$

$$\mathbf{S}_{ij}^2 = (\mathbf{H}^0)^{-1} (\mathbf{R}_{ij}^2 - \mathbf{H}_i^1 \mathbf{S}_j^1 - \mathbf{H}_{ij}^2 \mathbf{S}^0) \quad (8.47)$$

Mean and covariance of \mathbf{S} can be obtained as (Benjamin and Cornell, 1970):

$$\mathbf{E}[\mathbf{S}] = \mathbf{S}^0 + \sum_i \mathbf{S}_i^1 \mathbf{E}[r_i] + \sum_i \sum_j \mathbf{S}_{ij}^2 \mathbf{E}[r_i r_j] + \dots \quad (8.48)$$

$$\text{COV}[\mathbf{S}] = \sum_i \sum_j \mathbf{S}_i^1 \mathbf{S}_j^{1T} \text{COV}[r_i, r_j] + \dots \quad (8.49)$$

However, γ 's and φ 's are measurement errors, thus r_i 's are expected to have null mean value $\mathbf{E}[r_i] = 0$ and to be uncorrelated. Remembering that

$$\text{COV}[x, y] = \mathbf{E}[(x - \mathbf{E}[x])(y - \mathbf{E}[y])] = \mathbf{E}[xy] - \mathbf{E}[x]\mathbf{E}[y] \quad (8.50)$$

in this particular case where $\mathbf{E}[x] = \mathbf{E}[y] = 0$ the covariance matrix is

$$\text{COV}[x, y] = \mathbf{E}[xy] \quad (8.51)$$

Therefore, Eqs. (8.48) and (8.49) are restated as follows:

$$\mathbf{E}[\mathbf{S}] = \mathbf{S}^0 + \sum_i \mathbf{S}_{ii}^2 \sigma_i^2 + \dots \quad (8.52)$$

$$\text{COV}[\mathbf{S}] = \sum_i \mathbf{S}_i^1 \mathbf{S}_i^{1T} \sigma_i^2 + \dots \quad (8.53)$$

where σ_i^2 is the variance of r_i .

Equation (8.53) gives a second order approximation of the covariance matrix, but to estimate the error, an even better index is the Coefficient Of Variation (C.O.V.)

$$\text{C.O.V.} = \frac{\sigma(EA)}{E[EA]} \quad (8.54)$$

In order to use Eq. (8.54), and therefore Eqs. (8.53) and (8.52), σ_i^2 can be estimated using the knowing the precision of the measurements, while \mathbf{S}^0 , \mathbf{S}_i^1 and \mathbf{S}_{ii}^2 must be restated as explicit functions of \mathbf{H}_0 , \mathbf{H}_i^1 , \mathbf{H}_{ii}^2 , \mathbf{R}_0 , \mathbf{R}_i^1 and \mathbf{R}_{ii}^2 . For the sake of clarity, from here onward the index notation is used, thus $(\mathbf{M})_{rc}$ indicates the element on the row r and the column c of the matrix \mathbf{M} .

First of all, the basic matrix \mathbf{H} is analyzed:

$$\begin{aligned} (\mathbf{H})_{st} &= \left(\sum_{k=1}^K \mathbf{P}_k^T \mathbf{P}_k \right)_{st} = \\ &= \sum_{k=1}^K (\mathbf{P}_k^T \mathbf{P}_k)_{st} = \\ &= \sum_{k=1}^K \sum_{p=1}^n (\mathbf{P}_k^T)_{sp} (\mathbf{P}_k)_{pt} = \\ &= \sum_{k=1}^K \sum_{p=1}^n (\mathbf{P}_k)_{ps} (\mathbf{P}_k)_{pt} = \\ &= \sum_{k=1}^K \sum_{p=1}^n \varepsilon_s^k (\mathbf{I}_s)_p \varepsilon_t^k (\mathbf{I}_t)_p = \\ &= \sum_{k=1}^K \sum_{p=1}^n (\hat{\varepsilon}_s^k + \gamma_s^k) (\mathbf{I}_s)_p (\hat{\varepsilon}_t^k + \gamma_t^k) (\mathbf{I}_t)_p = \\ &= \sum_{k=1}^K \sum_{p=1}^n (\mathbf{I}_s)_p (\mathbf{I}_t)_p (\hat{\varepsilon}_s^k \hat{\varepsilon}_t^k + \hat{\varepsilon}_s^k \gamma_t^k + \varepsilon_t^k \gamma_s^k + \gamma_s^k \gamma_t^k) \end{aligned} \quad (8.55)$$

therefore,

$$\left(\frac{\partial \mathbf{H}}{\partial \varphi_d^c} \right)_{st} = 0 \quad \forall s, t, d, c \quad (8.56)$$

while

$$\begin{aligned}
\left(\frac{\partial \mathbf{H}}{\partial \gamma_e^c}\right)_{st} &= \sum_{k=1}^K \sum_{p=1}^n (\mathbf{I}_s)_p (\mathbf{I}_t)_p \frac{\partial}{\partial \gamma_e^c} \hat{\varepsilon}_s^k \hat{\varepsilon}_t^k + \\
&+ \sum_{k=1}^K \sum_{p=1}^n (\mathbf{I}_s)_p (\mathbf{I}_t)_p \frac{\partial}{\partial \gamma_e^c} \hat{\varepsilon}_s^k \gamma_t^k + \\
&+ \sum_{k=1}^K \sum_{p=1}^n (\mathbf{I}_s)_p (\mathbf{I}_t)_p \frac{\partial}{\partial \gamma_e^c} \hat{\varepsilon}_t^k \gamma_s^k + \\
&+ \sum_{k=1}^K \sum_{p=1}^n (\mathbf{I}_s)_p (\mathbf{I}_t)_p \frac{\partial}{\partial \gamma_e^c} \gamma_s^k \gamma_t^k
\end{aligned} \tag{8.57}$$

The terms of Eq. (8.57) value:

$$\sum_{k=1}^K \sum_{p=1}^n (\mathbf{I}_s)_p (\mathbf{I}_t)_p \frac{\partial}{\partial \gamma_e^c} \hat{\varepsilon}_s^k \hat{\varepsilon}_t^k = 0 \tag{8.58}$$

$$\sum_{k=1}^K \sum_{p=1}^n (\mathbf{I}_s)_p (\mathbf{I}_t)_p \frac{\partial}{\partial \gamma_e^c} \hat{\varepsilon}_s^k \gamma_t^k = \begin{cases} \sum_{p=1}^n (\mathbf{I}_s)_p (\mathbf{I}_t)_p \hat{\varepsilon}_s^c & \text{if } e = t \\ 0 & \text{otherwise} \end{cases} \tag{8.59}$$

$$\sum_{k=1}^K \sum_{p=1}^n (\mathbf{I}_s)_p (\mathbf{I}_t)_p \frac{\partial}{\partial \gamma_e^c} \hat{\varepsilon}_t^k \gamma_s^k = \begin{cases} \sum_{p=1}^n (\mathbf{I}_s)_p (\mathbf{I}_t)_p \hat{\varepsilon}_t^c & \text{if } e = s \\ 0 & \text{otherwise} \end{cases} \tag{8.60}$$

$$\sum_{k=1}^K \sum_{p=1}^n (\mathbf{I}_s)_p (\mathbf{I}_t)_p \frac{\partial}{\partial \gamma_e^c} \gamma_s^k \gamma_t^k = \begin{cases} 2\gamma_e^c \sum_{p=1}^n (\mathbf{I}_s)_p (\mathbf{I}_t)_p & \text{if } e = t = s \\ \gamma_t^c \sum_{p=1}^n (\mathbf{I}_s)_p (\mathbf{I}_t)_p & \text{if } e = s \neq t \\ \gamma_s^c \sum_{p=1}^n (\mathbf{I}_s)_p (\mathbf{I}_t)_p & \text{if } e = t \neq s \\ 0 & \text{otherwise} \end{cases} \tag{8.61}$$

Equation (8.57) has to be computed for $\mathbf{r} = \mathbf{0}$, so all the terms of Eq. (8.61) are negligible. Therefore

$$\left(\frac{\partial \mathbf{H}}{\partial \gamma_e^c}\right)_{st} \Big|_{\mathbf{0}} = \sum_{p=1}^n (\mathbf{I}_s)_p (\mathbf{I}_t)_p (\delta_{et} \hat{\varepsilon}_s^c + \delta_{es} \hat{\varepsilon}_t^c) \tag{8.62}$$

being δ_{et} and δ_{es} “Kronecker delta” functions.

Then, the same operations are performed on vector \mathbf{R} .

$$\begin{aligned}
 (\mathbf{R})_s &= \left(\sum_{k=1}^K \mathbf{P}_k^T \mathbf{F}_k \right)_s = \\
 &= \sum_{k=1}^K (\mathbf{P}_k^T \mathbf{F}_k)_s = \\
 &= \sum_{k=1}^K \sum_{p=1}^n (\mathbf{P}_k^T)_{sp} (\mathbf{F}_k)_p = \\
 &= \sum_{k=1}^K \sum_{p=1}^n (\mathbf{P}_k)_{ps} (\mathbf{F}_k)_p = \\
 &= \sum_{k=1}^K \sum_{p=1}^n \varepsilon_s^k (\mathbf{I}_s)_p f_p^k = \\
 &= \sum_{k=1}^K \sum_{p=1}^n (\hat{\varepsilon}_s^k + \gamma_s^k) (\mathbf{I}_s)_p (\hat{f}_p^k + \varphi_p^k) = \\
 &= \sum_{k=1}^K \sum_{p=1}^n (\mathbf{I}_s)_p (\hat{\varepsilon}_s^k \hat{f}_p^k + \hat{\varepsilon}_s^k \varphi_p^k + \hat{f}_p^k \gamma_s^k + \gamma_s^k \varphi_p^k)
 \end{aligned} \tag{8.63}$$

The derivative with respect to φ are

$$\begin{aligned}
 \left(\frac{\partial \mathbf{R}}{\partial \varphi_d^c} \right)_s &= \sum_{k=1}^K \sum_{p=1}^n (\mathbf{I}_s)_p \frac{\partial}{\partial \varphi_d^c} \hat{\varepsilon}_s^k \hat{f}_p^k + \\
 &+ \sum_{k=1}^K \sum_{p=1}^n (\mathbf{I}_s)_p \frac{\partial}{\partial \varphi_d^c} \hat{\varepsilon}_s^k \varphi_p^k + \\
 &+ \sum_{k=1}^K \sum_{p=1}^n (\mathbf{I}_s)_p \frac{\partial}{\partial \varphi_d^c} \hat{f}_p^k \gamma_s^k + \\
 &+ \sum_{k=1}^K \sum_{p=1}^n (\mathbf{I}_s)_p \frac{\partial}{\partial \varphi_d^c} \gamma_s^k \varphi_p^k
 \end{aligned} \tag{8.64}$$

The single terms value

$$\sum_{k=1}^K \sum_{p=1}^n (\mathbf{I}_s)_p \frac{\partial}{\partial \varphi_d^c} \hat{\varepsilon}_s^k \hat{f}_p^k = 0 \quad (8.65)$$

$$\sum_{k=1}^K \sum_{p=1}^n (\mathbf{I}_s)_p \frac{\partial}{\partial \varphi_d^c} \hat{\varepsilon}_s^k \varphi_p^k = (\mathbf{I}_s)_d \hat{\varepsilon}_s^c \quad (8.66)$$

$$\sum_{k=1}^K \sum_{p=1}^n (\mathbf{I}_s)_p \frac{\partial}{\partial \varphi_d^c} \hat{f}_p^k \gamma_s^k = 0 \quad (8.67)$$

$$\sum_{k=1}^K \sum_{p=1}^n (\mathbf{I}_s)_p \frac{\partial}{\partial \varphi_d^c} \gamma_s^k \varphi_p^k = (\mathbf{I}_s)_d \gamma_s^c \quad (8.68)$$

Equation (8.64) has to be computed for $\mathbf{r} = \mathbf{0}$, so all the terms of Eq. (8.68) are negligible. Therefore

$$\left(\frac{\partial \mathbf{R}}{\partial \varphi_d^c} \right) \Big|_{\mathbf{0}} = (\mathbf{I}_s)_d \hat{\varepsilon}_s^c \quad (8.69)$$

The derivative with respect to γ are

$$\begin{aligned} \left(\frac{\partial \mathbf{R}}{\partial \gamma_e^c} \right)_s &= \sum_{k=1}^K \sum_{p=1}^n (\mathbf{I}_s)_p \frac{\partial}{\partial \gamma_e^c} \hat{\varepsilon}_s^k \hat{f}_p^k + \\ &+ \sum_{k=1}^K \sum_{p=1}^n (\mathbf{I}_s)_p \frac{\partial}{\partial \gamma_e^c} \hat{\varepsilon}_s^k \varphi_p^k + \\ &+ \sum_{k=1}^K \sum_{p=1}^n (\mathbf{I}_s)_p \frac{\partial}{\partial \gamma_e^c} \hat{f}_p^k \gamma_s^k + \\ &+ \sum_{k=1}^K \sum_{p=1}^n (\mathbf{I}_s)_p \frac{\partial}{\partial \gamma_e^c} \gamma_s^k \varphi_p^k \end{aligned} \quad (8.70)$$

Single terms value

$$\sum_{k=1}^K \sum_{p=1}^n (\mathbf{I}_s)_p \frac{\partial}{\partial \gamma_e^c} \hat{\varepsilon}_s^k \hat{f}_p^k = 0 \quad (8.71)$$

$$\sum_{k=1}^K \sum_{p=1}^n (\mathbf{I}_s)_p \frac{\partial}{\partial \gamma_e^c} \hat{\varepsilon}_s^k \varphi_p^k = 0 \quad (8.72)$$

$$\sum_{k=1}^K \sum_{p=1}^n (\mathbf{I}_s)_p \frac{\partial}{\partial \gamma_e^c} \hat{f}_p^k \gamma_s^k = \begin{cases} \sum_{p=1}^n (\mathbf{I}_s)_p \hat{f}_p^c & \text{if } e = s \\ 0 & \text{otherwise} \end{cases} \quad (8.73)$$

$$\sum_{k=1}^K \sum_{p=1}^n (\mathbf{I}_s)_p \frac{\partial}{\partial \gamma_e^c} \gamma_s^k \varphi_p^k = \begin{cases} \sum_{p=1}^n (\mathbf{I}_s)_p \varphi_p^c & \text{if } e = s \\ 0 & \text{otherwise} \end{cases} \quad (8.74)$$

Equation (8.70) has to be computed for $\mathbf{r} = \mathbf{0}$, so all the terms of Eq. (8.74) are negligible. Therefore

$$\left(\frac{\partial \mathbf{R}}{\partial \gamma_e^c} \right) \Big|_{\mathbf{s}, \mathbf{0}} = \sum_{p=1}^n (\mathbf{I}_s)_p \hat{f}_p^c \delta_{es} \quad (8.75)$$

being δ_{es} a “Kronecker delta” function.

Equation (8.52) involves also \mathbf{S}_{ii}^2 , that can be obtained inverting Eq. (8.47)

$$\mathbf{S}_{ii}^2 = (\mathbf{H}^0)^{-1} (\mathbf{R}_{ii}^2 - \mathbf{H}_i^1 \mathbf{S}_i^1 - \mathbf{H}_{ii}^2 \mathbf{S}^0) \quad (8.76)$$

Therefore, the second derivatives \mathbf{H}_{ii}^2 and \mathbf{R}_{ii}^2 must be computed.

The definition of \mathbf{H}_{ii}^2 , i.e. Eq. (8.38), can be rewritten as

$$\mathbf{H}_{ii}^2 = \frac{\partial^2 \mathbf{H}}{\partial r_i^2} \Big|_{\mathbf{0}} = \frac{\partial}{\partial r_i} \left(\frac{\partial \mathbf{H}}{\partial r_i} \right) \Big|_{\mathbf{0}} \quad (8.77)$$

By means of Eq. (8.56), it is trivial to obtain

$$\frac{\partial}{\partial \varphi_d^c} \left(\frac{\partial \mathbf{H}}{\partial \varphi_d^c} \right) \Big|_{\mathbf{0}} = \frac{\partial}{\partial \varphi_d^c} (\mathbf{0}) \Big|_{\mathbf{0}} = \mathbf{0} \quad (8.78)$$

For what concern the derivative with respect to γ , Eqs (8.57)–(8.61) are used. In this case, single terms value

$$\sum_{k=1}^K \sum_{p=1}^n (\mathbf{I}_s)_p (\mathbf{I}_t)_p \frac{\partial^2}{\partial \gamma_e^c} \hat{\varepsilon}_s^k \varepsilon_t^k = 0 \quad (8.79)$$

$$\sum_{k=1}^K \sum_{p=1}^n (\mathbf{I}_s)_p (\mathbf{I}_t)_p \frac{\partial^2}{\partial \gamma_e^c} \hat{\varepsilon}_s^k \gamma_t^k = 0 \quad (8.80)$$

$$\sum_{k=1}^K \sum_{p=1}^n (\mathbf{I}_s)_p (\mathbf{I}_t)_p \frac{\partial^2}{2\partial\gamma_e^{c^2}} \hat{\varepsilon}_t^k \gamma_s^k = 0 \quad (8.81)$$

$$\sum_{k=1}^K \sum_{p=1}^n (\mathbf{I}_s)_p (\mathbf{I}_t)_p \frac{\partial^2}{2\partial\gamma_e^{c^2}} \gamma_s^k \gamma_t^k = \begin{cases} \sum_{p=1}^n (\mathbf{I}_s)_p (\mathbf{I}_t)_p & \text{if } e = t = s \\ 0 & \text{otherwise} \end{cases} \quad (8.82)$$

Therefore

$$\left(\frac{\partial^2 \mathbf{H}}{2\partial\gamma_e^{c^2}} \right)_{st} \Big|_0 = \sum_{p=1}^n (\mathbf{I}_s)_p (\mathbf{I}_t)_p \delta_{et} \delta_{es} \quad (8.83)$$

Note that Eq. (8.83) does not depend on c .

The second derivatives of vector \mathbf{R} are zeros. In fact, by means of Eqs. (8.65)–(8.68) and (8.71)–(8.74) the following results are obtained:

$$\sum_{k=1}^K \sum_{p=1}^n (\mathbf{I}_s)_p \frac{\partial^2}{2\partial\varphi_d^{c^2}} \hat{\varepsilon}_s^k \hat{f}_p^k = 0 \quad (8.84)$$

$$\sum_{k=1}^K \sum_{p=1}^n (\mathbf{I}_s)_p \frac{\partial^2}{2\partial\varphi_d^{c^2}} \hat{\varepsilon}_s^k \varphi_p^k = 0 \quad (8.85)$$

$$\sum_{k=1}^K \sum_{p=1}^n (\mathbf{I}_s)_p \frac{\partial^2}{2\partial\varphi_d^{c^2}} \hat{f}_p^k \gamma_s^k = 0 \quad (8.86)$$

$$\sum_{k=1}^K \sum_{p=1}^n (\mathbf{I}_s)_p \frac{\partial^2}{2\partial\varphi_d^{c^2}} \gamma_s^k \varphi_p^k = 0 \quad (8.87)$$

$$\sum_{k=1}^K \sum_{p=1}^n (\mathbf{I}_s)_p \frac{\partial^2}{2\partial\gamma_e^{c^2}} \hat{\varepsilon}_s^k \hat{f}_p^k = 0 \quad (8.88)$$

$$\sum_{k=1}^K \sum_{p=1}^n (\mathbf{I}_s)_p \frac{\partial^2}{2\partial\gamma_e^{c^2}} \hat{\varepsilon}_s^k \varphi_p^k = 0 \quad (8.89)$$

$$\sum_{k=1}^K \sum_{p=1}^n (\mathbf{I}_s)_p \frac{\partial^2}{2\partial\gamma_e^{c^2}} \hat{f}_p^k \gamma_s^k = 0 \quad (8.90)$$

$$\sum_{k=1}^K \sum_{p=1}^n (\mathbf{I}_s)_p \frac{\partial^2}{2\partial\gamma_e^{c^2}} \gamma_s^k \varphi_p^k = 0 \quad (8.91)$$

Finally, all the terms involved by Eqs. (8.45)–(8.47) can be summarized as follow as functions of the input data:

$$\left. \frac{\partial \mathbf{H}}{\partial \varphi_d^c} \right|_{\mathbf{0}} = \mathbf{0} \quad (8.92)$$

$$\left(\frac{\partial \mathbf{H}}{\partial \gamma_e^c} \right)_{st} \Big|_{\mathbf{0}} = \sum_{p=1}^n (\mathbf{I}_s)_p (\mathbf{I}_t)_p (\delta_{et} \hat{\varepsilon}_s^c + \delta_{es} \hat{\varepsilon}_t^c) \quad (8.93)$$

$$\left(\frac{\partial \mathbf{R}}{\partial \varphi_d^c} \right)_{s} \Big|_{\mathbf{0}} = (\mathbf{I}_s)_d \hat{\varepsilon}_s^c \quad (8.94)$$

$$\left(\frac{\partial \mathbf{R}}{\partial \gamma_e^c} \right)_{s} \Big|_{\mathbf{0}} = \sum_{p=1}^n (\mathbf{I}_s)_p \hat{f}_p^c \delta_{es} \quad (8.95)$$

$$\left. \frac{\partial^2 \mathbf{H}}{2\partial \varphi_d^{c^2}} \right|_{\mathbf{0}} = \mathbf{0} \quad (8.96)$$

$$\left(\frac{\partial^2 \mathbf{H}}{2\partial \gamma_e^{c^2}} \right)_{st} \Big|_{\mathbf{0}} = \sum_{p=1}^n (\mathbf{I}_s)_p (\mathbf{I}_t)_p \delta_{et} \delta_{es} \quad (8.97)$$

$$\mathbf{R}_{ii} = \mathbf{0} \quad (8.98)$$

These results can be used for a direct estimation of the coefficient of variation of the identification procedure, as expressed in Eq. (8.54).

8.5.2 Monte Carlo Simulation, for Statically Indeterminate Structures

To estimate the coefficient of variation of the estimate in the case of externally redundant structures, the Monte Carlo Simulation is used. In this numerical example, it has been applied to the structure represented in Fig. 8.4 and described in Sec. 8.4.1.

Three load conditions have been added to the two already presented in Sec. 8.4.1: a vertical force of modulus $-10kN$ applied to the node number 6, a horizontal force of modulus $10kN$ applied to the node number 6 and a vertical force of modulus $-10kN$ applied to the node number 3. Tables 8.4

Bar No.	Load condition				
	1	2	3	4	5
1	26.7	23.8	0.9	9.2	-17.4
2	-116.3	23.8	0.9	9.2	-17.4
3	-37.6	-33.6	-1.3	-13.0	24.6
4	158.7	-142.8	1.1	162.7	4.0
5	306.5	-419.0	-7.6	278.3	-28.2
6	25.4	18.7	5.2	2.8	120.3
7	-1.2	-5.0	4.2	136.5	-5.2
8	-4.0	-102.1	-3.6	-17.4	-13.4
9	17.0	71.1	-59.8	90.0	73.0
10	2.9	-70.7	2.5	12.3	9.4
11	-1.2	-5.0	-138.6	-6.3	-5.2

Table 8.4: Results for the structure represented in Fig. 8.4. Axial strains (10^{-6}).

Bar No.	Load condition				
	1	2	3	4	5
1	18.6	16.6	0.7	6.4	-12.2
2	-81.4	16.6	0.7	6.4	-12.2
3	-26.3	-23.5	-0.9	-9.1	17.2
4	111.1	-99.9	0.7	113.9	2.8
5	21.5	-29.3	-0.5	19.5	-2
6	17.8	13.1	3.6	2	84.2
7	-0.8	-3.5	3	95.5	-3.6
8	-2.8	-71.4	-2.5	-12.2	-9.3
9	1.2	5	-4.2	6.3	5.1
10	2	-49.5	1.8	8.6	6.6
11	-0.8	-3.5	-97	-4.5	-3.6

Table 8.5: Results for the structure represented in Fig. 8.4. Axial stresses ($\frac{N}{m^2} 10^{-4}$).

Bar No.	Number of load conditions							
	First 2		First 3		First 4		All 5	
	E[EA] [MN]	C.O.V. [%]	E[EA] [MN]	C.O.V. [%]	E[EA] [MN]	C.O.V. [%]	E[EA] [MN]	C.O.V. [%]
1	69.8	5.9	69.5	5.9	69.5	4.2	69.7	2.4
2	70	1.2	70	1.2	70	0.8	70	0.8
3	70	4.7	69.7	4.7	69.7	3.3	70	1.6
4	70	1.5	70	1.6	70	0.9	70	0.7
5	7	4	7	4	7	2.3	7	1.8
6	70.6	7.3	69.6	6.5	69.5	5.3	70	0.9
7	65.3	32.7	68.6	15	70	0.8	70	0.7
8	70.4	4.4	70.2	3.9	70.2	2.3	70	1.8
9	6.5	24.1	6.9	6.9	7	4.2	7	3.5
10	69.6	4.4	69.8	3.9	69.8	2.3	70	1.7
11	66	26.8	70	0.8	70	0.8	70	0.7

Table 8.6: Results for the structure represented in Fig. 8.4. Estimated stiffnesses and coefficients of variation.

and 8.5 collect the dilatations and axial stresses simulated by FEA. The superimposed noises described in Sec. 8.4.1 have been applied also to the last three load tests. Finally, Table 8.6 shows the estimated stiffnesses and the respective coefficients of variation. These coefficients have been computed by means of the Monte Carlo Simulation, using 1500 samples. Fig. 8.10 shows that such a number of samples is sufficient to meet convergence in the case of two load conditions. Similar results have been obtained also for the other cases. Histograms represented in Fig. 8.11 shows the results obtained for the C.O.V.'s. It should be noticed that the C.O.V. decrease when the number of load conditions is increased. In particular, it drops down when a load condition in which the bar achieves a “sufficient” stress level is taken into account. For example it happens to the bar 11 when the condition number 3 is considered.

The results presented in Table 8.6 show that the proposed iterative algorithm have the same accuracy and robustness of the method proposed by Liu and Chian (1997), but the new one is applicable also to externally redundant structures.

Finally, Fig. 8.12 shows the stiffnesses estimated using five load tests and in Fig. 8.13 the convergence of the iterative algorithm to the exact solution is

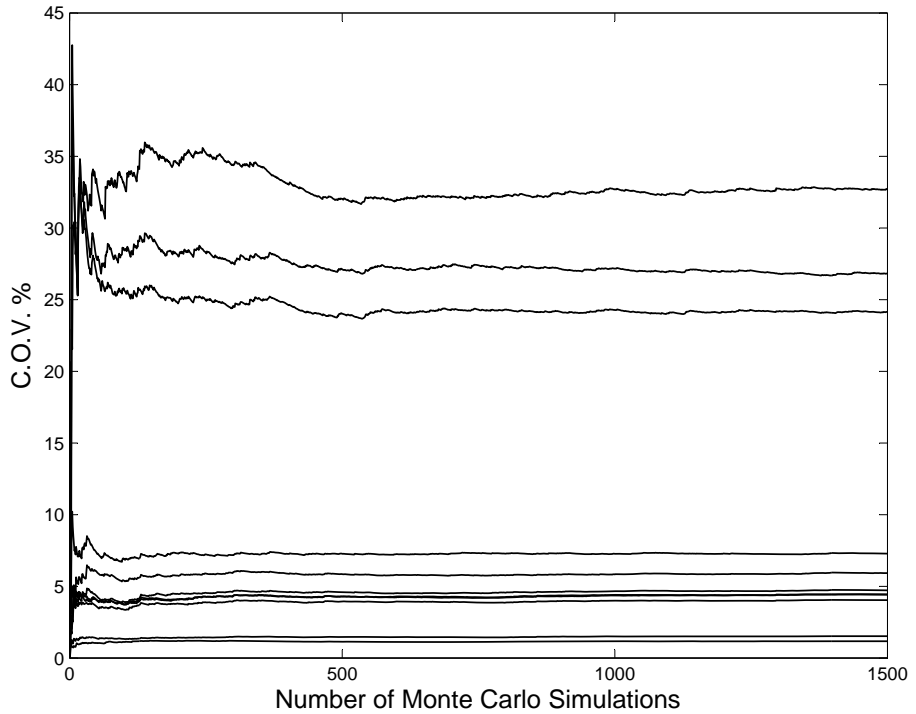


Figure 8.10: Results for the structure represented in Fig. 8.4. Convergence of the coefficients of variation versus the number of Monte Carlo Simulations. Each line represents the C.O.V. of a bar. 1500 samples are sufficient to meet convergence. This plot refers to the case of two load conditions, analog results have been obtained also for the other numbers of load conditions.

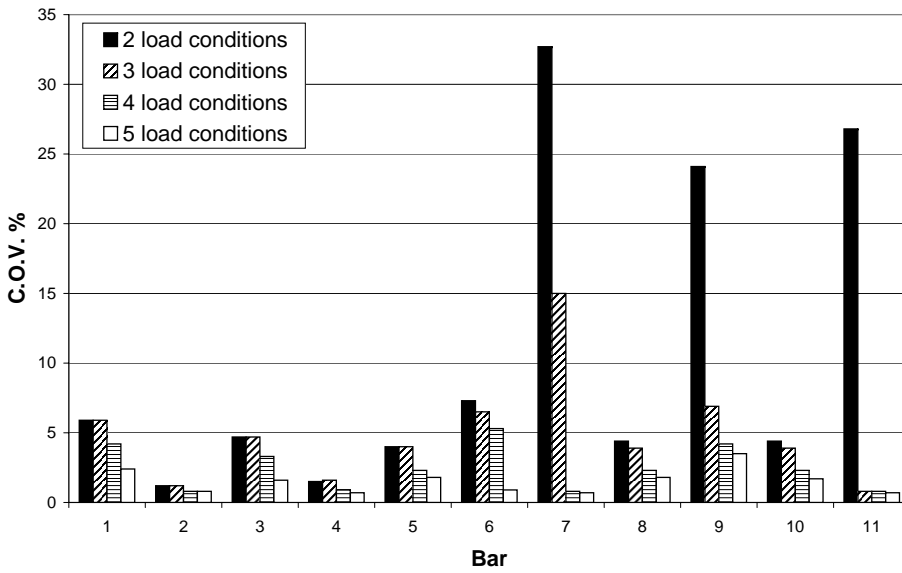


Figure 8.11: Results for the structure represented in Fig. 8.4. Coefficients of variation obtained using different numbers of load conditions.

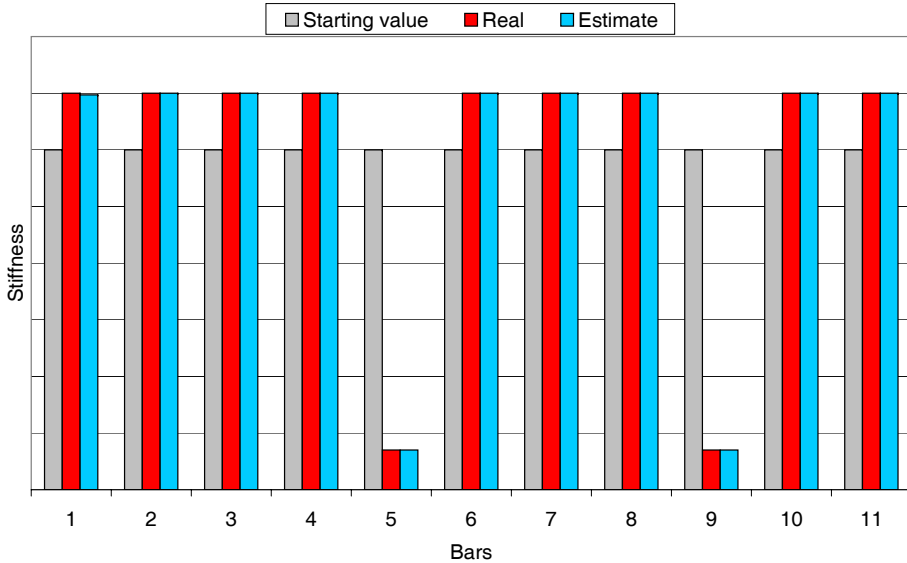


Figure 8.12: Stiffnesses estimated for the redundant plane truss in Fig. 8.4 using five load tests, compared to the starting values of the iterative procedure and to the real values. The accuracy is good for all the bars.

shown.

8.6 Concluding Remarks

The algorithm proposed in this Chapter is able to identify the stiffness of the elements of a three-dimensional truss structure with any kind of redundancy. Static loads and strain measurements are used.

The loads have to be applied so that every bar reaches a significant stress level in at least one test. If this is done properly², the numerical applications have shown that the code has good accuracy and low coefficients of variation of the results. When, on the contrary, a bar never reaches a significant stress level, the relative influence of the measurement error on the strains (modeled by the random noises) increases, so reducing the accuracy of the information and,

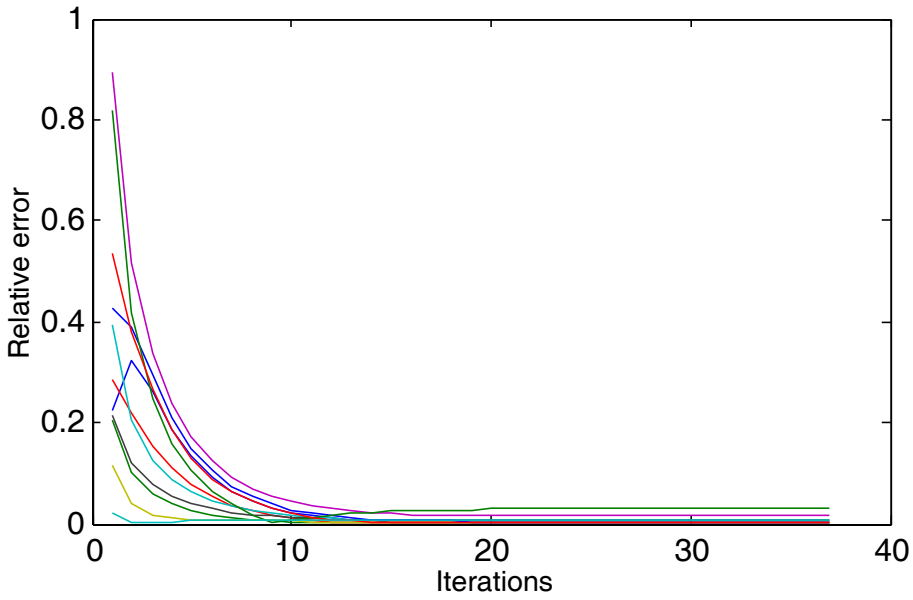


Figure 8.13: Convergence of the iterative procedure. Each line represents the evolution of the relative error between the estimated stiffnesses and the real values. Even if the starting values are completely wrong, the estimates rapidly converge to the real values.

therefore, of the identification procedure.

By means of this technique, it is possible to estimate the residual stiffness of elements subject to uniform corrosion (e.g. internal corrosion in tubular elements that can not be seen from outside) or to any kind of damage that affects the entire element (e.g. a global reduction of the Young modulus because of aging). On the contrary, the code is not sensitive to sectional or localized damage. For this reason, a new approach is proposed in Chapter 9.

²In some cases, it is not trivial satisfy the condition of sufficient loading for every bar. In fact, the presence of weak bars that converge to the same node could avoid the transmission of stresses to the other bars that converge to that node.

The application of the procedure to three-dimensional trusses has particularly enlightened this problem.

There are no analytical solutions for this issue, but the absence of a “sufficient” loading is recognized by the procedure, therefore further investigations (or new loading conditions) on the specific area are suggested.

Chapter 9

Local Damage Identification with Genetic Algorithms

*Evolution is a change from an indefinite, incoherent, homogeneity
to a definite, coherent, heterogeneity,
through continuous differentiations and integrations.
-Herbert Spencer-*

Sommario. *La tecnica di identificazione illustrata nel Capitolo precedente richiede la conoscenza delle dilatazioni di tutte le aste. In certi casi, però, tali informazioni potrebbero non essere disponibili, perché le aste potrebbero essere inaccessibili o le misure potrebbero essere corrotte. Tuttavia, nel caso di strutture iperstatiche la rigidità di ogni asta influenza anche lo stato tenso-deformativo del resto della struttura. Questa considerazione sta alla base del tentativo di ricavare informazioni anche sulle aste non strumentate, usando i dati relativi al resto della reticolare.*

Gli algoritmi genetici sono parsi lo strumento più adatto per la risoluzione del problema di ottimizzazione che si pone. Essi, infatti, simulano le rigidità delle aste per le quali non si conoscono le dilatazioni ed identificano il valore più compatibile con il comportamento globale della struttura.

Il passo successivo consiste nella identificazione di danni che non interessino l'asta per l'intera lunghezza. In questo caso, in generale, l'estensimetro misura il valore di dilatazione della zona intatta dell'asta, fornendo così un valore che non è rappresentativo dello stato deformativo globale dell'elemento. Perciò, in questo caso il dato sperimentale non solo non consente l'identificazione diretta del danno, ma risulta addirittura fuorviante. Paradossalmente, sarebbe preferibile non disporre di tale misura e simulare il comportamento dell'asta attraverso gli algoritmi genetici. Questa osservazione induce a confrontare i risultati ottenuti usando tutte le misure di dilatazione, con quelli ottenuti ignorandone una alla volta. Per le aste in cui la rigidezza stimata usando gli algoritmi genetici (cioè ricavando informazioni dal resto della reticolare) risulta sensibilmente più bassa di quella valutata usando la dilatazione misurata, si deve concludere che sono presenti riduzioni locali delle caratteristiche meccaniche, che non interessano l'area su cui è stato applicato l'estensimetro.

Per entrambi i problemi (misure mancanti e danni locali) vengono presentati esempi numerici che mostrano le potenzialità della soluzione proposta.

Alcune considerazioni finali concludono il Capitolo.

9.1 Introductory Remarks

In Chapter 8 a technique for the structural identification of three-dimensional redundant truss structures has been presented. It uses static loads and measurements of the strain of every investigated bar.

However, in some cases the measurements relative to certain bars can be missing for various reasons. For instance, the bar could be unaccessible, or the measurement could be corrupted, or (even if it seems counterintuitive) we could decide to ignore it.

To address this issue, there are useful numerical tools that can be applied proficiently. As in the previous Chapter, inverse problems are often solved through the formulation of an optimization problem. However, when the closed form expression of the objective function is not available, traditional techniques are not suitable. In this kind of problems, optimization methods that make use only of the values of the objective function and do not require additional information

(such as gradients) are required. These optimization procedures are generally known as “direct search methods”. Points are generated and tested for the satisfaction of objectives and constraints through the evaluation of the objective function. The most used class of direct search techniques are Evolutionary Algorithms. They are numerical optimization procedures that find their origin in the Darwinian theory of evolution. Genetic Algorithms (Tomassini, 1995; Abu-Lebdeh and Benekohal, 1999) are one of the specific methodologies that belong to this class.

Genetic Algorithms (GA), or the more general case of Evolutionary Algorithms, have been widely used in many fields of engineering, including structural identification (see, among the others, Mares and Surace, 1996; Chou and Ghaboussi, 2001; Liu and Han, 2003; Faravelli et al., 2005; Casciati, 2006; Vincenzi and Savoia, 2006) and are here applied to the methodology described in Chapter 8 to make it able to estimate the stiffnesses of bars for which a strain measurement is not available (Sec. 9.2).

This consideration allows a further step. When a bar is not entirely damaged, but only a portion of it presents a reduction of the stiffness (e.g. because of local corrosion), the technique proposed in Chapter 8 can not identify the problem. Indeed, the measurement of the strain of that bar will not be affected at all by the presence of the local damage, unless the strain gauge is applied exactly on the damaged area, on purpose¹ or by chance. What is more, the measurement of the strain in the intact portion leads to a wrong estimate of the overall stiffness of the bar, that in the case of redundant structures is also necessary for an accurate estimation of all the other stiffnesses. The paradox is that it would be better to do not have the measurement (and therefore use GA to estimate the stiffness of the element) rather than have a misleading value.

To overcome this problem, it is possible to apply the algorithm once using the whole set of measurements and then m other times (where m is the number of bars) ignoring one measurement at each time. The bars for which results are significantly different when their strain measurement is ignored require further investigation for local damages.

¹This case is not considered here. It is assumed that there is no visual evidence of the local damage. This can be the case of internal damages in tubular elements. Otherwise it can represent the case of a monitored structure where the strain gauges are applied once and the measurements are done periodically, with no further direct access to the location of the gauge. Finally it can be the case of real time control of mechanical structures.

If, on the contrary, the local damage can be visually identified, other techniques are much more suitable than the one proposed in this thesis.

In conclusion, with respect to the algorithm presented in Chapter 8, this further extension allows to deal with missing measurements and with local damages that are not captured by the strain measure².

9.2 Missing Measurements

In the case of a missing measurement (or several missing measurements) the identification procedure is composed by two phases.

The first phase is the identification of the stiffnesses of the bars for which the measurements are available. This task is accomplished using the procedure already described in Sec. 8.3.

The second phase consists in the identification of the remaining stiffnesses by means of Genetic Algorithms.

It should be noticed that the procedure presented in this Section has some known issues and limits of applicability. First of all, it can be applied only to externally statically determinate structures. In fact, the procedure in Sec. 8.3 requires an at least approximate knowledge of the stiffnesses of the “external” bars, while in this case these quantities are the object of the analysis. Moreover, the procedure can be applied only to structures with redundant elements. In fact, if the truss is completely statically determinate, the strains are not dependent on the relative stiffnesses. Thus, the measured strains give no information on the “external” elements. Finally, the accuracy of the results is problem dependent. When only one measurement is missing, the accuracy is high, but when many stiffnesses have to be recovered using GA, the cases of non-unique solutions are frequent.

9.2.1 Proposed Method

The first step of the identification procedure consists in the definition of all the bars for which the strains have been measured as “internal” elements, according to Sec. 8.3. Then the algorithm for the identification of substructures computes the stiffnesses of all the internal bars.

At this point, Genetic Algorithms are applied to simulate the stiffnesses of the bars for which the strains are not available.

²Part of the scientific results reported in this Chapter have already been presented by Viola and Bocchini (2007).

An exhaustive description of the characteristics and of the capabilities of Genetic Algorithms is beyond the purposes of this thesis (refer, for instance, to Goldberg, 1989). However, the most important settings used for the identification procedure are summarized in the following, along with a brief description of the technique.

GA initialize a “population” of twenty individuals, that represent the possible solutions of the optimization problem. In this case, each individual is a vector whose elements are potential stiffnesses α_e^* of the “external” bars. The initial population is defined by the user, but one of the most important properties of GA is that the result is usually almost insensitive to the initial population. For every individual, the objective function (called “fitness function”) is evaluated.

For this identification problem, four different fitness functions have been considered. The first is defined as

$$Fit_1 = - \max_i \left[\max_k (|\varepsilon_{ik}^* - \varepsilon_{ik}|) \right] \quad (9.1)$$

where ε_{ik} is the strain measured on the “internal” element i during the load test k ; ε_{ik}^* is the theoretical strain of the element i obtained by means of a structural analysis with load condition k and stiffnesses α_e^* for the external elements. This fitness function measures the maximum difference between the measured strains and those induced by the stiffnesses α_e^* .

The second fitness function is obtained considering energies. For each load condition k , the work of external forces and the total strain energy can be equated:

$$\underbrace{\frac{1}{2} \sum_f F_f \eta_f^*}_{\text{external work}} = \underbrace{\frac{1}{2} \sum_i \alpha_i \varepsilon_i^2 l_i}_{\text{energy internal elements}} + \underbrace{\frac{1}{2} \sum_e \frac{(N_e^*)^2 l_e}{\alpha_e^*}}_{\text{energy external elements}} \quad (9.2)$$

where f is the index of the applied loads; l_e and l_i are the length of external and internal bars, respectively; α_i is the stiffness of the internal element i (previously identified), η_f^* is the displacement of the degree of freedom to which the load f is applied, obtained by means of a structural analysis with stiffnesses α_e^* for the external elements; N_e^* is the axial force in the external element e , computed by the same analysis. Since the α_e^* 's are not the real stiffnesses, in general Eq. (9.2) is not satisfied. The second fitness function is the sum of the residuals

of Eq. (9.2):

$$Fit_2 = - \sum_{k=1}^K \left| \sum_f F_f \eta_f^* - \sum_i \alpha_i \varepsilon_i^2 l_i - \sum_e \frac{(N_e^*)^2 l_e}{\alpha_e^*} \right|_k \quad (9.3)$$

The third fitness function is a sort of quadratic norm:

$$Fit_3 = - \sqrt{\sum_i \left[\sum_{k=1}^K (\varepsilon_{ik}^* - \varepsilon_{ik})^2 \right]} \quad (9.4)$$

where the notation is the same as Eq. (9.1).

The last fitness function is

$$Fit_4 = - \sum_i \left(\sum_{k=1}^K |\varepsilon_{ik}^* - \varepsilon_{ik}| \right) \quad (9.5)$$

where the notation is the same as Eq. (9.1). This fitness function measures the total difference between the measured strains and those induced by the stiffnesses α_e^* .

The first two fitness functions have shown the highest accuracy, robustness and sensitivity for the problems of local damage identification (see Sec. 9.3), the third is usually better for the problems of missing measurements. However, by means of a preliminary numerical test, the user can easily understand which one is more suitable for a particular structural problem.

When one of the proposed fitness functions has been chosen and evaluated for every individual of the population, they are sorted from the one with the highest fitness to the one with the lowest ("Rank fitness scaling").

At this point, the generation of the offspring starts. The two most fitted elements ("Elite") are directly transferred to the offspring. Fourteen individuals ("Crossover fraction" $\cong 0.8$) are generated by "scattered" crossover, that means that they are generated by random combination of two parents. Four more individuals are obtained by "adaptive feasible" mutation of four individuals of the previous generation. This means that a small random perturbation is applied to four individuals, in directions (of the space of admissible solutions) that are adaptive with respect to the last successful or unsuccessful generation.

In this way, a new population of twenty individuals is complete and the algorithm can iterate the evaluation of the fitness and the generation of a new

offspring. The algorithm proceeds until a convergence criterion is satisfied. The convergence criterion determines the end of the iterations when the weighted³ average change in the fitness function value over a limit number of generations (“stall generations”) is less than a certain tolerance.

During the whole optimization procedure, the obvious condition that the stiffnesses have to be positive is taken into account by using a lower bound.

The stiffnesses that maximize the fitness function are chosen as stiffnesses of the external bars.

9.2.2 Numerical Application

The three-dimensional truss structure in Fig. 9.1 is considered for a numerical application. The three columns have a product $EA = 500MN$, while the horizontal bars and the diagonal braces have $EA = 260MN$. Bars 5–8, 2–4 and 5–7 are damaged and their stiffnesses have been reduced by 5%, 10% and 20%, respectively. The strain values for bar 5–7 have not been used for the identification procedure.

Vertical test loads have been applied to nodes 7, 8 and 9; a horizontal load in the y direction has been applied to node 9. All the forces have a modulus of $100kN$. A random noise, uniformly distributed in the interval $[-1kN, 1kN]$, has been applied to the loads and another one uniformly distributed in the interval $[-10^{-6}, 10^{-6}]$ has been superimposed to the resulting strains.

The starting value for the stiffnesses have been computed multiplying the real EA by a random factor uniformly distributed in the interval $[0.5, 1.5]$.

The third fitness function in Eq. (9.4) has been used.

The results are reported in Table 9.1 and in Fig. 9.2. It can be noticed that the resulting stiffnesses are accurate for all the bars, including those relative to the damaged elements and the one for which the strain values were not available.

9.3 Local Damages

The basic ideas presented in Sec. 9.2 are used for the identification of local damages. In this Section the hypothesis of constant stiffness along the bar is removed. The “local damage” is modeled as a reduction of the stiffness in a

³The individuals with the highest ranks have a larger weight.

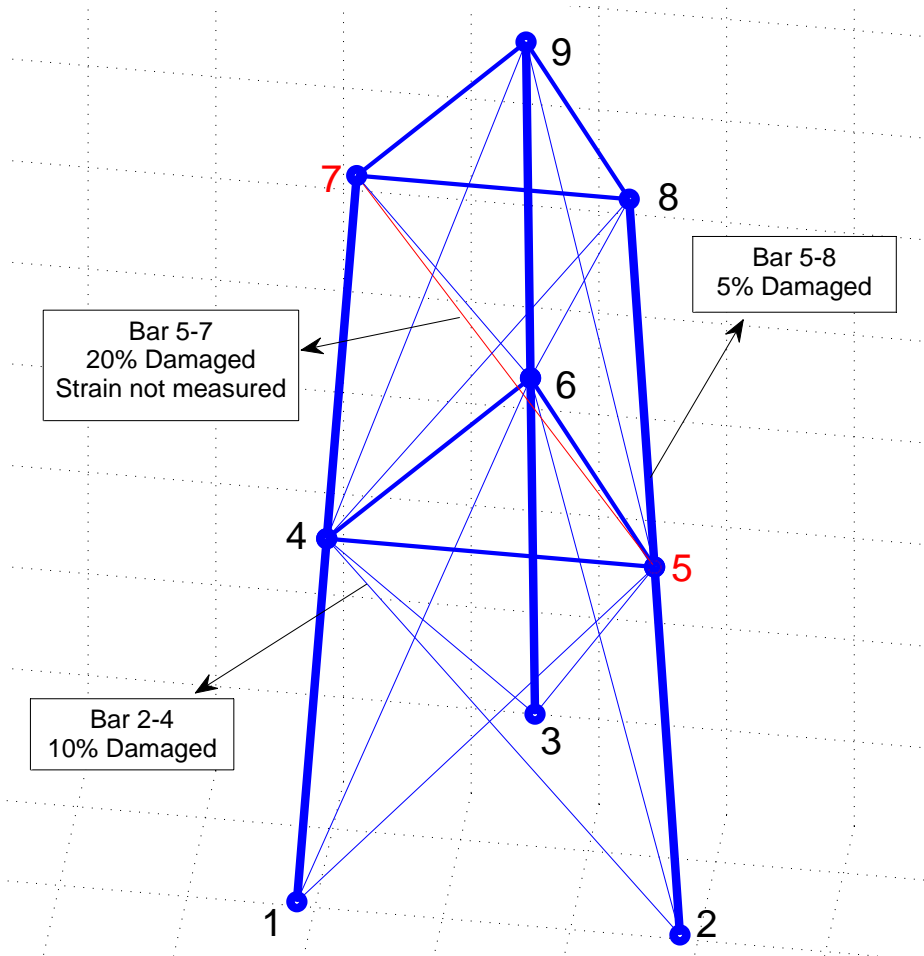


Figure 9.1: Three-dimensional truss structure. The displacements in the x direction are restrained at node 1; the displacements in the y direction are restrained at nodes 1 and 2; the vertical displacements are restrained at nodes 1, 2, and 3.

Bar number	Bar nodes	Starting stiffness <i>MN</i>	Real stiffness <i>MN</i>	Estimated stiffness <i>MN</i>	Percentage error
1	1-4	397.6298	500	501.1966	0.2%
2	4-7	469.9104	500	495.6273	0.9%
3	2-5	729.8900	500	500.0699	0.0%
4	5-8	728.9258	475	481.9681	1.5%
5	3-6	709.9988	500	500.4787	0.1%
6	6-9	740.3070	500	499.1665	0.2%
7	4-5	363.7472	260	254.8917	2.0%
8	5-6	186.4613	260	264.5828	1.8%
9	6-4	179.5987	260	262.7818	1.1%
10	7-8	217.4499	260	258.6364	0.5%
11	8-9	325.2085	260	260.1329	0.1%
12	9-7	370.0673	260	263.6021	1.4%
13	1-5	163.6789	260	256.4323	1.4%
14	1-6	271.7900	260	264.7547	1.8%
15	2-4	194.3111	234	227.1598	2.9%
16	2-6	372.7995	260	261.5243	0.6%
17	3-4	366.4729	260	266.3674	2.4%
18	3-5	352.7563	260	259.1279	0.3%
19	4-8	186.0993	260	267.5147	2.9%
20	4-9	209.3012	260	263.2370	1.2%
21	5-7	376.8568	208	209.4818	0.7%
22	5-9	291.0418	260	266.2242	2.4%
23	6-7	247.7684	260	259.5376	0.2%
24	6-8	372.5815	260	253.9513	2.3%

Table 9.1: Stiffnesses estimated for the three-dimensional truss in Fig. 9.1.

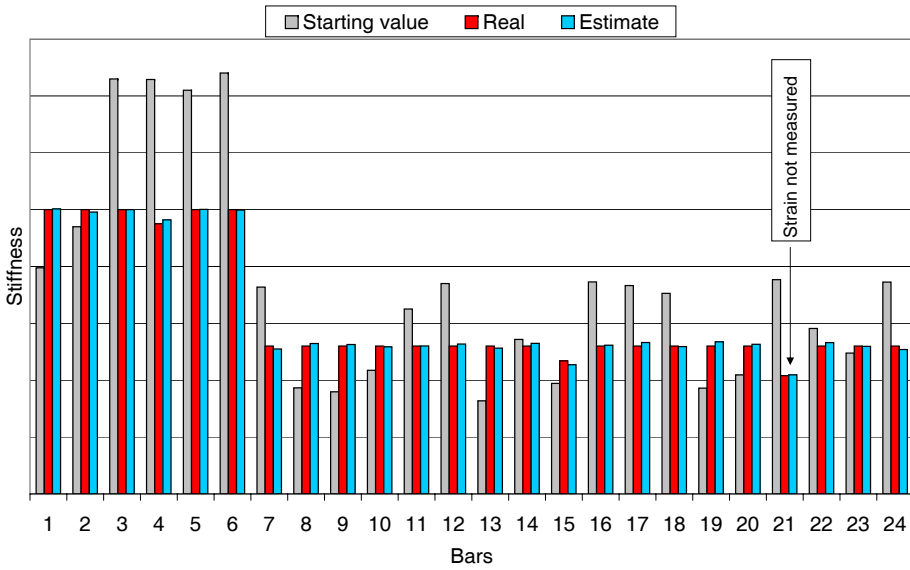


Figure 9.2: Stiffnesses estimated for the three-dimensional truss in Fig. 9.1, compared to the starting values of the iterative procedure and to the real values. The accuracy is good for all the bars, including the bar for which the strain values were not available.

portion of the bar, while the strain gauge measures the strains in the main (intact) part of the bar⁴. The axial force N is constant along the length of the bar:

$$N = \alpha_u \varepsilon_u = \alpha_d \varepsilon_d = \alpha_g \varepsilon_g \quad (9.6)$$

where the subscript u denotes the quantities relative to the undamaged part, the subscript d denotes the quantities relative to the damaged part and the subscript g denotes the virtual equivalent (“global”) quantities relative to the whole bar as if it had constant stiffness. The overall variation of length Δl_g of the bar can be computed as:

$$\begin{aligned} \Delta l_g &= \Delta l_u + \Delta l_d \\ \frac{Nl}{\alpha_g} &= \frac{Nl_u}{\alpha_u} + \frac{Nl_d}{\alpha_d} \end{aligned} \quad (9.7)$$

Using Eq. (9.7), the equivalent overall axial stiffness α_g of the bar is given by:

$$\alpha_g = l \frac{\alpha_u \alpha_d}{l_u \alpha_d + l_d \alpha_u} \quad (9.8)$$

As already mentioned, in this case the values of the strains are misleading, and a better estimation of the overall stiffness of the bar can be obtained by means of Genetic Algorithms, as explained in Sec. 9.2.

It should be noticed that this procedure is applicable only to (internally and/or externally) redundant structures, because for statically determinate structures the stiffness of a bar does not affect the behavior of the others.

9.3.1 Proposed Method

To identify local damages, the proposed code works as follows. Firstly the code computes the stiffnesses of all the bars using the procedure explained in Sec. 8.2. For the bars with local damages, the strains ε_u are used, therefore the results of this identification are inaccurate, especially for the bars with local damages, whose stiffnesses are overestimated.

The next step depends on the external constraints. If the structure is externally statically determinate, the code performs m identification procedures

⁴It could also happen that the strain gauge is accidentally located in the damaged portion. In this case, the algorithm presented in Chapter 8 identifies a damage. This case is not treated in the present Chapter.

(where m is the number of bars) as explained in Sec. 9.2.1, disregarding each time the stress measurements of one bar (i.e. each time one of the m bar is considered “external”). In this way, each one of the m sets of stiffness values is completely independent from the strains on one bar. If the structure is externally redundant, the procedure presented in Sec. 9.2.1 can not be used. In this case the algorithm uses m times a modified version of the aforementioned procedure, in which, for the “internal” bars, the stiffnesses computed in the first analysis (the one in which all the measurements are employed) are used. Therefore, in this case it is not true that each one of the m sets of stiffness values is completely independent from the strains on one bar. In fact, the stiffnesses of the internal bars are computed using all the measurements. Nevertheless, also in this case, the value of the stiffness on a bar obtained when it is considered “external” is much less dependent on its strains than the value obtained considering all the measurements.

At this point, it is possible to identify the bars with local damages comparing the values of the stiffnesses obtained using all the strain measurements with the value obtained for each bar when it has been considered “external”. If the latter value is significantly⁵ lower, a local damage is present.

In the case of externally statically determinate structures, no more steps are required. When a local damage is identified in a bar, the value of stiffness computed by GA is assumed as overall equivalent stiffness α_g .

In the case of externally redundant structures, some further operations are necessary. The algorithm identifies the bar whose stiffness results the most reduced when computed by GA. For this element, the stiffness computed by GA is assumed as overall equivalent stiffness α_g . Then the code corrects the value of the strains measured on this bar replacing them with the equivalent overall strains ε_g computed inverting Eq. (9.6):

$$\varepsilon_g = \frac{\alpha_u \varepsilon_u}{\alpha_g} \quad (9.9)$$

In this way, the element with local damage is completely replaced by a virtual equivalent element with constant stiffness along its length. Then the code, repeats the procedure presented in this Section (called a “run”) to check if other local damages are present. When, at the end of a run, all the differences between the values of the stiffnesses obtained using all the strain measurements and the

⁵The threshold of significant difference depends on the expected accuracy of the method and on the amount of noise (i.e. the precision of the measures). Usually, the estimation error is lower than 5%, therefore the threshold on the percentage difference should be around 5%.

values obtained for each bar when it is considered “external” are lower than the accuracy of the method, it means that all the bars with local damages have been identified and replaced by their equivalent uniform element.

9.3.2 Numerical Applications

The case of externally statically determinate structures with local damages reduces to the application of the procedure proposed in Sec. 9.2. Thus, no more examples are presented.

Two numerical applications for the more interesting case of externally redundant trusses are presented.

The plane truss represented in Fig 8.4 is considered again. In this case, bars 5 and 9 have stiffness reduced to $7MN$, while bar 1 has a local damage modeled as a reduction of the 50% of its stiffness over one seventh of its length (thus, the overall equivalent stiffness is $61.25MN$). The same 5 loads used in Sec. 8.5.2 are applied.

The results of the analysis are presented in Table 9.2 and Fig. 9.3. It can be seen that after the first run of the procedure presented in Sec. 9.3.1, the stiffness of bar 1 estimated ignoring its strains is almost 10% lower than the stiffness evaluated considering all the measurements. Therefore, the local damage in bar 1 is identified.

Then, the algorithm replaces bar 1 (stiffness and strains) with its equivalent uniform bar and a second run of the procedure presented in Sec. 9.3.1 is performed. After the second run, all the differences are lower than the 5% threshold, so no more local damages are present.

It should be noticed that the algorithm not only identifies the bar with local damage, but also computes the overall stiffness of that element with good accuracy.

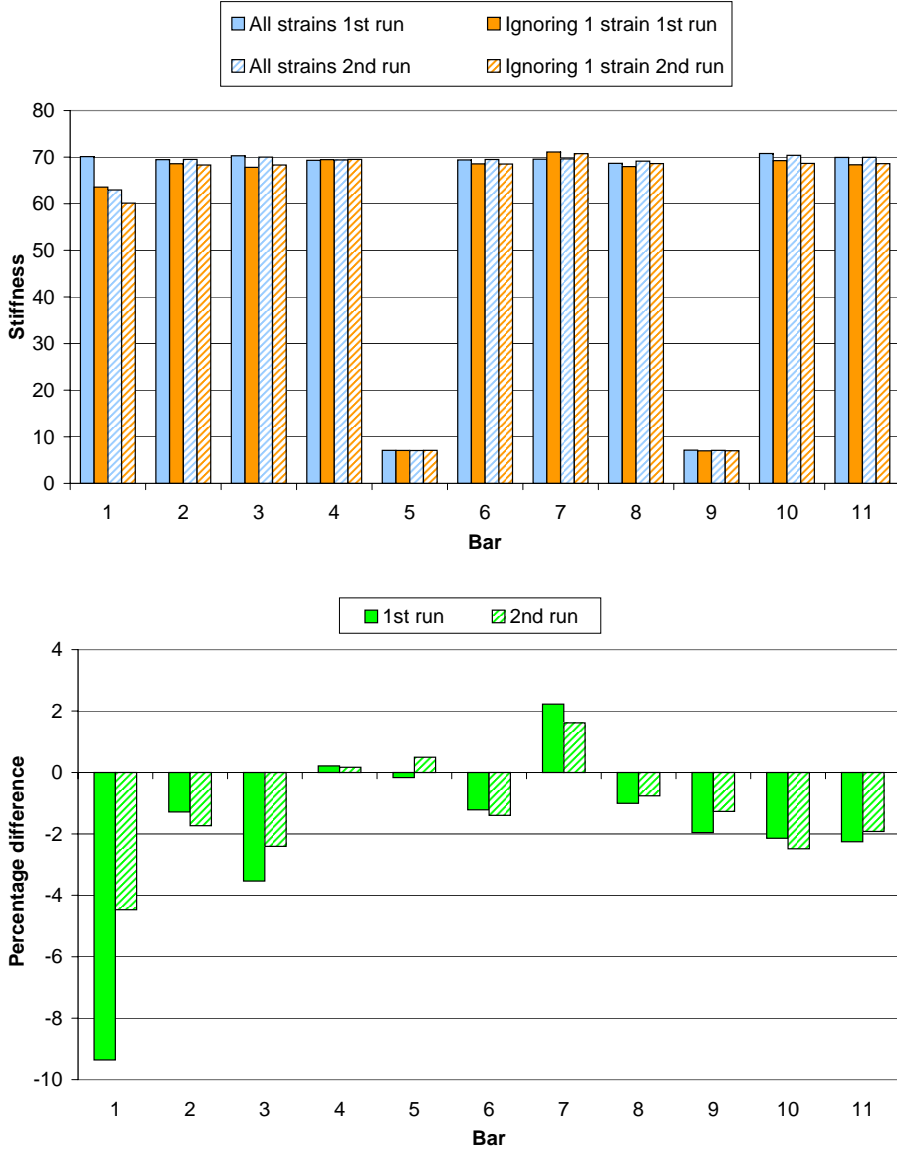


Figure 9.3: Stiffnesses estimated for the truss in Fig. 8.4 with local damage. After the first run the stiffness estimated for the first bar disregarding its strain value is almost 10% lower than the one obtained considering the strain. After the identification of the local damage, all the difference are less than 5%.

Bar no.	Bar nodes	Stiffness with all strains 1 st run <i>MN</i>	Stiffness ignoring 1 strain 1 st run <i>MN</i>	% diff. 1 st run	Stiffness with all strains 2 nd run <i>MN</i>	Stiffness ignoring 1 strain 2 nd run <i>MN</i>	% diff. 2 nd run
1	1–2	70,1	63,6	-9,4	62,9	60,1	-4,5
2	2–4	69,5	68,6	-1,3	69,5	68,3	-1,7
3	2–3	70,3	67,8	-3,5	70,0	68,3	-2,4
4	1–4	69,3	69,5	0,2	69,4	69,5	0,2
5	1–3	7,1	7,1	-0,2	7,1	7,1	0,5
6	3–4	69,4	68,6	-1,2	69,5	68,5	-1,4
7	4–6	69,6	71,1	2,2	69,6	70,7	1,6
8	4–5	68,7	68,0	-1,0	69,1	68,6	-0,8
9	3–6	7,1	7,0	-2,0	7,1	7,0	-1,3
10	3–5	70,8	69,3	-2,1	70,4	68,6	-2,5
11	5–6	69,9	68,4	-2,3	69,9	68,6	-1,9

Table 9.2: Stiffnesses estimated for the truss in Fig. 8.4 with local damage.

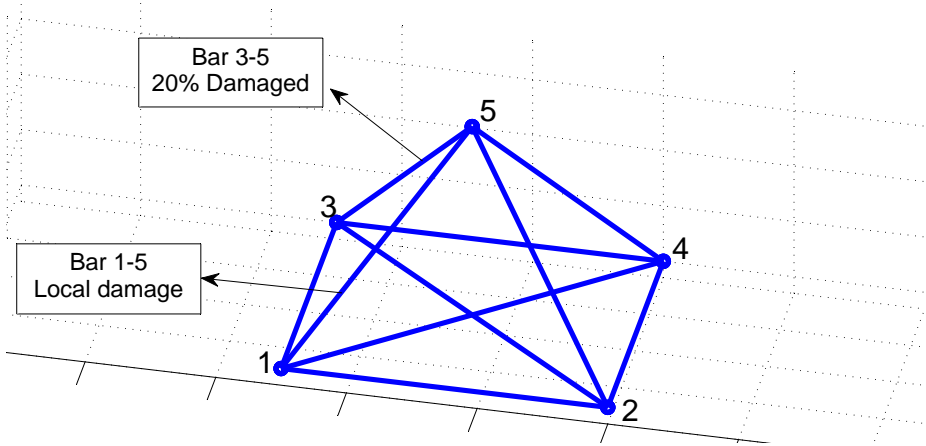


Figure 9.4: Three-dimensional truss structure. The displacements in the x direction are restrained at node 1; the displacements in the y direction are restrained at nodes 1 and 2; the vertical displacements are restrained at nodes 1, 2, 3 and 4.

The second numerical application involves the three-dimensional redundant truss in Fig. 9.4. The intact bars have a stiffness of $40MN$. Bar 3–5 has a stiffness uniformly reduced by 20% (resulting $32MN$). Bar 1–5 has a local damage, modeled as a stiffness of $20MN$ over one fifth of its length.

Only three load conditions have been applied: three orthogonal forces at node 5.

The results of the analysis are presented in Table 9.3 and Fig. 9.5. After the first run of the procedure presented in Sec. 9.3.1, the stiffnesses of bars 4 and 5 estimated ignoring their respective strains are significantly lower than the stiffnesses evaluated considering all the measures. The algorithm replaces the bar for which the results exhibits the largest difference, that is bar 5 (the one actually damaged). After the second run, all the percentage differences are lower than 2%, that means that no more local damages are present. In this case, the difference on the stiffnesses of bar 4 was a collateral effect of the damage in bar 5. However, the difference relative to bar 5 was much larger than the difference relative to bar 4, so it was very clear in which bar was more probable

Bar no.	Bar nodes	Stiffness with all strains 1 st run <i>MN</i>	Stiffness ignoring 1 strain 1 st run <i>MN</i>	% diff. 1 st run	Stiffness with all strains 2 nd run <i>MN</i>	Stiffness ignoring 1 strain 2 nd run <i>MN</i>	% diff. 2 nd run
1	1-2	40,2	46,7	16,2	40,1	40,6	1,1
2	2-4	40,4	42,8	6,1	40,5	40,0	-1,4
3	4-3	40,2	40,9	1,8	40,4	40,4	0,1
4	3-1	40,5	36,0	-11,3	40,6	40,0	-1,4
5	5-1	40,8	33,6	-17,5	33,2	33,5	0,8
6	5-2	40,4	41,2	2,0	40,5	40,2	-0,6
7	5-3	32,1	32,4	0,9	32,1	32,1	0,1
8	5-4	39,8	46,3	16,3	40,2	39,9	-0,7
9	1-4	39,5	53,1	34,5	40,0	39,8	-0,5
10	2-3	39,9	74,1	85,5	39,7	39,3	-0,9

Table 9.3: Stiffnesses estimated for the truss in Fig. 9.4 with local damage.

to find the local damage. The results of the second run have confirmed that the guess was correct.

9.4 Concluding Remarks

Genetic algorithms have been used to handle the problems of missing measurements and local damages.

The procedure presented in Chapter 8 is well established, while the extensions proposed in this Chapter are still works in progress. For instance, the best set of parameters for GA (in particular the fitness function) is still a topic of investigation. Moreover, the code presents a loss of accuracy when the number of missing measurements increases. Finally, in three-dimensional trusses there are so many possible load paths that the algorithm can easily lose sensitivity to some stiffnesses.

Nevertheless, the presented numerical results prove that, within the aforementioned limits of applicability, the method exhibits a good accuracy and a strong potential. In particular, the inherent capabilities of GA to avoid local extremes, to manage multi-dimensional objective functions and, most of all, to

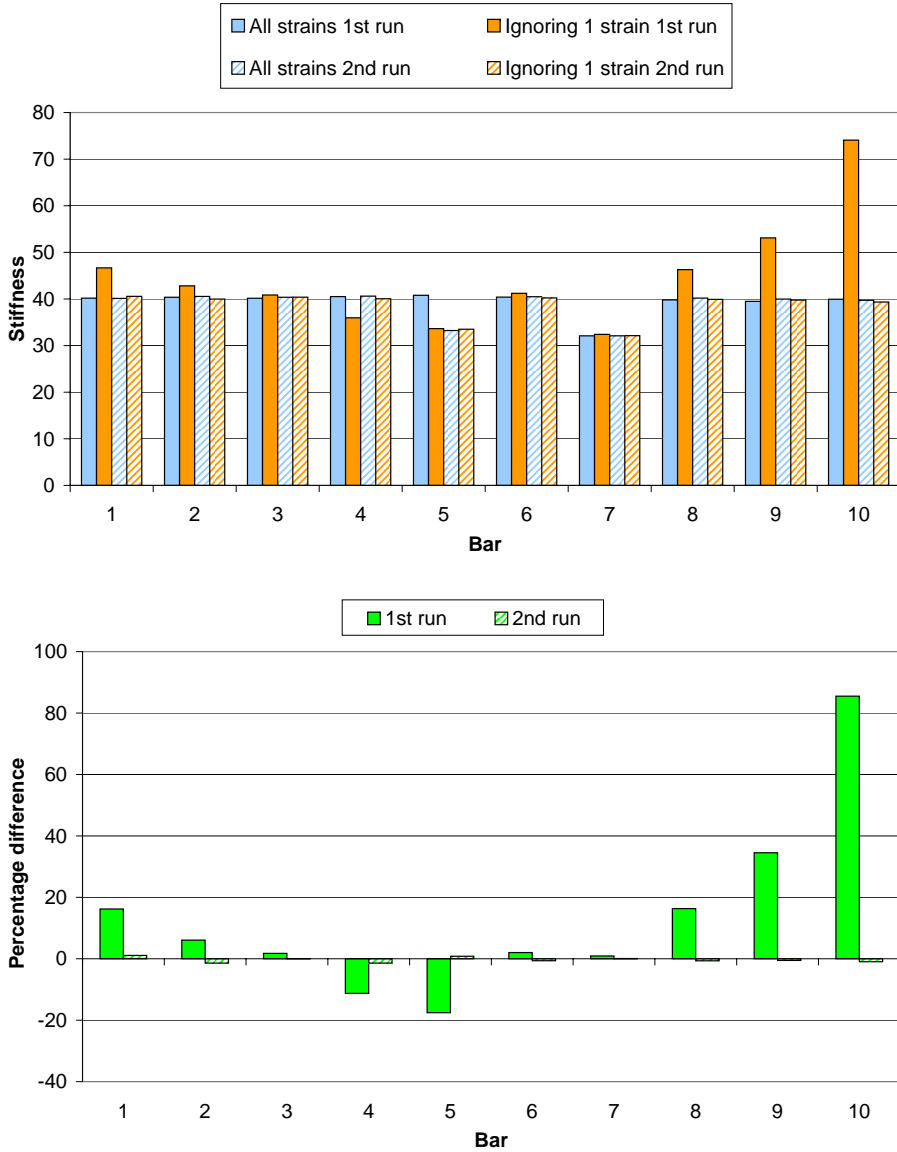


Figure 9.5: Stiffnesses estimated for the truss in Fig. 9.4 with local damage. After the first run the stiffness estimated for bar 5 disregarding its strain value is almost 20% lower than the one obtained considering the strain. After the identification of the local damage, all the difference are less than 2%.

do not require gradients and closed form definitions of the objective function are very interesting, promising and matching the characteristics required by this particular structural identification approach.

Chapter 10

General Conclusions

*The principal means for ascertaining truth
(induction and analogy) are based on probabilities;
so that the entire system of human knowledge
is connected with the theory of probability
-Pierre Simon Laplace-*

Sommario. *Le tecniche di simulazione di campi aleatori omogenei, multidimensionali e multivariati presentate nella prima parte della tesi sono uno strumento completo e versatile che migliora ed espande le possibilità di applicazione dell'analisi probabilistica in generale e della Simulazione alla Monte Carlo in particolare. I numerosi esempi numerici ed i confronti con le altre metodologie mostrano le capacità degli algoritmi proposti in termini di accuratezza, robustezza e possibilità di simulare campi con le distribuzioni di probabilità anche più fortemente non-Gaussiane. Il generatore di campi multivariati, con la sua capacità di identificare la "underlying Gaussian coherence" è probabilmente il risultato scientificamente più interessante fra quelli presentati. In questo settore, i possibili sviluppi sono un'estensione dell'analisi comparativa ai casi multidimensionali e multivariati, ma, soprattutto, il completamento delle applicazioni pratiche presentate al Capitolo 7.*

La tecnica di identificazione presentata al Capitolo 8 consente di rag-

giungere ottimi livelli di accuratezza nell'identificazione delle caratteristiche meccaniche degli elementi che costituiscono strutture reticolari piane e spaziali, isostatiche ed iperstatiche. L'utilizzo congiunto di tale tecnica con gli algoritmi genetici per risolvere i problemi di misure mancanti e danni locali è ancora oggetto di studio. Tuttavia, già allo stato attuale si possono ottenere ottimi risultati per i problemi meno complessi. Gli studi futuri verteranno sul raffinamento della metodologia per renderla più robusta e quindi espanderne il campo di applicabilità.

Lo sviluppo più interessante, però, potrebbe essere l'utilizzo congiunto delle conoscenze, degli strumenti, delle abilità e dei risultati ottenuti nei due settori di studio sin qui analizzati per iniziare ricerche nel campo dell'identificazione probabilistica.

10.1 Final Remarks

In this thesis, some advancements in the field of probabilistic approaches and tools for civil engineering problems have been presented.

The core of the thesis, **Part I**, deals with the simulation of random fields. The goal reached by the research work presented in this Part is the development of a versatile procedure for the generation of homogeneous, multi-dimensional, multi-variate random samples with any kind of marginal probability distribution, including the most strongly non-Gaussian ones.

The presented original procedure can be considered as the latest development of a class of Spectral-Representation-based methods. This new technique synthesizes the best characteristics of its predecessors, as a numerical comparison has shown. The accuracy in matching both the prescribed spectral density and marginal probability is comparable with the one of the most accurate methods. The underlying field remains Gaussian throughout the iterations of the algorithm and, therefore, the produced samples have all the desired and useful properties of translation fields (e.g. crossing rates and distribution of extremes). The identification of the underlying Gaussian field is computationally expensive, but it is less expensive than the procedure suggested by Shi and Deodatis (2004), while the generation of random samples is as efficient as the one adopted by the Shi and Deodatis method. In the framework of Monte Carlo Simulation, the overall computational effort for the production of a large number of random

samples with the prescribed characteristics by means of the proposed technique is usually negligible with respect to the cost of the other phases of the simulation. The compatibility between marginal distribution and spectral density is obtained in a “natural” way, without a forced and artificial spectral preconditioning that can lead to an unnatural target SDF. Moreover, the capability of this technique to search for the best underlying Gaussian field in a wide range of possible solutions has made the issue of compatibility appear less restrictive than what seemed in the past years.

The robustness of the technique has allowed to experiment the generation of samples with marginal distributions with extreme non-Gaussianity. Also in these cases, the algorithm has exhibited good accuracy. Only in one numerical example the matching of the prescribed SDF has been relatively poor. This can be interpreted as the limit of applicability of the method, or as the limit of the range in which an arbitrary choice of target SDF and PDF can be made with no significant problems of compatibility.

The generalizations to the simulation of multi-dimensional and multi-variate fields have widely extended the possible practical applications. Moreover, this latter generalization has introduced the concept of “underlying Gaussian Coherence” and a procedure for its identification. Also in this case, the numerical examples involving strongly non-Gaussian fields have proved the accuracy and robustness of the proposed approach. This original contribution is probably the most interesting scientific result presented in this thesis.

The global result of Part I is a comprehensive simulation tool for (strongly) non-Gaussian translation fields. The usefulness of this technique depends on the fact that very often the physical quantities involved in engineering problems present non-Gaussian characteristics. At the moment, two practical applications in the fields of stochastic geomechanics and bridge reliability have been set up.

Besides this, an investigation on the simulation of multi-variate Gaussian fields has been conducted. It has been shown that the numerical technique commonly used for the generation of vector fields by Spectral Representation implies a slight difference between the resulting SDF and the target, whose magnitude increases with the roughness of the discretization in the wave number domain. A closed form expression that describes the actual CSDM of the produced samples has been provided. This, in turn, has two effects. The first is that the proof of ergodicity of the samples that previously applied only to the “continuous” case has been extended to the case of simulation with the use of Fast Fourier Transform (i.e. almost any practical applications). The second

effect is that knowing a priori the resulting spectrum, the prescribed target can be tuned so that the samples match exactly the desired SDF.

The topics of **Part II** are structural identification and damage assessment. A procedure for the identification of three-dimensional redundant truss structures with static loads and strain measurements has been presented. The method appears robust, effective and accurate, but requires two major hypothesis: the stiffnesses of all the bars are measured and they are constant along the length. Genetic Algorithms, an optimization technique based on the concepts of evolution, random combination and random mutation, are employed to remove the two aforementioned hypothesis.

The basic idea is that the redundancy of the structure implies that the characteristics of a bar affect also the static (stresses and strains) condition of the other elements. Therefore, even when the information relative to a bar is missing or is misleading (in the case of local damages) its stiffness can be estimated using data regarding the other ones.

Several issues that arise and certain limits of applicability have been enlightened. However, the numerical examples have shown that the proposed methods have attractive capabilities and an interesting potential and, therefore, that they are worthy of further investigations.

10.2 Future Developments

The methods proposed in **Part I** are already well established, therefore the most interesting and natural development of the work in this field is their application. Besides the two aforementioned fields, many other can be found. In fact, Monte Carlo Simulation is suitable (and often required) for the solution of any kind of stochastic mechanics problem.

Nevertheless, some further studies should be conducted. The first is the realization of a code for the generation of non-Gaussian samples that are both multi-dimensional and multi-variate. In fact, until now the two problems have been treated using different codes, but in some cases the physical quantities are described by vector fields in two- or three-dimensional domains. The second investigation is a comparison between the original technique for the multi-variate case and other methodologies, especially the one presented by Chen and Deodatis (2004), that present some similarities. This can also be the occasion to investigate the limits of applicability of the procedure, as it has been done for

the uni-variate case.

As for the techniques presented in **Part II**, some of the possible developments have already been mentioned in Sec. 9.4 and regard the use and the settings of Genetic Algorithms.

Moreover, the design of the experiment has to be optimized. In particular, the methods have presented a strong sensitivity to the maximum level of stress/strain reached by every bar in the load tests. This sensitivity is increased when GA are applied, because the input data are reduced in quantity (missing measurements) or quality (local damages). The applications presented in Chapter 8 have shown that in problems like these, the numerical and practical aspects are more important than the theoretical ones. In this case, in fact, the condition to make each bar reach a sufficient stress level has proved to be much stricter than the analytical ones. In the same way, some “practical rules” should be found also for the cases of missing measurements and local damages.

The most interesting development, however, would be a convergence of the topics studied in the **two Parts** of the thesis. In fact, today the most interesting and challenging structural and damage identification problems have to be approached in a fully probabilistic way. Ocean waves on offshore structures, gusts on airplane wings, wind on tall buildings, pressure waves in pipe systems are some of the random loads that can be used as test loads for identification and control purposes. However, these loads can be known and described only in a probabilistic sense, therefore in these applications the theories of simulation and random fields have to be used together with the techniques that belong to the topic of inverse problems. The skills, the tools and the knowledge acquired studying the two fields separately can be employed in the best possible way in problems that involve both of them.

Appendix A

Random Fields

*The theory of probabilities is basically
just common sense reduced to calculus;
it makes one appreciate with exactness
that which accurate minds feel with a sort of instinct,
often without being able to account for it.
-Pierre Simon Laplace-*

Sommario. *I concetti di base della teoria dei campi aleatori richiamati dagli algoritmi di simulazione presentati nella prima parte della tesi vengono qui brevemente illustrati.*

Si è scelto di ridurre al minimo i formalismi e prediligere un taglio più ingegneristico ed applicativo.

A.1 Introductory Remarks

A random field is a continuous or discrete function that is not defined deterministically, but only through a probabilistic characterization. The formal theory of random fields is a well-established discipline with applications in many areas of engineering and science. In mechanics, the most common physical domains are space, time, and spacetime. Traditionally, the phrase “random field” indicates

a function in the n -dimensional space domain, “stochastic process” (or “random process”) refers to an uncertainty in the time domain, while “stochastic wave” (or “random wave”) denotes a function in the $(n + 1)$ -dimensional spacetime. In this thesis, the case of random fields in the space domain is considered. The extension to the case of stochastic processes is straightforward.

Many authors have written exhaustive monographs that treat the theory of random fields. Here a brief description of the basic properties and characteristics that are useful for the purposes of the thesis is provided. A more complete and formal background may be found on the texts by Lin (1967); Vanmarcke (1983); Bendat and Piersol (1986); Grigoriu (1995) and Elishakoff (1999) among the others. Exhaustive monographs on the theory of probability in engineering problems have been written, for instance, by Benjamin and Cornell (1970); Beck and Arnold (1977); Ang and Tang (1984).

A.2 General Definition

A one-dimensional, uni-variate random field $W(x)$ is an ensemble of space functions that can be characterized statistically. An equivalent definition is the following: a random field $W(x)$ is a parametered family of random variables, with the parameters belonging to an indexing set. Other, more mathematical, definitions can be found in the literature.

A single “realization” or “sample function” of the random field is indicated by $W_i(x)$. The infinity of realizations is the random field. From this point of view, the first definition of random field describes it as an ensemble of complete realizations (i fixed), on the contrary, the second definition focuses on an ensemble of the values assumed at a certain point (x fixed) by the various realizations.

In increasing order of completeness, the probabilistic structure of a random field is described by the following series of probability densities:

$$\left\{ \begin{array}{l} f_{W(x_1)}(w_1) \\ f_{W(x_1)W(x_2)}(w_1, w_2) \\ \vdots \\ f_{W(x_1)W(x_2)\dots W(x_n)}(w_1, w_2, \dots, w_n) \\ \vdots \end{array} \right. \quad (\text{A.1})$$

or

$$\left\{ \begin{array}{l} f_{\{W\}}(w, x) \\ f_{\{W\}}(w_1, x_1; w_2, x_2) \\ \vdots \\ f_{\{W\}}(w_1, x_1; w_2, x_2; \dots; w_n, x_n) \\ \vdots \end{array} \right. \quad (\text{A.2})$$

However, it is almost impossible to compute joint probabilities of order greater than two. Anyway, if the higher-order probability densities are known, the lower-order ones can be computed by means of a closed form formula. The first order probability density determines the “marginal distribution” of the random field.

Even if in theory the whole set of probability densities is required for the description of the field, for practical applications only the first two orders are usually considered.

A.3 Description of a Random Field

A random field can be described by moments of various order:

$$\text{mean: } \mu_W(x) = E[W(x)] = \int_{-\infty}^{\infty} w f_{\{W\}}(w, x) dw \quad (\text{A.3})$$

where $E[\cdot]$ denotes the expected value,

$$\text{mean square: } E[W^2(x)] = \int_{-\infty}^{\infty} w^2 f_{\{W\}}(w, x) dw \quad (\text{A.4})$$

$$\text{variance: } Var\{W(x)\} = E[\{W(x) - \mu_W(x)\}^2] = E[W^2(x)] - \mu_W^2(x) \quad (\text{A.5})$$

and the standard deviation is defined as

$$\text{std: } \sigma_W(x) = \sqrt{Var\{W(x)\}} \quad (\text{A.6})$$

These quantities describe the probabilistic characteristics of values at a single point. Other quantities describe the relations between the values at different points:

$$\text{autocorrelation: } R_{WW}(x_1, x_2) = E[W(x_1)W(x_2)] \quad (\text{A.7})$$

$$f_{\{W\}}(w_1, x_1; w_2, x_2) = f_{\{W\}}(w_1, 0; w_2, x_2 - x_1) \quad (\text{A.15})$$

therefore the first order density is constant and the second order joint density depends only on the lag $\xi = x_2 - x_1$

$$R_{WW}(x_1, x_2) = R_{WW}(x_2 - x_1) = R_{WW}(\xi) \quad (\text{A.16})$$

In the thesis, since only the first two order statistical descriptors are considered, the weekly homogeneity is sufficient and is called simply “homogeneity”.

A.5 Properties of the Correlation Functions

A.5.1 General Case

Symmetry:

$$\begin{cases} R_{WW}(x_1, x_2) = R_{WW}(x_2, x_1) \\ R_{WZ}(x_1, x_2) = R_{ZW}(x_2, x_1) \end{cases} \quad (\text{A.17})$$

Non-negative definiteness:

$$\sum_{j=1}^n \sum_{k=1}^n R_{WW}(x_j, x_k) h(t_j) h(t_k) \geq 0 \quad \forall h(x) \quad (\text{A.18})$$

The second property is a strict condition on the domain of admissible functions that can represent an autocorrelation.

A.5.2 Homogeneous Case

Symmetry:

$$\begin{cases} R_{WW}(\xi) = R_{WW}(-\xi) \\ R_{WZ}(\xi) = R_{ZW}(-\xi) \end{cases} \quad (\text{A.19})$$

Non-negative definiteness:

$$\sum_{j=1}^n \sum_{k=1}^n R_{WW}(x_j - x_k) h(t_j) h(t_k) \geq 0 \quad \forall h(x) \quad (\text{A.20})$$

$$\sum_{j=1}^n \sum_{k=1}^n R_{WZ}(x_j - x_k) h(t_j) h(t_k) \geq 0 \quad \forall h(x) \quad (\text{A.21})$$

Inequalities:

$$|R_{WW}(\xi)| \leq R_{WW}(0) \quad (\text{A.22})$$

$$|R_{WZ}(\xi)| \leq \sqrt{R_{WW}(0) R_{ZZ}(0)} \quad (\text{A.23})$$

Limits:

$$\lim_{\xi \rightarrow 0} R_{WW}(\xi) = E[W(x)W(x)] = E[W^2(x)] \quad (\text{A.24})$$

$$\lim_{\xi \rightarrow \infty} R_{WW}(\xi) = 0 \quad (\text{A.25})$$

except for periodic fields.

A.6 Ergodic Theorem

For random field theory to be useful, it should be possible to estimate mean and autocorrelation from measurements.

A first possible way to determine the autocorrelation is the so called “ensemble averaging”: it averages over the entire set of n sample functions.

$$\text{mean value: } \mu_W(x_1) = E[W(t_1)] = \frac{1}{n} \sum_{i=1}^n W_i(x_1) \quad \forall t_1 \quad (\text{A.26})$$

$$\begin{aligned} \text{autocorrelation: } R_{WW}(x_1, x_2) &= E[W(t_1)W(t_2)] = \\ &= \frac{1}{n} \sum_{i=1}^n W_i(t_1)W_i(t_2) \quad \forall t_1, t_2 \end{aligned} \quad (\text{A.27})$$

However, usually the number of available samples is too low to consider the average significant.

There is a class of homogeneous random fields for which it is possible to estimate mean and autocorrelation from one sample function. Such homogeneous fields are called “ergodic” and the “spatial averaging¹” is defined as:

$$\langle W(x) \rangle = \frac{1}{L} \int_0^L W_i(x) dx \quad (\text{A.28})$$

¹Actually, the phrase “temporal averaging”, that is associated to ergodic stochastic processes, is more common.

$$\langle W(x)W(x + \xi) \rangle = \frac{1}{L - \xi} \int_0^{L-\xi} W_i(x + \xi)W_i(x) dx \quad (\text{A.29})$$

where L indicates the length of the sample function.

A homogeneous random field is “ergodic in the mean” when

$$E[W(x)] = \langle W(x) \rangle \quad \text{as } L \rightarrow \infty \quad (\text{A.30})$$

The necessary and sufficient conditions for $W(x)$ to be ergodic in the mean are:

1. $E[W(x)] = \text{constant}$
2. $E[W(x)W(x + \xi)] = \text{function of } \xi \text{ only}$
3. $\lim_{L \rightarrow \infty} \frac{1}{L} \int_0^\infty R_{WW}(\xi) d\xi = 0$

where the first two conditions imply weak homogeneity and the third one is quite commonly verified, because of Eq. (A.25). Therefore, the majority of the homogeneous fields are ergodic in the mean.

A homogeneous random field is “ergodic in correlation” when

$$E[W(x)W(x + \xi)] = \langle W(x)W(x + \xi) \rangle \quad \text{as } L \rightarrow \infty \quad (\text{A.31})$$

The necessary and sufficient conditions for ergodicity in correlation are:

1. $E[W(x)W(x + \xi)] = \text{function of } \xi \text{ only}$
2. $Q_{WW}(\xi, \eta) = E[\{W(x + \xi)W(x) - R_{WW}(\xi)\}\{W(x + \xi + \eta)W(x + \eta) - R_{WW}(\xi)\}]$ independent of x
3. $\lim_{L \rightarrow \infty} \frac{1}{L} \int_0^\infty Q_{WW}(\xi, \eta) d\eta = 0$

where η is a second space lag.

Unfortunately, the statistical tests for ergodicity are very weak. For the artificially generated fields (Chapters 3–5) the ergodicity can be verified analyzing the generation procedure.

A.7 Spectral Density Function

The Spectral Density Function (SDF), also called “power spectral density” or “power spectrum” of a random field is defined as the Fourier transform² of the autocorrelation function:

$$S_{WW}(\kappa) = \frac{1}{2\pi} \int_{-\infty}^{\infty} R_{WW}(\xi) e^{-i\kappa\xi} d\xi \quad (\text{A.32})$$

where κ is the wave number. The inverse transformation is given by:

$$R_{WW}(\xi) = \int_{-\infty}^{\infty} S_{WW}(\kappa) e^{i\kappa\xi} d\kappa \quad (\text{A.33})$$

Eqs. (A.32) and (A.33) are known as the “Wiener-Khintchine theorem”.

It is worth to stress that $R_{WW}(\xi)$ and $S_{WW}(\kappa)$ are perfectly equivalent, they bring the same information on the field and can be obtained the one from the other through Eqs. (A.32)–(A.33).

A.7.1 Properties of the SDF

1. S_{WW} is a real and even function of κ :

$$S_{WW}(\kappa) = S_{WW}(-\kappa) \quad (\text{A.34})$$

and therefore, the Wiener-Khintchine theorem can be rewritten as

$$S_{WW}(\kappa) = \frac{1}{\pi} \int_0^{\infty} R_{WW}(\xi) \cos \kappa\xi d\xi \quad (\text{A.35})$$

$$R_{WW}(\xi) = 2 \int_0^{\infty} S_{WW}(\kappa) \cos \kappa\xi d\kappa \quad (\text{A.36})$$

²Equation (A.32) is not exactly a Fourier transform, because of the coefficients but it is perfectly equivalent.

2. $S_{WW}(\kappa)$ is a non-negative function:

$$R_{WW}(\xi) \geq 0 \quad (\text{A.37})$$

This property is equivalent to the property of the autocorrelation being non-negative definite (“Bochner’s theorem”)

3. $S_{WW}(\kappa)$ describes the distribution of the mean square over the wave number domain:

$$R_{WW}(0) = E[W^2(x)] = \int_{-\infty}^{\infty} S_{WW}(\kappa) \, d\kappa \quad (\text{A.38})$$

4. If $E[W^2(x)]$ is finite, then $S_{WW}(\kappa)$ goes down to zero as $\kappa \rightarrow \pm\infty$ faster than $\frac{1}{\kappa}$

A.7.2 Cross-Spectral Density Function

Similarly to the definition of the SDF, the Cross-Spectral Density Function (CSDF) for two homogeneous fields is defined as the Fourier transform of the cross-correlation:

$$S_{WZ}(\kappa) = \frac{1}{2\pi} \int_{-\infty}^{\infty} R_{WZ}(\xi) e^{-i\kappa\xi} \, d\xi \quad (\text{A.39})$$

The inverse transformation is given by:

$$R_{WZ}(\xi) = \int_{-\infty}^{\infty} S_{WZ}(\kappa) e^{i\kappa\xi} \, d\kappa \quad (\text{A.40})$$

The properties of the CSDF are described in the following.

1. $S_{WZ}(\kappa)$ is complex in general.
2. Symmetry (“Hermitian property”):

$$S_{WZ}(\kappa) = S_{WZ}^*(-\kappa) \quad (\text{A.41})$$

where the asterisk denotes the complex conjugate.

3. If $E[W(x)Z(x)]$ is finite and $E[W^2(x)]$, $E[Z^2(x)]$ are finite too, then $S_{WZ}(\kappa)$ goes down to zero as $\kappa \rightarrow \pm\infty$ faster than $\frac{1}{\kappa}$

A.7.3 Estimation of the SDF from One Sample

Assuming homogeneity and ergodicity, the space averaging is equivalent to the ensemble averaging. This means that every single realization has all the information³ about the entire field. Therefore, the spectral density can be computed as:

$$S_{WW}(\kappa) = \frac{\left| \int_0^L w(x) e^{-i\kappa x} dx \right|^2}{2\pi L} \quad (\text{A.42})$$

It appears evident that Eq. (A.42) can be numerically computed by means of a Fast Fourier Transform (FFT) of the sample.

In the same way, for two homogeneous and ergodic samples of the same length:

$$S_{WZ}(\kappa) = \frac{\int_0^L w(x) e^{i\kappa x} dx \int_0^L z(x) e^{-i\kappa x} dx}{2\pi L} \quad (\text{A.43})$$

A.8 Gaussian Random Fields

As well as for a Gaussian random variable, the marginal probability distribution function of a Gaussian random field is Gaussian:

$$f_{\{W\}}(w, x) = \frac{1}{\sqrt{2\pi}\sigma_W(x)} \exp \left\{ -\frac{[w(x) - \mu_W(x)]^2}{2\sigma_W^2(x)} \right\} \quad (\text{A.44})$$

Gaussian random fields $W(x)$ possess the following properties.

1. They are fully defined by the first two moments.
2. Under linear operations, they remain Gaussian (see the following properties).
- 3.

$$Z(x^*) = \int_a^b W(x)h(x, x^*) dx \quad \text{is Gaussian } \forall h(x, x^*) \quad (\text{A.45})$$

³We are still considering only the first two orders statistical descriptors.

4.
$$\frac{dW(x)}{dx}, \frac{d^2W(x)}{dx^2}, \dots \quad \text{are Gaussian} \quad (\text{A.46})$$

5.
$$Z(x) = aW(x) + b \quad \text{is Gaussian} \quad (\text{A.47})$$

6. If in the equation of motions the force is a Gaussian random process $W(t)$:

$$m \frac{d^2Z(t)}{dt^2} + c \frac{dZ(t)}{dt} + k = W(t) \quad (\text{A.48})$$

then the displacement $Z(t)$ is a Gaussian random process too.

7.
$$W^2(x), W^3(x), \dots \quad \text{are not Gaussian} \quad (\text{A.49})$$

A.9 Multi-Dimensional Random Fields

All the definition and the properties considered for one-dimensional random fields can be easily extended to multi-dimensional random fields $W(x_1, x_2, \dots, x_n)$.

In particular, the Wiener-Khintchine theorem for a two-dimensional field becomes:

$$S_{WW}(\kappa_1, \kappa_2) = \frac{1}{(2\pi)^2} \int_{-\infty}^{\infty} \int_{-\infty}^{\infty} R_{WW}(\xi_1, \xi_2) \exp[-i(\kappa_1 \xi_1 + \kappa_2 \xi_2)] d\xi_1 d\xi_2 \quad (\text{A.50})$$

$$R_{WW}(\xi_1, \xi_2) = \int_{-\infty}^{\infty} \int_{-\infty}^{\infty} S_{WW}(\kappa_1, \kappa_2) \exp[-i(\kappa_1 \xi_1 + \kappa_2 \xi_2)] d\kappa_1 d\kappa_2 \quad (\text{A.51})$$

Eq. (A.42), for a two-dimensional random field becomes:

$$S_{WW}(\kappa_1, \kappa_2) = \frac{\left| \int_0^{L_1} \int_0^{L_2} w(x_1, x_2) \exp(-i\kappa_1 x_1, -i\kappa_2 x_2) dx_1 dx_2 \right|^2}{4\pi^2 L_1 L_2} \quad (\text{A.52})$$

For any homogeneous two-dimensional random field the symmetry of the autocorrelation with respect to the origin of the domain is still valid:

$$R_{WW}(\xi_1, \xi_2) = R_{WW}(-\xi_1, -\xi_2) \quad (\text{A.53})$$

For a special class of homogeneous two-dimensional random fields the following relation is valid:

$$R_{WW}(\xi_1, \xi_2) = R_{WW}(\xi_1, -\xi_2) = R_{WW}(-\xi_1, \xi_2) = R_{WW}(-\xi_1, -\xi_2) \quad (\text{A.54})$$

that means that the autocorrelation is symmetric with respect to the two axes ξ_1, ξ_2 , therefore the information on a single quadrant is sufficient to fully describe the autocorrelation. Such fields are called “quadrant-symmetric fields” (or “quadrant fields”).

A.10 Multi-Variate Random Fields

A “multi-variate random field”, also called “vector field” is a field that has a number of correlated components.

The spectral characteristics of a vector field are collected in the Cross-Spectral Density Matrix (CSDM):

$$\mathbf{S}(\kappa) = \begin{pmatrix} S_{11}(\kappa) & S_{12}(\kappa) & \cdots & S_{1n}(\kappa) \\ S_{21}(\kappa) & S_{22}(\kappa) & \cdots & S_{2n}(\kappa) \\ \vdots & \vdots & \ddots & \vdots \\ S_{n1}(\kappa) & S_{n2}(\kappa) & \cdots & S_{nn}(\kappa) \end{pmatrix} \quad (\text{A.55})$$

The CSDM is symmetric, the diagonal terms are autospectra and the off-diagonal terms are cross-spectra. These are sometimes expressed by means of the “coherence function” γ_{ij} :

$$S_{ij}(\kappa) = \gamma_{ij}(\kappa) \sqrt{S_{ii}(\kappa) S_{jj}(\kappa)} \quad (\text{A.56})$$

The coherence describes the degree of correlation between the components i and j and is always in the interval $[0, 1]$. When $\gamma_{ij} = 1$ the two components are said to be perfectly correlated, when $\gamma_{ij} = 0$ the two components are uncorrelated. The coherence is a real function, therefore, when the coherence is used, also the cross-spectra are real.

List of Figures

3.1	Flow chart of the proposed simulation algorithm.	24
3.2	Comparison between the SDF estimated using one sample function $\hat{f}(x)$ and the SDF estimated using 60 sample functions $\hat{f}(x)$	31
3.3	Representative example of random perturbation of $S_{gg}(\kappa)$	33
3.4	Four probability density functions compared with the Standard Gaussian.	35
3.5	Lognormal distribution: non-Gaussian ensemble-averaged spectral density functions compared with the corresponding target (E denotes the error).	37
3.6	Lognormal distribution: non-Gaussian ensemble-averaged probability density functions compared with the corresponding target.	38
3.7	Lognormal distribution: computed non-Gaussian spectral density functions compared with the corresponding target. The computed SDF's have been determined using the double integration formula (E denotes the error).	40
3.8	Uniform distribution: non-Gaussian spectral density function compared with the corresponding target. The computed SDF has been determined using the double integration formula (E denotes the error).	42
3.9	Ensemble-averaged Uniform probability density function compared with the corresponding target.	43

3.10	U-shaped Beta distribution: non-Gaussian spectral density function compared with the corresponding target. The computed SDF has been determined using the double integration formula (E denotes the error).	44
3.11	Ensemble-averaged U-shaped Beta probability density function compared with the corresponding target.	45
3.12	L-shaped Beta distribution: non-Gaussian spectral density function compared with the corresponding target. The computed SDF has been determined using the double integration formula (E denotes the error).	47
3.13	Ensemble-averaged L-shaped Beta probability density function compared with the corresponding target.	48
4.1	Two-dimensional underlying Gaussian spectrum.	56
4.2	Contour plot of the “empirical” SDF estimated using 20 sample functions compared to the target SDF. The lines represent equipotential curves at the levels 0.07, 0.06, 0.05, 0.04, 0.03, 0.02, 0.01, starting from the origin.	57
4.3	Marginal PDF estimated using 20 sample functions compared to the target Lognormal.	58
5.1	Flow chart of the proposed algorithm.	68
5.2	Wind velocity fluctuation simulation. The underlying Gaussian coherence computed by the algorithm is compared to the target non-Gaussian coherence defined by Eq. (5.58). Only the “significant zone” of the coherence is affected by the modifications. . . .	84
5.3	Wind velocity fluctuation simulation. The “empirical” spectral density functions and the cross-spectral density obtained by ensemble averaging over 100 generated samples match the target non-Gaussian functions almost perfectly. The graphs are sorted as the elements of the CSDM. Only the lower part is plotted, because the upper part is symmetric. The negligible imaginary part present in the empirical cross-spectrum because of the non-ergodicity of the produced samples has been disregarded.	85

5.4 Wind velocity fluctuation simulation. Both the PDF computed by ensemble averaging of 100 generated samples match the respective Lognormal targets. 86

5.5 Artificially Correlated Spectrum. The underlying Gaussian coherences computed by the algorithm are compared to the target non-Gaussian coherences. 88

5.6 Artificially Correlated Spectrum. The “empirical” spectral density functions and the cross-spectral densities obtained by ensemble averaging over 100 generated samples match the target non-Gaussian functions almost perfectly. The graphs are sorted as the elements of the CSDM. Only the lower part is plotted, because the upper part is symmetric. The negligible imaginary part present in the empirical cross-spectra because of the non-ergodicity of the produced samples has been disregarded. 90

5.7 Artificially Correlated Spectrum. All three PDF’s computed by ensemble averaging of 100 generated samples match the respective non-Gaussian targets. 91

6.1 Theoretical target triangular spectrum. It is the same for every component. 105

6.2 The values given to the code as target are $S^0 \frac{\Delta\kappa}{m} = [1, 2, 3, 2, 1, 0]'$. 105

6.3 Triangular spectrum, empirical autospectrum of the second component. 106

6.4 Triangular spectrum, empirical autospectrum of the third component. 106

6.5 Triangular spectrum, cross-spectral density matrix. The “Empirical SDF” has been computed applying Eq. (6.19) to one produced sample; the “Closed form expression” represents the results of Eq. (6.26) or Eqs. (6.27)–(6.28); the “Target spectrum” is the input given to the simulation algorithm. 108

6.6 Triangular spectrum, cross-spectral density matrix. Data are computed as in Fig. 6.5, but at intervals of width $\Delta\kappa$, rather than $\frac{\Delta\kappa}{m}$. Each value in this plot is the sum of m values in Fig. 6.5. It is clear that also with this “resolution”, the closed form expression perfectly describes the spectrum of the produced samples but it is different from the target one. 109

- 6.7 Triangular spectrum, cross-spectral density matrix. Data are computed as in Fig. 6.5. N has been set equal to 256, therefore $\frac{\Delta\kappa}{m} = \frac{6}{3 \cdot 256} \cong 0.0078$. Measuring the CSDM at intervals of $\frac{\Delta\kappa}{m}$, the empirical CSDM is always scattered, as long as $\Delta\kappa$ is finite. 110
- 6.8 Triangular spectrum, cross-spectral density matrix. Data are computed as in Fig. 6.6. N has been set equal to 256, therefore $\Delta\kappa = \frac{6}{256} \cong 0.0234$. The empirical CSDM is much closer to the target than the one in Fig. 6.6. 111
- 6.9 Triangular spectrum, difference between the “empirical spectrum” computed as in Fig. 6.6 and the target. N has been set equal to 2. 112
- 6.10 Triangular spectrum, difference between the “empirical spectrum” computed as in Fig. 6.6 and the target. N has been set equal to 256. The absolute value of the difference is constant, because the derivatives of the SDF’s are constant. 113
- 6.11 Triangular spectrum, difference between the “empirical spectrum” computed as in Fig. 6.6 and the target for different values of N . The absolute value of the difference is constant, as shown by Figs. 6.9–6.10 and it decreases as N increases (i.e. as $\Delta\kappa$ decreases). 114
- 6.12 Parabolic spectrum, cross-spectral density matrix. The “Empirical SDF” has been computed applying Eq. (6.19) to one produced sample; the “Closed form expression” represents the results of Eq. (6.26) or Eqs. (6.27)–(6.28); the “Target spectrum” is the input given to the simulation algorithm. The values are computed at intervals of width $\Delta\kappa$ and N is equal to 2. 116
- 6.13 Parabolic spectrum, cross-spectral density matrix. The “Empirical SDF” has been computed applying Eq. (6.19) to one produced sample; the “Closed form expression” represents the results of Eq. (6.26) or Eqs. (6.27)–(6.28); the “Target spectrum” is the input given to the simulation algorithm. The values are computed at intervals of width $\Delta\kappa$ and N is equal to 64. 117
- 6.14 Parabolic spectrum, difference between the “empirical spectrum” computed as in Fig. 6.12 and the target. N has been set equal to 2. Note that in this case the difference appears a constant function because only 2 values are available. Its nature of linear function is clearly represented in Fig. 6.15. 118

6.15 Parabolic spectrum, difference between the “empirical spectrum” computed as in Fig. 6.6 and the target. N has been set equal to 64. The difference is a linear function, because the derivatives of the SDF’s are linear. 119

6.16 Kaimal spectrum, cross-spectral density matrix. The “Empirical SDF” has been computed applying Eq. (6.19) to one produced sample; the “Closed form expression” represents the results of Eq. (6.26) or Eqs. (6.27)–(6.28); the “Target spectrum” is the input given to the simulation algorithm. The values are computed at intervals of width $\Delta\kappa$ and N is equal to 2048. 120

7.1 Graphical post-processor for Dynaflow. Meshes of the plane frame and of the soil. 126

7.2 Graphical post-processor for Dynaflow. Nominal stresses in the soil at the first step of the non-linear analysis. 127

7.3 Graphical post-processor for Dynaflow. Bending moments in the frame at the first step of the non-linear analysis. 128

7.4 Graphical post-processor for Dynaflow. Time history of the displacement of a specific node in the soil. 129

7.5 The Williamsburg Bridge, between Manhattan and Brooklyn, New York City. 131

8.1 Bar in a three-dimensional reference system: vectors. 141

8.2 Bar in a three-dimensional reference system: angles. 142

8.3 Flow chart of the proposed iterative procedure. 148

8.4 Externally redundant plane truss structure. 151

8.5 Stiffnesses estimated for the redundant plane truss in Fig. 8.4, compared to the starting values of the iterative procedure and to the real values. The accuracy is good for all the bars except bar 11, for which other load tests are required (see Sec. 8.5.2 and Fig. 8.12). 154

8.6 Externally redundant plane truss structure. 155

-
- 8.7 Three-dimensional redundant truss structure. The displacements in the x direction are restrained at nodes 1 and 5; the displacements in the y direction are restrained at nodes 1 and 4; the vertical displacements are restrained at nodes 1, 4, 5, 8 and 10. 156
- 8.8 Stiffnesses estimated for the redundant three-dimensional truss in Fig. 8.7, compared to the starting values of the iterative procedure and to the real values. The accuracy is good for all the bars. 157
- 8.9 Convergence of the iterative procedure. Each line represents the evolution of the relative error between the estimated stiffnesses and the real values. Even if the starting values are completely wrong the estimates rapidly converges to the real values. 159
- 8.10 Results for the structure represented in Fig. 8.4. Convergence of the coefficients of variation versus the number of Monte Carlo Simulations. Each line represents the C.O.V. of a bar. 1500 samples are sufficient to meet convergence. This plot refers to the case of two load conditions, analog results have been obtained also for the other numbers of load conditions. 172
- 8.11 Results for the structure represented in Fig. 8.4. Coefficients of variation obtained using different numbers of load conditions. 173
- 8.12 Stiffnesses estimated for the redundant plane truss in Fig. 8.4 using five load tests, compared to the starting values of the iterative procedure and to the real values. The accuracy is good for all the bars. 174
- 8.13 Convergence of the iterative procedure. Each line represents the evolution of the relative error between the estimated stiffnesses and the real values. Even if the starting values are completely wrong, the estimates rapidly converge to the real values. 175
- 9.1 Three-dimensional truss structure. The displacements in the x direction are restrained at node 1; the displacements in the y direction are restrained at nodes 1 and 2; the vertical displacements are restrained at nodes 1, 2, and 3. 184

-
- 9.2 Stiffnesses estimated for the three-dimensional truss in Fig. 9.1, compared to the starting values of the iterative procedure and to the real values. The accuracy is good for all the bars, including the bar for which the strain values were not available. 186
- 9.3 Stiffnesses estimated for the truss in Fig. 8.4 with local damage. After the first run the stiffness estimated for the first bar disregarding its strain value is almost 10% lower than the one obtained considering the strain. After the identification of the local damage, all the difference are less than 5%. 190
- 9.4 Three-dimensional truss structure. The displacements in the x direction are restrained at node 1; the displacements in the y direction are restrained at nodes 1 and 2; the vertical displacements are restrained at nodes 1, 2, 3 and 4. 192
- 9.5 Stiffnesses estimated for the truss in Fig. 9.4 with local damage. After the first run the stiffness estimated for bar 5 disregarding its strain value is almost 20% lower than the one obtained considering the strain. After the identification of the local damage, all the difference are less than 2%. 194

List of Tables

6.1	Triangular spectrum. The empirical spectra do not match the target neither in an average sense.	107
8.1	Axial strains (10^{-6}) simulated for the redundant plane truss in Fig. 8.4.	152
8.2	Stiffnesses estimated for the redundant plane truss in Fig. 8.4. . .	153
8.3	Stiffnesses estimated for the redundant three-dimensional truss in Fig. 8.7.	158
8.4	Results for the structure represented in Fig. 8.4. Axial strains (10^{-6}).	170
8.5	Results for the structure represented in Fig. 8.4. Axial stresses ($\frac{N}{m^2}10^{-4}$).	170
8.6	Results for the structure represented in Fig. 8.4. Estimated stiffnesses and coefficients of variation.	171
9.1	Stiffnesses estimated for the three-dimensional truss in Fig. 9.1. .	185
9.2	Stiffnesses estimated for the truss in Fig. 8.4 with local damage.	191
9.3	Stiffnesses estimated for the truss in Fig. 9.4 with local damage.	193

Bibliography

- Abu-Lebdeh, G. and Benekohal, R. F. (1999) , Convergence variability and population sizing in micro-genetic algorithms, *Computer-Aided Civil and Infrastructure Engineering* **14**(5), 321–334.
- Ang, A. H.-S. and Tang, W. H. (1984) , *Probability concepts in engineering planning and design*, John Wiley and sons, New York.
- Banan, M. R., Banan, M. R. and Hjelmstad, K. D. (1994a) , Parameter estimation of structures from static response. i. computational aspects, *Journal of Structural Engineering* **120**, 3243–3258.
- Banan, M. R., Banan, M. R. and Hjelmstad, K. D. (1994b) , Parameter estimation of structures from static response. ii: Numerical simulation studies, *Journal of Structural Engineering* **120**, 3259–3283.
- Beck, J. V. and Arnold, K. J. (1977) , *Parameter estimation in engineering and science*, John Wiley and sons, New York.
- Bendat, J. S. and Piersol, A. G. (1986) , *Random Data: Analysis and Measurement Procedures*, 2 rev exp edn, Wiley-Interscience.
- Benjamin, J. R. and Cornell, C. A. (1970) , *Probability, statistics, and decision for civil engineers*, McGraw-Hill.
- Bocchini, P. and Deodatis, G. (2008) , Critical review and latest developments of a class of simulation algorithms for strongly non-Gaussian random fields, *Probabilistic Engineering Mechanics* . doi:10.1016/j.probenmech.2007.09.001.
- Bowman, A. W. and Azzalini, A. (1997) , *Applied Smoothing Techniques for Data Analysis*, Oxford University Press.

- Casciati, S. (2006) , Algoritmi evolutivi differenziali in ingegneria strutturale, in F. Ubertini, E. Viola, S. de Miranda and G. Castellazzi (eds), *Proceedings of the 16th Meeting of the Italian Group of Computational Mechanics, GIMC2006*.
- Chen, Y. and Deodatis, G. (2004) , Simulation of highly-skewed non-Gaussian vector processes, in S. Srinivasan and B. Bhattacharya (eds), *Proceedings of the Ninth ASCE Speciality Conference on Probabilistic Mechanics and Structural Reliability*.
- Chou, J.-H. and Ghaboussi, J. (2001) , Genetic algorithm in structural damage detection, *Computers and Structures* **79**(14), 1335–1353.
- Cope, A. D., Gurley, K. R., Gioffre, M. and Reinhold, T. A. (2005) , Low-rise gable roof wind loads: Characterization and stochastic simulation, *Journal of Wind Engineering and Industrial Aerodynamics* **93**(9), 719–738.
- Davenport, A. G. (1968) , The dependence of wind load upon meteorological parameters, *Proc. Int. Res. Seminar on Wind Effects on Buildings and Structures*, University of Toronto Press, Toronto, Canada, pp. 19–82.
- Deodatis, G. (1996) , Simulation of ergodic multivariate stochastic processes, *Journal of Engineering Mechanics* **122**(8), 778–787.
- Deodatis, G. and Micaletti, R. C. (2001) , Simulation of highly skewed non-Gaussian stochastic processes, *Journal of Engineering Mechanics* **127**(12), 1284–1295.
- Di Paola, M. and Bilello, C. (2004) , An integral equation for damage identification of euler-bernoulli beams under static loads, *Journal of Engineering Mechanics* **130**, 225–234.
- Di Paola, M. and Gullo, I. (2001) , Digital generation of multivariate wind field processes, *Probabilistic Engineering Mechanics* **16**, 1–10.
- Elishakoff, I. (1999) , *Probabilistic Theory of Structures*, 2 edn, Dover Publications.
- Falsone, G. and Lombardo, M. (2007) , Stochastic representation of the mechanical properties of irregular masonry structures, *International Journal of Solids and Structures* **44**, 8600–12. Copyright 2007, The Institution of Engineering and Technology.

- Faravelli, L., Farina, M. and Marazzi, F. (2005) , Genetic algorithms for structural identification, *in* G. Augusti, G. I. Schuëller and M. Ciampoli (eds), *Safety and Reliability of Engineering Systems and Structures. Proceedings of the Ninth International Conference on Structural Safety and Reliability*, Millpress, pp. 3115–3121.
- Fenton, G. A. and Griffiths, D. V. (2002) , Probabilistic foundation settlement on spatially random soil, *Journal of Geotechnical and Geoenvironmental Engineering* **128**, 381–390.
- Fenton, G. and Griffiths, D. (2003) , Bearing-capacity prediction of spatially random $c - \phi$ soils, *Canadian Geotechnical Journal* **40**, 54–65.
- Fenton, G. and Vanmarcke, E. (1998) , Spatial variation in liquefaction risk, *Geotechnique* **48**, 819–831.
- Frigo, M. and Johnson, S. G. (2005) , The design and implementation of FFTW3, *Proceedings of the IEEE* **93**(2), 216–231. Special issue on “Program Generation, Optimization, and Platform Adaptation”.
- Ghanem, R. G. and Spanos, P. D. (2003) , *Stochastic Finite Elements*, Dover Publications.
- Gioffre, M. and Gusella, V. (2002) , Numerical analysis of structural systems subjected to non-gaussian random fields, Vol. 37 of *Meccanica*, Kluwer Academic Publishers, Palermo, Italy, pp. 115–128.
- Gioffre, M., Gusella, V. and Grigoriu, M. (2000) , Simulation of non-Gaussian field applied to wind pressure fluctuations, *Probabilistic Engineering Mechanics* **15**, 339–345.
- Goldberg, D. E. (1989) , *Genetic Algorithms in Search, Optimization, and Machine Learning*, 1 edn, Addison-Wesley Professional.
- Graham, L. L., Gurley, K. and Masters, F. (2003) , Non-Gaussian simulation of local material properties based on a moving-window technique, *Probabilistic Engineering Mechanics* **18**(3), 223–234.
- Griffiths, D. and Fenton, G. (2001) , Bearing capacity of spatially random soil: The undrained clay prandtl problem revisited, *Geotechnique* **51**, 351–359.

- Griffiths, D. and Fenton, G. A. (2004) , Probabilistic slope stability analysis by finite elements, *Journal of Geotechnical and Geoenvironmental Engineering* **130**, 507–518.
- Grigoriu, M. (1984) , Crossings of non-Gaussian translation processes, *Journal of Engineering Mechanics* **110**(4), 610–620.
- Grigoriu, M. (1993) , On the spectral representation method in simulation, *Probabilistic Engineering Mechanics* **8**, 75–90.
- Grigoriu, M. (1995) , *Applied Non-Gaussian Processes*, Prentice Hall.
- Grigoriu, M. (1998) , Simulation of stationary non-Gaussian translation processes, *Journal of Engineering Mechanics* **124**(2), 121–126.
- Gurley, K. R. and Kareem, A. (1998) , Conditional simulation of non-normal velocity/pressure fields, *Journal of Wind Engineering and Industrial Aerodynamics* **77**, 39–51.
- Gurley, K. R., Tognarelli, M. A. and Kareem, A. (1997) , Analysis and simulation tools for wind engineering, *Probabilistic Engineering Mechanics* **12**(1), 9–31.
- Hearn, G. and Testa, R. B. (1991) , Modal analysis for damage detection in structures.
- Hjelmstad, K. D. and Shin, S. (1997) , Damage detection and assessment of structures from static response, *Journal of Engineering Mechanics* **123**, 568–576.
- Hurtado, J. E. and Barbat, A. H. (1998) , Monte carlo techniques in computational stochastic mechanics, *Archives of Computational Methods in Engineering* **5**(1), 3–30.
- Jenkins, C. H., Kjerengtroen, L. and Oestensen, H. (1997) , Sensitivity of parameter changes in structural damage detection, *Shock and Vibration* **4**(1), 27–37.
- Kaimal, J., Wyngaard, J., Izumi, Y. and Cote, O. (1972) , Spectral characteristics of surface-layer turbulence, *Quarterly Journal of the Royal Meteorological Society* **98**, 563–89. Copyright 1972, IEE.
- Koutsourelakis, S., Prevost, J. H. and Deodatis, G. (2002) , Risk assessment of an interacting structure-soil system due to liquefaction, *Earthquake Engineering and Structural Dynamics* **31**, 851–879.

- Kristensen, L. and Jensen, N. (1979) , Lateral coherence in isotropic turbulence and in the natural wind, *Boundary-Layer Meteorology* **17**, 353–73. Copyright 1980, IEE.
- Li, L., Phoon, K. and Quek, S. (2007) , Comparison between Karhunen-Loeve expansion and translation-based simulation of non-Gaussian processes, *Computers & Structures* **85**(5-6), 264–276.
- Li, Y. and Kareem, A. (1993) , Simulation of multivariate random processes: hybrid dft and digital filtering approach, *Journal of Engineering Mechanics* **119**, 1078–1098.
- Lin, Y. K. (1967) , *Probabilistic Theory of Structural Dynamics*, McGraw-Hill.
- Liu, G. R. and Han, X. (2003) , *Computational inverse techniques in nondestructive evaluation*, CRC Press.
- Liu, P.-L. and Chian, C.-C. (1997) , Parametric identification of truss structures using static strains, *Journal of Structural Engineering* **123**(7), 927–933.
- Mares, C. and Surace, C. (1996) , An application of genetic algorithms to identify damage in elastic structures, *Journal of Sound and Vibration* **195**(2), 195–215.
- Matsumoto, M. and Kurita, Y. (1992) , Twisted GFSR generators, *ACM Transactions on Modeling and Computer Simulation* **2**(3), 179–194.
- Matsumoto, M. and Nishimura, T. (1998) , Mersenne twister: a 623-dimensionally equidistributed uniform pseudo-random number generator, *ACM Transactions on Modeling and Computer Simulation* **8**(1), 3–30.
- Matteo, J., Deodatis, G. and Billington, D. P. (1994) , Safety analysis of suspension-bridge cables: Williamsburg bridge, *Journal of Structural Engineering* **120**, 3197–3211.
- Matthies, H. G., Brenner, C. E., Bucher, C. G. and Soares, C. G. (1997) , Uncertainties in probabilistic numerical analysis of structures and solids-stochastic finite elements, *Structural Safety* **19**(3), 283–336.
- Ohtomo, K. and Shinozuka, M. (1990) , Development and validation of fragility curves for liquefaction, *Proceedings of the US National Conference on Earthquake Engineering* p. 745.

- Paice, G. M., Griffiths, D. V. and Fenton, G. A. (1996) , Finite element modeling of settlements on spatially random soil, *Journal of Geotechnical Engineering* **122**, 777–779.
- Popescu, R., Deodatis, G. and Nobahar, A. (2005) , Effects of random heterogeneity of soil properties on bearing capacity, *Probabilistic Engineering Mechanics* **20**, 324–341.
- Popescu, R., Deodatis, G. and Prevost, J. H. (1998) , Simulation of homogeneous non-Gaussian stochastic vector fields, *Probabilistic Engineering Mechanics* **13**(1), 1–13.
- Popescu, R., Prevost, J. and Deodatis, G. (1997) , Effects of spatial variability on soil liquefaction: Some design recommendations, *Geotechnique* **47**, 1019–1036.
- Popescu, R., Prevost, J. and Deodatis, G. (2005) , 3d effects in seismic liquefaction of stochastically variable soil deposits, *Geotechnique* **55**, 21–31.
- Prevost, J. H. (2002) , Dynaflow: a nonlinear transient finite element analysis program, version 02, *Technical report*, Department of Civil and Environmental Engineering, Princeton University.
- Puig, B., Poirion, F. and Soize, C. (2002) , Non-Gaussian simulation using Hermite polynomial expansion: Convergences and algorithms, *Probabilistic Engineering Mechanics* **17**(3), 253–264.
- Sakamoto, S. and Ghanem, R. (2002a) , Polynomial chaos decomposition for the simulation of non-Gaussian nonstationary stochastic processes, *Journal of Engineering Mechanics* **128**(2), 190–201.
- Sakamoto, S. and Ghanem, R. (2002b) , Simulation of multi-dimensional non-Gaussian non-stationary random fields, *Probabilistic Engineering Mechanics* **17**(2), 167–176.
- Salawu, O. S. (1997) , Detection of structural damage through changes in frequency: a review, *Engineering Structures* **19**, 718–723.
- Sanayei, M. and Onipede, O. (1991) , Damage assessment of structures using static test data, *AIAA Journal* **29**(7), 1174–1179.

- Sanayei, M. and Saletnik, M. J. (1996a) , Parameter estimation of structures from static strain measurements. i: formulation, *Journal of Structural Engineering* **122**(5), 555–562.
- Sanayei, M. and Saletnik, M. J. (1996b) , Parameter estimation of structures from static strain measurements. ii: error sensitivity analysis, *Journal of Structural Engineering* **122**(5), 563–572.
- Schueller, G. (1997) , State-of-the-art report on computational stochastic mechanics, *Probabilistic Engineering Mechanics* **12**, 197–321.
- Shapiro, J. F. (1979) , *Mathematical programming, structures and algorithms*, John Wiley & Sons.
- Shi, Y. (2006) , *Simulation of Stationary Non-Gaussian Stochastic Processes/Fields with Application in Suspension Bridge Cable Strength Estimation*, PhD thesis, Columbia University.
- Shi, Y. and Deodatis, G. (2004) , A novel approach for simulation of non-Gaussian fields: Application in estimating wire strengths from experimental data, in S. Srinivasan and B. Bhattacharya (eds), *Proceedings of the Ninth ASCE Speciality Conference on Probabilistic Mechanics and Structural Reliability*.
- Shi, Y., Deodatis, G. and Betti, R. (2005) , Recent developments in simulation of non-Gaussian processes/fields with application in suspension cable strength estimation, in G. Augusti, G. I. Schuëller and M. Ciampoli (eds), *Safety and Reliability of Engineering Systems and Structures. Proceedings of the Ninth International Conference on Structural Safety and Reliability*, Millpress.
- Shi, Y., Deodatis, G. and Betti, R. (2007) , Random field-based approach for strength evaluation of suspension bridge cables, *Journal of Structural Engineering* **133**, 1690–1699.
- Shinozuka, M. (1974) , Digital simulation of random processes in engineering mechanics with the aid of fft technique, in S. T. Ariaratnam and H. H. E. Leipholz (eds), *Stochastic Problems in Mechanics*, University of Waterloo press, pp. 277–286.
- Shinozuka, M. and Deodatis, G. (1991) , Simulation of stochastic processes by spectral representation, *Applied Mechanics Reviews* **44**(4), 191–204.

- Shinozuka, M. and Deodatis, G. (1996) , Simulation of multi-dimensional Gaussian stochastic fields by spectral representation, *Applied Mechanics Reviews* **49**(1), 29–53.
- Shinozuka, M. and Jan, C. M. (1972) , Digital simulation of random processes and its applications, *Journal of Sound and Vibration* **25**(1), 111–128.
- Shinozuka, M., Kamata, M. and Yun, C.-B. (1989) , Simulation of earthquake ground motion as multi-variate stochastic process, *Technical Report 1989.5*, Princeton-Kajima Joint Res., Dept. of Civ. Engrg and Op. Res., Princeton University, Princeton, NJ.
- Simiu, E. and Scanlan, R. H. (1986) , *Wind Effects on Structures: An Introduction to Wind Engineering*, 2 sub edn, Wiley-Interscience.
- Steinman, Boynton, Gronquist and Birdsall (1988) , Bridge cable investigation program: Final report submitted to the New York State Dept of Transp. and New York City Dept. of Transp., New York, N.Y. Williamsburg Bridge Technical Advisory Committee., *Technical report*, Columbia University.
- Strang, G. (1986) , *Introduction to applied mathematics*, Wellesley - Cambridge press.
- Tomassini, M. (1995) , A survey of genetic algorithms, *Annual Reviews of Computational Physics* **3**.
- Vanmarcke, E. (1983) , *Random Fields: Analysis and Synthesis*, The MIT Press.
- Vincenzi, L. and Savoia, M. (2006) , Identificazione dinamica attraverso algoritmi di ottimizzazione evolutivi, *in* F. Ubertini, E. Viola, S. de Miranda and G. Castellazzi (eds), *Proceedings of the 16th Meeting of the Italian Group of Computational Mechanics, GIMC2006*.
- Viola, E. and Bocchini, P. (2007) , Identification of damaged bars in three-dimensional redundant truss structures by means of genetic algorithms, *Key Engineering Materials* **348-349**, 229–232.
- Wang, D. Q., Chukova, S. and Lai, C. D. (2005) , Reducing quadratic programming problem to regression problem: stepwise algorithm, *European Journal of Operational Research* **164**(1), 79–88.
- Yamazaki, F. and Shinozuka, M. (1988) , Digital generation of non-Gaussian stochastic fields, *Journal of Engineering Mechanics* **114**(7), 1183–1197.

-
- Yang, J. N. (1972) , Simulation of random envelope processes, *Journal of Sound and Vibration* **25**(1), 73–85.
- Yang, J. N. (1973) , On the normality and accuracy of simulated random processes, *Journal of Sound and Vibration* **26**(3), 417–428.
- Zerva, A. (1992) , Seismic ground motion simulations from a class of spatial variability models, *Earthquake Engineering & Structural Dynamics* **21**(4), 351–361.

Curriculum Vitae



Paolo Bocchini received his Laurea Degree (equivalent to the Bachelor and Master of Science degrees) with highest honor in Civil Engineering from the University of Bologna in 2004. In the same year, he received also the Degree of the “Collegio Superiore Alma Mater Studiorum” (for details refer to www.collegio.unibo.it) and obtained the Licence of Professional Engineer.

From January 2005 to December 2007 he attended the Ph.D. program in Structural Mechanics at the University of Bologna.

From August 2006 to July 2007 he attended the Civil Engineering and Engineering Mechanics Department of Columbia University as Visiting Scholar.

Since 2005 he has been working as Lecturer and Teaching Assistant at the Schools of Engineering and Architecture of the University of Bologna.

Contacts

DISTART Department – Scienza delle Costruzioni
School of Engineering
Alma Mater Studiorum – University of Bologna

Viale del Risorgimento 2,
40136 Bologna - Italy
Phone: +39 0512093377
Mobile: +39 3479787325
Fax: +39 0512093495
E-mail: paolo.bocchini@unibo.it